



University
of Glasgow

Bellini, Eleonora (2011) *Characterisation of magnetic nanostructures for spintronic applications by electron microscopy*.
PhD thesis.

<http://theses.gla.ac.uk/3011/>

Copyright and moral rights for this thesis are retained by the author

A copy can be downloaded for personal non-commercial research or study, without prior permission or charge

This thesis cannot be reproduced or quoted extensively from without first obtaining permission in writing from the Author

The content must not be changed in any way or sold commercially in any format or medium without the formal permission of the Author

When referring to this work, full bibliographic details including the author, title, awarding institution and date of the thesis must be given

Characterisation of magnetic nanostructures for spintronic applications by electron microscopy

Eleonora Bellini, M.Sc.



Presented as a thesis for the degree of Ph.D. at the
School of Physics and Astronomy, University of Glasgow

September 2011

@ Eleonora Bellini 2011

Lo duca e io per quel cammino ascoso
intrammo a ritornar nel chiaro mondo;
e sanza cura aver d'alcun riposo,
salimmo sù, el primo e io secondo,
tanto ch'i' vidi de le cose belle
che porta 'l ciel, per un pertugio tondo.
E quindi uscimmo a riveder le stelle.

(The Guide and I into that hidden road
Now entered, to return to the bright world;
And without care of having any rest
We mounted up, the first and I the second,
Till I beheld through a round aperture
Some of the beauteous things that Heaven doth bear;
Thence we came forth to rebehold the stars.)

Dante Alighieri, Inferno, XXXIV, 133 - 139

ABSTRACT

The work presented in this PhD thesis concerns the characterisation of the physical structure, composition and domain structure of advanced magnetic materials by electron microscopy within the FP6 European Research Training Network "Spinswitch". In particular the investigations concerned MgO/CoFeB/MgO multilayers to be employed in magnetic sensors (this work was done in collaboration with INESC-MN Lisbon-Portugal); $\text{Ni}_{80}\text{Fe}_{20}$ /Cu electrodeposited nanowires to be employed as spin transfer torque devices (this work was done in collaboration with NIRDTP Iasi-Romania and University of Salamanca); multilayers with perpendicular anisotropy which represent potential candidates to be employed in the next generation of MRAMs (this work was done in collaboration with Spintec-CEA-Grenoble).

Chapter 1 will provide an overview of the physics behind the topics treated during this work and a description of the general motivations of the research carried out. Chapter 2 will provide an overview of all the experimental techniques employed for the fabrication and characterisation of the samples investigated for this research.

Chapter 3 aims to present an investigation using conventional transmission electron microscopy (CTEM) and Lorentz microscopy (LTEM) to characterise respectively the physical microstructure and the domain structure of the CoFeB free layer, embedded in a multilayer composed by $\text{SiN}/\text{MgO}(50)/\text{CoFeB}(t)/\text{MgO}(15)$, with t from 30 Å down to 14 Å. We carried out first the investigation of the physical structure performed by selected area diffraction and bright field imaging of planar samples and physically the plan view sections show the structure of the films appears similar. The magnetization reversal behaviour observed during Lorentz TEM experiments are found to vary considerably with the CoFeB thickness, with both domain wall formation and magnetisation rotation seen. In the thicker film the behaviour was characteristic of a typical soft magnetic material with uniaxial anisotropy. However the magnetic reversal of the thinner film was more complex. A particular characteristic of the 14 Å CoFeB layer is the variation of domain wall angle seen when varying the orientation of the applied field. This wall asymmetry suggests the presence of a unidirectional anisotropic energy term. To assist in the interpretation of these experimental results a modified Stoner–Wohlfarth model has been constructed and calculations have been carried out by using a MATLAB code.

The purpose of the project presented in Chapter 4 was the advanced characterisation of multilayered electrodeposited NiFe/Cu nanowires grown in alumina and polycarbonate templates. In particular the objective was the characterisation of the structure and local chemistry of the nanowires by TEM and the classification of nanowire switching deduced by Lorentz microscopy experiments, which are challenging for this specific material system. In order to perform TEM studies on single nanowires, they should be extracted from their template. The chemical etching used to remove the nanowires from the template in addition to issues related to the deposition of Cu, led to nanowires with edge and compositional irregularities, detrimental for their magnetic properties. Indeed, we were not able to classify the nanowire switching and investigate domain walls forming during the reversal process, but we could only observe a change in the magnetising state. A lot of the work described in this chapter deals with the difficulties associated with imaging these challenging nanowires. Issues were discovered that may have resulted from deposition and/or etching for TEM preparation, therefore we do rely heavily on simulations and calculations.

The research presented in Chapter 5 will describe the investigation of the reorientation process of the easy axis for two different multilayer systems magnetised out of plane, and the evolution of their domain structure for increasing temperature, and trying to understand the role of the insertion of a Co/Pt/Ni/Pt multilayer from a microscopic point of view. The two multilayers represent the free layer of a perpendicular MTJ (pMTJ) and this study represents a state of development of materials for pMTJs. Experiments were performed by MOKE magnetometry in polar configuration and Lorentz Microscopy in Fresnel mode. Materials were prepared in Spintec-CEA, Grenoble (France) where the MOKE experiments were also carried out, and Lorentz Microscopy experiments were performed in Glasgow. For the first multilayer (with Co/Pt/Ni/Pt) we found that for lower temperatures (25°C - 220°C) the specimen appears to have a strong perpendicular anisotropy. We observed a small scale random domain structure that we can ascribe to perpendicularly magnetised domains. For higher temperatures (220°C - 300°C) we found a behaviour typical of a soft magnetic material magnetised in plane with low anisotropy and high susceptibility. For the second multilayer (without Co/Pt/Ni/Pt), for instrumental reasons, we were not able to investigate the magnetic behaviour of the specimen for temperatures above 110°C. The magnetisation is out of plane for all the temperatures investigated. The sample develops a different domain structure when the sample is heated below 100°C or above 100°C. In the first case isotropic serpentine domain structure is

visible, with a large periodicity, whereas in the second case, an anisotropic stripe domain structure is visible with a small periodicity.

ACKNOWLEDGMENTS

Another step of my life is getting close to the end and I wish to say thanks to all those who gave a contribution to my work in these years, in terms of help, advices and support. First and foremost I would like to thank my first supervisor Dr Stephen McVitie and Prof John Chapman, my second supervisor during my first year, for their excellent guidance, support and advices for which I am really grateful. A little thank you also to my second supervisor during my second and third year, Dr Damien McGrouther.

A special thank to Dr Donald MacLaren for the patience and support with MATLAB, Dr Ian MacLaren for guidance and support with EELS and EFTEM, Dr Sam McFadzean for guidance and support with EDX and all the work he does to have all the labs working as much as possible. I would like to thank Colin, Brian, Billy and Lucy for their great support and all the people of the SSP group I had the pleasure to work with. I would like to say thanks to the all Spinswitch members. A particular thanks goes to: Prof. Burkard Hillebrands, Dr Britta Leven, Florin Ciubotaru, Philipp Pirro and all the PhD students and Post Docs of the Group of Prof. Hillebrands from the Technical University of Kaiserslautern (Germany) for their great hospitality, support and excellent training during my secondment; Prof Bernard Dieny, Sebastien Bandiera, Dr Christian Papusoi and Dr Jérôme Moritz from Spintec- CEA Grenoble (France) for useful discussions, training and guidance during my secondment at Spintec; Prof. Luis Lopez Diaz for his support with OOMMF simulations. Mauricio, Spyros, Elzibieta, Joao, Rita, Florin for fun and laughs during the social times at the Spinswitch meetings. A big thanks goes to the European Commission for financial support.

Now it is the turn of the closest people in Glasgow...Dr Rumyana Petrova for her friendship and support during the last months of my stay in Glasgow and Dr Kerry O'Shea for great training in Fresnel imaging, excellent support for everything and helpfulness, and Dr Riccardo Bassiri for great chats. They all made the difference! Thanks to Teresa & Sancta Familia's people for friendship and hospitality in the last four months of my stay in Glasgow; Marzia and Guy for their friendship, chats and hospitality; Angie & family for their friendship.

The last, but not the least...A huge thanks to my parents for their huge love and support...without them I wouldn't have made it...to Nunzio for his love, his patience, his

advices and his help. My grannies, my cousin Maria, my brother and my sister in law. Antonio Mattia for his help with the Visual Basic script to rotate OOMMF data of my nanowires. The friends from the non-profit organisation "Cercasi un Fine": Pino G., Antonella, Domingo, Pasquale, Franco G., Franco F., Carole, Massimo, Emanuele, Pino F., and in particular Prof Rocco D'Ambrosio for his spiritual guidance and support. Claudia and Mina for their friendship and nice evenings-out. Luisa and Davide from "Laicità e Diritti". Finally all my students from "Liceo G.Galilei" and "Scuola Media Galileo Galilei", and the students I tutored, Annamaria and Piercosimo.

DECLARATION

This thesis is a record of the work carried out by myself in the Solid State Physics Group of the School of Physics and Astronomy at the University of Glasgow during the period 2007 - 2010. The work described herein is my own work with the exception of: growth and VSM hysteresis loops of MgO/CoFe/MgO multilayers carried out by Dr. Jangwei Cao from INESC-MN Lisbon (Portugal); electrodeposition of nanowires and chemical etching of the template carried out at NIRDTP Iasi (Romania); OOMMF micromagnetic simulations of nanowires were performed by Prof Luis Lopez Diaz from University of Salamanca (Spain); growth and MOKE hysteresis loops of multilayers with perpendicular anisotropy was carried out by Sebastien Bandiera from Spintec - CEA Grenoble (France).

Some of the work reported in this thesis was presented at the following conferences:

1. E.Bellini, J.N.Chapman, K.O'Shea, S.McVitie, *TEM Characterisation of CoFeB-based structures for MTJ sensor applications*, **SPINSWITCH Workshop- Spin Momentum Transfer**, Krakow, Poland, 3- 5 September 2008.
2. E.Bellini, S.McVitie, K.O'Shea, J. Chapman, J. Cao, S. Cardoso, *TEM Characterisation of CoFeB ultrathin films for MTJ sensor applications*, **Spin Torque Transfer and Domain Wall Dynamics - SPINDYNAMICS Summer School**, Iasi, Romania, 14- 18 September 2009.
3. E. Bellini, S. McVitie, K. O'Shea, J. N. Chapman, J. Cao, S. Cardoso and P.P. Freitas, *TEM Characterisation of CoFeB ultrathin films for Magnetic Tunnel Junction sensor applications*, **Fourth Seeheim Conference on Magnetism**, Frankfurt, Germany, 28th March - 1st April 2010.

This thesis has not previously been submitted for a higher degree.

TABLE OF CONTENTS

CHAPTER 1 - FUNDAMENTALS OF FERROMAGNETISM AND SPINTRONICS

1.1	Introduction.....	1
1.2	Fundamentals of ferromagnetism.....	2
1.3	Introduction to Magnetic Energy Terms.....	5
1.3.1	Exchange Energy.....	5
1.3.2	Anisotropy Energy.....	6
1.3.3	Magnetostatic Energy.....	8
1.3.4	Zeeman Energy.....	10
1.3.5	Magnetostriction.....	10
1.3.6	Total Energy and micromagnetic equation.....	11
1.4	Micromagnetic Simulations.....	12
1.5	Magnetic domains and domain walls.....	13
1.6	Hysteresis loops.....	18
1.7	Stoner - Wohlfarth model.....	19
1.8	Fundamentals of Spintronics.....	23
1.8.1	Giant Magnetoresistance and spin valve.....	24

1.8.2 TMR and Magnetic Tunnel Junctions.....	25
1.8.3 Spin transfer torque.....	27
1.8.4 Introduction to thermally assisted MRAMs based on perpendicular MTJ....	27
Bibliography.....	35
 CHAPTER 2 - INSTRUMENTATION AND EXPERIMENTAL TECHNIQUES	
2.1 Introduction.....	40
2.2 Samples preparation.....	40
2.2.1 Sputtering deposition technique.....	41
2.2.2 Electrodeposition of nanowires in porous templates.....	44
2.3 Transmission Electron Microscopy.....	47
2.3.1 The electron gun.....	48
2.3.2 The microscope column.....	49
2.3.2.1 The condenser system.....	51
2.3.2.2 The objective and intermediate lenses.....	52
2.3.2.4 The camera.....	53
2.3.2.5 STEM systems.....	53
2.4 TEM diffraction and Imaging.....	54

2.4.1 Diffraction.....	56
2.4.2 Bright field and dark field imaging.....	59
2.4.3 High Resolution Imaging.....	60
2.5 Lorentz Microscopy.....	62
2.5.1 Fresnel Mode.....	64
2.5.2 Differential Phase Contrast Mode.....	67
2.6 Analytical Techniques.....	70
2.6.1 Electron Energy Loss Spectroscopy.....	71
2.6.2 Energy Filtered Transmission Electron Microscopy.....	72
2.6.3 X-Ray Dispersive Spectroscopy.....	74
2.7 Polar Kerr Magnetometry.....	74
2.8 Summary.....	77
Bibliography.....	78

CHAPTER 3 - INVESTIGATION OF MgO/CoFeB/MgO MULTILAYERS FOR MAGNETIC TUNNEL JUNCTION SENSOR APPLICATIONS

3.1 Introduction.....	81
3.2 Fabrication of the samples.....	83
3.3 Investigation of the physical microstructure	85

3.4 Investigation of the magnetic structure.....	86
3.4.1 CoFeB 30 Å.....	87
3.4.2 CoFeB 14 Å.....	92
3.5 Interpretation of the results by means of Stoner-Wohlfarth model based calculations.....	98
3.6 Discussion on the physical meaning of the unidirectional term.....	108
3.6.1 Exchange bias: a brief overview.....	108
3.6.2 Possible evidence for an interfacial exchange bias effect.....	110
3.7 Summary.....	112
Bibliography.....	114
 CHAPTER 4 - INVESTIGATION OF ELECTRODEPOSITED Ni₈₀Fe₂₀/Cu NANOWIRES FOR APPLICATIONS IN SPIN TRANSFER TORQUE DEVICES	
4.1 Introduction.....	116
4.2 Nanowires grown in anodic alumina templates.....	118
4.2.1 Morphology.....	119
4.2.2 Physical Structure.....	120
4.2.3 Composition.....	122
4.3 Nanowires grown in polycarbonate templates.....	128

4.3.1 Physical Structure.....	129
4.3.2 Composition.....	133
4.4 Characterisation of magnetic properties of nanowires grown in polycarbonate templates.....	136
4.4.1 Fresnel Images Simulations.....	136
4.4.2 Experimental Fresnel Imaging.....	140
4.4.3 Micromagnetic Simulations.....	144
4.4.4 DPC Images Simulations.....	146
4.4.5 DPC Imaging.....	151
4.5 Summary.....	155
Bibliography.....	158
 CHAPTER 5 - INVESTIGATION OF TEMPERATURE-INDUCED ANISOTROPY CROSSOVER IN MAGNETIC MULTILAYERS FOR STORAGE APPLICATIONS	
5.1 Introduction.....	159
5.2 Experimental details.....	160
5.3 Investigation of the magnetic behaviour in temperature of Ta(3)/ Pt(20)/ (Co(0.45)/ Pt(0.6)/ Ni(0.5) / Pt(0.6)) ₃ / CoFeB(1.8)/ MgO(1.4) multilayer.....	165
5.3.1 Investigation of regime 1 (25°C < T < 130°C).....	165

5.3.2 Investigation of regime 2 ($130^{\circ}\text{C} < T < 220^{\circ}\text{C}$).....	169
5.3.3 Investigation of regime 3 ($220^{\circ}\text{C} < T < 300^{\circ}\text{C}$).....	173
5.4 Investigation of the behaviour in temperature of Pt(3)/ CoFeB(1)/ MgO(1.4) multilayer.....	176
5.5 Summary.....	182
Bibliography.....	186
 CHAPTER 6 - GENERAL SUMMARY AND FUTURE WORK	
6.1 Summary.....	187
6.2 Future work.....	192
 APPENDIX 1 - MATLAB CODE	 194

CHAPTER 1

Fundamentals of ferromagnetism and spintronics

1.1 Introduction

Thousands of years ago people discovered magnetism, and for many centuries magnetism has stimulated progress in science and technology. For a long time, the focus had been on macroscopic magnetism, as exemplified by the compass needle and by the ability of electromagnets and permanent magnets to do mechanical work. Atomic scale magnetic phenomena, such as quantum-mechanical exchange, crystal-field interaction and spin-orbit coupling, were discovered in the first half of the last century and are now exploited, for example, in advanced permanent-magnets. However, in recent decades new phenomena at the nanoscale were discovered and this has led to the development of a variety of magnetic nanostructures. The scientific and technological importance of magnetic nanostructures is due to three main reasons: first of all there is an overwhelming variety of structures with interesting physical properties; then the involvement of nanoscale effects in the explanation and improvement of the properties of advanced magnetic materials, and finally nanomagnetism has opened the door for completely new technologies.

The work presented in this PhD thesis fits in this frame, since it concerns the characterisation of the physical structure, composition and domain structure of advanced magnetic materials by transmission electron microscopy within the FP6 European project Spinswitch [1]. In particular the investigations concerned MgO/ CoFeB/ MgO multilayers to be employed in magnetic sensors [2] and described in chapter 3, Ni₈₀Fe₂₀/Cu electrodeposited nanowires to be employed as spin transfer torque devices and described in chapter 4 and multilayers with perpendicular anisotropy to be employed in the next generation of MRAMs (Magnetic Random Access Memories), described in chapter 5. This chapter will provide an overview of the physics behind the topics treated during this work and a description of the general motivations behind each single project.

1.2 Fundamentals of ferromagnetism

The story of magnetism begins with a mineral called magnetite (Fe_3O_4), the first magnetic material known to man. Its property of attracting iron was known 2500 years ago. In ancient China around 247 B.C. [33] it was found that a pivoted iron needle, if previously rubbed with magnetite, would turn until it pointed approximately north or south. This is the origin of the compass, an instrument used for navigation by the 11th century.

The first scientific study of magnetism was made by Gilbert, who published the book “On the Magnet” in 1600. In the book he reported his experiments performed with lodestones and iron magnets that allowed the scientist to acquire a clear picture of the Earth’s magnetic field. In 1820 Oersted discovered that an electric current produces a magnetic field. This was of great importance for the development of the first electromagnet in 1825 which was one of the founding steps of research on magnetism.

At the beginning of the 19th century, scientists such as Ampère [3], began to realise that magnetic materials consist of elementary magnets and these small components play a role analogous to atoms and molecules for ordinary materials. Moreover this theory explained the impossibility of isolating magnetic north and south poles, and the phenomenon of magnetic saturation in which all elementary magnets are oriented in the same direction.

In 1905 Langevin developed a theory of paramagnetism by using the methods of statistical thermodynamics [4]. He showed that independent molecular magnets at room temperature lead only to weak magnetic phenomena, and strong magnetism must be due to some interaction among the elementary magnets. The last idea of Langevin about strong magnetism was elaborated by Weiss in 1907 [5]. He followed Van der Waals’ treatment of the condensation of gases [6] and he introduced a “molecular field” to model the average effect of magnetic interaction. His theory succeeded in deriving the general shape of the temperature dependence of magnetisation. Adjusting the strength of the interaction so that the observed Curie temperature is reproduced, Weiss formally obtained a very large “molecular field”. This field was later identified by Heisenberg as due to the quantum-mechanical exchange effect [7]. Moreover in his original work he just mentioned the possibility that a crystal can be composed of regions with different orientation of magnetisation without giving a name to these substructures. Nowadays the term domain

structure has been adopted to describe the subdivision into uniformly magnetized regions inside a magnetic material.

The first confirmation of the domain concept was provided by Barkhausen [8]. He discovered that the magnetization process is often discontinuous, giving rise to a characteristic noise when made audible by an amplifier. This was first interpreted as domain switching. Langmuir [9] analyzed the dynamics of this process, and he concluded that the discontinuities in the magnetising process could be due to the propagation of a boundary between domains (domain walls) of opposite magnetization. This hypothesis was then confirmed by the experiments of Sixtus and Tonks [9] who followed the propagation of a the domain boundary in a stressed wire. The first theoretical analysis of the boundaries between domains was carried out by Bloch [10]. He found that the walls must have a width of several hundred lattice constants due to the balance between Heisenberg's exchange interaction which tend to increase the width of the wall and the anisotropy that tend to decrease the width of the wall. Wide domain walls effectively average over local inhomogeneities, such as point defects; this result explain why domains walls can be so easily moved as observed in the Sixtus and Tonks experiment.

Akulov [11], Becker [12] and Honda [13] investigated the effects of anisotropies, magnetostriction, and internal stresses on magnetic microstructure. Their most important result was that crystal anisotropy (the preference of the magnetization vector to align with so called easy crystal axes) and magnetostriction (the spontaneous deformation of the crystal related to the magnetization direction) are independent material properties that cannot be derived from the Weiss theory of ferromagnetism or from Heisenberg's exchange interaction but are connected to spin-orbit coupling effects.

Frenkel and Dorfman [14] and Heisenberg [15] introduced the magnetic dipole interaction in the theory. They realized that the magnetic dipole interaction, known as magnetostatic energy or stray field energy was missing. It was also well understood that a uniformly magnetized single crystal carries an excess energy (the demagnetizing energy) which can be large compared to the usual anisotropy energies in certain materials. In some cases demagnetising energy is high, depending on the specific configuration.

In 1931 Håmos and Thiessen [16], and Bitter [17] showed the first pictures of magnetic micropatterns obtained with the help of an improved powder method. Even if none of the observed structures could be understood in detail at that time, the pictures demonstrated

that domains are static, they could be rather wide and they frequently had a periodic and regular appearance.

Landau and Lifshitz in 1933, stimulated by these first observations and by the first theoretical analysis done by Bloch, affirmed that domains are formed to minimize the total energy, an important part of which is the stray field energy [18]. Landau and Lifshitz also clarified a number of issues that were still debated at that time. They argued that the exchange interaction tends to align the neighbouring dipoles and causes them to act together; thermal agitation plays a role only in small particles or at temperatures close to the Curie point and under normal circumstances the equilibrium magnetic microstructure must be considered athermal.

The model of Landau and Lifshitz proved to be too simple to explain actual observations. Starting from their basic ideas, refinements and extensions were contributed in succeeding years. Experimental methods had improved considerably and in the article of Williams, Bozorth and Shockley (1949) the identity between domains of domain theory and the observed magnetic microstructure was convincingly demonstrated [19]. In the same year Kittel reviewed domain theory and experiments [20], and this review became the generally accepted reference for domain research.

In the last 20 years a new field has emerged due to the need to understand what happens when magnetic systems are reduced to nanoscale. The study of the novel physical phenomena that arise from miniaturisation is known as magnetism in a small scale [21]. These phenomena occur because magnetic processes are characterised by specific length scales. When the physical size of a magnetic system is engineered to dimensions comparable to or smaller than these characteristic lengths, novel behaviour is observed, including, for example, giant magnetoresistance (GMR), tunnel magnetoresistance (TMR), which are transport properties influenced by magnetism, perpendicular anisotropy, etc. [21]. These phenomena place ultimate limits on device performance, improve current technology or generate new technology, and it is these ultimate materials/device engineering interests which are driving research in magnetism in a small scale. The electronics, data storage and computer industries are continuously pushing the limits of technology, trying to make things better, faster and cheaper. This has led to the development of novel devices as well as advancements in GMR for read heads in data storage, the investigations into domains in granular media for data storage, magnetic field

sensing for automotive sensors (and other applications which require sensors), MRAM and many others [21].

1.3 Introduction to Magnetic Energy Terms

Most of the characteristic mesoscopic length scales, as for example, domain size, domain wall width, exchange length, perpendicular anisotropy threshold in thin films are governed by minimisation of energy considerations. The balance among the energy terms present in the magnet (exchange, anisotropy, magnetostatic, Zeeman and magnetoelastic) defines the size of domains and the width of domain walls [21]. Different domain structures are possible, depending on what energy contribution is dominant and what the magnetic history is. In many materials three different energy terms dominate domain formation: magnetostatic (the energy due to the field produced by the magnet), exchange (the energy proportional to the angle between two spins), anisotropy (the energy proportional to the orientation of the magnetization relative to the crystalline axes) [22], although in soft materials (with low or zero anisotropy) only exchange and magnetostatic energy contribute to domain formation. In the next sections a description of all the energy terms mentioned before will be provided.

1.3.1 Exchange Energy

First proposed by Vleck [23], the energy term related to ordering, i.e. the energy required to align neighbouring magnetic moments parallel - ferromagnetic configuration - or antiparallel - antiferromagnetic configuration, is called the exchange energy E_{ex} . Direct exchange interaction is the sum of all of the different interactions, spin-spin, spin-orbit etc. The quantum mechanical expression is:

$$E_{ex} = -J\vec{S}_1 \cdot \vec{S}_2 \quad (1.1)$$

where J is the exchange parameter and it is in the order of 10^5 m^{-1} [24] and $\vec{S}_{1,2}$ is the spin of the electron. The classical expression is:

$$E_{ex} = -\sum_{i>j} 2J_{ij}\vec{S}_i \cdot \vec{S}_j \quad (1.2)$$

where J is the exchange integral linking the i -th atom with spin \vec{S}_i to the j -th atom with spin \vec{S}_j . Using the classical expression (eq. 1.2) and assuming that only the nearest neighbour interactions are important, the energy per unit area can be determined for a specific crystal lattice to be:

$$E_{ex} = \int_{-\infty}^{+\infty} \frac{JS^2}{a} (\nabla \vec{M})^2 dr^3 = \int_{-\infty}^{+\infty} A (\nabla \vec{M})^2 dr^3 \quad (1.3)$$

where $A = JS^2/a$ is the exchange stiffness constant (for example $A=13 \times 10^{-12}$ J/m for Permalloy [25]) and a is the lattice parameter. The exchange energy, results in a characteristic exchange length for the material defined as $l_{ex} = \sqrt{A/\mu_0 M_s^2}$, i.e. the distance over which it is energetically favourable for all of the magnetic moments to be aligned. For Permalloy l_{ex} is 4 nm [26].

1.3.2 Anisotropy Energy

The energy of a ferromagnet depends also on the direction of magnetisation relative to the crystallographic directions of the material. This dependence, which results from spin-orbit interactions, is described by the magnetocrystalline anisotropy energy. It is the energy required to rotate the entire magnetisation vector without changing the relative orientations of the spins. Therefore, when the magnetic moments are directed along certain axes called the easy axes, which are determined by the symmetry of the crystal, the energy is minimised. Along other directions, called hard axes, the energy is maximised.

For hexagonal or uniaxial materials, the anisotropy energy can be expressed in a series expansion. Taking into account only the first term of the series, the energy can be expressed in first order approximation as [27]:

$$E_K = \int K_u \sin^2 \varphi dV \quad (1.4)$$

where φ is the angle between the anisotropy axis and magnetisation direction. Typical values of anisotropy constant K_u can go up to 10^7 J/m³ for permanent magnet materials [28].

In the case of a cubic crystal, the anisotropy energy can be written in terms of the direction cosines ($\alpha_1, \alpha_2, \alpha_3$) of the magnetisation vector \vec{M} with respect with the three cube edges in first approximation as [27]:

$$E_K = \int \left[K_1 (\alpha_1^2 \alpha_2^2 + \alpha_2^2 \alpha_3^2 + \alpha_3^2 \alpha_1^2) + K_2 \alpha_1^2 \alpha_2^2 \alpha_3^2 \right] dV \quad (1.5)$$

where $K_{1,2}$ are the anisotropy constants. Typical values for the constant K_1 are of the order of $\pm 10^4 \text{ J/m}^3$ for Fe [28] and -10^3 J/m^3 for Ni [29] and for the constant K_2 are of the order of $\pm 10^2 \text{ J/m}^3$ for Fe and -10^3 J/m^3 for Ni [29]. The sign of K_1 and K_2 determines whether the $\langle 100 \rangle$ ($K_{1,2} > 0$) or the $\langle 111 \rangle$ ($K_{1,2} < 0$) directions are the easy directions for magnetisation [27].

In polycrystalline materials the constituent grains can be oriented randomly in space, and in this case the anisotropy of individual grains will average out and the whole body will exhibit no overall anisotropy. In such a random oriented material, the local variation of magnetisation leads to the formation of ripples in TEM Fresnel images and this phenomenon will be described in detail in chapter 2.

Another form of anisotropy can be present. This is the surface-interface anisotropy, introduced by Néel in 1954 [30], effect attributed to the prominent presence of symmetry breaking elements such as planar interfaces and surfaces, which affects particularly such systems as ultrathin magnetic films and multilayers. One manifestation of this effect is the change in the preferential direction of magnetisation from the commonly observed in plane to the direction perpendicular to the plane [31]. This phenomenon is usually referred to as perpendicular magnetic anisotropy (PMA) and it is particularly important for data storage applications, and the balance between this anisotropy term and the volume anisotropy described above will determine the behaviour of $(\text{Co/Pt/Ni/Pt})_x/\text{CoFeB}$ multilayers that will be described in chapter 5. In a structurally isotropic medium, magnetic surface-interface anisotropy can be expressed to first order as [27]:

$$E_K = \int K_S \left[1 - (\vec{M} \cdot \hat{n}) \right] dS \quad (1.6)$$

where K_s that has dimensions of J/m^2 is the surface-interface anisotropy constant and its order of magnitude ranges from 10^{-3} to 10^{-4} J/m^2 ; \vec{M} represents the magnetisation vector and \hat{n} is the surface normal.

Equation 1.4 applies also if a uniaxial anisotropy is induced in the material. This can be achieved because the symmetry of the crystal is reduced, as in the case of polycrystalline or amorphous materials, or artificially by deposition of the material and annealing in a magnetic field. The induced uniaxial anisotropy is present both in the CoFeB layer within the MgO/CoFeB/MgO multilayers described in chapter 3 as well as in the magnetic multilayers with perpendicular anisotropy described in chapter 5 where it represents the volume contribution to the total anisotropy. For example, typical values for uniaxial anisotropy in CoFeB are of the order of 10^4 J/m^3 [32].

1.3.3 Magnetostatic Energy

A uniformly magnetised domain produces free surface magnetic poles (N and S), which give rise to stray fields and, therefore, magnetostatic energy. This energy term is given by [27]:

$$E_d = \frac{1}{2} \mu_0 \int_{\text{allspace}} H_d^2 dV = -\frac{1}{2} \mu_0 \int_{\text{sample}} \vec{H}_d \cdot \vec{M} dV \quad (1.7)$$

Where \vec{H}_d is the stray field generated by the divergence of the magnetization \vec{M} . The average stray field can be written as [33]:

$$\vec{H}_d = -N_d \vec{M} \quad (1.8)$$

where N_d is the demagnetising factor and its value depends mainly on the shape of the body and has a single calculable value only for an ellipsoid. In general it depends on the geometry of the sample, but also on the permeability of the material [33].

The stray field can be calculated easily for simple cases, as for example, an infinitely extended plate. In this case the magnetisation direction depends only on the z coordinate, as fig.1.1 shows, and the integration of eq.1.7 yields:

$$H_d = -\frac{M_S}{\mu_0} M_z(z) \quad (1.9)$$

$$E_d = \frac{M_S^2}{2\mu_0} M_z^2(z)$$

This solution applies also if the magnetisation distribution has a cylindrical symmetry [34] as it is the case of the electrodeposited nanowires described in chapter 4.

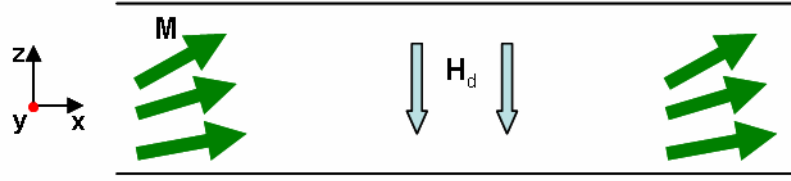


Figure 1.1: Overview of the stray field in a one-dimensional magnetisation distribution. The figure shows the cross section through a plate that is infinitely extended along the x,y plane. The y axis is directed inside the plane of the page.

An effect related to the magnetostatic energy is the shape anisotropy. This effect tends to dominate over magnetocrystalline anisotropy in polycrystalline specimens having no preferred orientation of their grains and a weak magnetocrystalline anisotropy. In order to describe shape anisotropy, let's assume a prolate spheroid with semi-major axis c and semi-minor axis a and that the magnetisation \vec{M} makes an angle ϕ with the c axis. It can be demonstrated that the magnetostatic energy E_d can be expressed as [33]:

$$E_d = \mu_0 \left[\frac{1}{2} M^2 N_c + \frac{1}{2} (N_a - N_c) M^2 \sin^2 \phi \right] \quad (1.10)$$

where N_c and N_a are the demagnetising coefficients along c and a respectively. This expression for the magnetostatic energy has an angle-dependent term of exactly the same form as uniaxial anisotropy energy. The long axis of the specimen plays the same role as the easy axis of the crystal and the shape anisotropy constant K_s is given by [33]:

$$K_S = \frac{1}{2} \mu_0 (N_a - N_c) M^2 \quad (1.11)$$

Its units are J/m^3 and its value depends on the axial ratio c/a which determines $N_a - N_c$ and on the magnitude of the magnetisation \vec{M} . Taking into account the values of $N_a - N_c$ as a function of c/a calculated by Stoner and Wohlfarth [35], the shape anisotropy constant K_s can be determined as a function of c/a for a prolate spheroid of polycrystalline Co with no preferred orientation. At an axial ratio of about 3.5, $K_s = 4.5 \times 10^6 \text{ J/m}^3$. This will be equivalent to the magnetocrystalline anisotropy constant of Co, thus the prolate spheroid, in this case, is equivalent to a cobalt crystal with uniaxial anisotropy [33].

1.3.4 Zeeman Energy

When the specimen is placed in an external field, the magnetic moments within the specimen will tend to align parallel to the applied field. The energy term associated with this phenomenon is called Zeeman energy and it takes into account the orientation of the magnetisation with respect to the applied field. It is given by [28]:

$$E_Z = -\mu_0 \int \vec{H}_{ext} \cdot \vec{M} dV \quad (1.12)$$

where H_{ext} is the external applied field.

1.3.5 Magnetostriction

Magnetostriction is the strain resulting from a change in dimensions of a ferromagnetic material [22] or the change in the magnetic properties produced by an applied stress. This effect was first discovered by Joule in 1847 [36]. From the phenomenological point of view two forms of magnetostriction can be distinguished: spontaneous magnetostriction arising from the ordering of magnetic moments into domains at the Curie temperature T_c , and field induced magnetostriction arising when domains with spontaneous magnetostriction are reoriented under the action of a magnetic field. In both cases the magnetostriction is defined as the fractional change in length $\lambda = dl/l$. The saturation magnetostriction λ_s occurs when the magnetisation in the direction of the magnetic field has a value of M_s for the material. For example, a film of Permalloy has a saturation magnetostriction λ_s in the range $\pm 2 \times 10^{-6}$ [37] where the \pm sign depends on whether a tensile (-) or compressive (+) stress is applied.

The associated energy term arises from the interaction of the strain in the lattice and the magnetisation and is given by [28]:

$$E_\lambda = \int \frac{3}{2} \lambda_s \sigma \sin^2 \alpha \, dV \quad (1.13)$$

where σ is the applied tensile force that causes the stress in the system and α is the angle between the direction of saturation magnetisation and σ . From this it can be determined that for magnetising a sample in a particular direction there is a magnetostrictive energy cost. For the samples investigated in this thesis, magnetostriction effects were minimal.

1.3.6 Total Energy and micromagnetic equation

The different energy terms described in the previous sections allows the determination of the total energy for a given configuration:

$$E_{tot} = E_{ex} + E_k + E_d + E_z + E_\lambda \quad (1.14)$$

The system tend to the lowest energy state which is the sum of these five energy terms. The competition of these interactions under different conditions is responsible for the overall behaviour of a magnetic system.

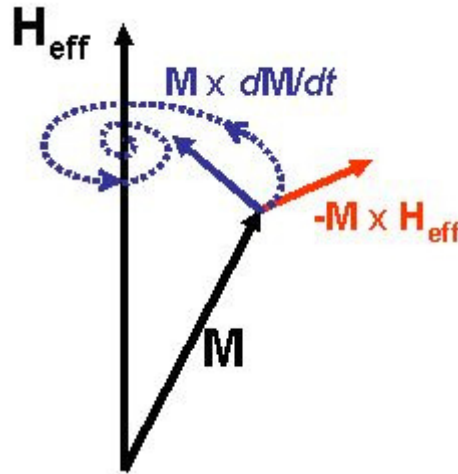


Figure 1.2: Representation of the dynamics of the magnetisation vector \vec{M} with respect to an effective field \vec{H}_{eff} . Vectors shown in bold. From [38].

The dynamics of a magnetic system is governed by the Landau-Lifshitz-Gilbert (LLG) equation [18]:

$$\frac{\partial \vec{M}}{\partial t} = -\gamma \vec{M} \times H_{eff} + \frac{\alpha}{M_s} \vec{M} \times \frac{\partial \vec{M}}{\partial t} \quad (1.15)$$

This equation describes the time evolution of the magnetisation vector as a function of the effective field within the material. γ represents the gyromagnetic ratio ($\gamma = 2.21 \times 10^5$ mA/s²) and it is the ratio between the magnetic dipole moment and the angular momentum. This first term describes the precession of the magnetisation vector. The second term represents a dissipation term. The dissipation is described phenomenologically by the damping coefficient α , which is material dependent. The term \vec{H}_{eff} is derived from eq.1.14 by variational calculus [28]. Fig. 1.2 represents a schematic of the precessional motion of the magnetisation vector.

1.4 Micromagnetic Simulations

The Object Orientated Micromagnetic Framework (OOMMF) [39] is a micromagnetic modelling package developed at the National Institute of Standards and Technology (NIST) [40]. It allows the user to simulate possible magnetization configurations that will be supported in a particular nanomagnet, as a consequence of the various energy terms in the system. This software has been used by Prof. L. L. Diaz at University of Salamanca (Spain) to simulate the easy axis behaviour of a multilayered electrodeposited nanowires and the output results of micromagnetic simulation have been used in chapter 4 to perform the calculations of the respective Fresnel and DPC images. The program determines the effective field at every point in a cell (2D or 3D), followed by calculation of the magnetisation by solving the Landau-Lifshitz equation (eq.1.15). The cell size is comparable with the exchange length of the simulated material and each cell is uniformly magnetised. With each spin iteration, the equation is re-evaluated until an equilibrium value is reached. The optional control point determines the conditions that cause the applied field to be stopped, or more precisely, end the simulation of the magnetization evolution for the current applied field. There are 3 recognized control point types: torque, time, and iteration. If a torque is given, then the simulation at the current applied field is ended when $\|M \times H\| / M_s^2$ at all spins in the simulation is smaller than the specified torque value. If a time is given, then the simulation at the current field is ended when the elapsed simulation time for the current field step reaches the specified time value. Similarly, an iteration steps the applied field when the iteration count for the current field

step reaches the iteration value. If multiple control point specifications are given, then the applied field is advanced when any one of the specifications is met.

1.5 Magnetic domains and domain walls

All energy terms described in the previous sections contribute to domain formation, even though in some materials two or three of them may dominate. Here we will focus on the effect of the magnetostatic energy on domain formation. The origin of domains can be understood by considering the structures in fig.1.3 representing a cross section of a large rectangular magnet with uniaxial anisotropy. In (a) a single domain is represented: as a consequence of the magnetic poles formed on the surface of the crystal, the configuration will have high values of magnetostatic energy with energy density of the order of 10^5 J/m^3 and M_s of the order of 10^3 A/m . In (b) the magnetostatic energy is reduced considerably by dividing the crystal in two domains magnetised in opposite directions, but this was achieved at the expense of an increase in exchange energy due to the formation of a domain wall. In (c) further domains reduce the magnetostatic energy of (a) because of the reduced spatial extension of the field, but this increases further the exchange energy. The configuration in (d) is the one with the lowest magnetostatic energy for hard materials with cubic anisotropy, but again a reduction in magnetostatic energy is balanced with an increase of exchange and anisotropy energy; (e) is the configuration with the lowest magnetostatic energy for materials with uniaxial anisotropy along the length and again the reduction of the magnetic moment is balanced by an increase in anisotropy and exchange energy. Domain structures are often more complicated than our simple examples, but a change in domain structure has always its origin in the possibility of lowering the energy of a system [41].

Domain boundaries are transition regions where spins gradually change their direction from one domain to the other. These transition layers are called domain walls. The reason why spins change their direction gradually is that the exchange energy of spin pairs increases as the square of the angle between neighbouring spins so that an abrupt change in the angle increases the exchange energy to a great extent. Thus the exchange energy tries to make the wall as wide as possible. On the other hand, the direction of each spin in the wall deviates from the easy axis, so that anisotropy energy is stored in the wall, thus the anisotropy energy tries to make the wall as narrow as possible in order to reduce the number of spins pointing in non-easy directions. As a result of this competition, the wall in

general has a nonzero width and a definite structure. Therefore the width of the wall, δ , for a 180° wall, is given by [24]:

$$\delta = \pi \sqrt{\frac{JS^2}{Ka}} \quad (1.14)$$

where J is the exchange integral, S is the spin of the electron, K is the anisotropy constant and a is the lattice constant. This equation applies for divergent walls (Bloch walls) in bulk materials. For example the wall width for Fe is $\delta = 4.2 \times 10^{-8}$ m. It has been assumed that the normal component of magnetisation is continuous across a domain wall so that no magnetic free poles exist in the wall (fig.1.4(a)). However, such a spin rotation must produce free poles on the sample surface where the domain wall terminates. In thick samples, these surface free poles have little effect, but in thin samples their contribution to the total energy of the system may not be negligible.

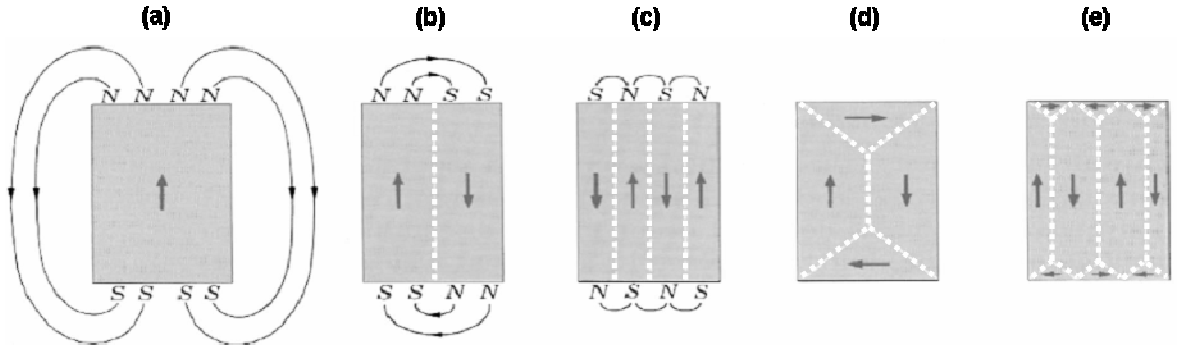


Figure 1.3: Overall pattern of domain formation in a large rectangular magnet. The dark grey arrows indicate the magnetization direction of each domain, the dashed white lines represent the domain walls. From [41].

Moreover, like any other interface, the wall has an energy per unit area of its surface, because the spins in it are not parallel to one another and not parallel to an easy axis. Thus the total energy of the wall per unit area γ in equilibrium state is given by [24]:

$$\gamma = E_{ex} + E_K = 2\pi \sqrt{\frac{JS^2 K}{a}} \quad (1.15)$$

For Fe $\gamma = 1.12 \times 10^{-3}$ J/m². Eq. (1.14) and (1.15) are obtained with the prior assumption that the rotation of spins occurs at constant rate.

Néel pointed out that in the case of very thin films a rotation of the spins in a plane parallel to the film surface (fig.1.4(b)) has less magnetostatic energy than rotation in a plane parallel to the wall [42] when the wall width is smaller than the sample thickness, because the demagnetising factor here is smaller than the demagnetising factor for a Bloch wall [27]. This type of wall is called Néel wall and is stable for relatively thin films, whereas the former one is called Bloch wall and it is stable for relatively thick films. The Néel wall energy is given by [24]:

$$\gamma = 4 \sqrt{A \left(K + \frac{M_s^2}{2\mu_0} \right)} \quad (1.16)$$

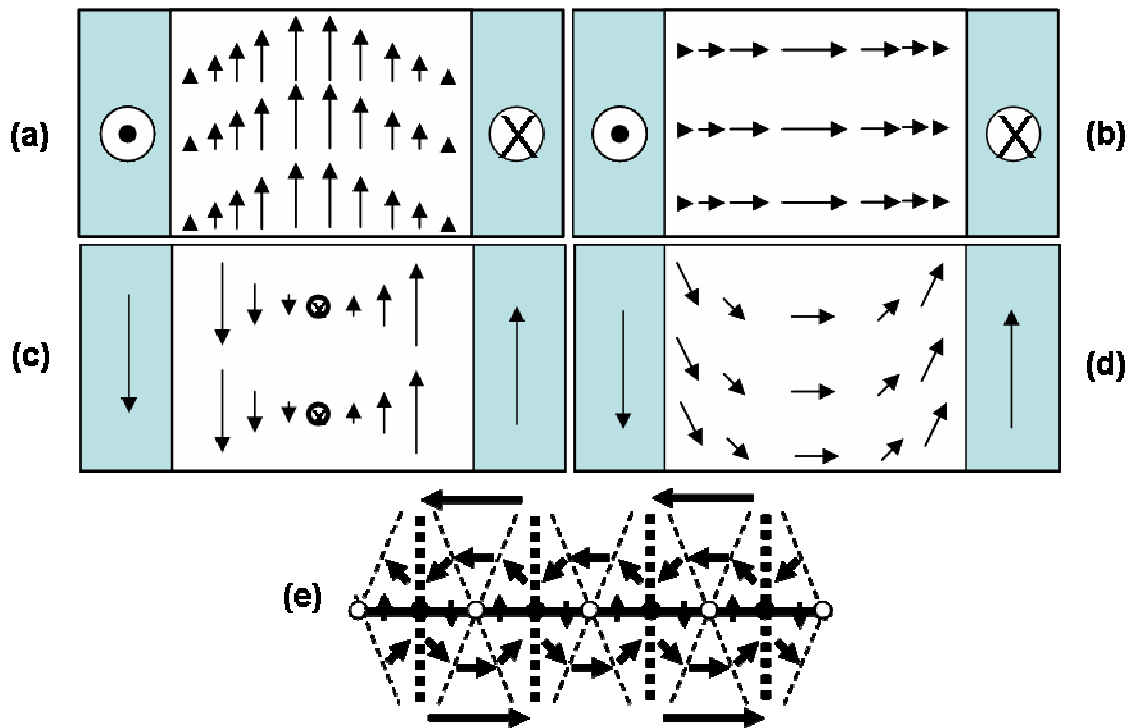


Figure 1.4: Cross section of a Bloch (a) and Néel (b) wall and plan view of a Bloch (c), Néel (d) and cross-tie (e) domain wall in a generic ferromagnetic film.

Fig.1.5 shows the variation of the wall energy as a function of the thickness of the specimen in a Permalloy film. For thicknesses lower than 40 nm Néel wall is the favoured configuration because it has lower energy than the Bloch wall; for thicknesses higher than 100 nm the Bloch wall is favoured. For intermediate values, depending on the thickness and width of the wall, a variety of different domain wall configurations, that combine the basic Néel and Bloch type walls, are possible [27]. One of the simplest examples is the cross-tie wall where the energies of both types of domain wall are comparable [43]. In this

wall, Bloch-type and Néel-type spin configuration appear alternatively along the wall. The spin arrangement on both sides of the wall is modified and results in cross-ties, where the spin direction changes discontinuously. An example of cross-tie wall is depicted in fig. 1.4(e).

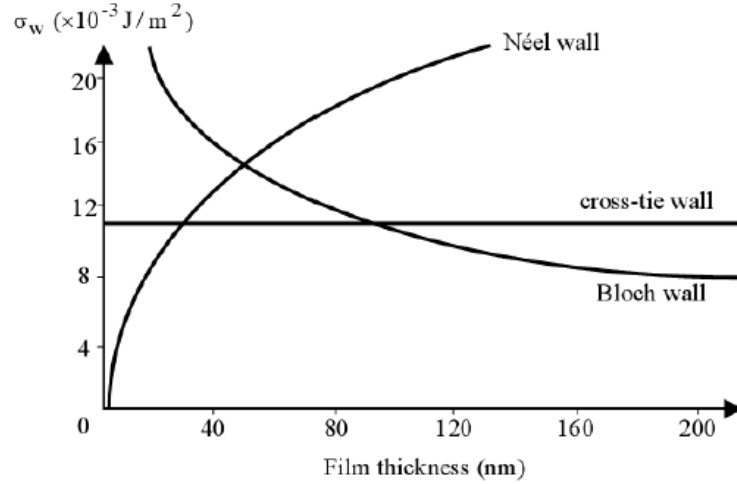


Figure 1.5: Phase diagram of wall types (Bloch, Néel, cross-tie) in a Permalloy film. It shows energy density of the wall as a function of film thickness. From [44].

Magnetic nanowires, fabricated by lithography or focused ion beams, are currently the subject of much interest with potential applications in logic devices and as memory storage [45, 46]. Much of the research has focused on planar nanowires and the behaviour and structure of the domain walls (DWs) that are present in such nanowires. Here, novel domain wall types emerge, when the wall spin structures start to be dominated by the geometry rather than by the intrinsic materials properties. This is particularly true for soft magnetic materials, where the effects of magnetocrystalline anisotropy and other material-dependent anisotropies are small and the element shape governs the domain wall spin structures. In soft magnetic nanostructures, the stray field energy leads to an alignment of the magnetization with the edges of the structures, in order to minimize the stray field. Thus, in elongated elements, such as wires, for example, the magnetization points along the long axis of the element and most often such a (quasi-) monodomain state constitutes the lowest energy magnetization configuration [47]. If such a structure is not in a monodomain state two domains with opposite direction exist (see figure 1.6(a)), and a 180° head-to-head domain wall has to be present in between the domains (blue area in figure 1.6(a)).

Nakatani, Thiaville and Miltat derived the phase diagram of the domain wall structure and the diagram of the wall-width parameter in Permalloy strips by micromagnetic simulations [48]. They predicted three different spin structures, the transverse wall (TW), the vortex wall (VW), and the asymmetric transverse wall (ATW). A schematic of these structures is depicted in fig.1.6(b-d). Each of these structures occurs depending on the ratio between the width of the strip w and the thickness η as visible from the diagram in fig. 1.6(e).

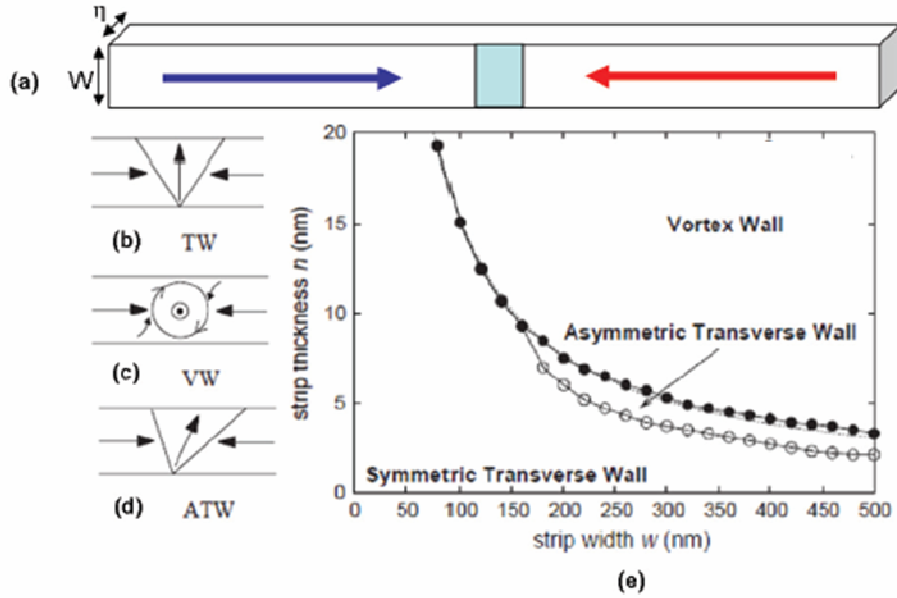


Figure 1.6: (a) Schematic of a nanowire with two domains pointing in opposite directions (red and blue arrows) and a domain wall (blue area) separating the domains. Domain wall structures in magnetic nanostrips with longitudinal magnetization. (b) (symmetric) transverse wall (TW), (c) vortex wall (VW), (d) asymmetric transverse wall (ATW). (e) Phase diagram of the domain wall structure in strips of Permalloy where w is the width of the strip and η is its thickness. From [48].

Electrodeposition into porous templates has proven to be a valid alternative to prepare a variety of magnetic nanowires and multilayers. The template allows for unidirectional growth, making it easy to vary the composition of the nanowire in the axial direction. As a result, a nanowire of the desired material is obtained within each pore [49]. For the electrodeposited nanowires investigated in this thesis, micromagnetic simulations performed by Prof. Luis Lopez Diaz at University of Salamanca (Spain), predicted the formation of vortex states. It has been revealed both theoretically and experimentally that for particular ranges of dimensions of cylindrical and other magnetic elements (Fig. 1.6) a curling in-plane spin configuration (vortex) is energetically favoured, with a small spot of the out-of-plane magnetization appearing at the core of the vortex [27, 29, 50]. It is

characterized by two binary properties, a chirality (counter clockwise or clockwise direction of the in-plane rotating magnetization) and a polarity (the up or down direction of the vortex core's magnetization).

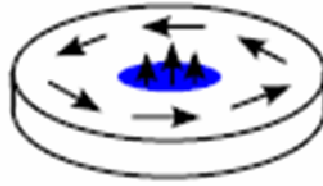


Figure 1.7: Examples of vortices appearing in a cylindrical element. Each vortex's center contains an out-of-plane polarized core except for the ring. In a multilayered element each ferromagnetic layer behaves as a single disk.

1.6 Hysteresis loops

A great deal of information can be learned about the magnetic properties of a material by studying its hysteresis loop. A hysteresis loop depicts the relationship between the magnetic induction (B) and the magnetic field (H). It is often referred to as the B-H loop. An example hysteresis loop is shown in fig.1.7. A ferromagnetic material that has never been previously magnetized or has been thoroughly demagnetized will follow the dashed line as H is increased. At point "a" almost all of the magnetic domains and the material has reached the point of magnetic saturation. When H is reduced to zero, the curve will move from point "a" to point "b." At this point, it can be seen that some magnetic flux remains in the material even though the magnetic field is zero. This is referred to as the point of remanence B_R on the graph and indicates the level of residual magnetism in the material. As the magnetic field is reversed, the curve moves to point "c", where the flux has been reduced to zero. This is called the point of coercivity H_C on the curve. As the magnetic field is increased in the negative direction, the material will again become magnetically saturated but in the opposite direction (point "d"). The behaviour of the curve from "d" back to "a" is exactly symmetric to behaviour of the curve from "a" to "d".

The coercivity is a very important parameter, since it allows to distinguish, for example, if the specimen is a hard or soft magnetic material [22]. In the first case the coercivity will be quite large as, for example in CoPt, and in the latter case it will be small as it is the case for all the specimens investigated in this thesis where the material used are, for example $Ni_{80}Fe_{20}$ and CoFeB. Hard materials are used mainly as permanent magnets, because their

high coercivity makes them resistant to the action of stray fields. Soft materials are used as flux multipliers and as microwave system components [33].

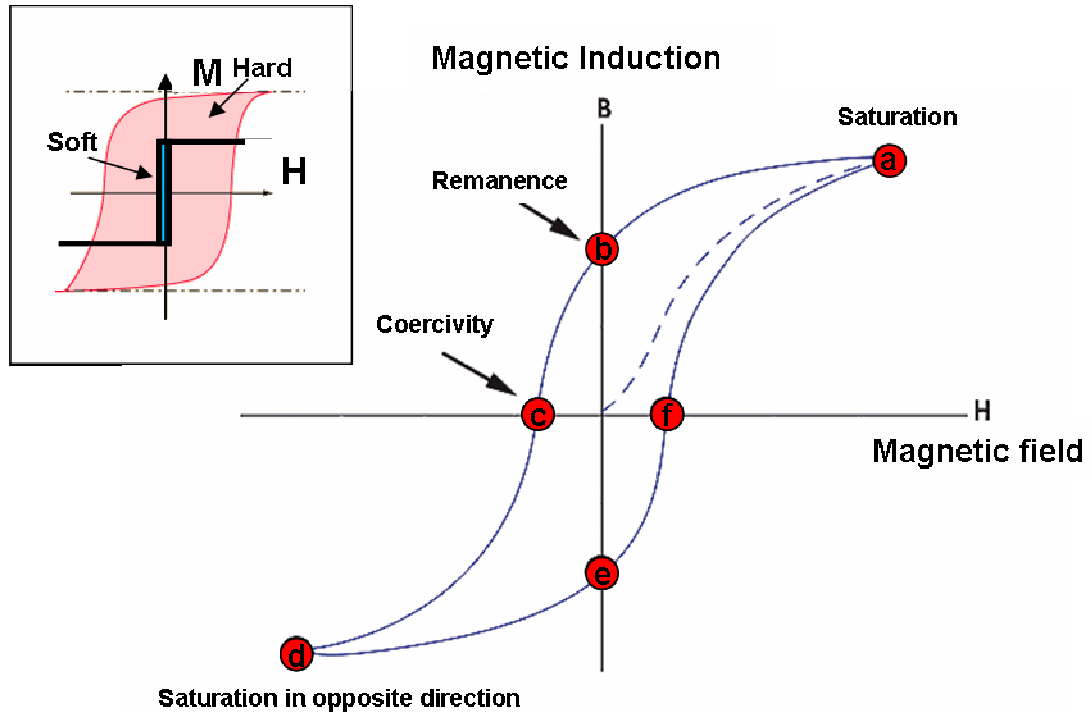


Figure 1.8: Schematic of a hysteresis loop. From [51]. In the inset a typical hysteresis loop of a hard and soft material.

1.7 Stoner - Wohlfarth model

The Stoner and Wohlfarth (SW) model [35], in its original formulation, describes how to obtain the direction of the magnetisation in a uniformly magnetised ellipsoid, where the orientation of magnetisation is dependent on the magnitude and direction of an external field with respect to the principal axes of the ellipsoid. Because of the complexity of a direct microscopic description of magnetic systems, the SW model can represent a good approximation to describe the physics of fine magnetic grains, the magnetization of which can be used, for example, in digital magnetic storage. The need of high density storage leads to finer magnetic grains and smaller size leads to magnetic grains so fine that they contain a single magnetic domain, i.e. a region in the material with a well defined uniform magnetization best described with the mathematics of the SW model. The model doesn't take into account that magnetic materials, in general, possess a multidomain structure, approximates grains as ellipsoids with uniaxial anisotropy (even though Fe and Ni possess cubic anisotropy) to simplify calculations. However, the SW provides a good overall

picture in uniformly magnetized materials even if some inadequacies exist in explaining some experimental details.

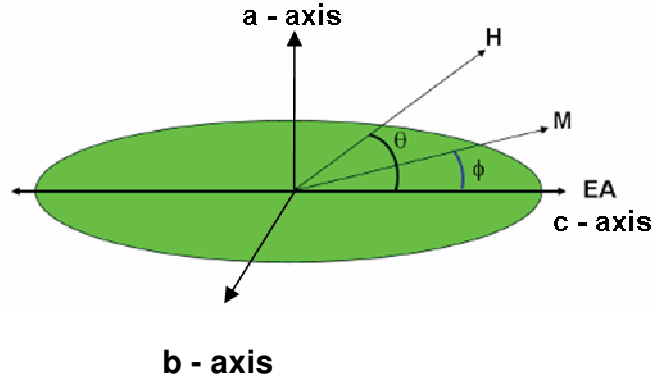


Figure 1.9: Two dimensional ellipsoidal grain with its easy axis along the longest axis and the angles ϕ and θ , that represent the orientation of the magnetization and field with respect to that axis.

In order to describe the model in its original formulation, consider a prolate ellipsoid with volume V_0 , uniformly magnetised, with uniaxial anisotropy aligned along the c-axis of the ellipsoid (fig.1.9). The energy terms acting on the particle are the magnetocrystalline anisotropy (eq. 1.4), the magnetostatic energy (eq.1.10) and the Zeeman energy (eq.1.12). Thus the total energy E can be expressed as:

$$E = K_u V_0 \sin^2 \phi + \frac{1}{2} \mu_0 M_s^2 V_0 ((N_a - N_c) \sin^2 \phi + N_c) - \mu_0 M_s V_0 H \cos(\theta - \phi) \quad (1.17)$$

where ϕ is the angle that the magnetisation \vec{M} makes with the c-axis of the ellipsoid and θ is the angle that the applied field makes with the easy axis, as depicted in fig.1.9. If we divide by $\mu_0 M_s^2 V_0$, neglect the constant terms that will disappear in the minimisation process and factorise, we get:

$$E' = \frac{1}{2} \left(\frac{2K_u}{\mu_0 M_s^2} + N_a - N_c \right) \sin^2 \phi - \frac{H}{M_s} \cos(\theta - \phi) \quad (1.18)$$

The terms inside the first set of brackets can be considered an effective anisotropy constant K_{eff} and the ratio H/M_s can be called h_a . If we set $h_{az} = h_a \cos \phi$ and $h_{a\perp} = h_a \sin \phi$ which are respectively the components of the applied field along the anisotropy direction, eq.1.18 becomes:

$$E' = \frac{1}{2} K_{eff} (1 - \cos^2 \phi) - h_{az} \cos \theta - h_{a\perp} \sin \theta \quad (1.19)$$

The magnetisation will align such that the total energy is minimised. The orientation change might occur smoothly (rotation) or suddenly (switching) implying that the magnetization is discontinuous at some values of the magnetic field H which are called switching fields. The equilibrium configuration can be found analytically by mean of the relationships $\partial E'/\partial \phi = 0$ and $\partial^2 E'/\partial \phi^2 = 0$. The solution of these equations leads to the expression for the Stoner and Wohlfarth astroid:

$$\begin{cases} h_{az} = -K_{eff} \cos^3 \phi \\ h_{a\perp} = K_{eff} \sin^3 \phi \end{cases} \quad (1.20)$$

In fig. 1.10 an example of Stoner and Wohlfarth astroid is provided. The plot works in such a way that when the applied field has components such that the point $(h_{az}, h_{a\perp})$ lies outside the astroid, only one minimum of energy is present, and this will represent the equilibrium position for the magnetisation. As soon as the is such that the point $(h_{az}, h_{a\perp})$ lies inside the astroid, the situation is more complicated since there exist two minima of energy. Which one will be reached by magnetization depends on the dynamics of magnetization motion.

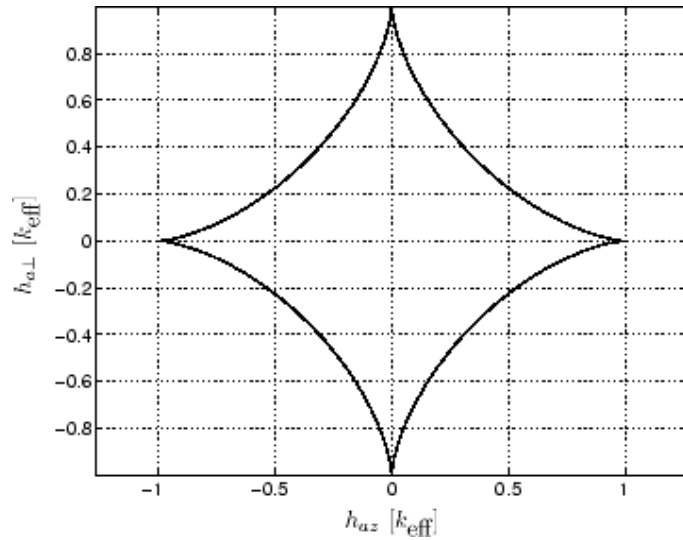


Figure 1.10: Representation of the Stoner and Wohlfarth astroid in the $h_{az}, h_{a\perp}$ plane. From [82].

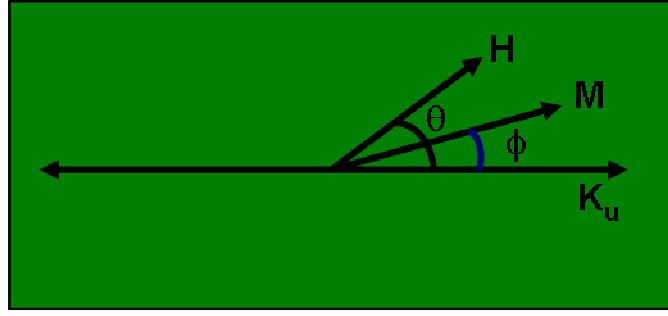


Figure 1.11: Schematic of a film in the approach of the SW model. The parameter involved in the model are present: the anisotropy axis K_u , the magnetisation M and its orientation ϕ with respect to the anisotropy axis and the applied field H and its orientation θ with respect to the anisotropy axis.

As mentioned at the beginning of this section, the Stoner and Wohlfarth model can also be used to describe a granular film, where each grain is a single domain particle, as the one described above, and the grains behave coherently as a single magnetic domain (fig.1.11), thus all multi-domain related effects, non-uniformities or inhomogeneities are not considered. A single domain occurs when the size of the grain is smaller than some critical length (4 nm^3) and contains about 10^{12} - 10^{18} atoms. In standard ferromagnetic transition metals (Fe, Ni and Co), the characteristic size is typically within a few 100 nm range. Also in this case, the magnetisation M is subjected to two competing alignment forces: one is due to the combination of shape and uniaxial anisotropy (K_{eff}) which tends to align M along the easy direction and the other is due to an external magnetic field H which tries to align M along its direction. The total energy is given by:

$$E = K_{eff} \sin^2 \phi - H\mu_0 M_s \cos(\theta - \phi) \quad (1.21)$$

We can simplify this equation and we can reduce the number of free parameters involved in this model with the introduction of the reduced energy functional $\Gamma = 2E/\mu_0 M_s$ and we can rewrite equation 1.21 as:

$$\Gamma = H_k \sin^2 \phi - 2H \cos(\theta - \phi) \quad (1.22)$$

where $H_k = 2K_u/\mu_0 M_s$ is called anisotropy field and can be determined experimentally from the slope break of the hysteresis loop when $\theta = 90^\circ$, implying the field H is along the hard axis. The equation cannot be solved analytically, except for $\theta = 0, \pi/4, \pi/2$. In all the other cases, an easy method to find solutions to the equation is to plot the reduced energy functional Γ as a function of ϕ for fixed values of θ and for different magnitudes of the

applied field, as shown in fig.1.12, and look for the minimum of energy, which will provide the orientation of the magnetisation for a given set of free parameters. This will be used in chapter 3 to model the behaviour of a CoFeB ultrathin film.

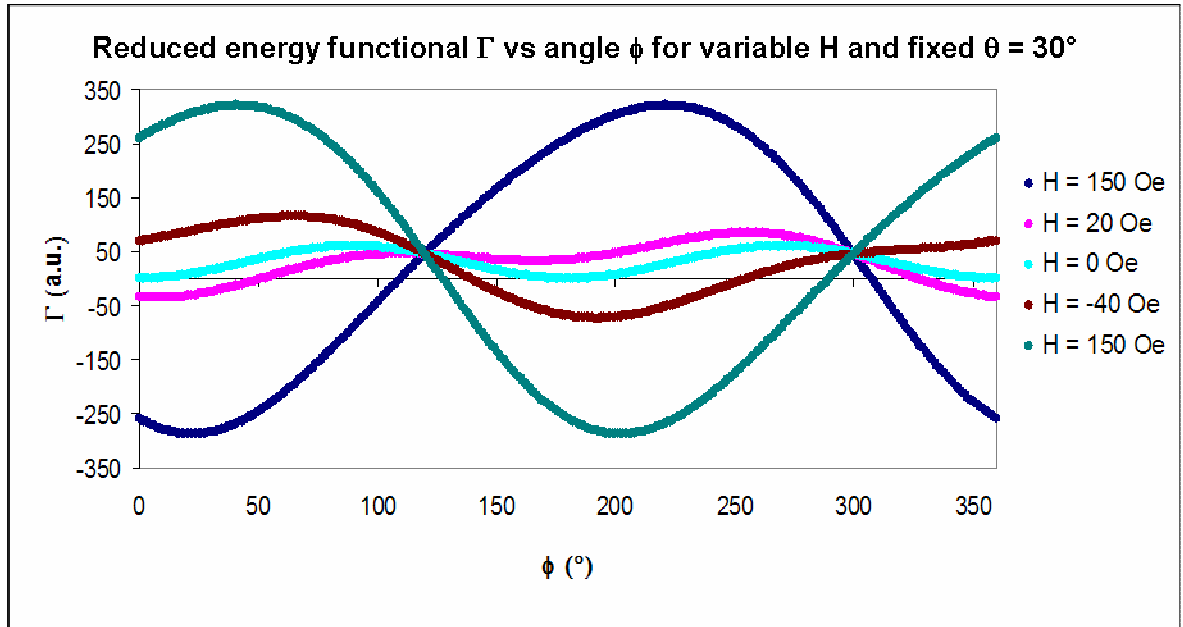


Figure 1.12: Variation of the energy landscape with angle ϕ for different values of the magnetic field H . The field orientation is held fixed at the value $\theta = 30^\circ$ with the anisotropy axis.

1.8 Fundamentals of Spintronics

Spintronics [52], which stands for Spin Transport Electronics, is an emerging field of technology which exploits two fundamental properties of the electron, the spin, in addition to the charge, traditionally used in solid state devices. One of the branches of spintronics, the metal-based spintronics, develops and improve new devices based on magnetic materials. Among the most important devices developed up to now are the spin valve, whose working principle is the giant magnetoresistance (GMR), the magnetic tunnel junction whose working principle is the tunnel magnetoresistance (TMR) and devices based on spin transfer torque, as for example the spin torque oscillators and SST-MRAMs. The research presented in this thesis will describe the characterisation of the physical structure, composition and domain structure of materials to be employed in magnetic tunnel junctions (MTJs), MRAMs and spin transfer torque based devices. In particular the investigations concerned MgO/CoFeB/MgO described in chapter 3, Ni₈₀Fe₂₀/Cu electrodeposited nanowires described in chapter 4, multilayers with perpendicular anisotropy described in chapter 5.

1.8.1 Giant Magnetoresistance and spin valves

The interdependence between magnetisation and charge transport was discovered in 1851 when William Thomson observed for the first time the anisotropic magnetoresistance (AMR), which links the value of the resistance to the respective orientation of magnetisation and current [53]. Nevertheless the exploitation of this phenomenon occurred only in 1975, when a sensor using the anisotropic magnetoresistance (AMR) of alloy films to read back information had been described [54].

The discovery of the giant magnetoresistance (GMR) [55, 56] was triggered by the capability of building magnetic multilayers with individual thicknesses comparable to the spin mean free paths, and led soon to the achievement of the definition of the spin-valve sensor [57]. In its simplest form, the spin valve is a trilayer of two identical ferromagnetic layers F1 and F2 sandwiching a non-magnetic metal spacer layer M (Fig. 1.13 (a-b)). When the two magnetic layers are magnetized parallel (fig.1.13(a)), the spin-up electrons, less susceptible to scattering, can easily travel through the sandwich providing a conductivity shortcut and a low resistance. On the contrary, in the antiparallel case (fig.1.13 (b)), both spin-up and spin-down electrons are more susceptible to scattering in one FM layer, giving rise to a high resistance. The amplitude of the GMR is calculated as the relative magnetoresistance ratio $\Delta R/R = (R_{AP} - R_P)/R_P$, and the value achieved during the discovery was 80% in Fe/Cr multilayers. The rotation of the free F1 layer magnetization under the application of an external field "opens" (in P configuration) or "closes" (in AP configuration) the flow of electrons, acting as a sort of valve. The first spin valve based device, a spin valve sensor, was commercialised by IBM in 1997. A schematic of a typical spin valve is displayed in fig. 1.13(c). From top to bottom, it is composed by a capping layer (Ta), an antiferromagnetic layer (FeMn) whose role is the pinning of the magnetisation in the first ferromagnetic layer (Co, in this example), a spacer (Cu, non magnetic metal), the free layer (NiFe in this example), a buffer layer (again Ta) and finally the Si substrate. The spin valve structure can be more complex than the one just described, with a multilayered structure replacing a single layer, in order to improve the properties of the device [58].

1.8.2 TMR and Magnetic Tunnel Junctions

Another big step forward the development of spintronics came from the creation of the magnetic tunnel junction (MTJ) in 1975 by Jullière [59]. Intense research on MTJs has been carried out, not only because of academic interests but also due to interest in integrated spin-electronic components, such as magnetic random access memory or various types of analog high sensitivity field sensors [60].

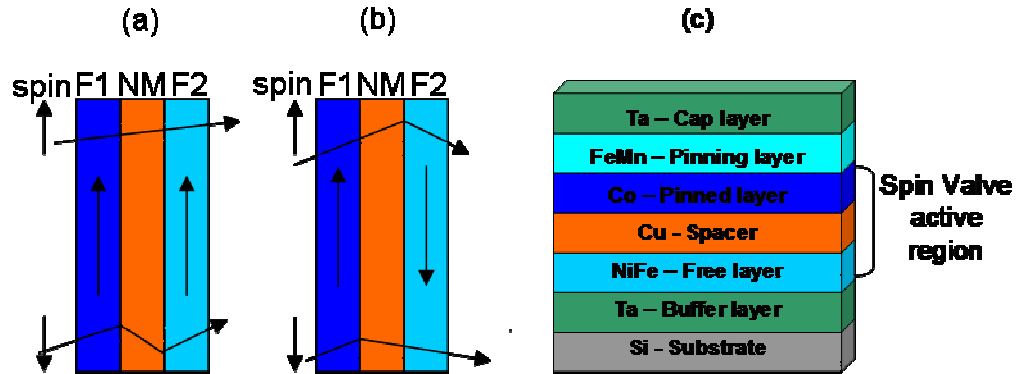


Figure 1.13: Schematic representation of the spin-valve effect in a trilayer film of two identical ferromagnetic layers F1 and F2 sandwiching a non-magnetic metal spacer layer NM, in parallel configuration (a) and antiparallel configuration (b). (c) Schematic of a typical spin valve composed by a multilayered structure required to improve the properties of the device.

In view of these interesting applications, the role of this research, in this project, was the investigation of the physical structure and the domain structure of a MgO/CoFeB/MgO trilayer which mimic the interface between the free layer and the barrier of a typical MTJ. This system was studied for different thicknesses of the CoFeB layer. This study is of high interest from the applicative point of view, because the performance of MTJ sensors depends critically on the way the magnetisation distribution evolves under the application of an external field which can be investigated with one of the TEM-based techniques, Lorentz microscopy. Moreover the magnetisation distribution can be dependent on the crystal structure, thus the investigations of the changes in the physical structure of the CoFeB layer, while reducing its thickness, can provide useful information. In addition, it provides an interesting insight into the fundamental micromagnetic properties of the material, especially for the lowest value of the thickness of the CoFeB layer. The outcomes of the investigation will be widely described in chapter 3.

A magnetic tunnel junction (MTJ), consists of a thin insulating layer (a tunnel barrier) sandwiched between two ferromagnetic (FM) metal layers. Analogously to the spin valve, briefly described in the previous section, the resistance of a MTJ depends on the relative magnetic alignment (parallel or antiparallel) of the electrodes as schematically illustrated in Fig.1.14. The change in resistance with the relative orientation of the two magnetic layers, is called tunnelling magnetoresistance (TMR) [61] and is defined in the same way as the relative magnetoresistance ratio $\Delta R/R$ in section 1.8.1. The origin of TMR arises from the difference in the electronic density of states at the Fermi level between spin-up and spin-down electrons, as explained in detail in [61].

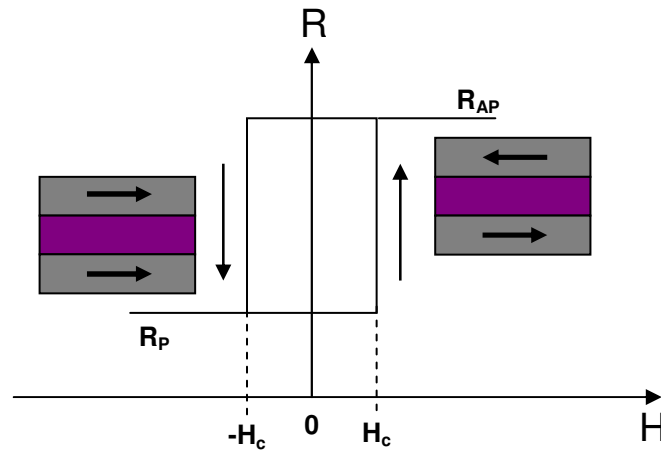


Figure 1.14: A typical magnetoresistance transfer curve of for a basic MTJ. H_c denotes a coercive field for the free layer of MTJ.

MTJs for practical applications need to have the stacking structure shown in figure 1.15. That is, they need to have a seed layer, an antiferromagnetic (AF) layer, a synthetic ferromagnetic structure (pinned layer), a tunnel barrier and a ferromagnetic layer (free layer). IrMn or PtMn are typically used as the antiferromagnetic layer for exchange-biasing. The top ferromagnetic layer acts as the free layer. The synthetic ferrimagnetic (SyF) structure, which consists of an antiferromagnetically coupled FM/NM/FM trilayer such as CoFe/Ru/CoFe, is exchange-biased by the AF layer and acts as the pinned layer. This type of pinned layer structure is indispensable for device applications because of its robust exchange-bias and small stray magnetic field acting on the top free layer [61].

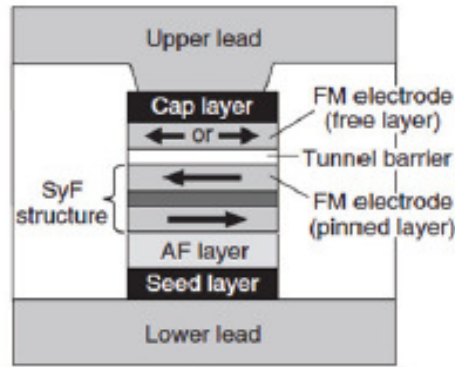


Figure 1.15: Schematic of the cross section of a typical MTJ developed for device applications. From [61].

1.8.3 Spin transfer torque

The spin transfer torque (SST) effect was predicted in 1996 [62, 63] when it was found that the magnetization orientation of a free magnetic layer could be controlled by direct transfer of spin angular momentum from a spin-polarized current. The spin-transfer phenomena have important applications as, for example coupled nano-oscillators [64, 65] and SST-MRAM [66-70], which require high control on the structural, magnetic, and compositional properties of the component materials. This was performed in this research and will be subject of chapter 4, where electrodeposited $\text{Ni}_{80}\text{Fe}_{20}/\text{Cu}$ nanowires (employed as oscillators) will be described, and chapter 5, where an investigation of the magnetic behaviour for increasing temperature of multilayers magnetised out of plane (employed for SST-TA MRAMs), will be presented.

1.8.4 Introduction to thermally assisted MRAMs based on perpendicular MTJ

Magnetic random access memories (MRAMs) integrate a magnetoresistive device with a silicon-based selection matrix. The key attributes of MRAM are non-volatility, low voltage operation and unlimited read and write endurance combined with fast read and write operation (in the GHz range). These characteristics give MRAM the potential to replace current memory types in specific applications. The interest in MRAM started almost 30 years ago with a cross-tie RAM concept [71], followed by the use of the anisotropic magnetoresistance (AMR) materials [72], later replaced by higher sensitivity giant

magnetoresistance (GMR) devices [73] and more recently using spin dependent tunnel junctions [61, 74].

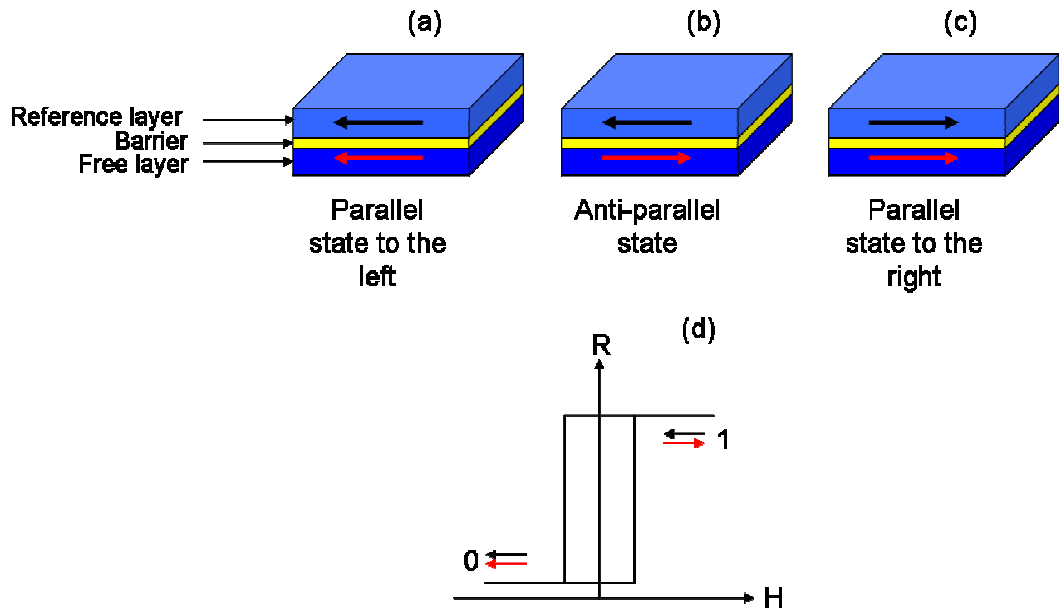


Figure 1.16: Schematic of the possible states of a MTJ, where we show only the reference layer, the barrier and the free layer. (a) MTJ in parallel state to the left, (b) antiparallel state, (b) parallel state to the right. The arrows represent the magnetisation vectors in the ferromagnetic layers. (d) Schematic view of a hysteresis loop showing the reversal of the storage layer and two corresponding resistance levels: high 1 and low 0.

In its most simple implementation an MRAM cell is composed by a magnetic tunnel junction (MTJ) with a size of $0.1\ \mu\text{m}$, connected to a selection transistor [75]. The basic structure of a MTJ, depicted in fig.1.16(a-b), has a trilayer structure: a ferromagnetic reference layer with a fixed direction of magnetisation; an insulating tunnel barrier; a ferromagnetic free layer where the magnetisation can be parallel (fig.1.16a) or antiparallel (fig.1.16b) to the direction of magnetisation in the reference layer depending on the value of the applied field, as shown in the hysteresis loop in fig. 1.16c where we can also see that the resistance of the memory bit is either low or high depending on the magnetization orientation of the free layer relative to the reference layer, parallel or antiparallel.

To read one bit, the selection transistor is turned on, and a read current flows through the tunnel junction as shown in figure 1.17(a). At read, the selection transistor is closed (on) and a small electrical current can pass through the MTJ cell, allowing the measure of its resistance. At write, the selection transistor is open (off) and the combination of two orthogonal magnetic fields ensures the selectivity. The value of the junction resistance is

then compared to a reference resistance half-way between the high and low resistance values. Initially the bit writing process proposed for MRAM relied on two orthogonal magnetic fields being applied to a cell. This switching approach is based on a coherent magnetization reversal, Stoner – Wohlfarth model (section 1.7). The magnetic fields are generated by a current flow in two perpendicular running bit and digit lines as shown in figure 1.17(b). Only the bit at the intersection of these two lines will be subjected to the field combination necessary for the free layer switching. This coherent reversal can be achieved in a few nanoseconds (3–7 ns) [76, 77]. The scalability of MRAM to smaller bit sizes is faced with challenges. Reducing the size of the tunnel junction below $0.1 \mu\text{m}^2$ creates issues related to the device uniformity, control of switching field, power consumption and long term bit stability.

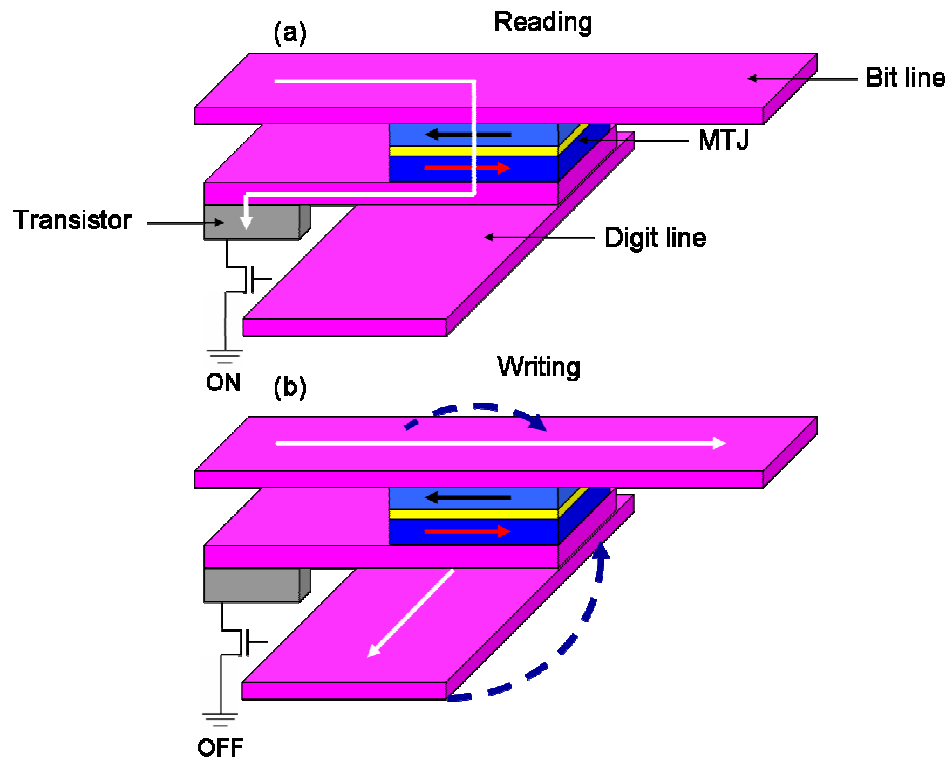


Figure 1.17: Reading (a) and writing (b) schemes used in the conventional MRAM architecture containing MTJ cells at the intersection of orthogonal writing lines and on top of a selection transistor. The white arrows represent the electrical currents, whereas the blue dashed arrows represent the lines of the magnetic field.

Recently a new write approach, called thermally assisted switching (TA-MRAM), was proposed to improve the thermal stability, write selectivity and power consumption in MRAM applications [67, 68]. In the scheme proposed by Dieny and Redon [69], the ordinary junction structure composed of a seed layer, an antiferromagnetic (AF) layer, a

synthetic ferromagnetic structure (pinned layer), a tunnel barrier, a ferromagnetic layer (free layer) and a capping layer, as described in section 1.8.2, is modified inserting an antiferromagnetic (AFM) layer which exchange biases the free layer. A schematic of this structure and the hysteresis loops at room temperature is shown in fig.1.18, where (a) represents the structure in the parallel state and (b) in the antiparallel state. The AFM layer is in both cases ferromagnetically coupled with the free layer.

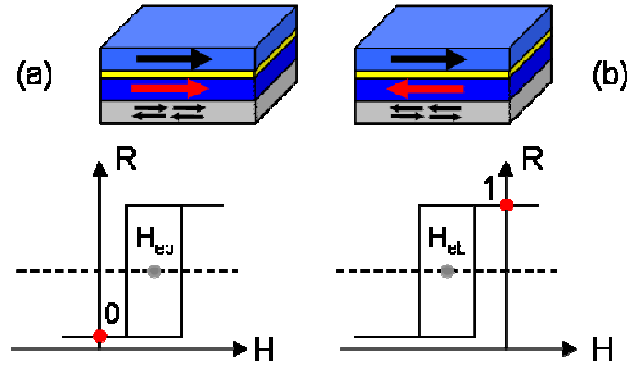


Figure 1.18: Schematic of the basic structure used for thermally assisted MRAM and hysteresis loop of the free layer in the parallel state (a) and antiparallel state (b). The gray layer is the antiferromagnetic layer used to exchange bias the free layer.

The writing scheme of a TA-MRAM, shown schematically in fig.1.19, works as follows. An external applied field set the initial orientation of the free layer to be parallel to the reference layer and the free layer is exchange biased by an AFM layer with its loop biased at positive field. This sets the bit in a low resistance state 0 as shown in fig.1.19(a). The reversal of the storage layer bias is achieved by heating the AFM layer above its blocking temperature T_b with a current pulse I_h (the blocking temperature is the temperature at or above which an antiferromagnetic layer loses its ability to "pin" the magnetization direction of an adjacent ferromagnetic layer and is usually lower than the Néel temperature) as shown in fig.1.19(b) - left. Simultaneously a current I_{sw} and an external magnetic field H_{sw} larger than the coercive field of the free layer are applied (fig.1.19(b)-center). The field is applied in a direction that favours the anti-parallel alignment of the free and reference layers and the magnitude of I_h , I_{sw} , H_{sw} strongly depends on the materials used for the free and AFM layer. The current pulse is, then, terminated and the system is cooled in a magnetic field (fig.1.19(b) - right). This maintains the free layer orientation. The reversal of the orientation of the free layer results in a bit state change to a high resistance 1 shown in fig.1.19(c). The free layer loop is now shifted towards negative values [79].

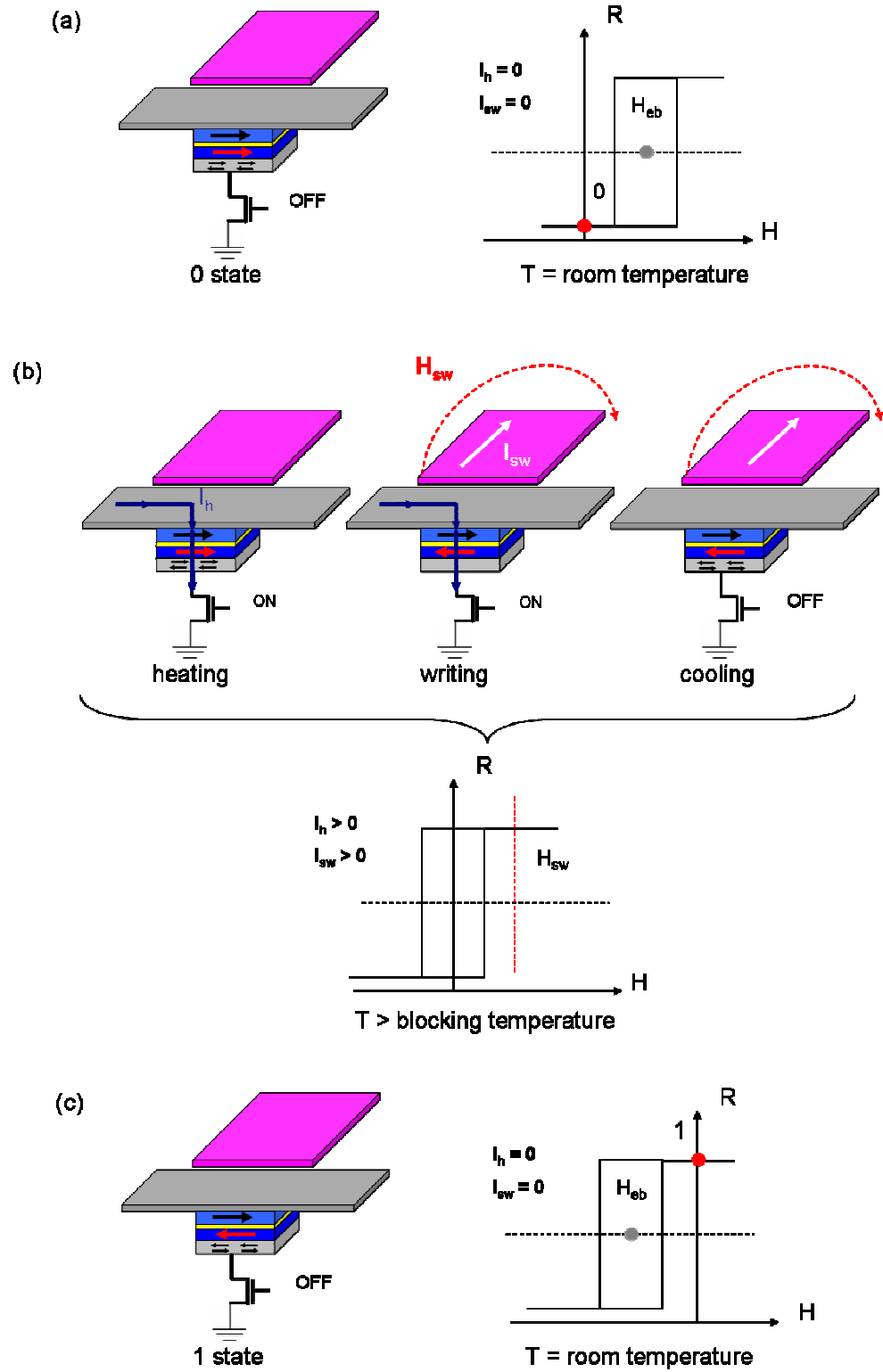


Figure 1.19: The writing steps of the thermally assisted switching approach. (a) Low resistance state 0 with the free layer biased at positive field. (b) Reversal of the free layer achieved heating the AFM layer above the blocking temperature T_b with a current pulse I_h and applying a magnetic field H_{sw} and a current I_{sw} . (c) The reversal of the free layer led to the high resistance state 1 with the free layer biased at negative field.

Thus, the write procedure implies heating the junction above the storage layer blocking temperature and cooling down in the presence of a magnetic field. The reference and the free layer must be exchange biased at different blocking temperatures. This is achieved using different AFM layers. This has multiple advantages and solves the limitations of the conventional MRAM architecture. First of all, as the write selection is temperature driven, a combination of magnetic field and heating current is needed to select a junction, virtually eliminating any addressing errors. Then, one single magnetic field is required to write, which leads to a reduced power consumption even in the presence of an additional heating current. The write power can be further reduced, by using circular elements with no shape anisotropy reducing the switching field. At the write temperature, the exchange bias vanishes. The bit orientation is then defined by the field setting the direction of the free layer during cooling [80]. At last the exchange bias anisotropy of the storage layer ensures the thermal stability and data retention for long time periods at the working temperature.

Spin-transfer torque (STT) switching demonstrated in 2005 in MgO MTJs with TMR 150% and small intrinsic switching current density [66] has stimulated considerable interest for developments of STT switched magnetic random access memory (STT MRAM). The main challenge for implementing STT writing mode in high-density and high-speed memory is the substantial reduction of the intrinsic current density J_{c0} required to switch the magnetization of the storage layer while maintaining high thermal stability required for long-term data retention. Minimal switching (write) current is required mainly for reducing the size of the selection transistor in series with MTJ to achieve the highest possible memory density, because the channel width of the transistor is proportional to the write current. Thus, a drastic decrease in the channel width is required for achieving ultimate smallest STT-MRAM cell size. Second, smaller voltage across MTJ decreases the probability of tunnelling barrier degradation and breakdown, ensuring write endurance of the device. This is particularly important for STT-MRAM, because both sense and write currents are driven through MTJ cells [70].

The reduction of the intrinsic switching current density J_{c0} (where J_{c0} is the current density required to switch a device for arbitrarily long pulse duration in the absence of thermal fluctuations at $T = 0K$) can be pursued through engineering materials and magnetic anisotropy and improvement in the MTJ and free layer structures. The main challenge associated with J_{c0} reduction is to lower J_{c0} while maintaining a high thermal stability $\Delta = K_u V / k_B T$ where $K_u V$ is the anisotropy energy and $k_B T$ the thermal energy. To

guarantee the bit information for long time periods it is necessary to take into account thermally activated switching processes. The energy barrier E_b between two stable magnetic configurations is proportional to the volume of the magnetic material, to the shape and uniaxial anisotropies and the saturation magnetization M_s . As the bit size is reduced, this energy barrier may become comparable to the thermal energy and unwanted thermally activated switching can occur, leading to data loss. The energy barrier is usually quoted as a dimensionless ratio to the thermal energy $\alpha = \Delta E / k_b T$. To guarantee thermal stability required for 10 years data retention a minimum energy barrier of $\alpha \approx 65$ is required [81]. The magnetic volume reduction associated with scaling must be compensated by higher anisotropy, leading to higher switching fields and an increase in write power consumption. The intrinsic current density is primarily governed by the in-plane anisotropy, because $4\pi M_s > 10 \text{ kOe}$ and H_k , dominated by shape anisotropy, is several hundred Oe. Therefore, the most efficient means of reducing J_{c0} would be to use a free layer with perpendicular anisotropy with $H_k > 4\pi M_s$. In this way the effective perpendicular anisotropy would become $H_k^\perp = H_k - 4\pi M_s$ [82].

There are many distinct advantages of perpendicular STT switching based MTJs, compared to in-plane MTJs [19]. The switching current density J_{c0} is expected to be reduced significantly in perpendicular MTJ (pMTJ), assuming the other materials parameters remain unchanged. In addition, for a pMTJ, the thermal energy barrier is provided by effective perpendicular anisotropy H_k^\perp , instead of shape anisotropy. Therefore elongated cell shape is no longer needed and pMTJ can use a circular cell shape, which facilitates manufacturability in smaller technology nodes beyond 45 nm [70].

Currently, perpendicular MTJs prepared using sputtering are actively being studied and have reached TMR ratios at room temperature (RT) of up to 64% with rare-earth transition metal alloys, 57% up to 120% with (Co, Fe)Pt, and up to 15% with Co/ (Pd, Pt) multilayers [84]. Multilayer electrodes have several advantages; first in multilayers is relatively easy to control M_s and H_k by changing the number of the layer stack and the thicknesses. In addition, in multilayer films is comparatively easy to realize perpendicular magnetic anisotropy, with high magnetic thermal stability. However, it is still not clear how one can achieve high TMR in MTJs based on multilayers. To understand the factors that can influence the TMR values achievable, Mizunuma *et al.* [84] investigated the TMR properties and the film structures of perpendicular MTJs with CoFe/Pd multilayer and different insertion layers such as CoFeB and Fe. They found that the insertion of CoFeB

layers between CoFe/Pd multilayers and MgO barrier resulted in an increase of TMR ratio from a few percent to up to 43%. By applying combination of bottom CoFeB and top Fe insertion layers, the TMR ratio reached 67%. And after the in-situ annealing a TMR ratio of 78% was observed. However, the TMR ratio rapidly decreased at annealing temperatures T_a above 250 °C. They explained the degradation of the TMR ratio for the MTJs annealed at high T_a with the possible crystallization of CoFe(B) into fcc(111) or bcc(011) texture resulting from the diffusion of B into Pd layers, as shown by HRTEM and SIMS analysis. To overcome this inconvenience and to achieve higher TMR ratio, they proposed, as an example, the preparation of bcc(001) orientated of CoFeB, which would suppress B diffusion between the CoFe/Pd multilayer and the CoFeB layer.

In the next chapter an overview of the experimental techniques used for the preparation and characterisation of the various material systems investigated throughout this research will be provided.

Bibliography

- [1] <http://www.spinswitch.eu>
- [2] Wisniowski P. *et al.*, *J. Appl. Phys.*, (2008), **103**, 07A910.
- [3] Pierce Williams L., *Contemp. Phys.*, (1962), **4**, 113.
- [4] Langevin P., *Ann. Chim. Phys.*, (1905), **5(8)**, 70.
- [5] Weiss P., *J. de Phys. Rad.*, (1907), **6**, 661.
- [6] Van der Waals J.D., *Thesis - University of Leiden*, (1873).
- [7] Heisenberg W., *Z. Phys.*, (1928), **49**, 619.
- [8] Barkhausen H., *Phys. Z.*, (1919), **20**, 401.
- [9] Sixtus K.J. and Tonks L., *Phys. Rev.*, (1931), **37**, 930.
- [10] Bloch F., *Z. Phys.*, (1932), **74**, 295.
- [11] Akulov N.S., *Z. Phys.*, (1931), **67**, 794.
- [12] Becker R., *Z. Phys.*, (1930), **62**, 253.
- [13] Honda K. and Kaya S., *Sci. Rep. Tohoku Imp. Univ.*, (1926), **15**, 721.
- [14] Frenkel J. and Dorfman J., *Nature*, (1930), **126**, 274.
- [15] Heisenberg W., *Z. Phys.*, (1931), **69**, 287.
- [16] v Håmos L. and Thiessen P.A., *Z. Phys.*, (1931), **69**, 287.
- [17] Bitter F., *Phys. Rev.*, (1931), **38**, 1903.
- [18] Landau L.D. and Lifshitz E., *Phys. Z. Sowjetunion*, (1935), **8**, 153.
- [19] Williams H.J. *et al.*, *Phys. Rev.*, (1949), **75**, 155.

- [20] Kittel C., *Rev. Mod. Phys.*, (1949), **21**, 541.
- [21] Dennis C.L. *et al.*, *J.Phys.: Condens. Matter*, (2002), **14**, 1175.
- [22] Jiles D., *Introduction to Magnetism and Magnetic Materials*, Taylor and Francis, (1998).
- [23] Vleck J.H.V., *Rev. Mod. Phys.*, (1945), **17**, 27.
- [24] Chikazumi S., *Physics of ferromagnetism - 2nd Edition*, Oxford: Clarendon, (1997).
- [25] Felton S. *et al.*, *J. Magn. Magn. Mater.*, (2004), **280**, 202.
- [26] <http://www.tcd.ie/Physics/Magnetism/lectures/5006/5006-7.pdf>.
- [27] Hubert A. and Schafer R., *Magnetic Domains - The Analysis of Magnetic Microstructures*, Springer, (2009).
- [28] Guggenheim E.A., *Proc. R. Soc. A*, (1936), **155**, 49.
- [29] Wachowiak A. *et al.*, *Science*, (2002), **298**, 577.
- [30] Néel L., *J. Physique Rad.*, (1954), **15**, 225.
- [31] Johnson M.T. *et al.*, *Rep. Prog. Phys.*, (1996), **59**, 1409.
- [32] Hindmarch A.T. *et al.*, *Phys.Rev.Lett.*, (2008), **100**, 117201.
- [33] Cullity B.D. and Graham C.D., *Introduction to Magnetic Materials - 2nd Edition*, John Wiley Sons Inc, (2009).
- [34] Bogdanov A.N. and Hubert A., *J. Magn. Magn. Mat.*, (1994), **138**, 255.
- [35] Stoner E.C. and Wohlfarth E.P., *Phil. Trans. R. Soc. London*, (1948), **A 240**, 599.
- [36] Joule J.P., *Phil. Mag.*, (1847), **30**, 76.
- [37] Klokholm E. and Aboaf J.A., *J. Appl. Phys.*, (1981), **52 (3)**, 2474.
- [38] <http://www.ptb.de/en/org/2/25/252/verweis/precession.htm>.

- [39] Donahue M.J. and McMichael R.D., *NISTIR 6376, National Institute of Standards and Technology*, Gaithersburg, MD, (1999).
- [40] <http://math.nist.gov/oommf/>
- [41] Kittel C., *Introduction to Solid State Physics – 8th edition*, John Wiley and Sons (2005).
- [42] Néel L., *C.R. Accad. Sci. Paris*, (1955), **241**, 533.
- [43] Hubert E. *et al.*, *J.Appl.Phys.*, (1958), **229**, 94.
- [44] Prutton M, *Thin Ferromagnetic films*, Butterworth (1964).
- [45] Allwood D.A. *et al.*, *Science*, (2005), **309**, 1688.
- [46] Parkin S.S.P. *et al.*, *Science*, (2008), **320**, 190.
- [47] Klauui M. and Vaz C.A.F., *Handbook of Magnetism and Magnetic Materials vol.2*, Wiley, (2007).
- [48] Nakatani Y. *et al.*, *J. Magn. Magn. Mat.*, (2005), **290-291**, 750.
- [49] Fert A. and Piraux, L., *J. Magn. Magn. Mater.*, (1999), **200**, 338.
- [50] Shinjo T., *et al.*, *Science*, (2000), **289**, 930.
- [51] <http://www.ndted.org/EducationResources/CommunityCollege/MagParticle/Physics/HysteresisLoop.htm>.
- [52] Zutic I. *et al.*, *Rev. Mod. Phys.*, (2004), **76**, 323.
- [53] Thomson W., *Math. Phys. Papers*, (1856), **2**, 267.
- [54] Thompson D.A. *et al.*, *IEEE Trans. Magn.*, (1975), **11**, 1039.
- [55] Baibich M.N. *et al.*, *Phys. Rev. Lett.*, (1988), **61**, 2472.
- [56] Binasch, G. *et al.*, *Phys. Rev. B*, (1989), **39**, 4828.

- [57] Dieny B. *et al.*, *Phys. Rev. B*, (1991), **43**, 1297.
- [58] http://www.ing.unitn.it/~colombo/hard_disks/Magnetic_Heads_003.html.
- [59] Jullière M., *Phys. Lett. A*, (1975), **54**, 225.
- [60] Jang Y. *et al.*, *Appl. Phys. Lett.*, (2006), **89**, 163119..
- [61] Yuasa S. *et al.*, *Nat. Mater.*, (2004), **3**, 868.
- [62] Slonczewski J.C., *J. Magn. Magn. Mater.*, (1996), **159**, L1.
- [63] Berger L., *Phys. Rev. B*, (1996), **54**, 9353.
- [64] Kaka S. *et al.*, *Nature*, (2005), **437**, 389.
- [65] Grollier J. *et al.*, *Phys. Rev. B*, (2006), **73**, 060409(R).
- [66] Diao Z. *et al.*, *Appl. Phys. Lett.*, (2005), **87**, 232502.
- [67] Prejbeanu I.L. *et al.*, *IEEE Trans. Magn.*, (2004), **40**, 2625.
- [68] Sousa R.C. *et al.*, *J. Appl. Phys.*, (2004), **95**, 6783.
- [69] Dieny B. and Redon O., *Magnetic device with magnetic tunnel junction, memory array and read/write methods using same*, Patent Specification, (2003), 2003043017.
- [70] Huai Y., *AAPPS Bulletin*, (2008), **18-6**, 33.
- [71] Schwee L.J. *et al.*, *J. Appl. Phys.*, (1982), **53**, 2762.
- [72] Pohm A. *et al.*, *IEEE Trans. Magn.*, (1987), **23**, 2575.
- [73] Tehrani S. *et al.*, *J. Appl. Phys.*, (1999), **85**, 5822.
- [74] Parkin S.S. *et al.*, *Nat. Mater.*, (2004), **3**, 862.
- [75] Durlam M. *et al.*, *ISSCC Digest of Technical Papers*, (2000), 130.
- [76] Koch R.H. *et al.*, *Phys. Rev. Lett.*, (1998), **81**, 4512.

- [77] Yamamoto T. *et al.*, *J. Appl. Phys.*, (2005), **97**, 10P503.
- [78] Prejbeanu I.L. *et al.*, *IEEE Trans. Magn.*, (2004), **40**, 2625.
- [79] Wang J. and Freitas P.P., *Appl. Phys. Lett.*, (2004), **84**, 945.
- [80] Nozières J-P. *et al.*, *Magnetic memory with a magnetic tunnel junction written in a thermally assisted manner and method for writing the same*, Patent Specification, (2004), 2005086171.
- [81] Akerman J. *et al.*, *Magnetoelectronics*, Elsevier, Amsterdam, (2004).
- [82] Sun J.Z., *Phys. Rev. B*, (2000), **62**, 570.
- [83] Klostermann U.K. *et al.*, *IEDM Technical Digest*, (2007), 187.
- [84] Mizunuma K. *et al.*, *Appl. Phys. Lett.*, (2009), **95**, 232516.
- [85] Mangin S. *et al.*, *Nature Mater.*, (2006), **5**, 210.

CHAPTER 2

Instrumentation and experimental techniques

2.1 Introduction

This chapter will provide an overview of all the experimental techniques employed for the fabrication and characterisation of the samples investigated for this research. Section 2.2 will describe the techniques used to grow the different specimens, sputtering and electrodeposition. Section 2.3 will include an overview of the structure of a transmission electron microscope (TEM) and 2.4 the main operating modes used for basic characterisation. Sections 2.5 and 2.6 will describe special applications of TEM, respectively Lorentz Microscopy used for the investigation of the magnetic domain structure of the specimens and widely employed in this work, and analytical electron microscopy (AEM) used for compositional analysis. Section 2.7 will provide an overview of MOKE magnetometry, used to characterise the hysteresis properties of multilayers with perpendicular anisotropy described in chapter 5.

2.2 Samples preparation

The next two sections will deal with the deposition techniques used to generate the samples investigated in this thesis. MgO/CoFeB/MgO multilayers, which will be the subject of Chapter 3 and (Co/Pt/Ni/Pt)_x/CoFeB multilayers with perpendicular anisotropy subject of chapter 5, have been deposited by magnetron sputtering on Si₃N₄ membranes. They consist of 35 nm thick amorphous Si₃N₄, supported on a Si frame with a 100μm x 100μm electron transparent window [1]. A schematic of these substrates is depicted in fig. 2.1. The membrane substrates are made by Kelvin Nanotechnology Ltd (KNT) based in the Department of Electronics and Electrical Engineering at the University of Glasgow. They have been used over the years, since they provide the electron transparency required of the substrate as well as providing a reasonably high quality, flat surface for film deposition,

even though recently different types of membranes were developed with improved properties, as for example, silicon dioxide membranes.

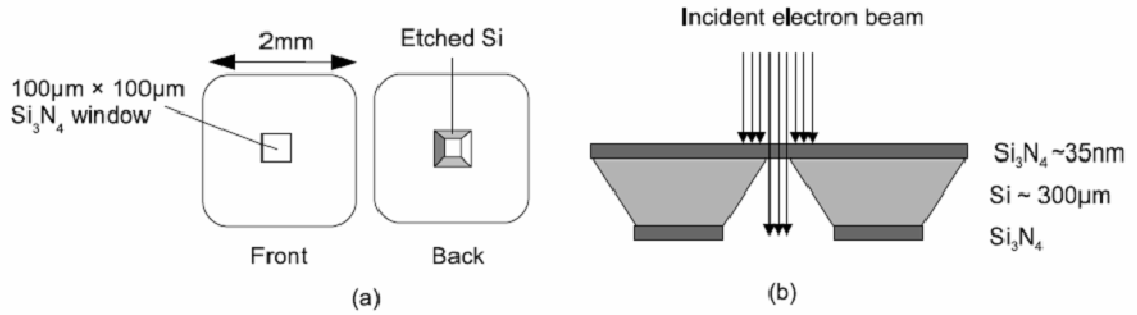


Figure 2.1: (a) Front, back and (b) cross-sectional schematics of single Si₃N₄ TEM membrane substrate.

NiFe/Cu nanowires, the subject of chapter 4, have been grown by electrodeposition in anodic alumina or polycarbonate templates. In the next two sections a description of sputtering and electrodeposition will be provided.

2.2.1 Sputtering deposition technique

The magnetron sputtering deposition of MgO/CoFeB/MgO multilayers investigated in this thesis has been carried out by the group of Prof. Freitas at INESC-MN, Lisbon (Portugal). The deposition of the multilayers with perpendicular anisotropy in chapter 5 has been performed by Sebastien Bandiera at Spintec (CEA) Grenoble (France).

Sputtering [2] is an experimental technique used for physical deposition of thin films. It is performed under vacuum, with the aid of a luminescent plasma. It allows the deposition of all types of materials, from single elements to compounds, refractory, alloys, conductors and dielectrics. The substrates typically used to perform the deposition are materials that can be heated up to temperatures of 60°-70°C and that can be put in a vacuum environment without a modification of their structure and their properties. A typical sputtering system is composed of a deposition chamber, a vacuum system, and a power supply which can provide continuous or alternate voltage difference depending on the type of material to deposit. The chamber, which is the most important part of a deposition machine, since it is the component where the deposition takes place, is shown schematically in fig. 2.2. Its main components are the target and the substrate. The target is connected to the cathode,

whereas the substrate requires to be connected to an electrode, the anode, only for diode sputtering.

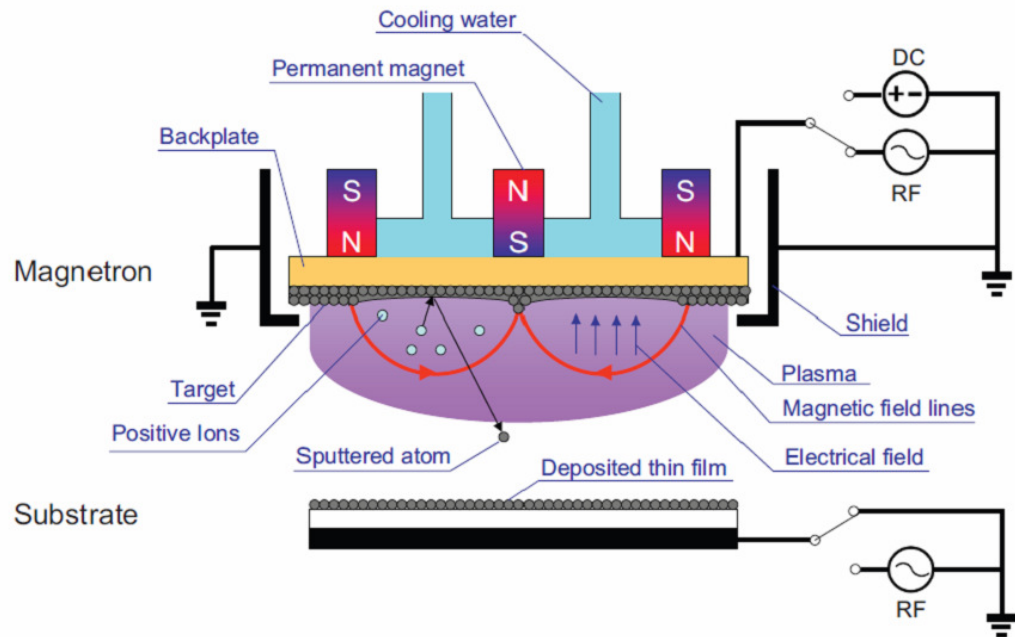


Figure 2.2: Schematic of a magnetron sputtering system.

The first step in the sputtering process is the creation of a plasma. This is done in a controlled way by introducing atoms of gas (typically Ar and Xe) at low pressure (10^{-1} - 10^{-2} Pa) in the vacuum chamber and by applying a voltage to the target. The gas between two electrodes contains some free electrons. When an electric field is applied between the electrodes, the electrons are accelerated and when they collide against the atoms of gas, they produce the ionisation of the gas with the consequent formation of a plasma. These ions positively charged, are going to be attracted by the target (negatively charged) where they will expel atoms and electrons under the effect of collisions. The electrons will be accelerated by the electric field and they will meet gas molecules on their way. They will ionise the gas molecules and at the same time further electrons will be produced. If the gas pressure is high enough, this process will be amplified and the equilibrium condition, where neutralisation will predominate over ionisation of gas atoms, will be met. The ejection of atoms is a purely mechanical effect due to ions hitting the material to be deposited. They transfer mechanical energy by transfer of momentum carried by the incident ion attracted by the target. The atom hit by the ion transfers the acquired momentum to the surrounding atoms in a cascade-type process which results in the final

ejection of surface atoms. The nature of the process is such that targets with single atomic species or compounds are both sputtered with the same efficiency [2].

When a continuous voltage is applied between the electrodes in order to generate the plasma the relative technique is called DC sputtering. It permits the deposition of all conductive materials as in the case of the CoFeB layer in the MgO/CoFeB/MgO system and Co, Pt, CoFeB in the magnetic multilayers with perpendicular anisotropy. The main limitation of DC sputtering is that this method is suitable only for deposition of conducting films. Indeed, the incoming ions reaching the target carry electrical charge besides momentum and energy. If the target is an electrical conductor these charges will be neutralized by the electrons provided by the power supply. If the target is an insulator there will be an accumulation of positive charges at the target surface. After a certain amount of time, the total charge will be large enough to repel any incoming ion and the sputtering process will cease. Davidse and Maissel in 1966 [4] proposed a successful way to overcome this main problem. They biased a dielectric target with a RF power supply to produce non conductive films. The RF sputtering works in such a way that when a RF voltage is supplied to a dielectric target, sputtering takes place in the negative voltage part of the cycle while neutralization of the target with plasma electrons takes place in the positive part of the cycle. This sputtering technique has been used for the deposition of MgO in the MgO/CoFeB/MgO system.

The magnetron cathode, patented by Penning in 1935 [3] is an evolution of the cathode traditionally used for sputtering. Its main advantage is the possibility of increasing the deposition rates. It introduces a high magnetic field that combines with the electric field created by the cathode. The magnetron effect works in such a way that if a magnetic field is superimposed on the electric field, where the magnetic field is parallel to the cathode and very close to it, the electrons ejected by the cathode have helical motion along the field lines of the magnetic field (red circular arrows in fig.2.2) and they increase the probability of ionisation of gas molecules close to the cathode. The increase of the ion density occurs in an area close to the target where the ions have high probability of being attracted by the cathode. As a result, there is an increase in the deposition rate and a decrease in the working pressure.

Sputtering processes have various advantages over other common techniques for thin film deposition (evaporation, Chemical Vapor Deposition (CVD), Molecular Beam Epitaxy

(MBE), laser ablation, ecc..) [1]: almost any material can be sputtered - including metals, multi-component films (alloys, compounds, etc.), and insulators; the ability to control the sputtering parameters (like pressure, sputtering gas, and energy), allows one to adjust deposition rates, thickness, uniformity and smoothness with high accuracy; high deposition rates in comparison to other thin film deposition techniques, other than evaporation.

2.2.2 Electrodeposition of nanowires in porous templates

The electrodeposition of NiFe/Cu nanowires into porous templates investigated in this thesis has been carried out by the group of Prof.Chiriac at The National Institute for Research and Development of Technical Physics (NIRDTP), Iasi (Romania). This method is a general approach for preparing a variety of nanowires and nanostructures. It entails synthesis of a desired material within the cylindrical pores of a porous material using electrochemical techniques. The template allows for unidirectional growth, making it easy to vary the composition of the nanowire in the axial direction. As a result, a nanowire of the desired material is obtained within each pore [2]. Thus this technique offers several practical advantages over more sophisticated vacuum deposition techniques, in terms of cost and growth rates [6]. Electrodeposition into the pores of track-etched polycarbonate and anodic aluminum oxide templates has proven to be reliable for the synthesis of a variety of magnetic nanowires and multilayers [7 - 10]. Indeed, the nanowires, subject of chapter 4, were grown inside the anodic aluminum oxide (AAO) templates provided by Synkera (USA) and in polycarbonate (PC) templates provided by *it4ip*, trademark which stands for ion track technology for innovative products (Belgium). The AAO templates used for electrodeposition of the nanowires had specific pore size of 35 nm and thicknesses of 40 μm . Prior to the electrodeposition the membranes were characterized by scanning electron microscopy (SEM) using a JEOL JSM 6390A. A SEM image of a typical AAO template indicates the hexagonal arrangement of the nanopores with nominal diameters of 35 nm (fig. 2.3a). The polycarbonate templates used for the preparation of nanowires by electrodeposition had specific pore sizes of 50 or 100 nm and thicknesses of up to 21 μm . A typical polycarbonate SEM image is presented in fig. 2.3b. AAO templates are preferably used when spin transfer torque measurements are performed on single nanowires embedded in the template, because the use of supported alumina templates prevents breaking of the fragile template during handling and/ or nanocontact fabrication process [5]. Polycarbonate templates, instead, represent a better choice when the physical structure, composition and magnetic structure of single nanowires, outside the template,

needs to be characterised, because polycarbonate templates are softer than AAO templates, thus they do not require strong solvents and/or long etching times and in this way, the morphology and the composition, in principle, will be preserved.

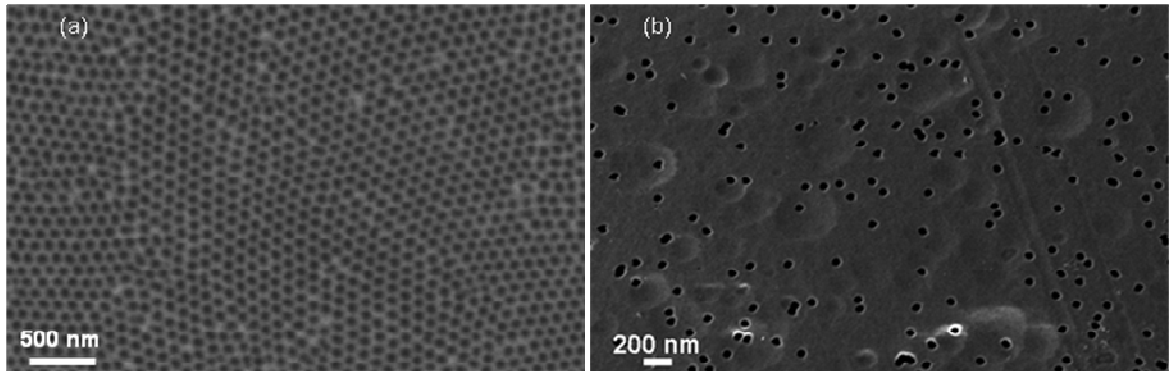


Figure 2.3: (a) Schematic top-view SEM micrograph of a highly ordered alumina membrane, (b) top-view SEM micrograph of a polycarbonate membrane.

A thin layer of Au and Cr was deposited by e-beam evaporation on one side of the AAO template, serving as a working electrode for subsequent electrodeposition. A three electrode cell with a platinum wire as counter electrode and an Ag/AgCl reference electrode was used to carry out the electrodeposition process. Multilayered structures of magnetic permalloy ($\text{Py} = \text{Ni}_{80}\text{Fe}_{20}$) and non-magnetic Cu were electrodeposited into the AAO or PC template nanopores as depicted in fig. 2.4. At least 100 sequences were electrodeposited consecutively, using a single bath consisting of an aqueous solution of NiSO_4 90g/L, FeSO_4 13.5g/L, CuSO_4 2g/L, and H_3BO_3 25g/L. The pH value of the electrolyte was adjusted to 3 by adding few drops of 0.5M H_2SO_4 solution or 1M NaOH solution. Multilayered structures Py (20, 30 or 50 nm)/Cu(5, 10 or 20 nm) were electrodeposited by switching between the deposition potentials of the two constituents (-1.4 V for Py and -0.3 V for Cu deposition). The voltage, applied in pulses [11], was controlled with a HEKA PG 340 bipotentiostat/galvanostat. The choice of the thicknesses of the layers is designed to have a large GMR effect in the nanowires (the non magnetic and magnetic layers should be thinner than the electron mean free path in the material to have large GMR effect) which is extremely important for the application as spin transfer torque oscillators because the GMR effect converts the magnetic precession into microwave electrical signals [49]. The potential depends on the material/alloy to be electrodeposited and also on the desired composition. By controlling the deposition time for each layer we obtained multilayered nanowires with different thicknesses of magnetic and non-magnetic layers.

In order to perform TEM studies, the nanowires should be extracted from their template. The dissolution of the template is performed by chemical etching in a solution composed by 3 Mol of KOH for alumina templates and trichloroethylene for polycarbonate templates. The free nanowires obtained after chemical dissolution of the membrane were magnetically separated from the hydroxide or trichloroethylene solution and rinsed several times with distilled water. Part of the resulting solution containing single nanowires or clusters is then dispersed on holey carbon grids (fig. 2.5). The selection of a grid made of a metal different from the components of the nanowires is important especially for the reliability of the analytical investigations.

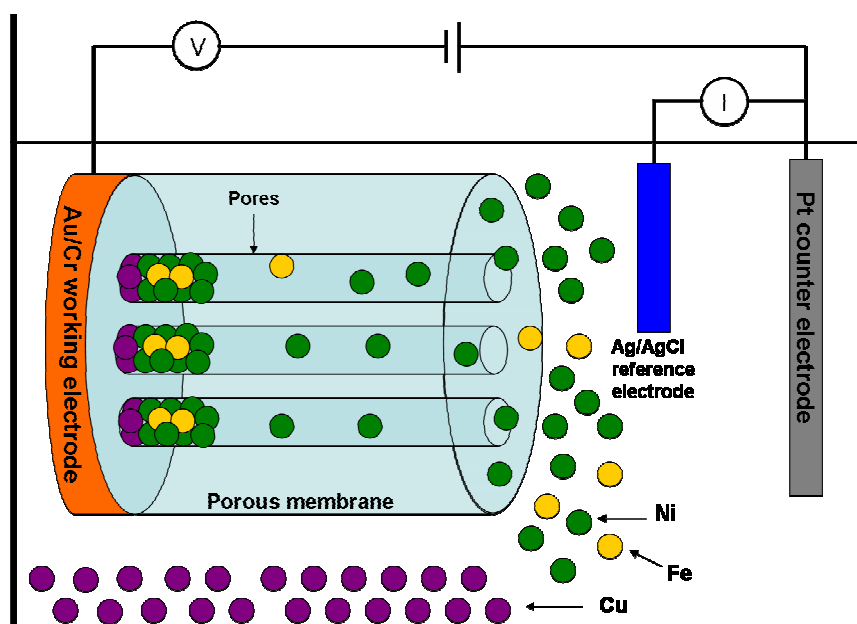


Figure 2.4: Schematic of the electrodeposition setup.

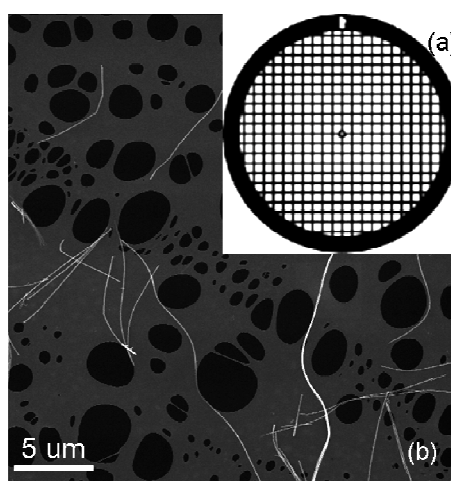


Figure 2.5: (a) Schematic of a holey carbon grid, (b) SEM image of nanowires in holey the carbon film.

2.3 Transmission Electron Microscopy

The Transmission Electron Microscope (TEM) was described for the first time in the paper of Knoll and Ruska published in *Z. Physik* in 1932 [12]. They developed a new kind of microscope that used electrons instead of light as source of illumination and electron lenses instead of glass lenses to focus the beam onto the specimen, and they showed the capability of obtaining images in this new way. The idea of using electrons instead of light came after the discovery of the dual wave – particle nature of the electrons, theorized by De Broglie in 1925 [13]. In the same decade Busch's studies [14] confirmed the focusing action of electric and magnetic fields on electron beams, similarly to what lenses and mirrors make on a light beam.

Nowadays TEM is a powerful technique which makes use of high energy (80-1000 keV) electrons. Atomic resolution can be achieved and used to perform a variety of tasks from characterisation of advanced technological material to investigation of biological matter [15]. It provides structural information by means of electron diffraction and electron imaging, which exploit elastic scattering processes between the electron beam and the specimen, and compositional information, by means of analytical techniques, which exploit inelastic scattering effects. TEM provides also an excellent platform from which to investigate the magnetic domain structure and magnetisation reversal behaviour of magnetic materials. Magnetic image contrast arises from small deflections of the electrons passing through the material. These deflections are a result of the Lorentz force and techniques that exploit this effect are known as Lorentz Microscopy [26].

TEMs can be operated in two main modes: conventional mode and scanning mode. In the first case the whole imaged specimen area is illuminated simultaneously by a parallel beam, and this mode is used primarily for TEM imaging and selected area diffraction (SAD). In the second mode, the specimen is scanned in a raster point-by-point with a small convergent beam and this mode is used mainly for scanning imaging, analytical techniques and convergent beam electron diffraction (CBED) [15, 16].

All the work involving TEM and presented in this thesis has been performed with the three microscopes available at Glasgow University: FEI T20 has been used for structural characterisation and energy-filtered imaging; FEI TF20 (fig. 2.6) has been used for EDX analysis and finally Philips CM20 to investigate the magnetic properties. The basic

structure of a TEM includes an electron gun, the column and the detection system. They will be described in the following sections. A picture of one of our TEMs (Technai TF20) including labels to the main components of a TEM is shown in fig.2.6.

2.3.1 The electron gun

The electron gun is the part of the TEM where the electrons are extracted from a metal with a weak work function and directed into the illumination system [16]. There are two ways used to achieve the extraction of the electrons. The first is the thermionic emission which is a thermal effect: a metallic filament is heated up to a temperature close to the melting point to extract electrons. This temperature is 2400°C for tungsten (W) and 1500°C for lanthanum hexaboride (LaB₆) the most common materials employed as thermionic electron emitters. The emitters are used as the cathode in a triode gun. In addition to the cathode, the gun includes a grid called Wehnelt cylinder and an anode at earth potential with a hole in its centre. Once emitted, the electrons are focused at the Wehnelt and in this way the crossover is formed. The crossover is extremely important since it defines the point source of the electrons.

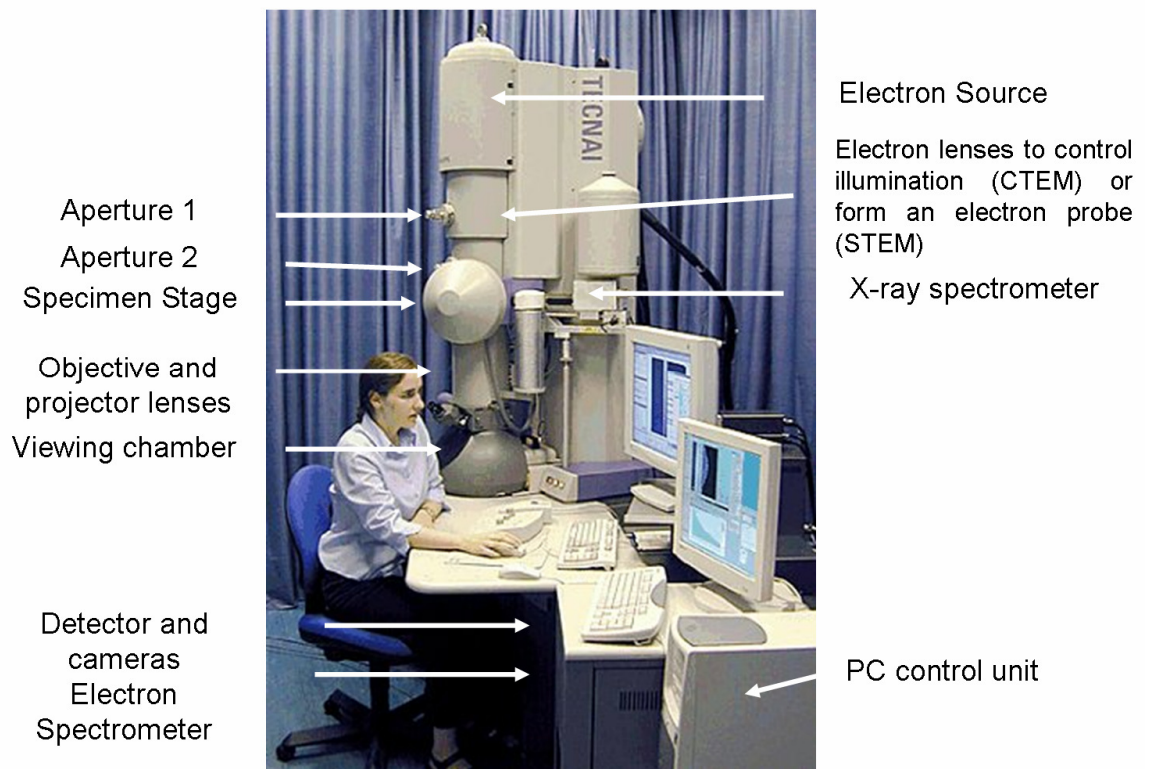


Figure 2.6: Example of TEM: Technai TF20.

The other principle exploited for electrons extraction is field emission and this is called field emission gun (FEG). Here the extraction is achieved when a potential of several kV is applied between a cathode with a point shape with a radius of curvature smaller than 0.1 μm , and an anode. A second anode located below the first one, has the role of accelerating the electrons to acquire the desired energy. The combined fields of the anodes act as a refined electrostatic lens to produce a crossover. The FEG needs to operate in ultra-high vacuum conditions (10^{-9} Pa) in order to avoid contamination and oxidation. An intermediate emitter, called Schottky emitter, couples the two effects. It is made of a tungsten hairpin heated at 1800°C to assist the emission of the electrons and the surface is treated with ZrO_2 to improve the emission characteristic and the stability of the source. The emission of a FEG is much brighter (higher current density per solid angle of the source) and much more coherent (electron closer in space) than thermionic sources. For example, for a 100 keV microscope, the brightness of a LaB_6 source is 5×10^{11} A/ m^2sr for a Schottky FEG is 5×10^{12} A/ m^2sr [15]. This makes a FEG particularly suitable to Lorentz imaging where it is necessary to have a small coherent beam with an angular convergence significantly less than the Lorentz deflection angle, but also for analytical TEM. Thus the Philips CM20 and the FEI TF20 used respectively for Lorentz imaging and analytical TEM are equipped with a FEG, in particular a Schottky emitter. Thermionic sources are found to be better suited to routine TEM work where large areas of the sample need be illuminated without loss of intensity on the viewing screen, thus the microscope used for routine experiment, the FEI T20 is equipped with a thermionic source (tungsten and LaB_6).

2.3.2 The microscope column

The electron column houses a series of electromagnetic lenses, apertures, deflection and alignment coils which are used to control the mode of operation of the microscope [16]. A magnetic electron lens is composed of a cylindrical symmetrical core of soft magnetic material called a polepiece, with a hole drilled through it. In most lenses there are two polepieces, upper and lower and the distance between them is called the gap. Each polepiece is surrounded by a coil of copper wire and when a current passes through the coil, a magnetic field is created in the bore. The strength of the field in a magnetic lens controls the ray paths. An aperture is often inserted into a lens. Physically, the aperture may reside above, in or below the plane of the lens. Usually the apertures are circular holes in metal disks and the disks are made of either Pt or Mo, which are both refractory metals.

All lenses are subject to aberrations [47]. There are two types of aberration that we must consider: chromatic aberration resulting from variations in energy of the electrons and spherical aberration arising from lens geometry or inhomogeneity.

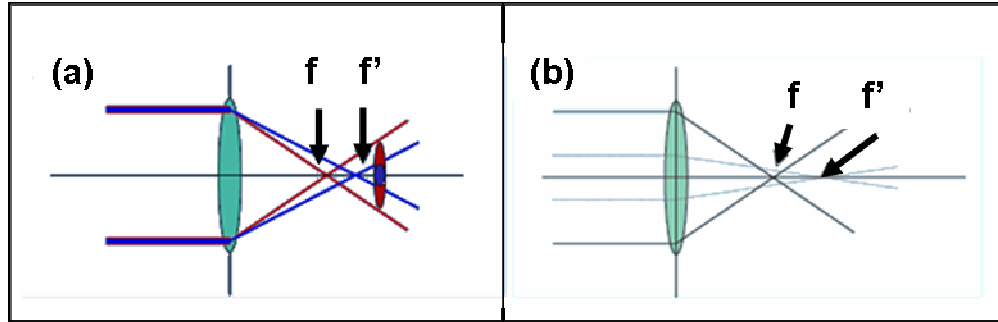


Figure 2.7: Schematic of (a) chromatic aberration where electrons with different energy are focused in different points (f and f') and (b) spherical aberration where points at different distance from the optic axis are focused in different points (f and f').

The dominant effect of chromatic aberration is that the lens brings electrons of different energy to focus at different points along the optic axis as shown in fig. 2.7(a). If a variety of electron energies are present, a lens has no unique focal length and will give rise to a disc of confusion rather than a point focus. This effect can be minimised with the use of a good design of electron gun that reduce the energy spread of the electron beam before it hits the specimen.

Spherical aberration occurs because for electromagnetic lenses the further off axis the electron is, the more strongly it is bent back towards the axis as schematised in fig. 2.7(b). As a result, a point object is imaged as a disk of finite size, which limits our ability to magnify detail because the detail is degraded by the imaging process. The radius of the spherical aberration disk r_{sph} in the Gaussian plane under non-paraxial conditions [15] is given by $r_{sph} = C_s \alpha^3$, where C_s is the spherical aberration coefficient, it is constant for a particular lens, has a dimension of a length, and for most TEMs it is between 1-3 mm, in high resolution instruments may be well below 1 mm and for a Lorentz lens is 8000 mm; α is the objective lens semi-angle of collection. The most recent TEMs are equipped with spherical aberration correctors. The correction is achieved in practice by a highly complex, computer controlled set of quadrupoles and hexapoles or octupoles. Astigmatism occurs when the electrons experience a non-uniform magnetic field as they spiral around the optic axis. This defect arises because soft iron polepieces can't be fabricated to be perfectly cylindrically symmetrical down the bore. The soft iron may have also structural

inhomogeneities which cause local variations in the magnetic field strength. Furthermore if the apertures are not clean, the contamination charges up and deflects the beam. Nevertheless astigmatism is easily corrected using stigmators, which are small octupoles that introduce a compensating field to balance the inhomogeneities causing the astigmatism. There are stigmators in both the condenser lens system, the imaging system and diffraction system. Thus the aberration that effectively limits the resolution, unless the microscope is equipped with an aberration corrector, is the spherical aberration. The resolution will be given by the combination of the Rayleigh criterion $r_{th} = 0.61 \lambda / \alpha$ and the spherical aberration [17]. The result of the derivation, which can be found in [16] and will give $r_{min} = 0.91(C_s \lambda^3)^{1/4}$ represents the practical resolution of the TEM. Typical values for r_{min} are between 0.25 and 0.3 nm, but high resolution instruments have $r_{min} \sim 0.15$ nm. Thus columns of atoms of crystalline materials can be resolved since their separation is close to r_{min} . For a Lorentz lens in focus the resolution is 2 nm as a result of the increase in spherical aberration.

A schematic of the electron column is shown in fig. 2.8. It is held under ultra high vacuum (better than 10^{-9} Pa) to reduce contamination and scattering of electrons in the sample. The column contains specifically the condenser lens system, the objective lens, a diffraction lens and a projector system.

2.3.2.1 The condenser system

Below the electron gun are two or more condenser lenses. In conventional TEMs, the first two condenser lenses are adjusted to illuminate the specimen with a parallel beam of electrons, typically several micrometers at reasonable magnification (20kX – 100kX). The first condenser lens C1 sets the demagnification of the gun crossover. The second lens C2 provides control of the convergence angle of the beam leaving the condenser assembly [48]. Further choice of the illumination conditions are provided by a set of apertures located below the C2 lens. Selection of a smaller aperture, for example, provides a beam with higher coherence, which is an advantage for the observation of small details on the specimen area, but it has the drawback of decreased current intensity. Below the condenser aperture is the condenser stigmator, whose function is to compensate for astigmatism in the illumination system and to create a circular beam profile at the specimen [47].

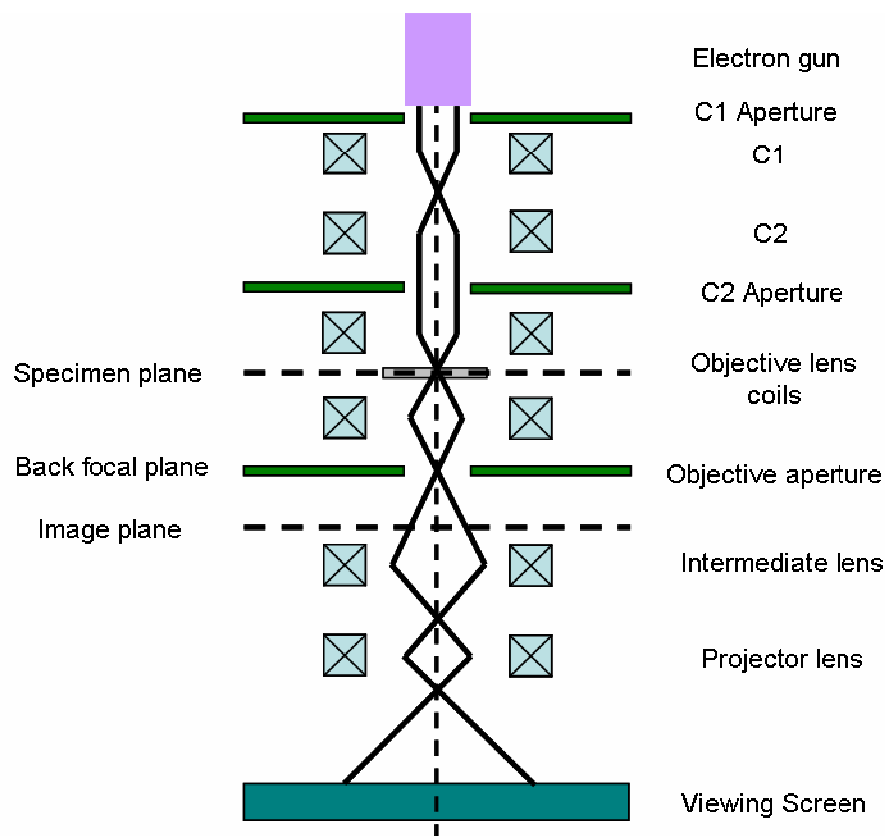


Figure 2.8: Diagram of the path of the electron beam inside the TEM column.

2.3.2.2 The objective and intermediate lenses

The TEM can work in two configurations: the standard configuration with the objective lens on and the field free configuration with the objective lens off. The role of the objective lens in the standard configuration is to form the first intermediate image and diffraction pattern, one or other of which is enlarged by the subsequent projector lenses and displayed on the viewing screen [48]. Diffraction and imaging will be described respectively in section 2.4. The specimen, objective aperture and objective stigmator coils all sit inside the objective lens gap.

When the objective lens operates in standard mode, it generates a magnetic field perpendicular to the specimen which can be greater than 1 Tesla. Nevertheless such a strong field can be detrimental when the subject of the investigation is the domain structure of a magnetic specimen. To this purpose a modified objective lens design is required. In the CM20 microscope the standard objective lens region has been modified to include two super mini-lenses above and below the objective pole-pieces. With the standard objective lens deactivated these two additional Lorentz lenses can perform as the main imaging

lenses yielding image resolution as good as 2 nm in-focus; but Lorentz microscopy in Fresnel mode (section 2.5.1) is a defocused technique, thus the resolution in this case will be much more than 2 nm and it depends on the value of defocus used. When operating in this mode, called field free mode, the objective lens coils can be used as a source of magnetic field by applying a weak excitation current producing a vertical magnetic field. A controllable component of magnetic field in the plane of the specimen is achieved by tilting and the maximum vertical field available is 6300 Oe. A schematic of the field free mode is depicted in fig.2.9.

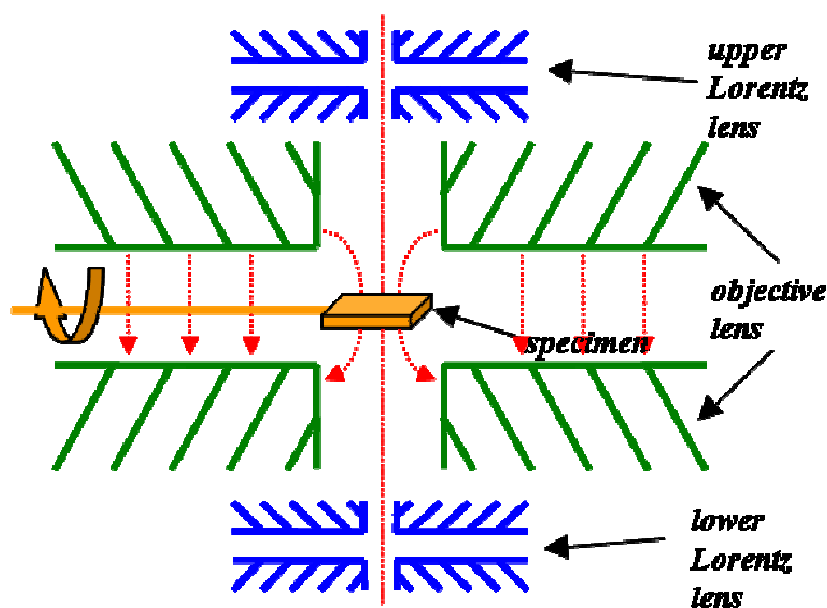


Figure 2.9: Schematic of the field free operating mode. The red dashed arrows represent the direction of the magnetic field. Courtesy of the SSP group.

2.3.2.4 The camera

Images are recorded by using a CCD (charge coupled device) camera, located below the column, which is exposed by lifting the viewing screen. A scintillator plate converts the electron image into a light image which is then transferred to the surface of the pixellated CCD through a fibre optic plate. The image data is read out directly to a computer which allows real time viewing and processing. Images are acquired and recorded through software, Digital Micrograph TM produced by Gatan, which is also used to process, analyse, simulate and present image and spectrum data. Photographic film is still commonly used to record diffraction patterns to avoid the intense spots burning the CCD.

2.3.2.5 STEM systems

Many modern TEMs can be used in scanning transmission (STEM) mode as in the FEI TF20 and Philips CM20. In this case the instrumental resolution is limited by the electron beam diameter at the specimen and a much finer beam is needed than for conventional TEM. The general approach in which the basic TEM components are used to provide a fine scanned beam is to use the condenser system to create a fairly fine beam (by using a strongly excited first condenser lens) and then to increase the excitation of the final condenser lens. The electron beam, whose diameter can vary in the range of 0.2 - 5 nm in standard mode [17] and is larger in a special technique described in section 2.5.2 (Differential Phase Contrast Microscopy) operated in field-free mode, is then rastered across the specimen by using two sets of deflection coils which keep the motion of the beam parallel to the optic axis. The transmitted electrons are, then, directed to a detector, the signal is amplified and modulated and sent on the computer display to build up an image [47]. STEM systems have the advantage of using detectors instead of lenses to form images. In this way the resolution is not limited by aberrations, but depends only on the diameter of the probe. Imaging in STEM mode will be described in section 2.4.2.

2.4 TEM diffraction and Imaging

Formation of diffraction patterns and images in TEM can be understood most easily in terms of the Abbe theory of image formation [18]. A schematic illustrating this process is depicted in fig.2.10. In first instance we assume that the specimen is illuminated by a plane wave. The effect due to the presence of a specimen is to modulate both its amplitude and phase and the wave emerging from its bottom surface may be written as:

$$\psi' = f(x, y)\exp(2ikz) \quad (2.1)$$

where $k = 1/\lambda$ is the wave-number and $f(x, y)$ is the specimen transmission function that has the form:

$$f(x, y) = A(x, y)\exp(i\phi(x, y)) \quad (2.2)$$

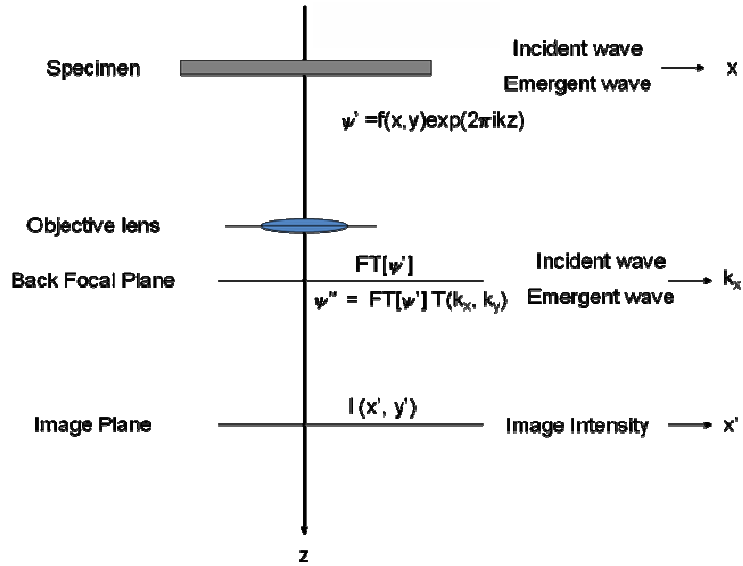


Figure 2.10: Schematic of the image formation in the TEM.

$A(x, y)$ is the amplitude, that can be simplified to 1 if we assume a specimen of uniform thickness and for applications as HRTEM and Lorentz microscopy; $\varphi(x, y)$ is the phase of the electron wave after passing through the sample. Thus only the phase of the electron wave is affected, in this approximation, and this is the reason why these application are included in a category known as phase microscopy. It is more convenient to illustrate the following part of the propagation of the electron wave to the image plane as a two stage process. When the electron wave enters in the back focal plane of the objective lens, it is more convenient to describe it in terms of the Fourier transform of the specimen transmittance (equivalent to the diffraction plane):

$$FT[\psi'] = g(k_x, k_y) = \iint [f(x, y) \exp(-2\pi i(k_x x + k_y y))] dx dy \quad (2.3)$$

where k_x and k_y are the x and y component of the spatial frequency and are the displacement in the back focal plane. All electron lenses are of finite size and suffer from aberrations and are equipped with apertures. This will further modify the wavefunction in such a way that the wave emerging from the back focal plane has the form $g(k_x, k_y)T(k_x, k_y)$ where the contrast transfer function:

$$T(k_x, k_y) = \Theta(k_x, k_y) \exp \left\{ -2\pi i \left[\frac{C_s \lambda^3 (k_x^2 + k_y^2)}{4} - \frac{\Delta z \lambda (k_x^2 + k_y^2)}{2} \right] \right\} \quad (2.4)$$

$\Theta(k_x, k_y)$ is the pupil function, C_s is the spherical aberration coefficient of the objective lens and Δz is the defocus, which allows for the possibility of the object and the specimen plane being non coincident. The form of the electron wave at the image plane ψ' will be given by the Fourier transform of the term $g(k_x, k_y)T(k_x, k_y)$ and the relative intensity of the image, $I(x', y')$ has the form:

$$I(x', y') = \left| \iint g(k_x, k_y) T(k_x, k_y) \exp[-2\pi i(k_x x' + k_y y')] dk_x dk_y \right|^2 \quad (2.5)$$

Thus, from eq.2.5, it is clear that the intensity depends on the sample, but also from the microscope parameters. At this point it is useful to describe diffraction and all the imaging techniques used for the research presented in this thesis.

2.4.1 Diffraction

Electron diffraction is a very important scattering phenomenon in the TEM. The reason for this importance is that we can use diffraction to determine crystal structure and orientation of planes in crystalline specimens. The interplanar spacings in different crystal structures are characteristic of that structure and the positions of the diffracted beams of electrons are determined by the size and shape of the unit cell and the intensities of the diffracted beams are governed by the distribution, number, and types of atoms in the specimen. Moreover diffraction can be used to generate contrast in TEM images which is controlled by the orientation of a crystal with respect to the electron beam and which can be controlled simply by tilting the specimen [16].

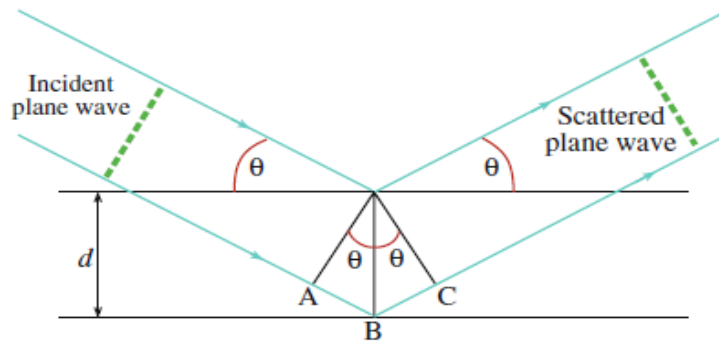


Figure 2.11: The Bragg description of diffraction in terms of the reflection of a plane wave (wavelength λ) incident at an angle θ to atomic planes of spacing d . The path difference between reflected waves is $AB + BC$. From [16].

The idea of using diffraction to probe the atomic structure of materials was accredited to Von Laue in Germany in 1912. He used the light optics approach to argue that the diffracted waves are in phase if the path difference between waves scattered by adjacent scattering centres is a whole number of wavelengths $n\lambda$ with n being an integer. For diffraction in the TEM, Von Laue's approach is simplified by Bragg [22] who argued that the waves behaved as if they were reflected off atomic planes as shown in fig.2.11. Bragg showed that the waves reflected off adjacent scattering centres, must have a path difference equal to an integral number of wavelengths if they are to remain in phase. Thus, if the "reflecting" planes are spaced a distance d apart and the wave is incident and reflected at an angle θ_B , and the total path difference is $2d \sin \theta_B$ where θ_B is the Bragg angle. Then we have the Bragg's law [22]:

$$n\lambda = 2d \sin \theta_B \quad (2.6)$$

This relationship (d is proportional to $1/\lambda$) is very important in diffraction pattern interpretation. So if we know λ for the incident electron and we can measure θ_B experimentally, we can work out the interplanar spacings in the crystal. A set of parallel crystal planes is defined by Miller indices (hkl) and a set of such planes is hkl . We define the direct beam as the 000 reflection and each diffracted beam as a reflection with different hkl indices.

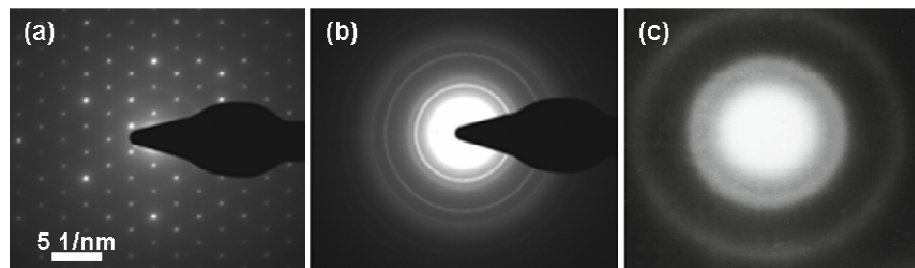


Figure 2.13: Diffraction patterns obtained in conventional TEM mode of (a) monocrystalline gold (b) polycrystalline aluminum and (c) amorphous carbon specimens. From [46].

From the observation of a diffraction pattern we can understand whether the specimen is a single crystal and in this case we will observe a spot pattern (fig. 2.12a); polycrystalline, and we will observe a ring pattern (fig. 2.12b); amorphous and we will observe a diffused ring pattern (fig. 2.12c). If the sample is determined to be crystalline from the diffraction pattern the crystallographic characteristics (lattice parameter, symmetry, etc) of the specimen can be worked out. If the specimen is polycrystalline, the grain morphology, how

large are the grains, what is the grain size distribution, the orientation of the specimen or of individual grains with respect to the electron beam can be measured.

The diffraction process can be described by mean of the wave-optics formulation. More details about it can be found in [17]. The wave-optics formulation allows the derivation of the structure factor $F(\theta)$ which is a measure of the amplitude scattered by a unit cell of a crystal structure. For a cell made of n atoms we can write [16]:

$$F_{hkl}(\theta) = \sum_{i=1}^n f_i \exp[2\pi i(hx_i + ky_i + lz_i)] \quad (2.7)$$

where θ is the scattering angle, f_i is the atomic scattering amplitude of the i -th atom of the unit cell and the phase factor takes account of the difference in phase between waves scattered from atoms on different but parallel atomic planes with the same Miller indices (hkl). The combination of the structure factor equation and Bragg's law allows the direction of all strongly diffracted beams from a crystal to be calculated. The structure factor equation is often summarised in diffraction rules, as for example, in the case of fcc crystal, only those planes with all even or all odd Miller indices give diffracted beams [48].

We can form diffraction patterns in the TEM in two complementary ways, Selected Area Diffraction (SAD) (technique used to obtain the diffraction patterns in fig.2.13) and Convergent Beam Electron Diffraction (CBED). Selected area diffraction (SAD) was invented by Le-Poole in 1947 [23]. It is operated in parallel illumination mode and it works in such a way that if we insert an aperture in a plane conjugate with the specimen, i.e. in one of the image planes, then it creates a virtual aperture at the plane of the specimen. The SAD pattern is often displayed on the viewing screen at a fixed magnification. This magnification can be changed by adjusting the intermediate lens. SAD is generally used to perform routine diffraction experiments and before any imaging experiments (when the operator wants to investigate the structure of a large portion of a specimen and the basics parameters as, for example, the order, the structure of the unit cell, the lattice spacing, etc...). CBED was originally developed by Kossel and Möllenstedt (1939) [24]. This technique is operated in convergent illumination mode and on the screen a set of discs, instead of spots or rings, is observed. From the analysis of the fine structure of the discs is possible to obtain information about the specimen thickness, crystal structure and lattice parameters. The use of a convergent beam allows determination of local information of the specimen, to investigate small particles, to measure the specimen thickness and the overall

symmetry of the CBED patterns obtained by aligning the incident beam along several prominent crystallographic directions (zone axes) it is possible to obtain the point and space groups of the crystal.

2.4.2 Bright field and dark field imaging

Formation of a diffraction pattern normally precedes electron imaging because bright field and dark field imaging is a way to generate diffraction contrast. When the SAD pattern is projected onto the viewing screen (fig. 2.14a), we can use the pattern to perform the two most basic operations in the TEM. The SAD pattern will contain a bright central spot which contains the direct electrons and some scattered electrons (fig. 2.13a). When we form images in the TEM we either form an image using the central spot or we use some or all of the scattered electrons. A way of doing this is to insert an aperture into the back focal plane of the objective lens, thus blocking out most of the diffraction pattern except that which is visible through the aperture. If the direct beam is selected (fig. 2.13b) we call the resultant image a bright-field image (BF), and if we select scattered electrons of any form (fig. 2.13c), we call it a dark field (DF) image.

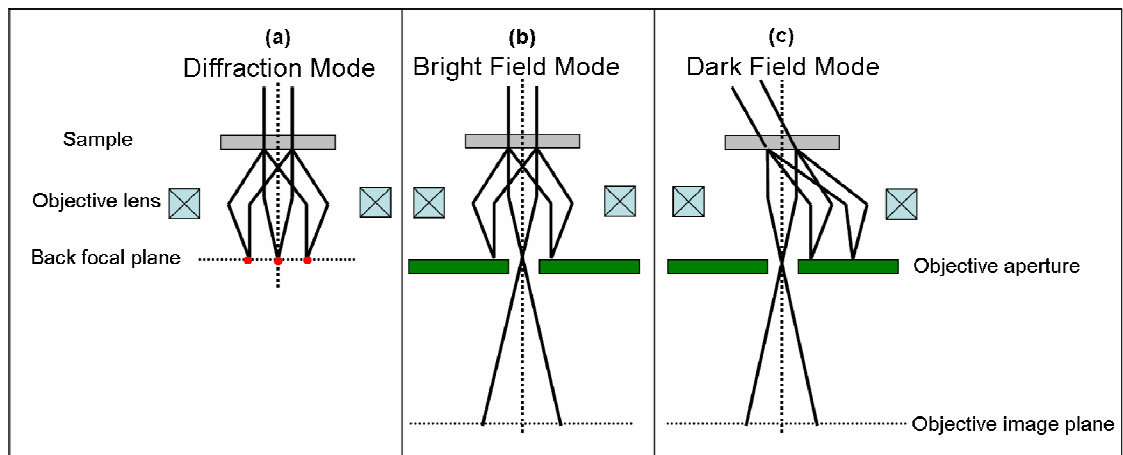


Figure 2.13: Schematic of the diffraction mode (a) bright field (b) and dark field (c) modes.

Fig. 2.14 shows an example of a BF (a) and a DF (b) image of $\text{Ni}_{80}\text{Fe}_{20}$ electrodeposited nanowires on holey carbon. In a BF image, regions of the specimen which are thicker or of higher density, will scatter more strongly and will appear darker in the image [48], as the densest areas in fig. 2.14a. In DF images, since diffracted beams have strongly interacted with the specimen, very useful information is present in DF images, e.g., about planar defects, stacking faults, particle size and orientation of crystallites in polycrystalline

specimens [16]. For example fig.2.14b highlights crystallites oriented in the same direction.

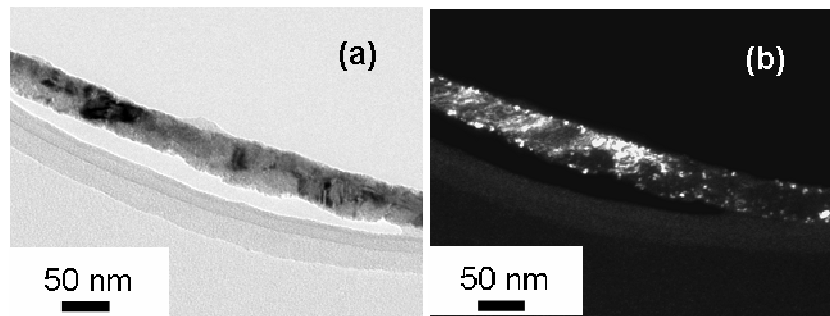


Figure 2.14: Example of a (a) bright field (b) and dark field image of a $\text{Ni}_{80}\text{Fe}_{20}$ electrodeposited nanowires on holey carbon.

Image formation in the scanning mode is completely different from conventional TEM [16]. The STEM detector, which is typically a semiconductor or scintillator-photomultiplier, acts as an aperture for a conventional system since it only allows the electrons from a specific direction to be selected. Thus a bright field detector, inserted onto the axis of the microscope, collects only the direct beam electrons and the related signal will vary in intensity depending on the specific point illuminated by the probe at that specific time. In this way a bright field image is formed. A dark field image is formed by selecting any of the scattered electrons rather than direct-beam electrons. To this purpose annular dark field detector is used. It is centred on the optic axis of the microscope and has a hole in the middle where the bright field detector sits. Electrons scattered at high angles can be collected by a third type of STEM detector which is called high-angle annular dark field detector (HAADF). It sits immediately outside the annular dark field detector and the resultant images highlight the Z-contrast, which is the contrast arising from a difference in atomic number. The column can house also other type of detectors as, for example, an energy loss spectrometer and a X-ray detector mounted near the specimen as in the case of the FEI TF20 used in this research.

2.4.3 High Resolution Imaging

Phase contrast, mentioned in the introduction to section 2.4, becomes really useful when two or more diffracted beams are allowed to pass through an objective aperture and interfere. Each pair of beams which interfere will in principle give rise to a set of fringes in the image. A common type of phase contrast image is formed when more diffracted beams

are used to form an image. By tilting the crystal such that the incident beam is accurately parallel to a zone axis in the crystal, many strong diffracted beams can be produced. Selecting several beams allows a structure image (often called high resolution image or HRTEM image) to be formed. The image is composed of lattice fringes that appear as lots of straight lines, which can provide information about the crystal orientation on a very fine scale and in the best case the atomic structure of the specimen can be worked out [48]. However, the interpretation of the contrast is not straightforward and requires an agreement between experimental and simulated images over a range of thicknesses and defocus values. Simulations are performed in weak phase approximation and they are extremely useful to be confident of the interpretation of contrast.

Simulations require understanding of the theory of image formation. Some general features of the theory of image formation have been presented in section 2.4 and we want to use them to give a quantitative description of HRTEM. As mentioned in section 2.4 for applications such as HRTEM eq.2.2 can be modified setting $A(x, y) = I$. Moreover it can be shown that the phase change only depends on the mean inner potential $V(x, y, z)$ which the electron sees as it passes through the specimen [16]:

$$\varphi_e = \sigma \int V(x, y, z) dz = \sigma V_t(x, y) \quad (2.8)$$

where $\sigma = \pi/\lambda E$, with E energy of the electron beam, is the interaction constant and $V_t(x, y)$ is the projected potential, with t being the thickness of the specimen. Thus eq. 2.1 becomes:

$$f(x, y) = \exp(i\sigma V_t(x, y)) \quad (2.9)$$

In very thin specimens so where $V_t(x, y) \ll I$, for $f(x, y)$ we can expand the exponential function series and if we neglect the high-order terms we have:

$$f(x, y) = 1 + i\sigma V_t(x, y) \quad (2.10)$$

Eq.2.10 represents the weak phase approximation (WPOA) which says that for a very thin specimen the amplitude of a transmitted wavefunction will be linearly related to the projected potential of the specimen and therefore for the phase. This approximation applies to specimens thinner than 10 nm and of low atomic number [17].

If we express the contrast transfer function (eq.2.4) in real space as $T(x, y) = \cos(x, y) + i \sin(x, y)$, eq. 2.5 in first approximation becomes [16]:

$$I = 1 + 2\sigma V_t(x, y) \otimes \sin(x, y) \quad (2.11)$$

From this equation we can say that the intensity is linearly related to the convolution of the specimen transmission function and the imaginary component of the contrast transfer function. It allows the calculation of simulated images, especially for constant conditions and variations of the specimen structure for HRTEM [17]. Another form of phase imaging is Lorentz Microscopy, which will be described in the following section.

2.5 Lorentz Microscopy

When TEM is applied to the study of magnetic materials it is known as Lorentz microscopy [26] due to the Lorentz interaction between the electron beam and the magnetic sample and the resolution achievable is less than 10 nm. The power of Lorentz microscopy is the capability of investigating magnetic structures in the as-grown state, remanent states, in the presence of applied fields or currents and for different temperatures. By imaging the magnetic structure of the material, information can be obtained on the nature of domain walls, where nucleation occurs, the importance or otherwise of domain wall pinning and many other related phenomena [28]. The basic interaction between the electron beam and the magnetic induction of a ferromagnetic specimen may be understood classically in terms of the Lorentz force [26]:

$$\vec{F} = -e\vec{v} \times \vec{B} \quad (2.12)$$

where e is the magnitude of the charge of the electron, \vec{v} is their velocity and \vec{B} is the magnetic induction. In the case of a uniformly in plane magnetized thin film an incident electron beam will be deflected by the Lorentz force due to the transverse component of the momentum imparted. Assuming that the arrangement of magnetic sample and electron beam is as shown in Figure 2.16a, the deflection will be in the x-direction through an angle $\beta_L(x)$ given by:

$$\beta_L(x) = \frac{e\lambda}{h} \int B_y(x, z) dz \quad (2.13)$$

where λ is electron wavelength, h is Planck's constant, and B_y is the y component of magnetic induction (the same result will be obtained if we put any of the components of the magnetic induction). For a specimen of thickness t , with uniform in-plane magnetization and saturation magnetic induction B_s , the above expression can be simplified to:

$$\beta_L = \frac{eB_s t \lambda}{h} \quad (2.14)$$

Typical values of Lorentz deflections are in the μrad range (for example, in 20 nm thick Py β_L is 12.7 μrad), which is significantly smaller than the 10 mrad typical of Bragg deflections.

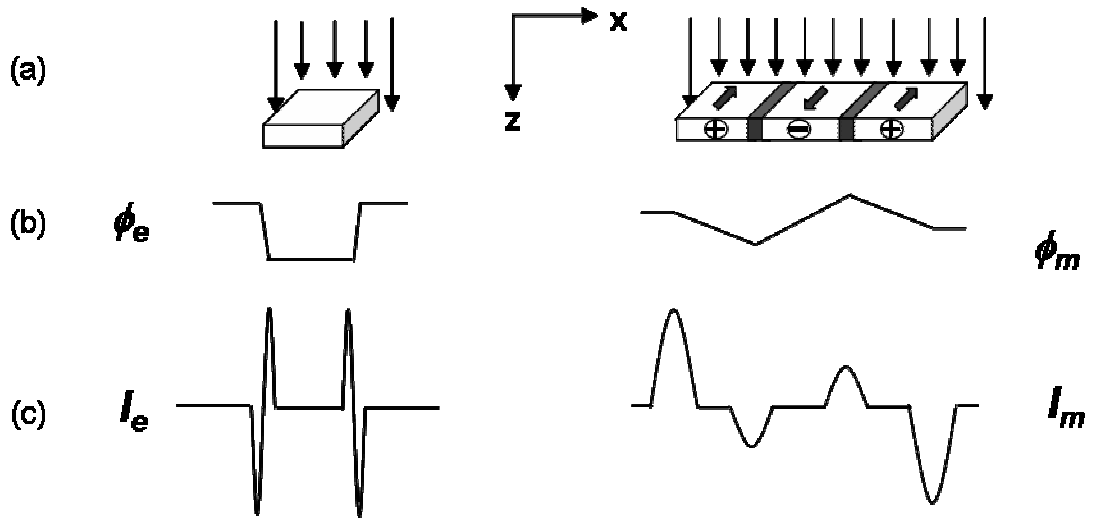


Figure 2.15: Schematic of how contrast arises from electrostatic (left) and magnetic (right) phase objects. (a) shows a representation of the geometrical structure of the objects, (b) the phase variation along the co-ordinate x , (c) the image intensity variation for the objects.

This classical approach is sufficient to qualitatively illustrate most principles of Lorentz microscopy. However, Lorentz microscopy can also be considered from a quantum wave optical approach which is necessary to extract quantitative information and doing image simulations from the technique. In this approach the deflection is proportional to a phase gradient ϕ experienced by the electrons when passing through the sample. By the theory of Aharonov and Bohm [29] the total phase shift is given by:

$$\varphi(x, y) = \varphi_e + \varphi_m = \sigma V_t(x, y) - \frac{e}{\hbar} \int_{-\infty}^{+\infty} \vec{A} \cdot d\vec{l} = \sigma V_t(x, y) - \frac{e}{\hbar} \int_S \vec{B} \cdot d\vec{S} \quad (2.15)$$

where φ_e is the electrostatic phase described in eq.2.8 and explained in the previous section, whereas the action of the magnetic induction on the phase (the magnetic phase φ_m) is described by the projection of the magnetic vector potential \vec{A} along a direction parallel to the beam direction \hat{n} , which is equivalent to the magnetic flux. A representation of each of the components of the total phase is given in fig.2.15.

In this research we used two of the three main Lorentz microscopy modes, Fresnel which is executed in conventional TEM and Differential Phase Contrast (DPC) which is performed with a scanning TEM (STEM) [26]. A brief description of the two modes is provided in the following subsections.

2.5.1 Fresnel Mode

In this particular mode, contrast arises wherever there is a varying component of magnetic induction. Thus magnetic domain walls are revealed as narrow dark or bright bands on, in general, a uniform background [26]. This can be explained in classical terms because the electrons are deflected on passing through the specimen due to the Lorentz force (fig. 2.16(a)). In the case of domain walls the electrons either side of the wall appear to be diverging or converging, so that by simply defocusing the image forming lens the walls are revealed as bright and dark lines (fig. 2.16(b)). In polycrystalline thin films with in-plane magnetisation (as in the case of CoFeB in the MgO/CoFeB/MgO multilayers), due to the fluctuations of the magnetisation direction between crystallites, magnetisation ripple, a wavelike magnetic fine structure, can be observed in the Fresnel image (fig. 2.16 b-c)).

Magnetization ripple (also known as dispersion) is the phenomenon whereby the magnetization direction varies locally and quasi periodically from its mean direction. It is a consequence of the anisotropy of the individual crystal grains and the random (in either two or three dimensions) distribution of the crystallite axes. Fuller and Hale, in their paper reporting the discovery of ripple [51], described two basic ripple components: longitudinal, in which the wave-fronts of the fluctuations of the magnetization direction are perpendicular to the mean magnetization, and lateral or transverse in which the wave-

fronts are parallel to the mean magnetisation. Since the volume pole density is very small for longitudinal ripple but not for transverse ripple, and since the two are equivalent with respect to exchange, random local anisotropy, and uniform forces, the main contribution to the magnetization ripple should be longitudinal. Fuller and Hale thus interpreted the fine-structure lines they observed as the loci of constant M , orthogonal to the mean magnetisation. They found a mean "wavelength" of $\sim 2 \times 10^{-4}$ cm and a mean amplitude of $\sim 10^{-2}$ rad. Fuchs has suggested that the origin of ripple is to be found in crystalline anisotropy forces, which vary randomly in direction from crystallite to crystallite. The magnetization does not follow these local wanderings of the direction of minimum anisotropy energy, but because of exchange coupling, which tends to straighten the path of \mathbf{M} follows the mean easy axis, averaged over a number of crystallites [50]. Thus the ripple can be exploited to infer the direction of magnetisation within domains.

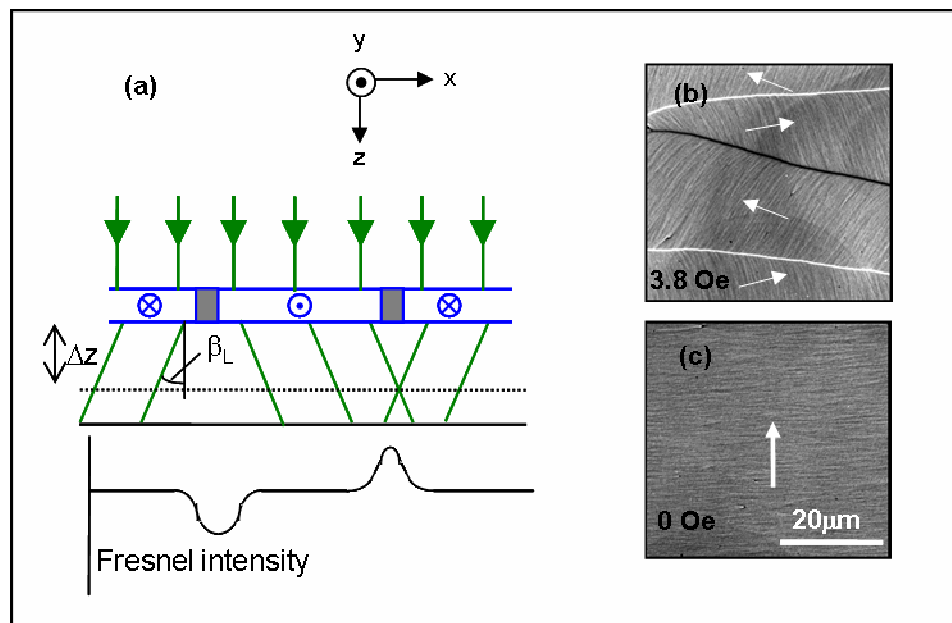


Figure 2.16: Schematic of Fresnel Imaging (a), Image displaying domain walls and (b) ripple contrast (c) in a Permalloy film 20 nm thick. Courtesy of SSP group.

The relationship between the image intensity and the specimen transmission function is generally nonlinear in Fresnel imaging, and this does not allow to quantify the spatial variation of magnetisation [26]. However, it is well suited for identifying domain geometries and looking at changes in magnetic structure with field. Image contrast is generated by simply defocusing the image forming lens and magnetisation reversal can be achieved by varying the sample orientation in the objective lens field resulting in a varying component of applied field in the plane of the sample.

As mentioned before, in order to perform image simulations, one should consider the wave optical approach. The expression of the image intensity in eq.2.6 can be simplified for small values of defocus Δz (i.e. $\Delta z \lambda k^2 < 0.1$), small angle approximation applied to the contrast transfer function [54], and for constant amplitude the image intensity to first order it can be expressed as [25]:

$$I(x, y) = 1 - \frac{\Delta z \lambda}{2\pi} \nabla_{\perp}^2 \varphi(x, y) \quad (2.16)$$

Therefore the image intensity, under these constraints, is linearly related to the in-plane Laplacian of the phase of the specimen transmission function. First order effects are dominant in this approximation, called linear imaging condition. However most of the images are acquired with a defocus larger than the upper limit achieved in the small defocus approximation (most of the images are acquired with a defocus of at least 200 μm) and this will affect the resolution achievable with this technique (in the best case this will be tens of nanometres). Moreover, to first order the intensity changes relate to the Laplacian of the phase (eq.2.16) and as such can be very large at the edges with the electrostatic effects many times larger than the magnetic effects. An indication of such effects for a 20nm thick NiFe film is that the electrostatic phase change at an edge may be 2π radians, whilst the phase gradient within a magnetic domain may be 2π radians per 200 nm. Therefore the electrostatic effects can be very large compared to the magnetic ones where the edges are sharp, however in samples of uniform thickness the electrostatic phase is constant and therefore this term does not contribute to the contrast of the Fresnel image. In this way the achievement of high level of contrast arising from the variation of the magnetic structure is possible and this allows in-situ measurements to be performed in real time.

Reference [25] shows that beginning with eq.2.16, and after the reformulation of the magnetic phase in eq.2.15 using fundamental equations of magnetism, the intensity of a Fresnel image at small defocus Δz , where $\Delta z \lambda k^2 \ll 1$, for a thin film normal to the beam with no magnetisation variation through the thickness can be written as:

$$I(x, y) = 1 - \frac{e\mu_0 \lambda t}{h} (\nabla \times \vec{M}(x, y))_z \quad (2.17)$$

In this way images can be calculated and this allows to have a better understanding of experimental results. This will be widely employed for the interpretation of the experimental results from magnetic experiments on electrodeposited nanowires. Eq.2.18 reveals that the image intensity can be calculated from knowledge of the microscope parameters and the out of plane component of the magnetisation curl when the linear imaging conditions are applicable. The spatial frequencies in the image determine the extent that this equation can be applied for a given defocus. To calculate the Fresnel image, we require a phase image and an amplitude image. The phase is calculated using the process detailed in [31]. A schematic of the phase variation along the x coordinate is depicted in fig.2.15b left. The x, y and z components of the magnetisation can be obtained from an OOMMF simulation or by creating three separate images each representing one component of the magnetisation. This process allows also the calculation of the integrated magnetic induction for that given configuration.

In the simplest case we can neglect amplitude modulation and can make it equal to 1 everywhere. This is the case of pure phase imaging. However, in some cases the amplitude and hence electrostatic phase from changes in the mean inner potential must be included. To include simply the amplitude, we can make a mask of the element being simulated, with a value of 1 in the patterned region and less than 1 everywhere else. To get the electrostatic phase, the electrostatic contribution in eq.2.16 can be simplified to:

$$\varphi_e = \pi \frac{V_0 t}{\lambda E} \quad (2.18)$$

where V_0 is the inner potential of the material, 21 V for Permalloy, t is the sample thickness, λ is the electron wavelength, and E is the electron accelerating voltage.

2.5.2 Differential Phase Contrast Mode

Differential phase contrast (DPC) [30] is a technique performed in a scanning transmission electron microscope (STEM). There is a direct relationship between the integrated magnetic induction in the sample and the measured signal which allows quantitative measurements of induction to be made. Figure 2.18a shows a schematic of the DPC imaging mode outlined here. The electron beam is focused into a small probe and scanned across the sample by two sets of deflection coils which keep the beam parallel to the optic axis. On transmission through the sample, the beam emerges as a cone of illumination in a

plane conjugate with the detector, pivot points project it onto a segmented detector in the far-field and the descan coils correct the scale. A magnetic sample will cause the beam to be deflected by the Lorentz force which is perpendicular to both the induction and the beam direction, and will be offset from the centre of the detector, as illustrated in figure 2.17 in detail and 2.18a. The difference signal from the quadrants of the detector gives a measure of the beam deflection which in turn is proportional to the integrated magnetic induction.

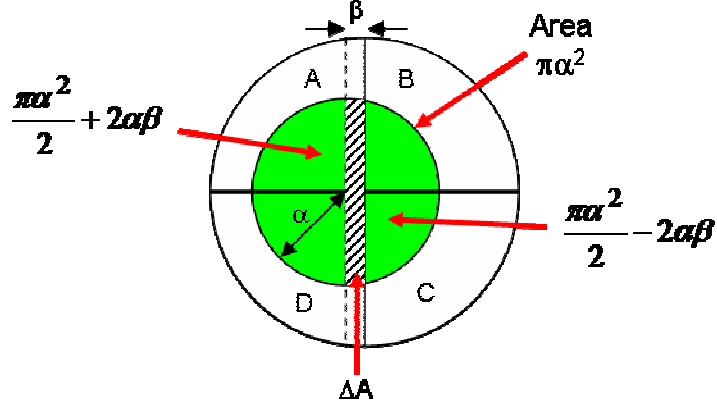


Figure 2.17: Schematic of the deflected beam hitting the quadrant detector.

If the convergent angle of the incident beam is denoted by α (fig.2.17) and is proportional to the radius of the disc, whereas the deflection angle is denoted by β (fig. 2.17), the difference signal can be written as [52]:

$$S = \frac{I}{\pi\alpha^2} \left[\left(\frac{\pi\alpha^2}{2} + 2\alpha\beta \right) - \left(\frac{\pi\alpha^2}{2} - 2\alpha\beta \right) \right] = \frac{4I\beta}{\pi\alpha^2} = \frac{4IeB_s\lambda t}{\pi\alpha^2 h} \quad (2.19)$$

where I is the intensity of the electron beam and $\pi\alpha$ is the area of the beam hitting the detector. The equation (2.19) indicates that the difference signal produced is linearly proportional to the Lorentz deflection, which is directly related to integrated magnetic induction. It is important to note that the linear relation in (2.19) is only valid when the deflection is small ($\beta < \alpha/10$).

The DPC mode is an in-focus imaging mode and the resolution of the image produced in the DPC mode is determined by the diameter of the probe (as seen in section 2.3.2.5 in relation to STEM systems) which is dependent on demagnification of source and diffraction/aberration effects. The demagnification of the source depends on whether the

system is aligned and set in low magnification scanning (LMS) or high magnification scanning (HMS). In LMS mode, which is the one used to characterise the magnetic structure of nanowires described in chapter 4, the upper Lorentz lens is turned off, resulting in a larger probe at the specimen due to a smaller demagnification of the optical system and smaller probe angle providing a resolution about 20-30 nm. However, as $\beta/\alpha \sim 10$, DPC signals are very sensitive to the changes of magnetic induction, and therefore producing high contrast. Summing all the signals from the detector will give an equivalent bright field image (as the one in fig. 2.18e) of the sample in perfect registration with the difference images, allowing direct correlation between magnetic and structural information. In fig. 2.8(b, c) is shown an example of induction maps of mutually orthogonal directions for a Permalloy element with in-plane dimensions $1000 \times 200 \text{ nm}^2$, 40 nm thick. In HMS mode (used to obtain the images in fig.2.18b-c) the upper Lorentz lens is switched on to form a finer probe below 10 nm with large probe angle. Therefore, a greater useful magnification is achievable with very high spatial resolution in HMS mode by scanning a smaller area of the sample with a finer probe. Nevertheless, since $\beta \sim \alpha/1000$, the signal is less sensitive to changes in magnetic induction, and a lower level of contrast is observed.

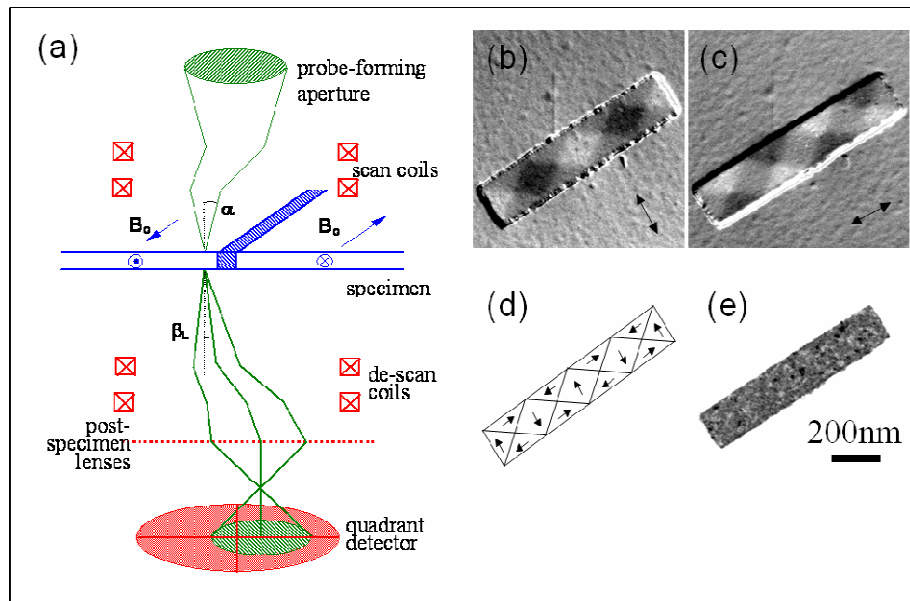


Figure 2.18: Schematic of DPC imaging (a), and DPC images of an $1000 \times 200 \text{ nm}^2$ permalloy element, 40 nm thick (b) and (c). The arrows in (b) and (c) represent respectively the orientation of the y and x component of the magnetic induction. (d) is the domain configuration of the element and (e) the relative bright field image. Courtesy of SSP group.

In order to consider the quantitative aspects of DPC, it is worth recall that the deflection (eq.2.13) is caused by induction components perpendicular to the electron beam trajectory. If we consider the quantum mechanical approach, the electron beam experiences a phase shift as it passes through the magnetic material, as we saw in eq.2.15. Mansuripur elaborated a procedure which uses the magnetic vector potential to calculate the phase changes imparted to the electron beam in Lorentz microscopy [31].

In differential phase contrast microscopy an in focus image is built up as the beam is rastered across the sample. Contrast in the final DPC image is generated by a segmented detector which converts phase changes into intensity variations. By taking the gradient derivative of the magnetic phase (ϕ_m in eq.2.15) in the plane of the film, perpendicular to the electron beam, we derive a quantity which is proportional to components of in plane integrated induction:

$$\nabla_{\perp} \phi(x, y) = -\frac{e}{\hbar} \int_{-\infty}^{+\infty} (\nabla \times \vec{A}) \times \hat{n} dl \quad (2.20)$$

And since $\nabla \times \vec{A} = \vec{B}$ eq. 2.20 becomes:

$$\nabla_{\perp} \phi(x, y) = -\frac{e}{\hbar} \int_{-\infty}^{+\infty} (\vec{B} \times \hat{n}) dl = \frac{2\pi}{\lambda} \beta \quad (2.21)$$

Therefore we can say that the DPC image is related to integrated magnetic induction perpendicular to the beam, which indicates that the differential phase produces a map of the deflection angle and thus of the integrated induction.

2.6 Analytical Techniques

Modern transmission electron microscopes provide a number of complementary capabilities together with high resolution imaging. One possibility is analytical electron microscopy (AEM) where electrons which have lost energy due to inelastic scattering processes (electron energy loss spectroscopy - EELS and energy filtered transmission electron microscopy - EFTEM) and emitted electromagnetic radiation (energy dispersive x-ray spectroscopy - EDX), acquired by specific detectors, provide information on chemical composition and local atomic environment with a spatial resolution down to 0.2 nm. A schematic of the interactions between electron beam and the specimen is depicted in

fig. 2.19. EFTEM was used to locate characteristic elements within the layers composing MgO/CoFeB/MgO system, described in chapter 3, whereas EELS, EFTEM and EDX were used to characterise the composition of nanowires described in chapter 4. The following sections will provide an overview of the three techniques.

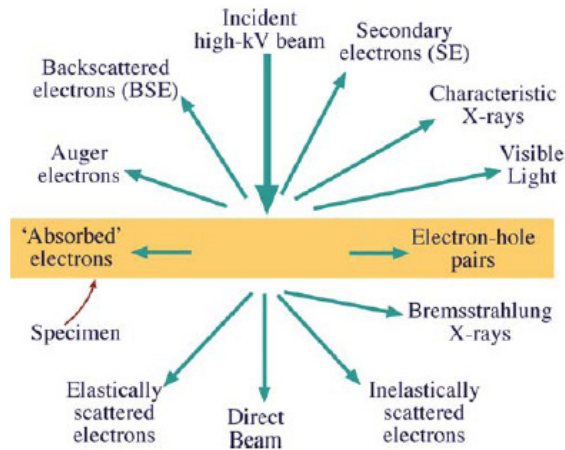


Figure 2.19: Signals generated when a high-energy beam of electrons interacts with a thin specimen. From [16].

2.6.1 Electron Energy Loss Spectroscopy

When an electron beam passes through a specimen it can lose energy by a variety of processes as shown in fig.2.19. Electron energy loss spectroscopy [32] is a technique that, by measuring the energy losses from a localised region of the specimen, can allow determination of the specimen composition. An energy analyser, fitted at the bottom of the TEM column (fig. 2.6), produces a spectrum of the energy distribution of the transmitted electrons.

An EELS spectrum can be divided into three regions: the zero loss peak, the low loss and the high loss region. These different regimes of energy losses can give us different information about the specimen [16]. The zero loss peak, which is the strongest peak in fig.2.20a consists primarily of elastic forward-scattered electrons, but also contains electrons that have suffered minor energy losses; if the specimen is thin, the predominant feature in the energy loss spectrum will be the zero-loss peak. It consists mainly of electrons that have completely retained the beam energy E_0 . It defines the energy resolution and it is essential for the calibration of the spectrum. The low loss region up to an energy of ~ 50 eV contains electrons which have interacted with the weakly bound

outer-shell electrons of the atoms of the specimen. It represents the peak at about 25 eV in fig.2.20a. In this part of the spectrum we come across electrons that have set up plasmon oscillations or have generated inter- or intra-band transitions. Thus they contain information about the electronic band structure of the specimen. The high-loss region contains electrons which have interacted with the more tightly bound inner-shell electrons. Inner-shell ionisation loss signal is called "edge". Since the typical energy resolution of EELS spectrometers is at best 0.3 eV, it is much easier to detect differences in spectra that arise from the presence of different energy states in the shell. In fig. 2.20b it is shown a high loss spectrum of the O K-edge, Ni and Fe L-edge. In reality we are dealing with atoms integrated into a crystal lattice or amorphous structure, the spectra become more complex. The ionisation edges are superimposed on a decreasing background intensity from electrons that have undergone random, plural inelastic scattering events. The edge shape may also contain fine structure around the position of the edge which is due to bonding effects and is termed energy-loss near-edge structure (ELNES). More than 50 eV above the edge, small intensity oscillations may be detectable due to diffraction effects from the atoms surrounding the ionised atoms and these oscillations are called extended energy-loss fine structure (EXELFS) [16].

2.6.2 Energy Filtered Transmission Electron Microscopy

A method to perform EELS in TEM is EFTEM. EFTEM utilizes a special spectrometer which has the capability to filter the energy lost by electrons that have interacted with the specimen. In this way, concentrating on a particular ionisation edge, it is possible to build up images which show a two-dimensional distribution of a specific element. The method used for the elemental mapping is the 3 windows method. It consist in the acquisition of two images with energy windows before and one after the ionisation edge of interest. In this way the background contribution can be removed from the integration window after the edge [32].

For EFTEM experiments performed in this thesis a post column energy-filter (GIF manufactured by Gatan [34,35]) installed as an attachment at the end of the column has been used. The spatial resolution obtained in an EFTEM image is limited by several factors such as delocalisation of inelastic scattering which is due to the ionization of an atom by a distant fast electron, chromatic aberration of objective lens, width of the slit, diffraction limit due to objective aperture, spherical aberration due to objective lens, statistical noise

due to low inelastic cross-sections, radiation damage of the specimen and some instrumental instabilities (high voltage drift, sample drift etc.). In the best cases taking in account all these factors, the spatial resolution of EFTEM elemental maps would be limited to 1 nm. An example of elemental maps is shown in fig.2.21. It refers to an electrodeposited nanowire. More details about these experimental images will be provided in chapter 4.

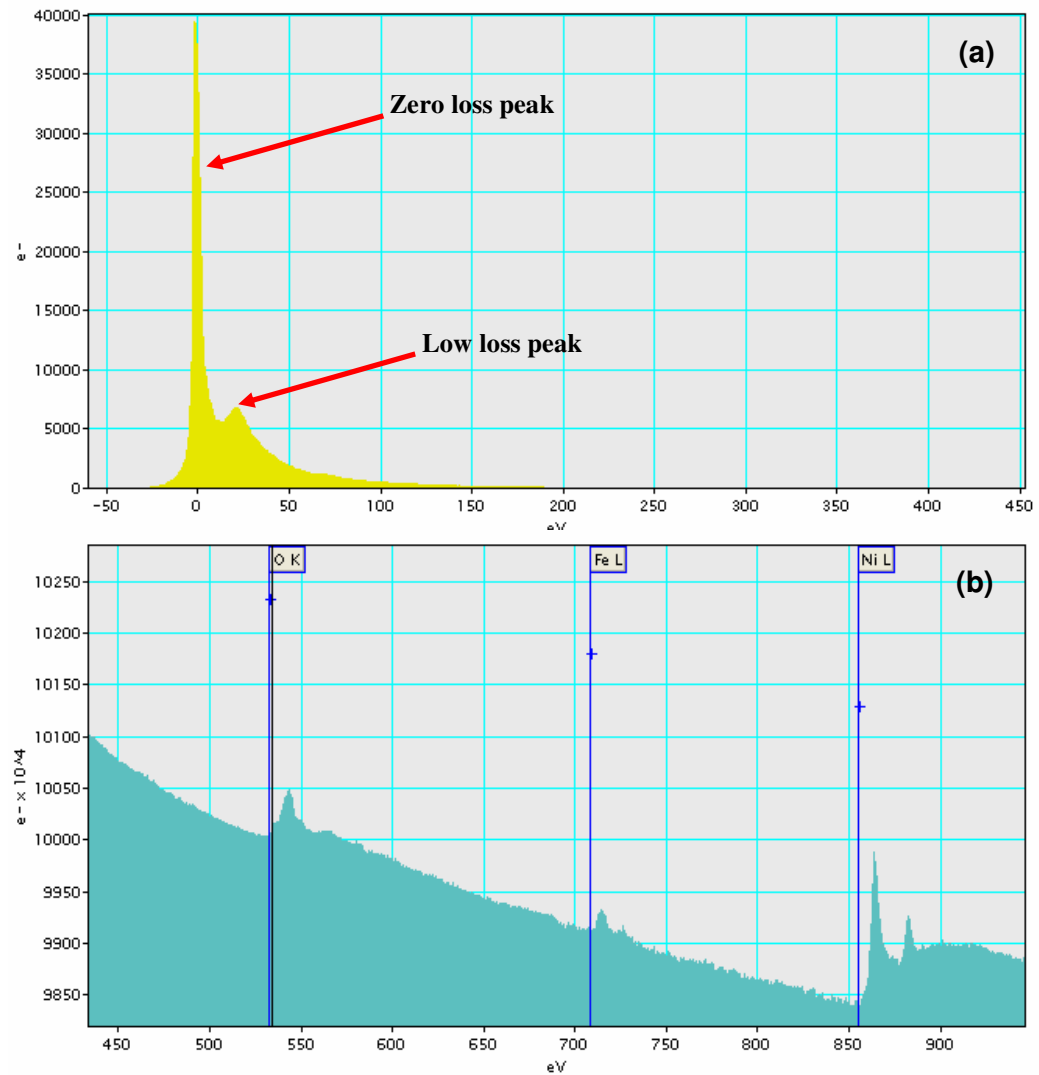


Figure 2.20: (a) Low loss spectrum and (b) high loss spectrum in the energy range 200-700 eV of a $\text{Ni}_{80}\text{Fe}_{20}$ electrodeposited nanowire displaying O, Fe and Ni edges, acquired with the microscope FEI T20.

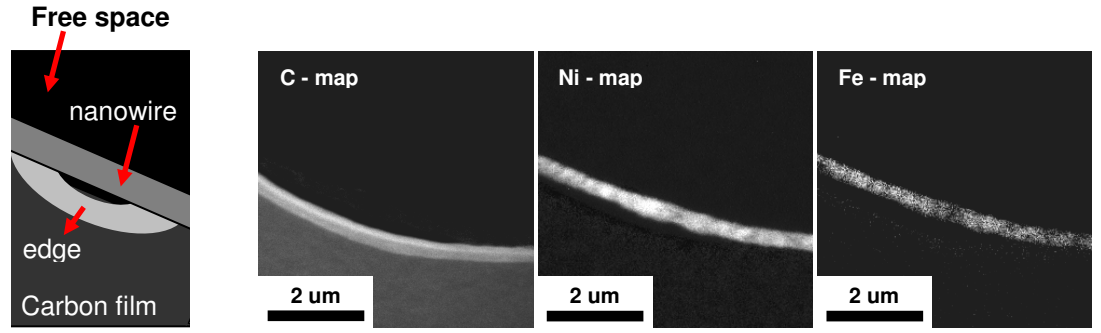


Figure 2.21: Elemental maps for C, Ni, Fe of a $\text{Ni}_{80}\text{Fe}_{20}$ electroposited nanowire on a holey carbon grid acquired with the FEI T20 and a schematic of the system.

2.6.3 X-Ray Dispersive Spectroscopy

Following an inner shell ionisation, the transition to the ground state may involve the emission of an x-ray, the x-ray wavelengths being specific to the atomic species in the volume excited by the electron probe. By measuring the energy of each emitted x-ray using a suitable spectrometer, a quantitative analysis of the composition of the specimen can be performed. Cliff and Lorimer in 1975 [39] showed that the quantification was possible using simply the ratio of the intensities I_a and I_b gathered from two elements a and b simultaneously. The weight percent of each element C_a and C_b can be related to the measured intensities by the so-called Cliff-Lorimer equation [39]:

$$\frac{C_a}{C_b} = K_{ab} \frac{I_a}{I_b} \quad (2.22)$$

The term K_{ab} is often termed the Cliff-Lorimer factor. It is actually not a constant, but it varies according to the TEM/XEDS system and the accelerating voltage. Normally standards are required to ensure a high level of accuracy as uncertainties still exist in the fundamental cross-sections and detector efficiencies. EDX was used in this research to investigate the presence of any copper within the electrodeposited nanowires (chapter 4) and to investigate whether Ni and Fe were in the correct proportions to form Permalloy. More details will be provided in chapter 4.

2.7 Polar Kerr Magnetometry

Magneto-optic Kerr effect (MOKE) [40 - 42] describes the interaction of electromagnetic waves with magnetic materials, which corresponds to the rotation or the change in the

intensity of the linearly polarized light upon reflecting from the magnetic materials subjected to the magnetic field. This effect was first observed by John Kerr in 1887 [43-44]. The Kerr signal is proportional to the magnetization of the magnetic materials, so it is useful to study the magnetic properties of ferromagnetic and ferrimagnetic films and materials. By measuring this Kerr rotation at various applied field values during a field-sweep, a plot of the hysteresis loop for a specimen is obtained. Hysteresis loop measurements for different temperatures using this technique (also known as Magneto Optical Kerr Effect, MOKE) on $(\text{Co/Pt/Ni/Pt})_x/\text{CoFeB}$ multilayers (described in chapter 5), were carried out during a secondment performed at Spintec (CEA) in Grenoble (France).

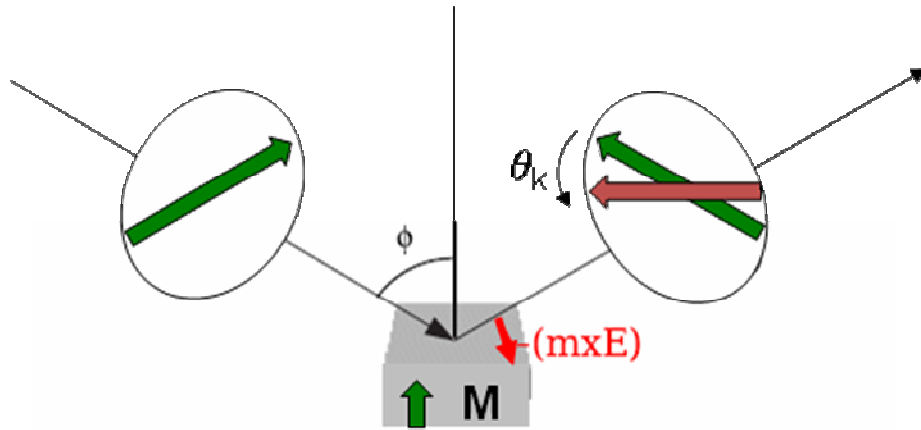


Figure 2.22: Mechanism of Kerr rotation in polar configuration.

There are three different modes of operation based on the orientation of magnetization with respect to the incident plane and the plane of the sample. The longitudinal and the transverse modes are used to study the samples exhibiting in-plane anisotropy, whereas polar mode is used to study the sample exhibiting out of plane anisotropy. We will focus on the description of the polar mode, since it is the one used for the investigation of the magnetic multilayers with perpendicular anisotropy, that will be described in chapter 5. In this configuration the magnetisation is oriented perpendicular to the surface as shown in fig.2.22. A linearly polarised light beam, making an angle ϕ with the normal to the surface of the specimen, will induce electrons to oscillate parallel to the plane of polarisation. A large proportion of the light is regularly reflected from the surface, polarised in the same plane as the incoming light. Additionally there is a small secondary reflected component which has its plane of polarisation at an angle θ_K (the Kerr rotation) to the regularly reflected light. At the same time the Lorentz force induces a small component of vibrational motion perpendicular to the primary motion and the direction of magnetisation.

The secondary motion, which is proportional to $-\vec{m} \times \vec{E}$, generates a secondary reflected component with a rotated plane of polarisation. The total amplitude of the Kerr signal relative to the incident amplitude, for the polar configuration can be expressed as [27]:

$$A_{tot} = -R_P \cos \Psi_P \sin \alpha_S + R_S \sin \Psi_P \cos \alpha_S + R_K^{pol} \cos(\alpha_S - \Psi_P) m_{pol} \quad (2.24)$$

where R_P and R_S are the reflection coefficient for the parallel and perpendicular component to the plane of incidence, Ψ_P is the angle that the polariser makes with the plane of incidence and α_S is the angle that the analyser makes with an axis perpendicular to the plane of incidence, R_K^{pol} is the Kerr amplitude for polar configuration and m_{pol} is the magnetisation. A_{tot} can be expressed as $A_N \pm A_K$ where A_N represents the sum of the first two terms, and A_K is the effective Kerr amplitude and the sign takes into account that domains can be oppositely magnetised. This leads to the definition of the Kerr rotation θ_K where we can see that the Kerr rotation is proportional to the magnetisation [27]:

$$\theta_K = \frac{A_K}{A_N} = \frac{R_K^{pol} \cos(\alpha_S - \Psi_P)}{-R_P \cos \Psi_P \sin \alpha_S + R_S \sin \Psi_P \cos \alpha_S} m_{pol} \quad (2.25)$$

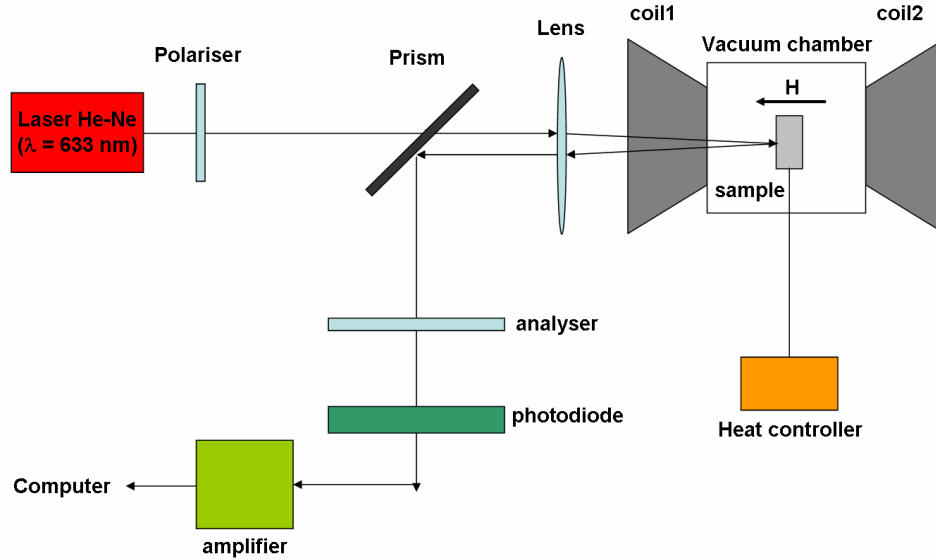


Figure 2.23: Schematic of the experimental setup for polar MOKE experiments in chapter 5.

Figure 2.23 shows the schematic layout of the polar MOKE magnetometer used to acquire the hysteresis loops in chapter 5. A He-Ne laser ($\lambda = 633$ nm) has been used as an incident

beam. The measured area was determined by the size of the laser spot, which is about 4mm. A couple of coils were used to provide the external field, and can generate fields up to 1T. They provide only a linear ramp, but it has a wide range of sweep time, which ensures enough data points at a required field are recorded. The laser light passes through the polarizer, which linearly polarizes the light. The emerging linearly polarized light is then guided on to the sample using reflecting mirror (prism). The reflected light from the sample is guided on to the Wollaston prism, in which the light is decomposed into two orthogonal linear polarized components. The intensities of both the components, I_1 and I_2 are measured with photodiodes. The normalised difference signal $(I_1 - I_2)/(I_1 + I_2)$, is proportional to the rotation of the polarization θ_K with respect to the axis of the prism. In order to suppress the varying stray light intensity, the whole unit is covered with a black box. The normalization in the signal unit suppresses the intensity fluctuation of the light source. In the signal conditioning unit the outputs from the photodiodes are amplified and the difference between the intensities is normalised over the sum of the intensities as mentioned earlier. The applied field and the Kerr signal are measured by simultaneous switching between the channels and the signal is then sent to a PC unit. A 5 μm laser spot gives a sensitivity to the magnetic moment of about 6×10^{-12} emu [53].

2.8 Summary

An overview of all the experimental techniques employed for the fabrication and characterisation of the samples investigated for this research was presented in this chapter. In Section 2.2 the techniques used to grow the different specimens, sputtering and electrodeposition was described. The overview of the structure of a transmission electron microscope (TEM) and the main operating modes used for basic characterisation was provided in Section 2.3 and 2.4. Sections 2.5 and 2.6 has described special applications of TEM, Lorentz Microscopy used for the investigation of the magnetic domain structure of the specimens and widely employed in this work, and analytical electron microscopy (AEM) used for compositional analysis. Finally Section 2.7 gave an overview of MOKE magnetometry, used to characterise the hysteresis properties of multilayers with perpendicular anisotropy described in chapter 5.

In the next chapter the investigation of the evolution of the physical structure and domain structure of MgO/CoFeB/MgO multilayers for decreasing thickness of the CoFeB layer will be described.

Bibliography

- [1] Khamsehpour B. *et al.*, *Vac. Sci. Technol.*, (1996), **14**, 3361.
- [2] Mattox D.M., *The Foundations of Vacuum Coating Technology*, Noyes Publications/William Andrew Publishing, Norwich, New York, USA, (2003).
- [3] Penning F.M., *Physica (Utrecht)*, (1936), **3**, 873.
- [4] Davidse P.D. and Maissel L.I., *J. Appl. Phys.*, (1965), **37(2)**, 574.
- [5] Piraux L. *et al.*, *Nano Letters*, (2007), **7(9)**, 2563.
- [6] Dubois S. *et al.*, *Appl. Phys. Lett.*, (1997), **70(3)**, 396.
- [7] Arai, K.I. *et al.*, *J. Magn. Soc. Jpn*, (1989), **13**, 789.
- [8] Whitney, T. *et al.*, *Science*, (1993), **261**, 1316.
- [9] Piraux L. *et al.*, *Appl. Phys. Lett.*, (1994), **65**, 2484.
- [10] Blondel A. *et al.*, *Appl. Phys. Lett.*, (1994), **65**, 3019.
- [11] Nielsch A. *et al.*, *Adv. Mater.*, (2000), **12(8)**, 582.
- [12] Knoll M. and Ruska E., *Z Physik*, (1932), **78**, 318.
- [13] De Broglie L., *Ann. de Physiques*, (1925), **3**, 22.
- [14] Busch H., *Arch. Electrotechnik*, (1927), **18**, 583.
- [15] Reimer L. and Kohl H., *Transmission Electron Microscopy - Physics of Image Formation - 5th Edition*, Springer, (2008).
- [16] Williams D.B. and Carter C.B., *Transmission Electron Microscopy*, McGraw Hill, (1983).
- [17] Hawkes P.W., *Electron Optics and Electron Microscopy*, Electron Optics and Electron Microscopy Taylor and Francis Ltd., London, (1972).

- [18] Born M. and Wolf E., *Principles of Optics*, Oxford: Pergamon, (1975).
- [19] Van Dyck D. and de Jong A.F., *Ultramicroscopy*, (1992), **47**, 266.
- [20] Cowley J.M., *Electron Diffraction Techniques 1*, Oxford Science Publication, (1992).
- [21] De Graef M. and Zhu Y., *J. Appl. Phys.*, (2001), **89**, 7177.
- [22] Bragg W.L., *The Crystalline State, I*, Cornell University Press, Ithaca, New York, (1965).
- [23] LePoole J.B., *Philips Tech. Rundsch.*, (1947), **9**, 33.
- [24] Kossel W. and Mllenstedt G., *Ann. Der Phys.*, (1939), **36**, 113.
- [25] McVitie S. and Cushley M., *Ultramicroscopy*, (2006), **106**, 423.
- [26] Chapman J.N., *Journal of Physics D*, (1984), **17**, 623.
- [27] Hubert A. and Schäfer R., *Magnetic Domains - The Analysis of Magnetic Microstrutures*, Springer, (2009), ch.2.
- [28] Chapman J.N and Scheinfein M.R., *J. Magn. Magn. Mater.*, (1999), **200**, 729.
- [29] Aharonov Y. and Bohm D., *Phys. Rev. B*, (1959), **115**, 485.
- [30] Chapman J.N *et al.*, *Ultramicroscopy*, (1978), **3**, 203.
- [31] Mansuripur J., *J.Appl.Phys.*, (1991), **69**, 2455.
- [32] Egerton R.F., *Electron Energy-Loss Spectroscopy in the Electron Microscope*, 2nd edition, Plenum Press, New York, (1996).
- [33] Crozier P.A, *Phil. Mag. B.*, (1990), **61**, 311.
- [34] Shuman H. *et al.*, *Scan. Elec. Microsc.*, (1985), 737.
- [35] Krivanek O.L. *et al.*, *Microsc. Microanal. Microst.*, (1991), **2**, 315.
- [36] Navidi-Kamai T. and Kohl H., *Ultramicroscopy*, (2000), **81**, 223.

- [37] Hillier J. and Baker R.F., *J.Appl.Phys.*, (1944), **15**, 663.
- [38] Castaing R., Thesis, University of Paris, (1951), ONERA Publication, 55.
- [39] Cliff G. and Lorimer G.W., *J. Microsc.*, (1975), **103**, 203.
- [40] Nederpel P.Q.J. and Martens J.W.D., *Rev. Sci. Instrum.*, (1985), **56**, 687.
- [41] Allwood D.A. *et al.*, *J. Phy. D: Appl. Phys.*, (2003), **36**, 2175.
- [42] Zak J. *et al.*, *J. Magn. Magn. Mater.*, (1990), **89**, 107.
- [43] Kerr J., *Phil. Mag.*, (1877), **3**, 321.
- [44] Kerr J., *Phil. Mag.*, (1878), **5**, 161.
- [45] Qiu Z.Q. and Bader S.D., *Rev. Sci. Instrum.*, (2000), **71**, 1243.
- [46] <http://www.pnas.org/content/102/20/7069/F3.expansion.html>
- [47] Chescocoe D. And Goodhew P.J., The Operation of Transmission and Scanning Electron Microscopes, Oxford University Press, (1990).
- [48] Goodhew P.J. *et al.*, Electron Microscopy and Analysis, 3rd edition, Taylor and Francis, (2001).
- [49] Grollier J. *et al.*, *Phys. Rev. B*, (2006), **73**, 060409(R).
- [50] Harte K.J., *J.Appl.Phys.*, (1968), **39**, 1503.
- [51] Hale M. E. *et al.*, *J. Appl. Phys.*, (1959), **30**, 789.
- [52] Chapman J.N. *et al.*, *IEEE Trans. Magn.*, (1994), **30**, 4479.
- [53] Allwood D.A. *et al.*, *J. Phys. D: Appl. Phys.*, (2003), **36**, 2175.
- [54] Beleggia M. *et al.*, *Ultramicroscopy*, (2004), **102**, 37.

CHAPTER 3

Investigation of MgO/CoFeB/MgO multilayers for magnetic tunnel junction sensor applications

3.1 Introduction

Magnetic tunnel junctions (MTJs) have been extensively studied in view of their technological applications as magnetic random access memories (MRAM) or high sensitivity field sensors. The achievement of high TMR values and a low level of noise are crucial in the construction of reliable magnetic devices, as mentioned in section 1.7.3. High values of TMR such as the 500% achieved by Lee *et al.* [1] can be obtained by a suitable choice of materials. In particular MgO as the barrier [2] and CoFeB as material for the ferromagnetic electrodes [3] have been proved to be particularly effective.

Additional to the first requirement for a reliable MTJ, the fulfilment of low noise level devices is still a challenge. Several strategies have been proposed during this time in order to find a way to minimise this issue. A cross magnetization pattern, in which the magnetization of a sensing layer is oriented perpendicular to the magnetization of a pinned reference layer, was proposed by Tondra *et al.* [8] to achieve both linearity and reversibility in MTJs. Another strategy includes the exploitation of coherent rotation of the magnetization in the sensing layer, which is responsible for linear field response and hysteresis-free switching. This has been induced by using an external bias field generated by specific circuitry, induced anisotropy in the sensing layer and combining the use of step bunched substrates with exchange biasing of the sensing layer [9]. However, these techniques require a complicated sensor design, which results in high power consumption and limited integration on Si chips. The exchange bias of antiferromagnetic/ferromagnetic bilayers and perpendicular anisotropy of the Pt/CoFe interface were proposed to circumvent the drawbacks, but these are still based on the crossed magnetization pattern [10, 11]. Jang *et al.* in 2006 [12] and more recently Wisniowski *et al.* in 2008 [13]

investigated the effect of CoFeB free layer thickness on the transfer curves of MgO tunnel junctions in order to understand whether this strategy lead to the creation of analog high-sensitivity field sensors with a relatively simple design, lower power consumption, and smaller aspect ratio compared with the previously reported sensors.

To this purpose Wisniowski *et al.* [13] fabricated a set of magnetic tunnel junctions by magnetron sputtering (Nordiko 2000 system) with a base pressure of 7×10^{-9} Torr with the following structure: glass/Ta(50)/Ru(180)/Ta(30)/PtMn(180)/CoFe(22)/Ru(9)/CoFeB(30)/MgO(13.5)/CoFeB(t_F)/Ru(50)/ Ta(50) (the thicknesses of the layers are expressed in Å). The free layer CoFeB thickness t_F was varied from 30 Å to 14.5 Å. A schematic of this structure is depicted in fig. 3.1(a). The easy axis of the magnetic layers was set by applying a 20 Oe field during deposition. The samples were annealed in high vacuum at 330° C, for 1h in a magnetic field of 5 kOe applied along the easy axis, and furnace cooled in the field.

The magnetic behaviour has been investigated by using a vibrating sample magnetometer (VSM) and the electrical properties with a dc four-probe setup. They found that below a critical thickness (15.5Å) the MTJ transfer curves became linear, highly sensitive and hysteresis-free as shown in fig. 3.1(b), suggesting a superparamagnetic behaviour of the CoFeB free layer. However, this was achieved at the expense of a fall in TMR as reported in fig.3.1(c), possibly caused by the formation of a discontinuous CoFeB free layer.

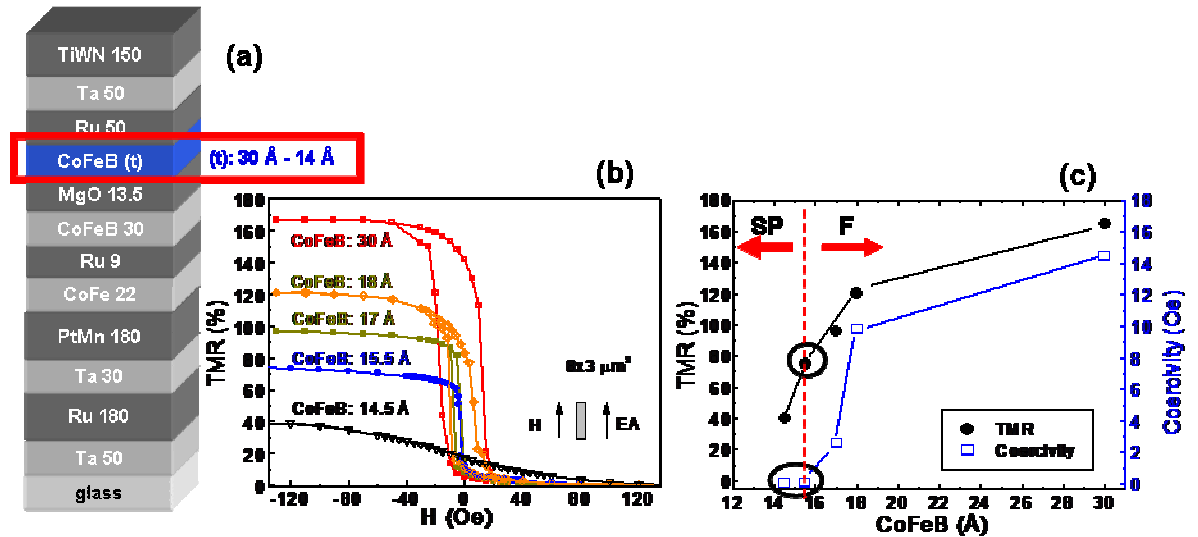


Figure 3.1: (a) Schematic of the MTJ structure investigated by Wisniowski *et al.* in [13]. (b) Transfer curves for field applied parallel to the easy axis of the free and pinned layers, for different thicknesses of CoFeB and after annealing at 330°C and (c) dependence of TMR and coercivity (H_c) on CoFeB thickness where S and F stand for superparamagnetic and ferromagnetic regime. Courtesy of Dr. P. Wisniowski.

Transmission electron microscopy (TEM) is an ideal technique to prove the hypothesis introduced by Wisniowski *et al.* to explain the behaviour they found, since it allows the investigation of evolution of the physical structure for decreasing thickness of the free layer (from 30 to 14 Å), thus achieving useful information to assess the continuity of the free layer. At the same time of great importance is the investigation of the magnetic microstructure because the performance of MTJ sensors depend critically on the way the magnetisation distribution evolves under the application of an external field. Moreover the investigation of the magnetic microstructure provides an interesting insight into the fundamental micromagnetic properties of the material, especially when the thickness of the CoFeB layer is reduced down to 14 Å.

The present chapter aims to present an investigation using conventional transmission electron microscopy (CTEM) and Lorentz microscopy (LTEM) to characterise respectively the physical microstructure and the domain structure of the CoFeB free layer, embedded in a multilayer composed of SiN/MgO(50)/CoFeB(t)/MgO(15), with t from 30 Å down to 14 Å, upon magnetic annealing at the MgO crystallization temperature (340°C). The chapter will be structured as follows. It will begin with the investigation of the physical structure performed by selected area diffraction and bright field imaging of planar samples; then the outcomes from the experiments performed by LTEM will be presented and finally the interpretation of the results by mean of a modified Stoner-Wohlfarth model.

3.2 Fabrication of the samples

The TEM experiments presented in this chapter cannot be performed if the specimens under investigation are full MTJ stacks due to a number of factors. First of all, the total thickness of a MTJ stack is about 500 nm (including substrate), which is far above the maximum thickness allowed to have electron transparency (100 nm). Moreover, some of the layers composing the stack could promote inelastic scattering which should be minimised when one wants to perform imaging experiments. To avoid these problems, a specific set of samples has been prepared by Dr. Jangwei Cao at INESC-MN, composed of a sandwich structure with a CoFeB layer (with the thickness of 14 and 30 Å) embedded in two MgO layers, the top layer 15 Å thick and the bottom layer 50 Å thick. This trilayer has been deposited on a Si₃N₄ membrane, described in section 2.2.1 by magnetron sputtering with a system Nordiko2000. A schematic of the sample is depicted in fig. 3.2.

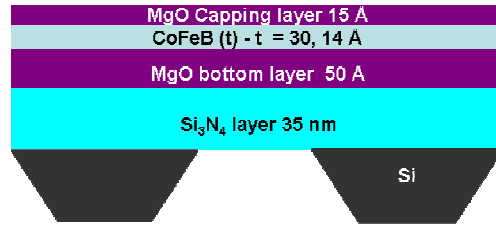


Figure 3.2: Schematic of the specimens investigated in the work presented in this chapter.

The MgO layers have been deposited with a power of 130 W and a pressure of 18 mTorr and a deposition rate of 0.21 Å/s , whereas the CoFeB layer has been deposited with a flow of Ar of 9 SCCM (Standard Cubic Centimetres per Minute), 45 mA current, 5 mTorr pressure, with a deposition rate of 0.58 Å/s . For the CoFeB layer the deposition occurs in a field of 20 Oe applied along one of the edges of the membrane, in order to create an induced anisotropy. The following step is the annealing in a field in which the specimen is kept at a temperature of 320°C in a 4 kOe field aligned along the same edge as the one selected before the deposition, for one hour.

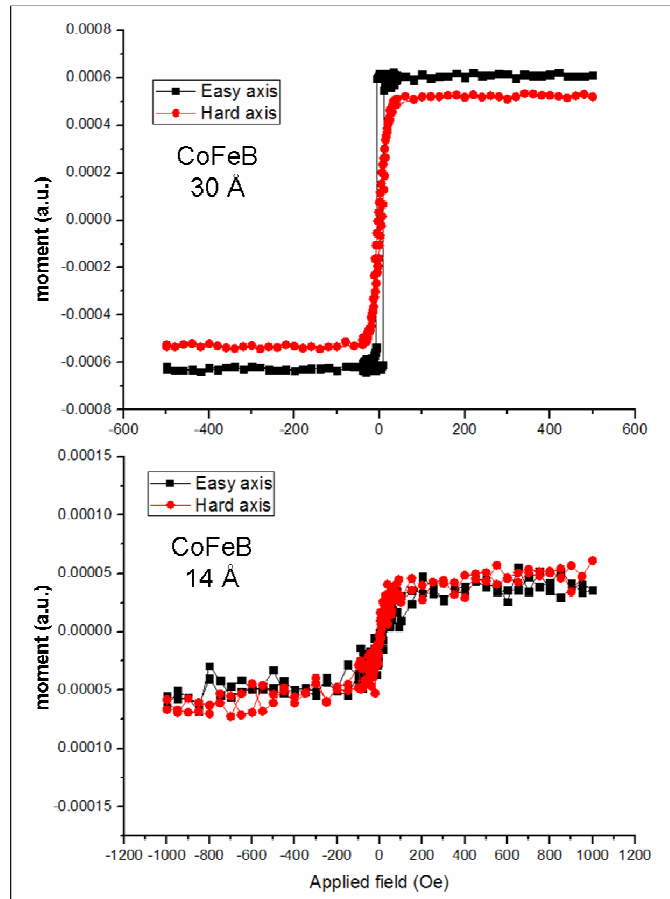


Figure 3.3: Easy axis (black) and hard axis (red) hysteresis loops obtained by Vibrating Sample Magnetometry (VSM) of equivalent samples with (a) CoFeB 30 Å and (b) CoFeB 14 Å.

Figure 3.3 shows the hysteresis loop of the easy axis (black) and hard axis (red) obtained after annealing in a field, by Vibrating Sample Magnetometry (VSM) for (a) CoFeB 30 Å and (b) CoFeB 14 Å. For CoFeB 30 Å (a), the easy axis loop is a square and narrow loop, and the hard axis is anhysteretic and narrow, as expected from a typical soft ferromagnetic thin film. The loops allow determination of the coercivity $H_c = 8.0 \pm 0.2$ Oe and the anisotropy field $H_k = 60 \pm 1$ Oe. The loops for CoFeB 14 Å (b) are quite noisy, but they do allow an estimate of the coercivity and anisotropy field, which are respectively $H_c = 16 \pm 2$ Oe and $H_k = 60 \pm 8$ Oe.

3.3 Investigation of the physical microstructure

The physical microstructure of the samples was investigated by conventional TEM with a FEI T20. This analysis was performed in order to understand how the structure of the specimen changed with decreasing thickness of the CoFeB layer and if any structural differences could be identified for the samples with CoFeB layer below the critical thickness.

It is worth mentioning that, since the specimens investigated are multilayers, the diffraction patterns and the bright field images in plan view (used to study the physical microstructure), will appear as a projection of all the layers. The diffraction patterns, shown in fig.3.4, are related to the sample with (a) CoFeB 30Å and (b) CoFeB 14Å. They show a spot pattern produced by the MgO layers, superimposed on a ring pattern which corresponds to the CoFeB layer. The patterns are similar and particularly the ring patterns are both typical of polycrystalline films with small grains randomly oriented.

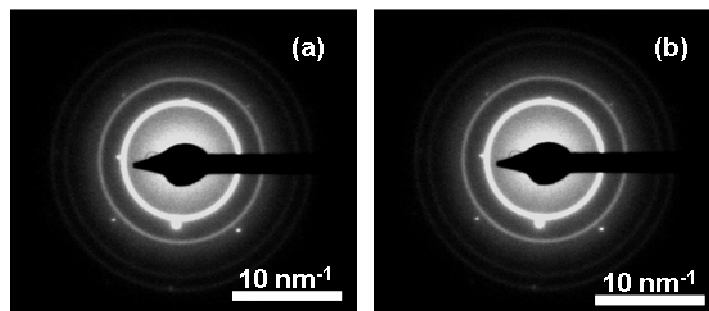


Figure 3.4: Polycrystalline diffraction pattern from (a) CoFeB 30 Å and (b) CoFeB 14 Å. The spot pattern is from the MgO layers in the stack.

Fig.3.5 shows a comparison of two bright field images in plan view of the sample with CoFeB layer 30Å (fig. 3.6(a)) and CoFeB layer 14Å (fig. 3.6(b)). The BF images show that

the CoFeB layer appears polycrystalline in character in both cases. They are consistent with diffraction patterns that show a random polycrystalline structure. The grain size distribution was obtained by measuring a significant number of grains (> 100) in the BF images. It was peaked at about 10 nm and it was also found to be the same in all samples investigated, although a larger number of smaller grains were found in the thinnest sample. The observation of a ring pattern in the diffractograms and a grain structure in the TEM bright field images are a clear indication of the polycrystalline nature of the CoFeB layer.

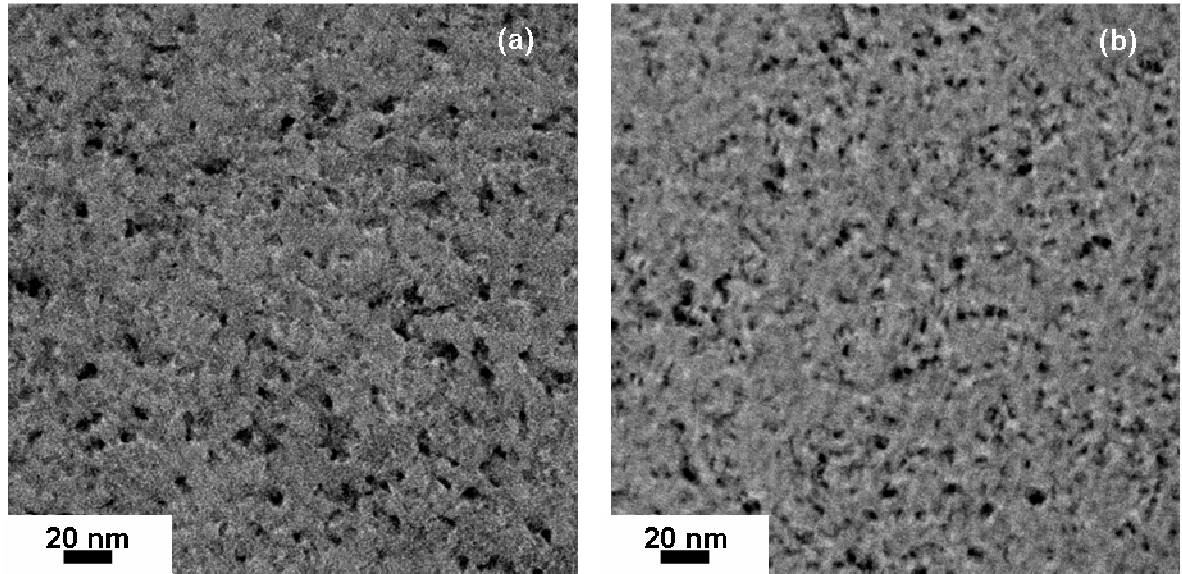


Figure 3.5: TEM plan view images for samples with CoFeB thicknesses 30 Å (a) and 14 Å (b).

3.4 Investigation of the magnetic structure

The magnetization reversal behaviour was investigated by Lorentz microscopy in Fresnel mode (described in section 2.5.1) with a Philips CM20, suitably modified for the investigation of the magnetic properties of a material. The experiments described in this section were carried out by applying fields in the range -90 Oe to 90 Oe and by weakly exciting the objective lens of the microscope and introducing a planar component of the field by tilting the specimen as explained in section 2.3.2.2. The hard axis (HA) was defined as the direction where we could see predominantly rotation of magnetisation and the behaviour during outward and return path of the hysteresis cycle was symmetric. The easy axis (EA) direction was obtained by rotating the sample by 90° from the HA. The defocus value used for the experiments carried out with CoFeB 30 Å is 3.69 cm, whereas the one used for the sample with CoFeB 14 Å is 10.4 cm. In order to have a complete picture of the behaviour of the sample with the thinnest CoFeB (14 Å) we decided to

record movies, this was a more compact way of recording the complete cycle of magnetic behaviour. The images that show the magnetic behaviour of this specimen (fig.3.10, 3.12 - 3.15) are frames extracted from these movies and their quality is poorer with respect to the images of the first sample in which a series of still images were recorded resulting in better signal to noise levels.

For the sample with CoFeB 30 Å we looked at orientation of the ripple and their wavelength with some domain walls also being observed during reversal. As discussed in chapter 2, the magnetisation ripple is the small wavelike fluctuations of the magnetisation direction that occurs in thin ferromagnetic films. It originates from random orientation of local anisotropy of each crystallite. The ripple effect is seen as a fine scale contrast present in the Fresnel image. For the sample with CoFeB 14 Å we looked at orientation of the ripple, their wavelength for the hard axis cycle and additionally the orientation of domain walls forming during the easy axis magnetising cycle. We observed a different length scale of ripple wavelength for the different samples, due to a different length scale of defocus used. In the following subsections a description of the general behaviour of the two samples will be provided.

3.4.1 CoFeB 30 Å

The behaviour found in the sample with 30 Å CoFeB layer was characteristic of a typical soft magnetic material with uniaxial anisotropy where rotation of magnetisation was observed for the external field applied along the hard axis (fig.3.6) and formation and propagation of large domains and formation and annihilation of 360° wall segments for the external field applied along the easy axis (fig.3.7). Such wall segments, whose formation depends on growth conditions, are fairly uncommon and unwanted, because they represent a source of noise in the device. They cannot be seen in a hysteresis loop and this represents one of the advantages of the use of Lorentz microscopy over other magnetic characterisation techniques.

The inset in each frame of fig.3.6 and 3.7 shows the fast Fourier transform image (FFT) from which the degree of dispersion of the ripple can be determined, but also the average orientation of the magnetisation can be evaluated.

The hard axis behaviour can be visualised in fig.3.6. The hard axis orientation is determined when a symmetric behaviour during the outward and return path of the

magnetising cycle is observed. Before the image sequence is acquired, the magnetic film is saturated by applying a field of 90 Oe in order to avoid recording images from a minor hysteresis loop. The magnetic field is then reduced down to negative values to acquire the sequence of the outward path of the hysteresis loop. The process observed is the rotation of the magnetisation clockwise (fig.3.6), which can be evaluated from the rotation of the magnetisation ripple (described in section 2.5.1). The rotation proceeds until the direction of magnetisation lies parallel to the direction of the applied field. At this point the field is taken down to -90 Oe and increased up to positive values to record the sequence of the return path of the hysteresis loop. Again the process observed is rotation of the magnetisation, but the rotation, this time, occurs anticlockwise.

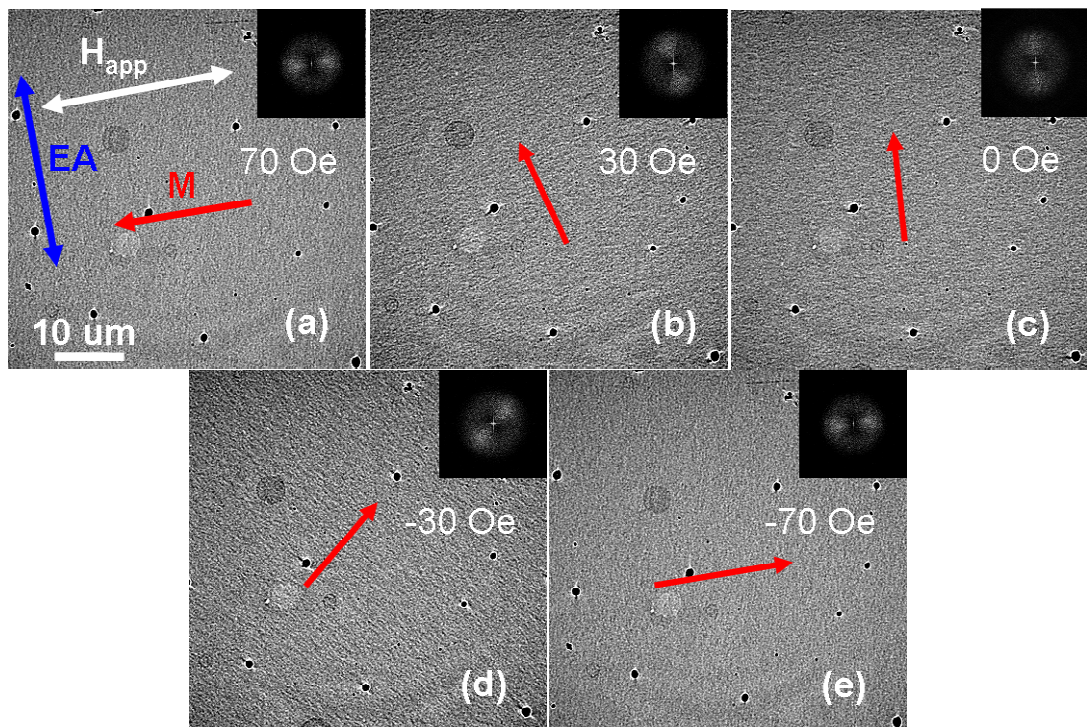


Figure 3.6: Fresnel image sequence of the outward path of the hard axis magnetising cycle for the sample with CoFeB 30Å. The red arrow represents the direction of magnetisation, the blue and white arrow the orientation respectively of the easy axis and applied field. Inset shows fast Fourier transform of the image from which the direction of magnetisation can be deduced.

The easy axis magnetising sequence is included in fig.3.7 where the outward branch of the cycle is shown. Again, the magnetic film is saturated by applying a field of 90 Oe in order to avoid recording images from a minor hysteresis loop. The magnetic field is then reduced down to negative values to acquire the sequence of the outward path of the hysteresis loop. The magnetisation is aligned along the direction of the applied field for values of the field up to 7 Oe (fig.3.7a). A decrease of the field down to 0 Oe produces a small rotation of the

magnetisation (fig.3.7b). After decreasing the field further, it was evident that a reversal event occurred presumably by creation and rapid propagation of a domain wall or walls, thus the magnetisation of the film is deduced as reversed at -4 Oe (fig.3.7c). The reversal was too rapid to record the domain wall. However a residual short section of 360° wall segment is present as indicated by the red circle in the figure, a field of -7 Oe is enough to annihilate this wall (fig. 3.7d).

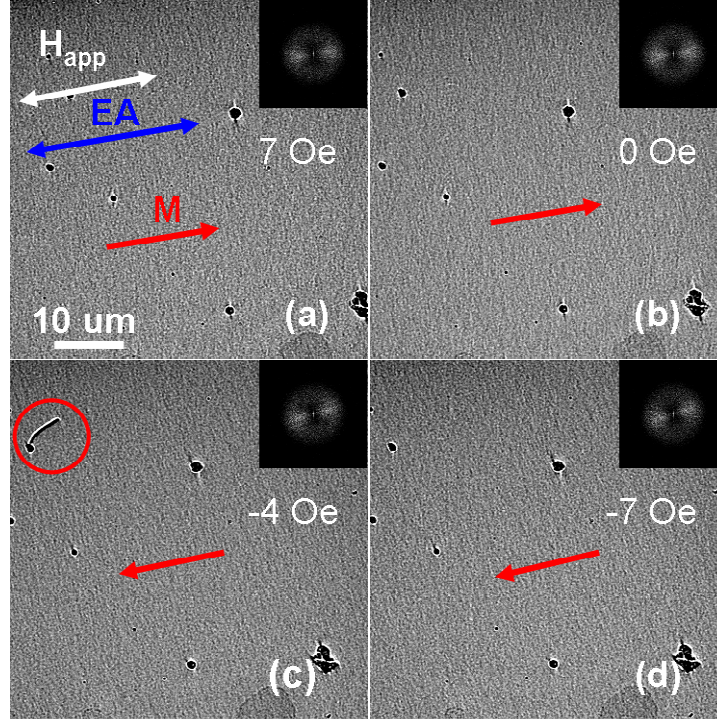


Figure 3.7: Fresnel image sequence of the outward path of the easy axis magnetising cycle for the sample with CoFeB 30Å. The red circle in (c) identifies the 360° wall segment.

At this point the field was taken down to -90 Oe and subsequently increased up to positive values to record the sequence of the return path of the hysteresis loop (as done for the hard axis sequence). Symmetric behaviour was seen in the return path of the magnetising cycle, where nucleation and fast propagation of a large domain wall through the film produces the reversal of the magnetisation of the film at +4 Oe, but also the annihilation of a 360° wall segment. This is consistent with the hysteresis loop in fig.3.3(a) and typical of a thin film made of a soft magnetic material. From the Fresnel images we can estimate the anisotropy field H_k which we found to be 70 Oe and the coercive field H_c which we found to be 4 Oe. It is not consistent with the value measured from VSM (8 Oe), because the hysteresis loops obtained by VSM refers to analogous samples deposited on SiO₂ substrates.

As we saw previously, much of the contrast in the Fresnel images is due to the magnetic ripple. The magnetic ripple can be characterised in terms of the mean wavelength and the mean angle of deviation of the local magnetisation. In principle, it is possible to measure the mean wavelength of the ripple. This can be done by analysing the Fresnel images in Fourier space.

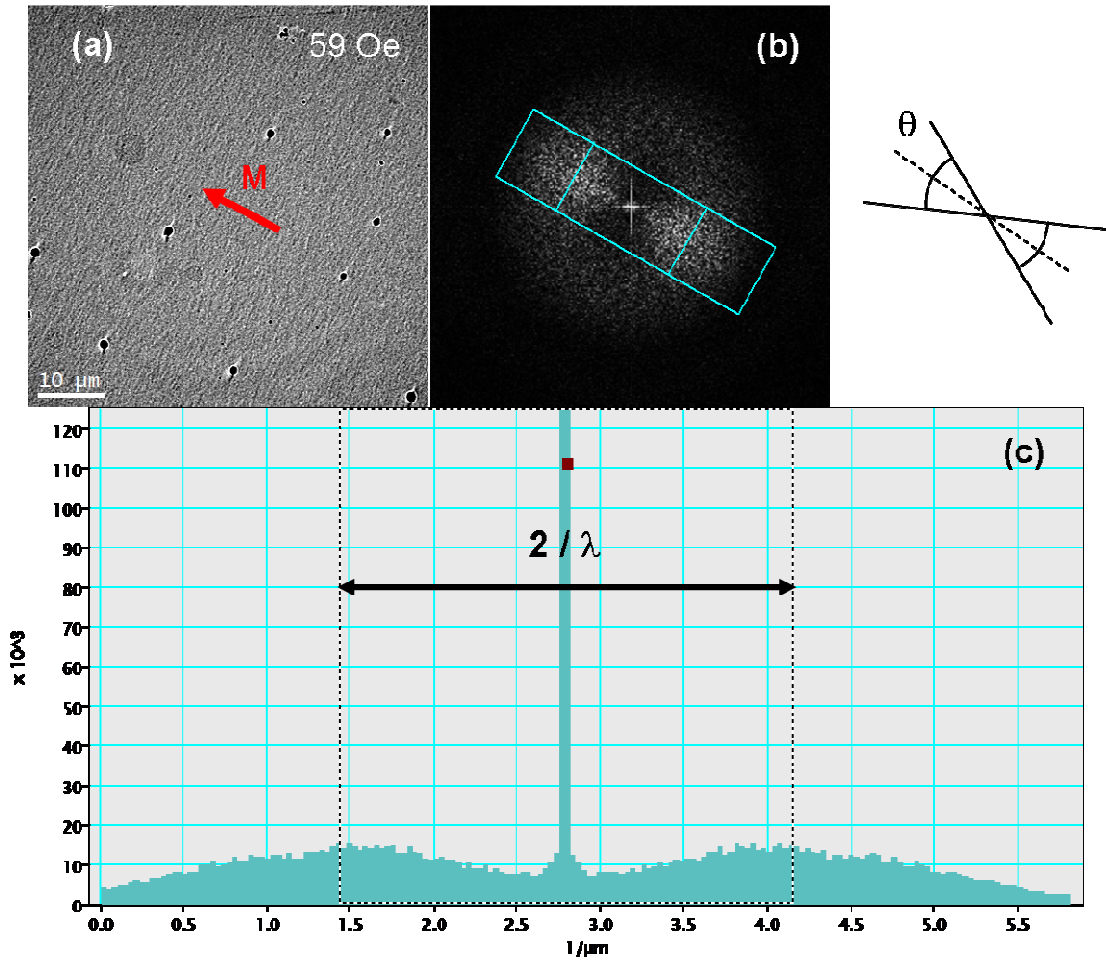


Figure 3.8: Procedure used to obtain ripple wavelength from Fresnel images. (a) Fresnel image taken from the HA magnetising sequence at a field of 59 Oe; (b) FFT of (a) on the left and a schematic of the angular dispersion of the ripple on the right; (c) intensity profile measured along the magnetisation direction (bisector depicted as a dashed line in (b)) allows determination of the ripple wavelength as reciprocal of the distance between the peaks.

In this part of the section we will see how we can determine the anisotropy field from the ripple wavelength with the aid of the ripple theory [14 - 17]. In order to do that, a Fresnel image with homogeneous ripple is firstly recorded (fig. 3.8(a)). A Fast Fourier transform (FFT) of the Fresnel image is, then, calculated (Fig. 3.8(b) left), providing a qualitative aspect of the angular dispersion of the ripple (a schematic of this is provided in fig.3.8(b) right). The mean wavelength value can be obtained from a line profile of the FFT image

modulus (fig. 3.9(c)) along the magnetisation direction (the dashed line in fig.3.8(b) right) as the distance between two peaks in the profile. This distance represents twice the reciprocal of the ripple wavelength. According to the ripple theory [16, 17], the mean wavelength is expected to vary as a function of the applied field as:

$$\lambda(H) = 2\pi \left(\frac{A}{K_u} \right)^{1/2} \left(\frac{H}{H_k} + 1 \right)^{-1/2} \quad (3.1)$$

where K_u is the uniaxial anisotropy constant and H_k is the anisotropy field. Eq.3.1 allows experimental determination of the anisotropy field H_k from the gradient of the following equation:

$$\lambda^{-2}(H) = \left[2\pi \left(\frac{A}{K_u} \right)^{1/2} \right]^{-2} \left(\frac{H}{H_k} + 1 \right) \quad (3.2)$$

To this purpose a plot of λ^{-2} vs H was obtained (as detailed from fig.3.9) and a linear fit was carried out. The gradient and intercept of the best fit line allowed the calculation of the anisotropy field $H_k = 76 \pm 5$ Oe which is consistent with the value estimated from the hard axis magnetising sequence.

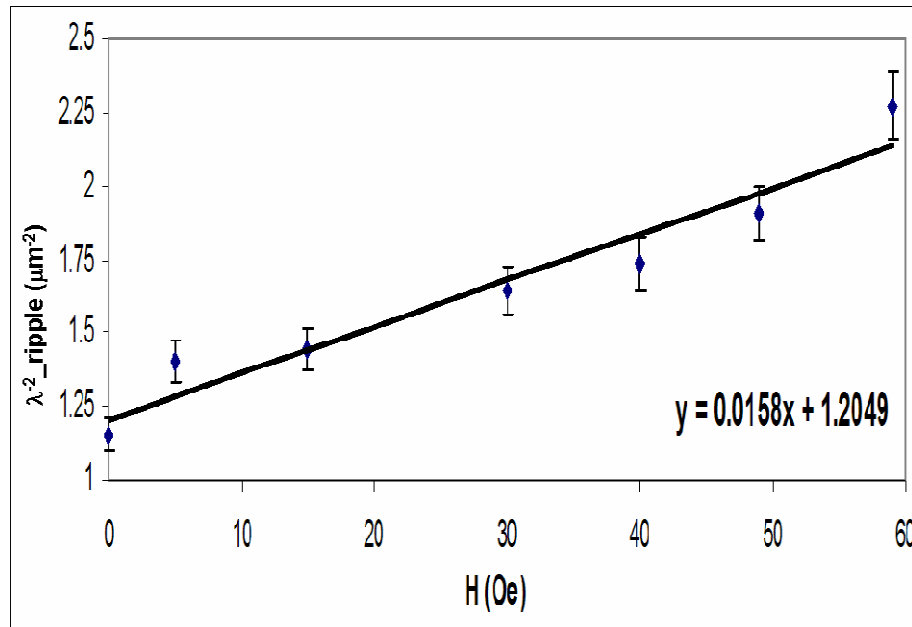


Figure 3.9: Inverse wavelength square as function of the applied field during the outward path of the reversal process on the hard axis for CoFeB 30 Å thick.

3.4.2 CoFeB 14 Å

The behaviour found for the sample with CoFeB 14Å thick was much more complex than for the thicker sample, although no evidence of superparamagnetic behaviour has been observed. Indeed, in a superparamagnetic specimen we would not expect to see any large scale domain structure, perhaps instead just some small local variations. Nevertheless magnetisation rotation and dispersion in the hard axis magnetising sequence was observed (fig.3.10). Also visible was the formation of long stable domain walls and their propagation in the easy axis magnetising sequence (fig.3.12 and 3.13). Furthermore we observed an unusual asymmetric behaviour both in hard axis and easy axis magnetising sequences. This behaviour was then the focus of further investigation. As indicated in the introduction to section 3.4, the images that we are going to show in this section are frames extracted from the movies we acquired to have a more complete picture of the behaviour of this sample. Thus their quality is poorer with respect to the images of the sample CoFeB 30 Å. However, since we are mostly interested to the measurement of domain wall angles, this does not strictly require particularly high quality images.

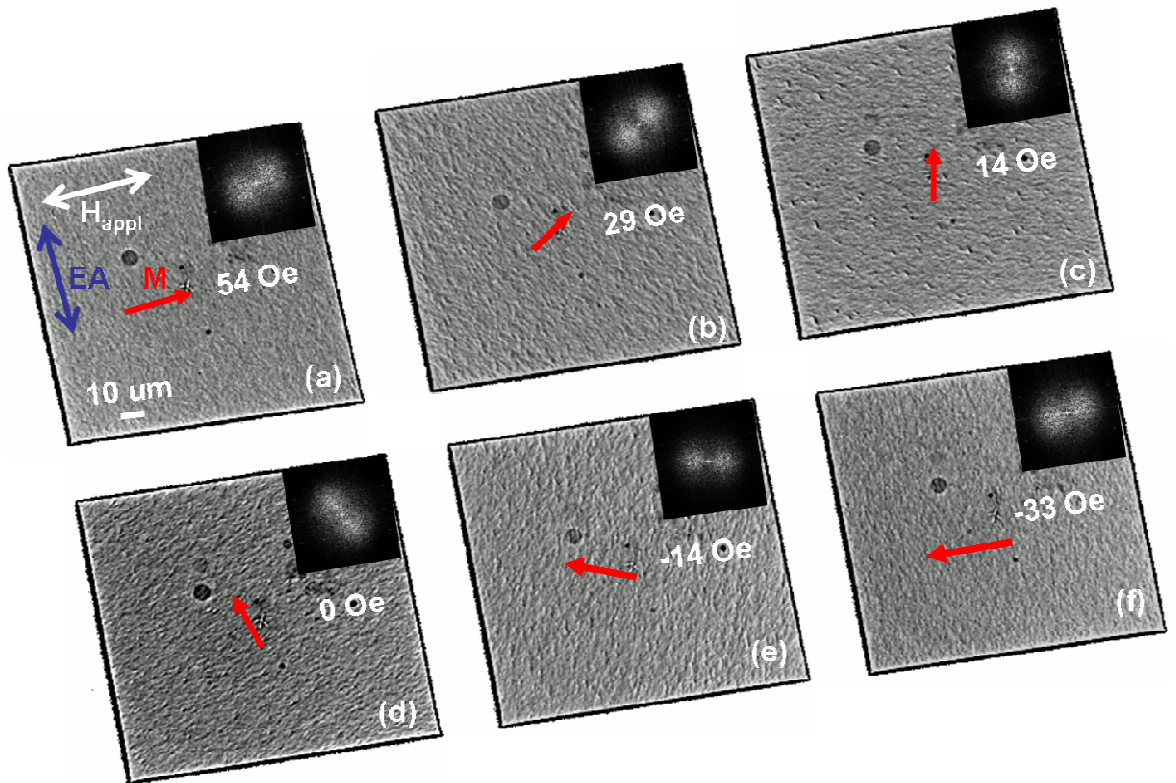


Figure 3.10: Fresnel image sequence of the outward path of the hard axis magnetising cycle for the sample with CoFeB 14Å. An asymmetry in the orientation of magnetisation is seen when a field of (c) +14 Oe and (e) -14 Oe, and (a) 54 Oe and (f) -33 Oe is applied.

Fig.3.10 depicts the outward path of the hard axis magnetising sequence. Magnetisation rotation anticlockwise is seen when the field decreases (fig. 3.10(a-c)) with an increase in magnetisation dispersion and rotation of ripple as shown by the cone angle in the FFT. At 0 Oe (fig.3.10(d)) an abrupt change in magnetisation direction of about 30° is observed and subsequently further magnetisation rotation anticlockwise was again observed with an increase in magnetisation dispersion and rotation of ripple (fig.3.10(d-f)). The rotation proceeds until the direction of magnetisation lies parallel to the direction of the applied field. It is worth noticing that at 0 Oe the magnetisation does not lie along the easy axis direction, but there is a deviation from it. Moreover the orientation of magnetisation at +14 Oe (fig.3.10(c)) and -14 Oe (fig.3.10(e)), but also at 54 Oe (fig.3.10(a)) and -33 Oe (fig.3.10(f)) is observed to be not symmetric. The observed asymmetry results, also, in the magnetisation being aligned with the hard axis at 70 Oe and -33 Oe. This could suggest the presence of a unidirectional anisotropy in the film in addition to the induced uniaxial anisotropy. The behaviour observed in the return path of the hysteresis loop is analogous to the outward path, except for the opposite sense of rotation of magnetisation.

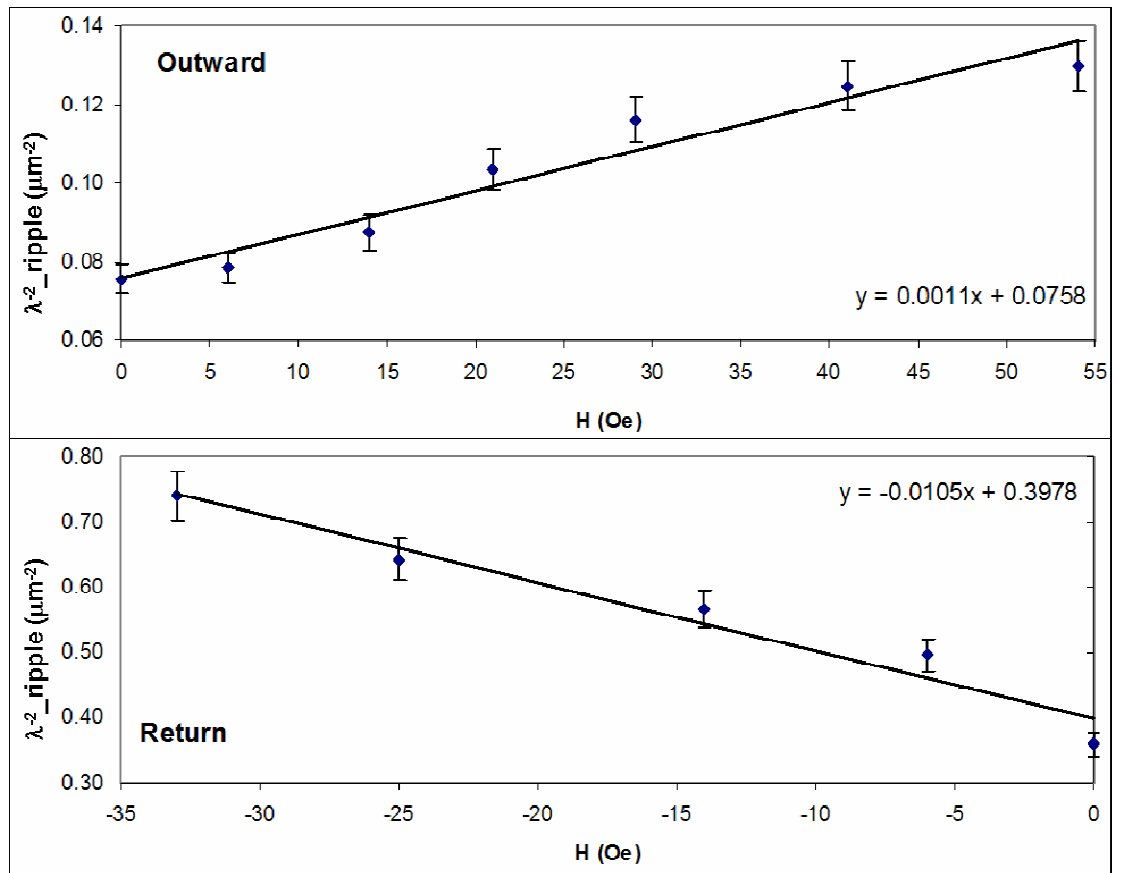


Figure 3.11: Inverse wavelength square as function of the applied field during the outward path (top) and return path (bottom) of the reversal process on the hard axis for CoFeB 14 Å thick.

As we saw in the previous section, eq.3.2 allows experimental determination of the anisotropy field H_k from the plot of the inverse wavelength square as a function of the applied field. The plot is shown in fig. 3.11 where a linear fit was carried out. On the top is displayed the plot for the outward direction and on the bottom the one for the return direction. The gradient and intercept of the best fit line allowed the calculation of the anisotropy field and for the outward direction we found $H_k = 69 \pm 6$ Oe which is consistent with the positive field where magnetisation is aligned with the hard axis, whereas for the return direction we found $H_k = 38 \pm 6$ Oe which is consistent with the negative field where magnetisation is aligned with the hard axis.

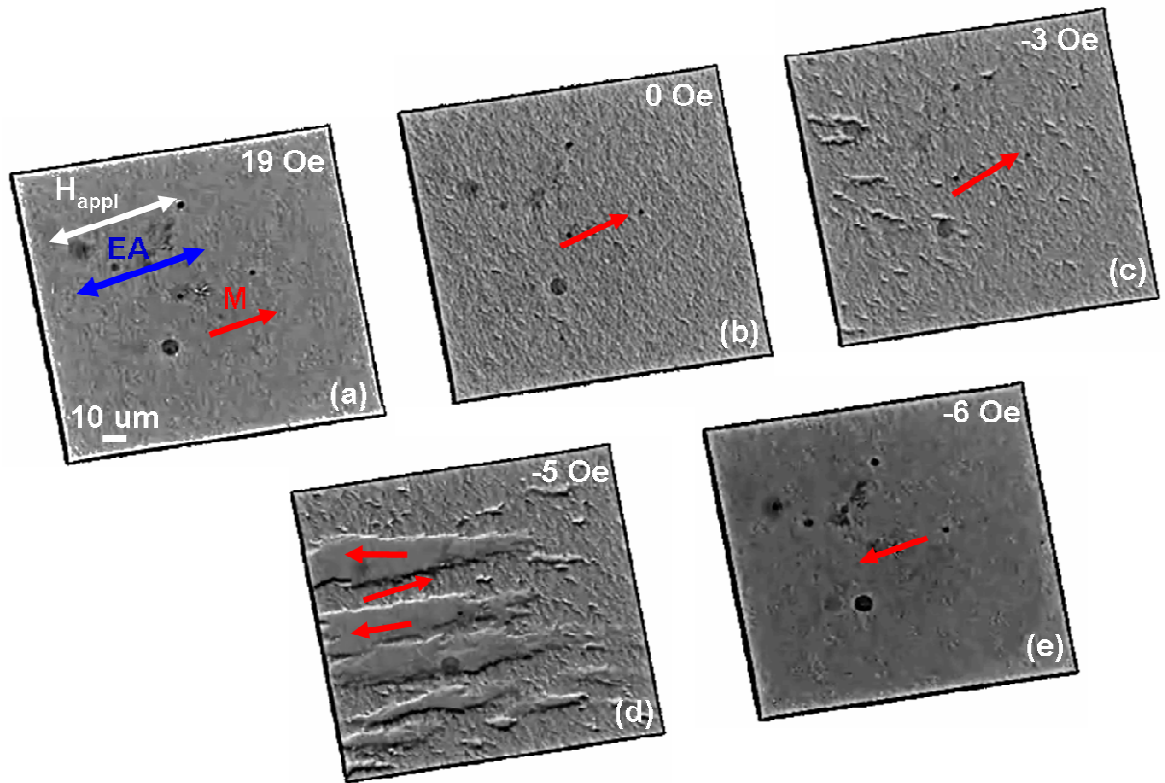


Figure 3.12: Fresnel image sequence of the outward path of the easy axis magnetising cycle for the sample with CoFeB 14Å.

The easy axis magnetising cycle is shown in fig.3.12 and 3.13. As in the previous cases, the film is saturated with a field of 90 Oe before the acquisition of the outward path sequence. As the field is reduced down to negative values, an increase of magnetisation dispersion is observed at 0 Oe (fig.3.12(b)) and, at the same time, a small rotation of magnetisation is seen (fig. 3.12(a-c)). At -3 Oe domains walls are seen to form (fig.3.12(c-d)) and propagate, leading to reversal of the magnetisation of the film which reaches the saturated state at -6 Oe (fig.3.12(e)).

Again, -90 Oe field is applied before recording the return path of the cycle. Analogous to the outward path, as the field is increased, an increase of magnetisation dispersion is observed at 12 Oe (fig.3.13(b)) and a small rotation of magnetisation is seen (fig. 3.13(a-c)). At 15 Oe domain walls are seen to start forming (fig.3.13(c-d)) and they propagate, causing reversal of the magnetisation of the film, and saturation is reached at 19 Oe (fig.3.13(e)). Inspection of the domain walls formed during outward (fig. 3.14(a)) and return path (3.14(b)) of the hysteresis cycle reveals that their orientation is different during the outward and return path, which is an unexpected result for a film with only uniaxial anisotropy. Further magnetising sequences were carried out where the orientation of the applied field relative to the easy axis direction was changed to try and understand the basis of this behaviour.

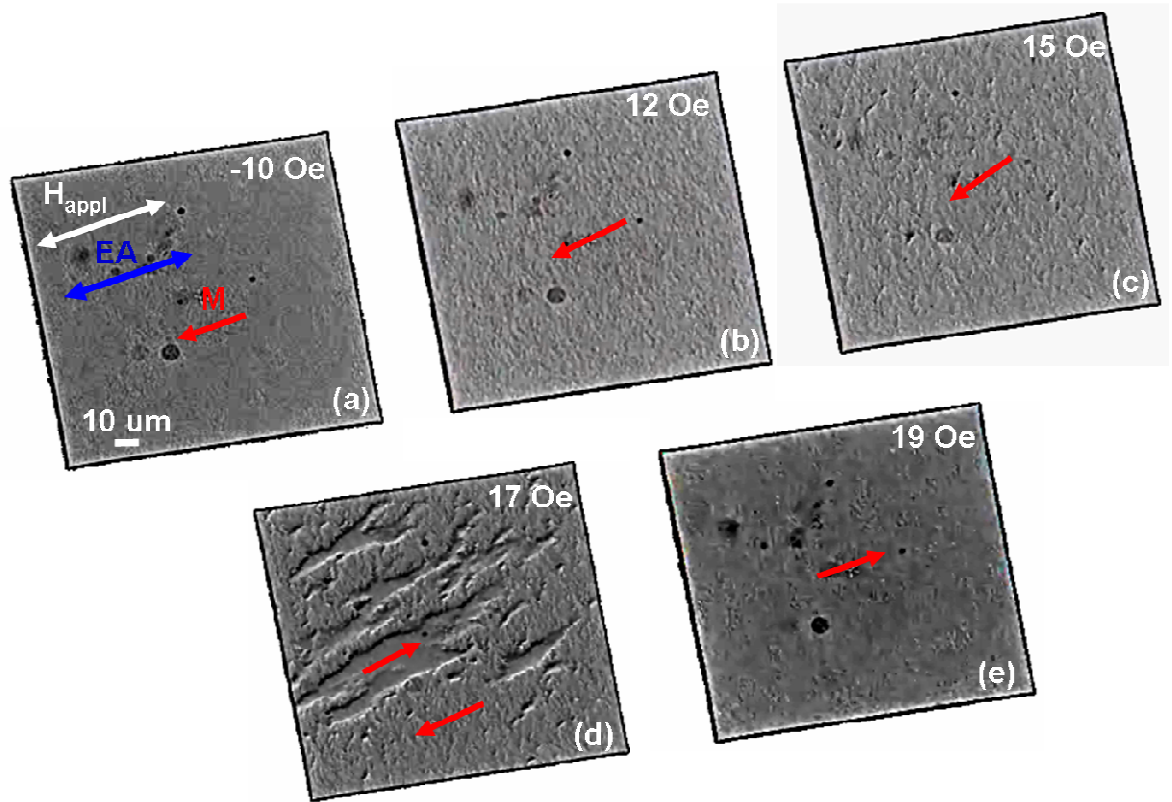


Figure 3.13: Fresnel image sequence of the outward path of the easy axis magnetising cycle for the sample with CoFeB 14Å.

In order to quantify this phenomenon, the average orientation of the domain walls forming during the outward and return path of the hysteresis cycles, with respect to the EA, was measured systematically for applied fields oriented in the range $\pm 30^\circ$ from the easy axis. Fig.3.15 shows a typical image of domain walls formed during the outward path of a hysteresis cycle and demonstrates how the domain wall orientation was measured. The

measurements were carried out with the imaging software Digital Micrograph TM, the software used to acquire, process, analyse, simulate and present images and spectrum data. We first selected the longest domain walls, and we measured the angles α they form with the horizontal direction (0°) by mean of a line like the pink one in fig.3.15. We then averaged the values of α we measured. If β is the orientation of the easy axis with respect to the horizontal direction (0°) we then calculated $\alpha - \beta$, we get the average orientation of the domain walls with respect to the easy axis. This procedure was repeated for orientations of applied field in the range $\pm 30^\circ$ to the easy axis, where asymmetric domain wall formation was seen. The measurements obtained from the domain walls are summarised in fig.3.16 where, interestingly, the dataset appears to have the shape of a hysteresis loop. The data points appear to cross the horizontal axis for a value of the field direction of about 10° .

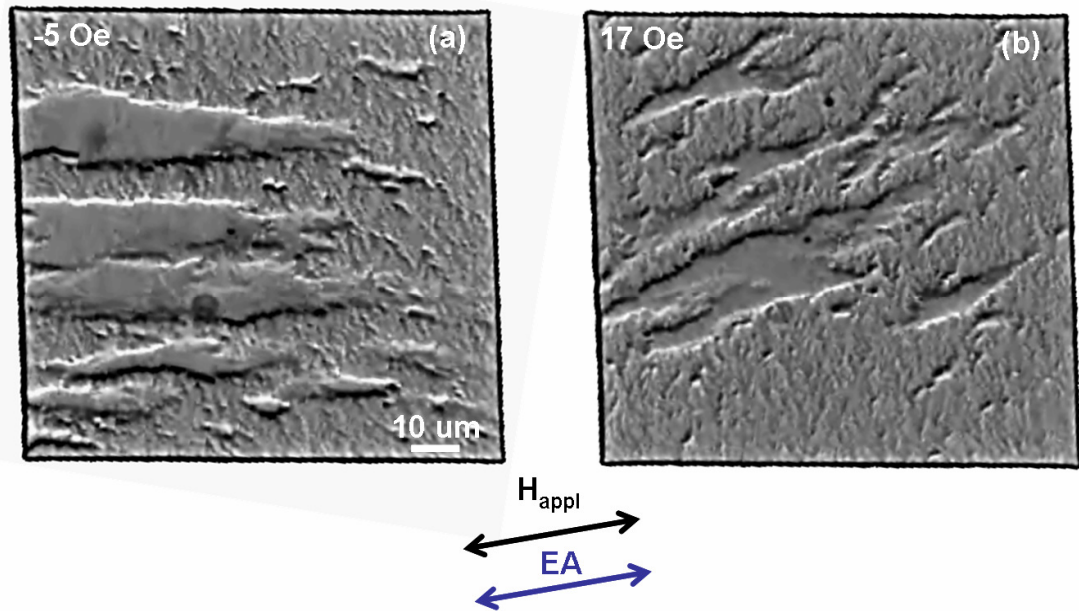


Figure 3.14: Comparison between frames displaying large domains formed during the outward path (a) and the return path (b) of the hysteresis cycle, that highlight the asymmetry in the domain wall orientation in (a) and (b).

The asymmetric behaviour we observed for the domain wall orientation appears to suggest the presence of a unidirectional anisotropy in the sample. We now attempt to investigate and quantify such a possibility. To assist in the interpretation of these experimental results a modified Stoner–Wohlfarth model [18] was constructed and calculations were carried out using a MATLAB code. The results obtained from this approach are described in the next section.

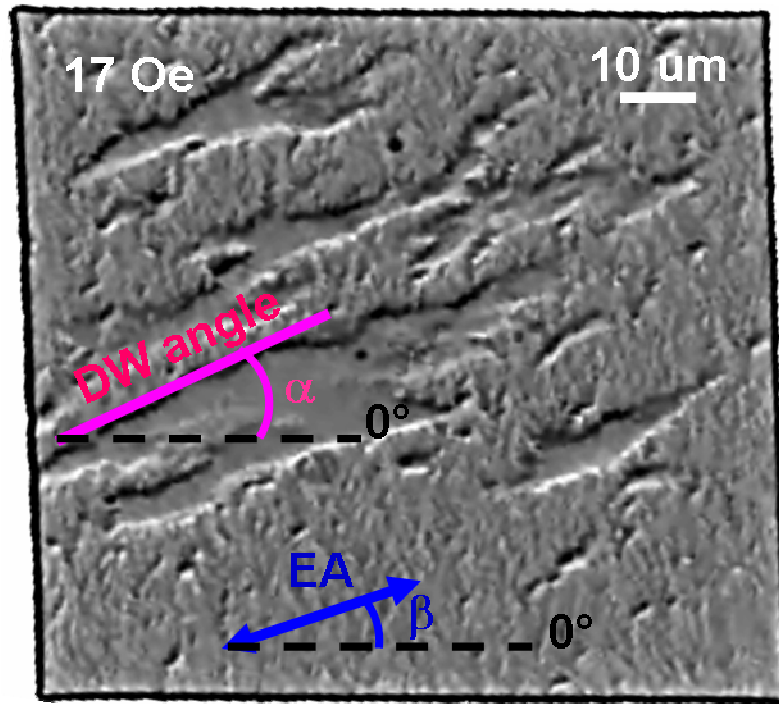


Figure 3.15: Frame displaying large domains formed during the outward path of the hysteresis cycle used as an example to show how the domain wall orientation was measured. The pink line represents the domain wall orientation α with respect to the horizontal (0°), whereas β is the orientation of the EA with respect to the horizontal (0°).

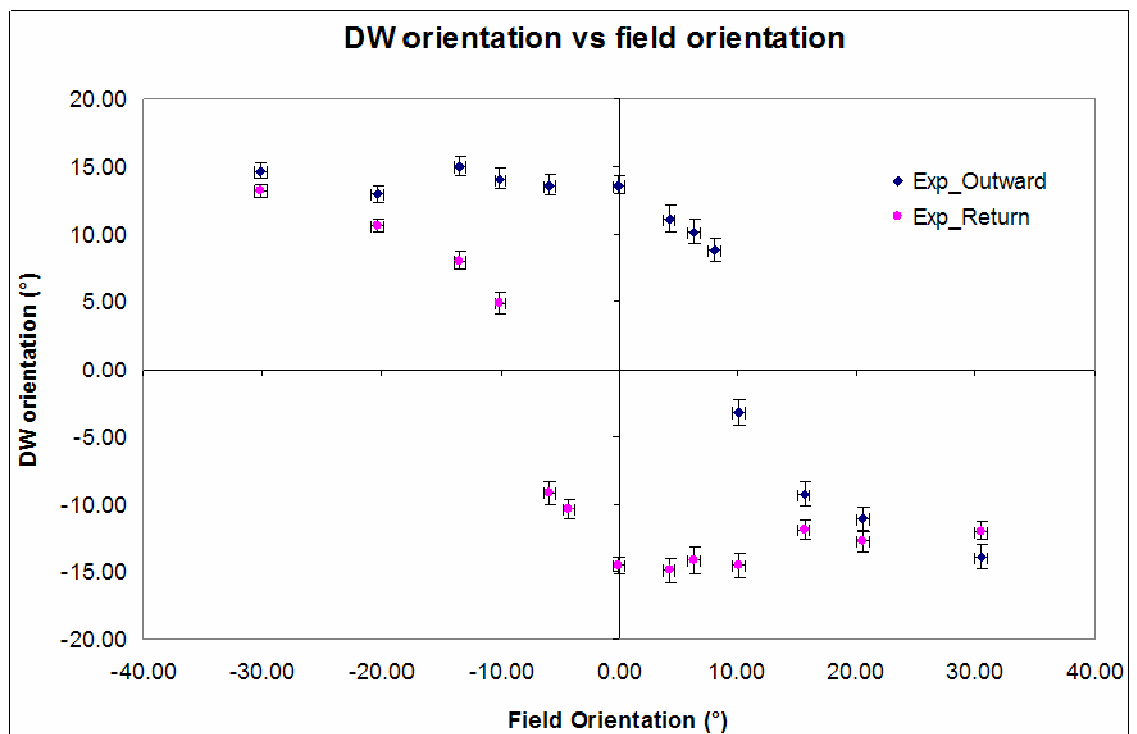


Figure 3.16: Orientation of domain walls forming during the outward (blue dots) and return (pink dots) path of the hysteresis loop for field orientation in the range -30° off the EA, 30° off the EA, measured with respect to the orientation of the EA for CoFeB 14 Å.

3.5 Interpretation of the results by means of Stoner-Wohlfarth model based calculations

As described in the previous section, a particular characteristic of the 14 Å thick CoFeB layer is the variation of domain wall angle during the outward and return path of the hysteresis loop (fig.3.14). This was further investigated by varying the orientation of the applied field around the easy axis direction (fig.3.16). To assist in the interpretation of this asymmetric behaviour we used a modified Stoner-Wohlfarth model [18]. We assumed that in the sample there exists a unidirectional field H_u in addition to the uniaxial anisotropy field H_k . With the additional unidirectional term, the reduced energy function in eq. 1.22 (Ch.1) becomes, in the presence of an applied magnetic field H :

$$\Gamma = H_k \sin^2 \phi - 2 [H \cos(\theta - \phi) + H_u \cos(\varepsilon - \phi)] \quad (3.3)$$

where ϕ is the angle that the magnetisation forms with the easy axis, θ is the angle that the applied field forms with the easy axis and ε is the direction of the unidirectional anisotropy with respect to the easy axis. A schematic of the parameters involved in the model is depicted in fig.3.17. Here we draw an arbitrary orientation of the unidirectional anisotropy U , we assume that a positive external field H (lower than the field required to saturate the sample) is applied, resulting in a positive orientation of magnetisation ϕ with respect to the anisotropy axis K . The uniaxial anisotropy direction K is used as the reference from which the angles are measured, consistent with practice in the previous section.

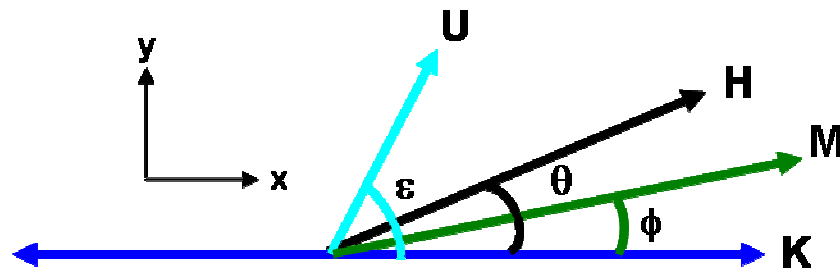


Figure 3.17: Schematic of the parameters involved in the model with K being the easy axis, H the direction of the applied field, θ is the angle between H and K , M is the direction of the magnetisation, ϕ is the angle between M and K , U is the unidirectional anisotropy axis and ε is the angle between U and K .

The model works in the following way: H_k , is the value determined experimentally from the hysteresis loop measurements which is also consistent with the hard axis magnetising sequence (fig 3.3). From these measurements H_k was then taken to be 60 Oe for the model. By applying a field H in a certain direction θ , we can solve equation 3.3 and we get the orientations of magnetisation ϕ that allow the calculation of domain walls if values of ε and H_u are chosen.

We saw in section 1.7 that eq.1.22 for the standard Stoner - Wohlfarth model cannot be solved analytically except for $\theta = 0, \pi/4, \pi/2$. This is still true for eq.3.3, which refers to the modified Stoner - Wohlfarth model. In the general case, to find solutions to the equation we can plot the reduced energy functional Γ as a function of ϕ for fixed values of θ, ε, H_u , and for different magnitudes of the applied field. Then we need to look for the minima of energy. They will provide the orientation of the magnetisation for a given set of parameters, analogously to the standard Stoner-Wohlfarth model as seen in section 1.7.

The issue, at this point, is trying to understand how the modified Stoner-Wohlfarth model can be useful to derive the orientation of the domain walls. In order to explain how to extract domain wall orientation we can consider an example. Let's consider the following set of parameters: $H_k = 60 \text{ Oe}$, $H_u = 10 \text{ Oe}$, $\varepsilon = 110^\circ$, $\theta = 20^\circ$. Let's build the plot of the reduced energy functional Γ as a function of the orientation of the magnetisation ϕ , for different values of the applied field H . It was shown already in section 1.7 that for those values of the applied field which lie inside the Stoner-Wohlfarth astroid there exist two minima of energy. This is still true for the modified model where we can find two minima of energy for a certain range of fields, which depends on the choice of the parameters. Fig.3.18(a) shows the plot of Γ vs ϕ for the above parameters and for $H = 35 \text{ Oe}$. The curve shows two minima ϕ_1 and ϕ_2 . Thus, two stable orientations of the magnetisation \mathbf{M} exist and we can infer the presence of two domains of magnetisation \mathbf{M}_1 and \mathbf{M}_2 , with an uncharged domain wall in between as shown in fig.3.18(c). The orientation of the domain wall can be obtained as follows. We can extract the position of the minima ϕ_1 and ϕ_2 and we can imagine the two magnetisation vectors M_1 and M_2 arranged as in fig.3.18(b). Both M_1 and M_2 are calculated with respect to the orientation of the easy axis, thus from basic geometry, and since the domain wall is located in a direction such that the perpendicular component of both magnetisation vector is conserved (in order to avoid formation of charges), we can calculate the DW orientation as drawn in fig.3.18(d).

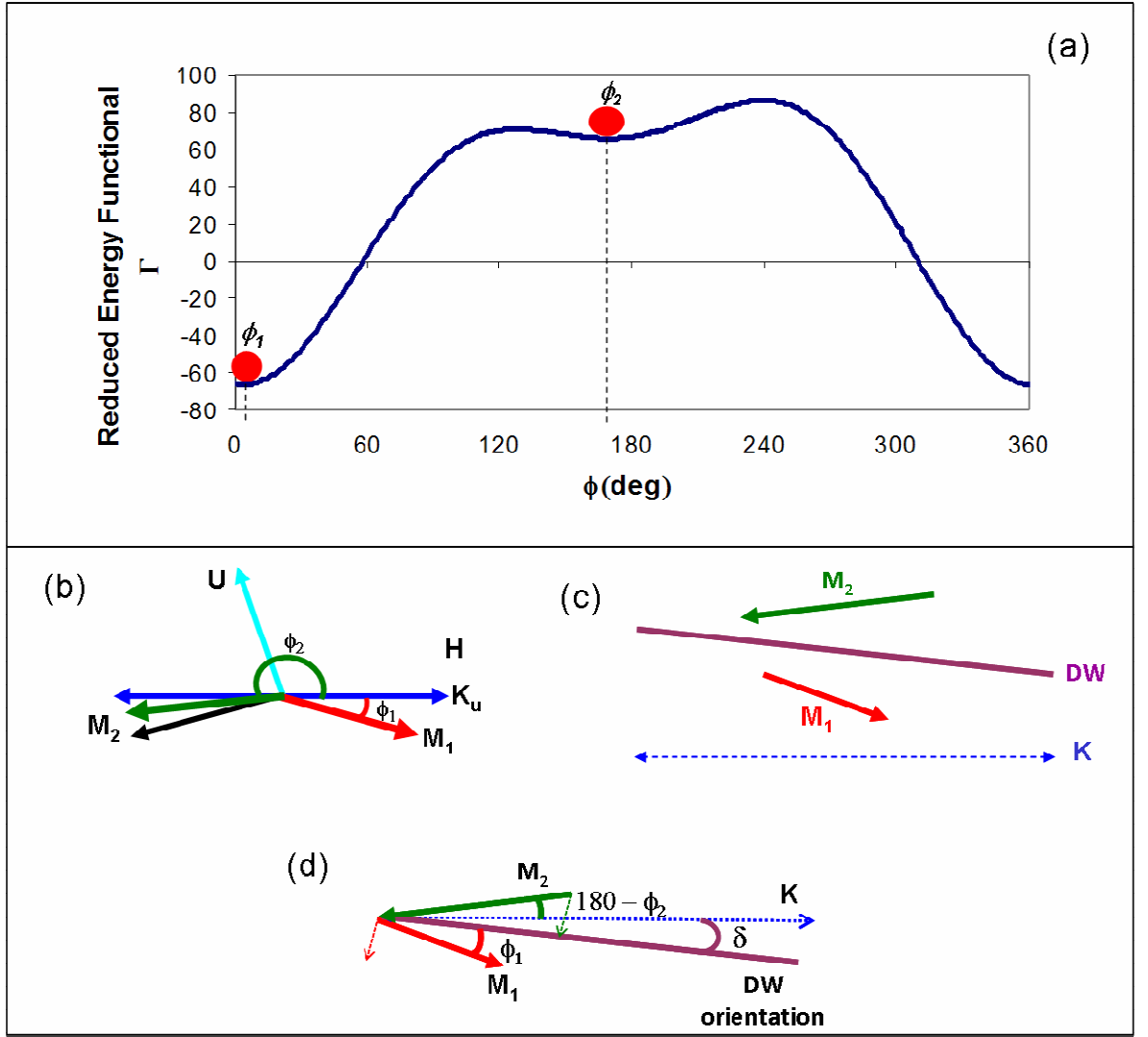


Figure 3.18: (a) Plot of the reduced energy functional Γ vs ϕ obtained with the set of parameters: $H_k = 60$ Oe, $H_u = 10$ Oe, $\varepsilon = 110^\circ$, $\theta = 20^\circ$ and $H = 35$ Oe. The plot shows the presence of two minima of energy (red dots), ϕ_1 and ϕ_2 . (b) Schematic of the two possible orientation of magnetisation M_1 (ϕ_1) and M_2 (ϕ_2) in relation to the orientation of the easy axis K_u , direction of the applied field H and unidirectional anisotropy U . (c) Schematic of two domains with magnetisation M_1 and M_2 and a domain wall in between. (d) How to evaluate the DW orientation δ once ϕ_1 and ϕ_2 are known.

The evaluation of the minima ϕ_1 and ϕ_2 is not as easy as one may think, since eq.3.3 is an equation with six variables. In order to deal with the complexity of a six dimensional parameter space, a MATLAB code (appendix 1) has been written and used. Initially values are assigned for H_k , H_u and ε , we then vary θ between -30° and $+30^\circ$ with a variable step size and H between -150 Oe and $+150$ Oe with a step size of 1 Oe. The output is a contour plot displaying the energy landscape is shown in fig. 3.19. From this the possible orientations of magnetisation and hence domain walls can be calculated.

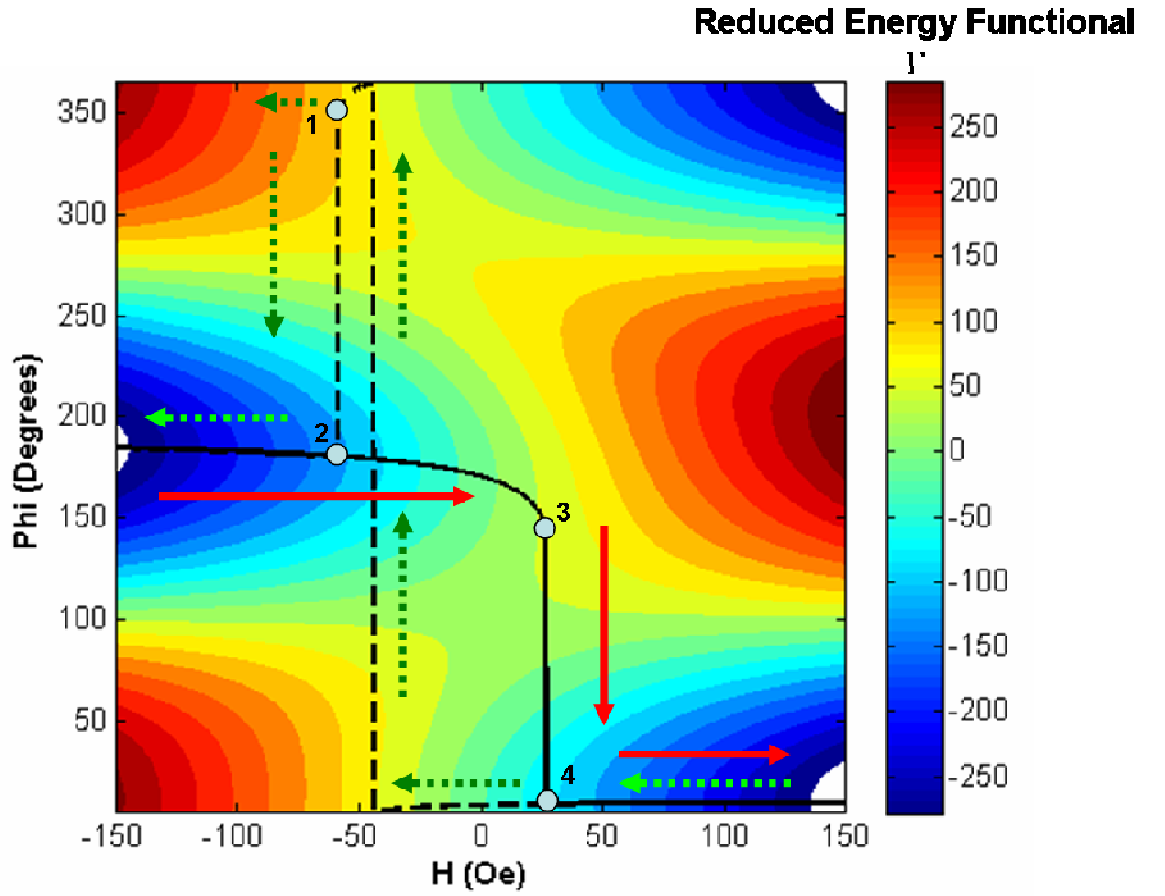


Figure 3.19: Contour plot displaying the energy landscape as a function of the applied field (x axis) and orientation of magnetisation ϕ (y axis) for $\varepsilon=70^\circ$; $\theta=10^\circ$; $H_k=60$ Oe, $H_u=10$ Oe. The solid line represents the minimum of energy path for the outward direction, the dashed line represents the minimum of energy path for the return direction. The green arrows give to the reader the direction of the outward path and the red arrows give the direction of the return path. The white dots mark the positions in the minimum of energy path before (1 and 3) and after (2 and 4) an abrupt change in the orientation of magnetisation occurs.

The energy landscape displays the variation of the reduced energy functional I' as a function of the applied field H and the orientation of the magnetisation ϕ . The solid and dashed lines represent respectively the minimum of energy path for the outward and return path of the magnetising sequence. For the sake of clarity a set of arrows indicate the outward (green arrows) and return direction (red arrows) of the minimum of energy path. The white dots mark the positions in the minimum of energy path before (1 and 3) and after (2 and 4) an abrupt change in the orientation of magnetisation occurs. The values of ϕ of these points represent ϕ_1 (1 and 3) and ϕ_2 (2 and 4) used for the calculation of the domain wall orientations. The approach with the MATLAB code was used to get behaviour similar to the experimental situation and to compare calculated and experimental

DW orientations. The aim is to reproduce correctly the magnetisation processes observed during the experiments, i.e. rotation and switching of magnetisation.

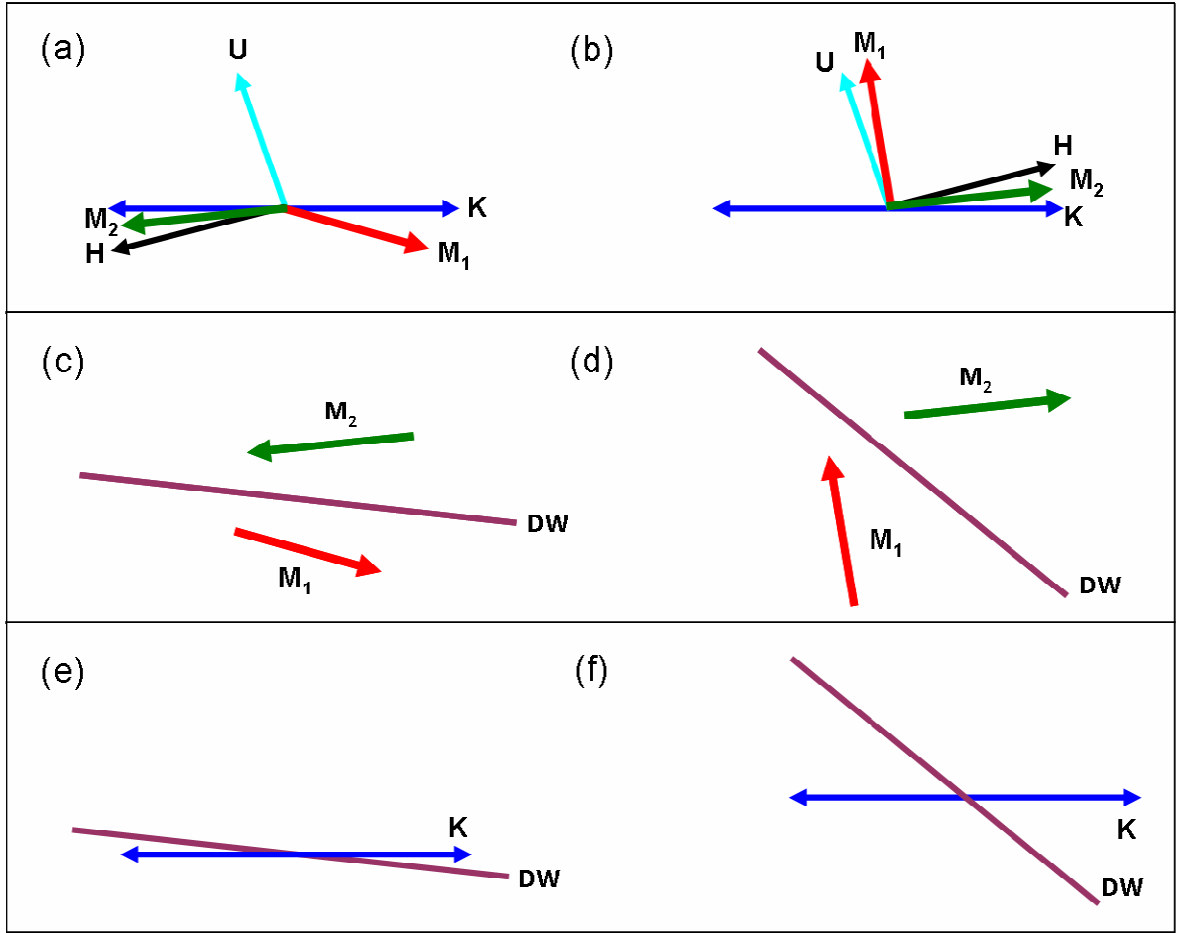


Figure 3.20: Diagram of the magnetisation configuration at the critical field where an abrupt change in the orientation of magnetisation occurs for the outward direction (a) and return direction (b). Schematic of two domains with magnetisation M_1 and M_2 and a domain wall in between for the outward (c) and return direction (d). DW orientation with respect to the uniaxial anisotropy for the outward (e) and return direction (f).

The orientation of the DWs is obtained from the analysis of the minimum of energy path in the energy landscape. The code provides as output also the values of ϕ_1 and ϕ_2 for the outward and return direction of the minimum of energy path. They represent the orientation of \mathbf{M}_1 and \mathbf{M}_2 , shown schematically in fig.3.20. In fig.3.20(a, b) is shown a diagram of the magnetisation configuration at the critical field where an abrupt change in the orientation of magnetisation occurs for the outward direction (fig.3.20(a)) and return direction (fig.3.20(b)). They correspond to the configurations marked respectively with the white dots 1 and 2 for the outward direction, and 3 and 4 for the return direction in the energy landscape in fig.3.19. Since two stable orientations of the magnetisation \mathbf{M} are

present, we can infer the presence of two domains of magnetisation \mathbf{M}_1 and \mathbf{M}_2 , with an uncharged domain wall in between for outward and return direction as shown respectively in fig.3.20(c), and 3.20(d). Furthermore due to the presence of the unidirectional anisotropy, the orientation of the domain wall is different for the outward and return direction. From the values of ϕ_1 and ϕ_2 obtained from the MATLAB code, we can calculate DW orientation with respect to the uniaxial anisotropy (fig.3.20(e, f)) as shown previously.

An example of simulated domain wall orientation for different applied field directions with respect to the easy axis is depicted in fig. 3.21. The plot was obtained with the same parameters used for the energy landscape in fig.3.19: $H_k = 60 \text{ Oe}$, $H_u = 10 \text{ Oe}$, $\varepsilon = 70^\circ$ and for field orientations between -30° off the EA and 30° off the EA.

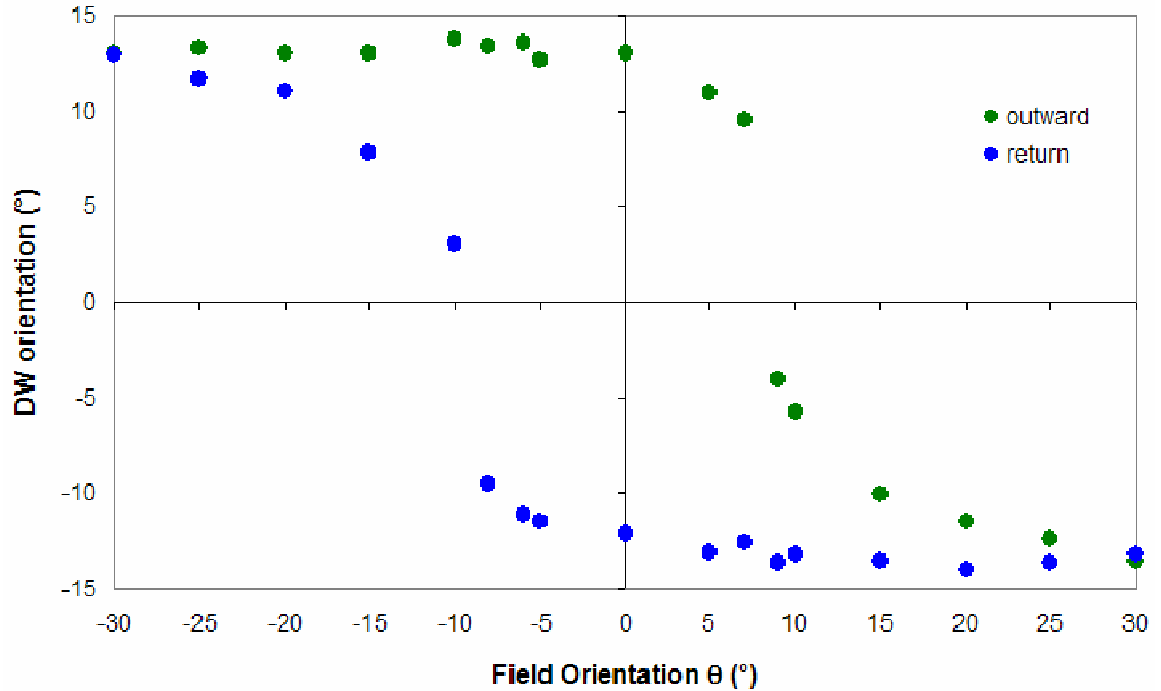


Figure 3.21: Plot of the simulated orientation of domain walls forming during the outward (green dots) and return (blue dots) path of the hysteresis loop for field orientation in the range -30° off the EA, 30° off the EA, calculated with respect to the orientation of the EA obtained with the following parameters: $H_k = 60 \text{ Oe}$, $H_u = 10 \text{ Oe}$, $\varepsilon = 70^\circ$.

The exploration of the parameter space has allowed the determination of the sets of parameters which best reproduce the experimental behaviour. As stated at the beginning of the section, H_k depends on material parameters, thus is fixed with a value of 60 Oe . We need to see the effect of the variation of the other parameters, in particular H_u and ε which are the key parameters that really influence the behaviour of DW orientation.

Fig.3.22 shows the influence of the parameter H_u on the behaviour of the simulated points. We can see that the variation of H_u produced a shift of the behaviour towards the right for the outward path (fig.3.22 top) and towards the left for the return path (fig.3.22 bottom). Moreover the behaviour crosses the horizontal axis for a field orientation that depends on the value of H_u . For $H_u = 2.5$ Oe the behaviour crosses the field axis at 2.5° , for $H_u = 5$ Oe and 10 Oe the behaviour crosses the field axis at 5° , and 10° respectively. The last value is the one that is in agreement with the experimental points, as seen in fig.3.16, the experimental results crosses the horizontal axis for a field orientation of about 10° . Thus we can consider $H_u = 10$ Oe the value of the parameter that better reproduce the experimental behaviour.

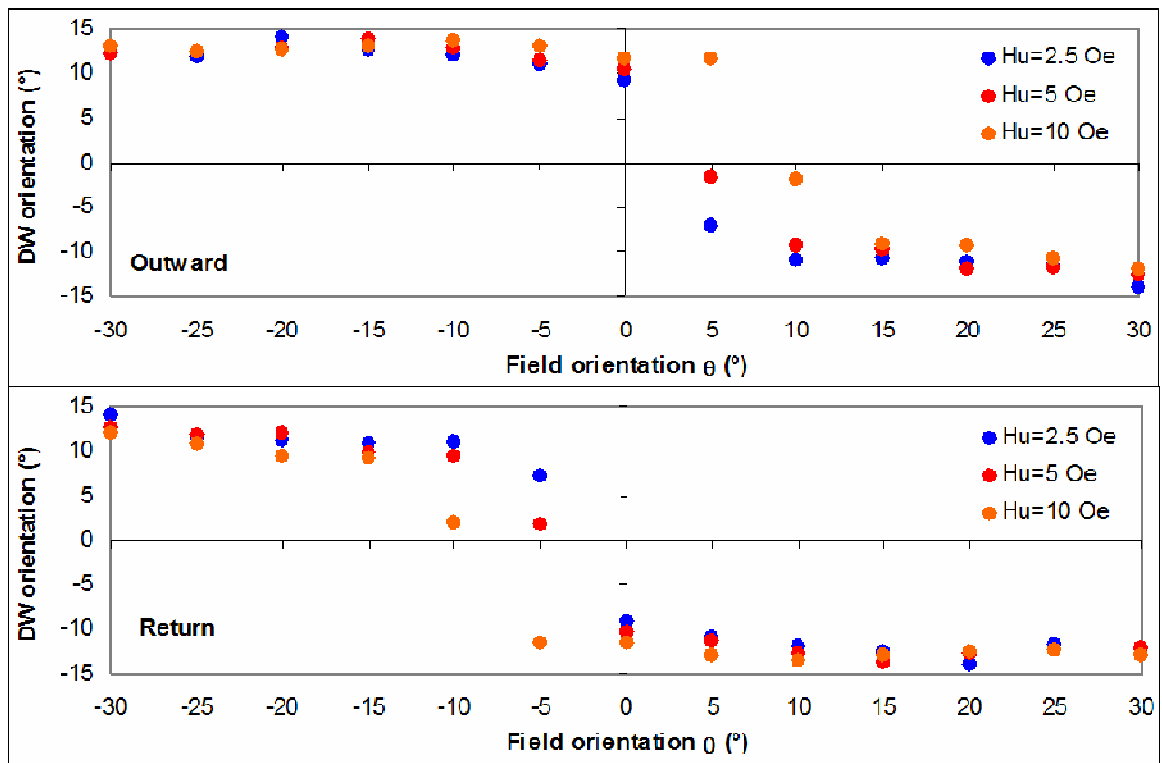


Figure 3.22: Plot of the simulated orientation of domain walls forming during the outward (top) and return (bottom) path of the hysteresis loop for field orientation in the range -30° off the EA, 30° off the EA, calculated with respect to the orientation of the EA obtained for $H_k = 60$ Oe, $\varepsilon = 90^\circ$ and $H_u = 2.5, 5, 10$ Oe.

The second parameter considered is ε , the orientation of the unidirectional anisotropy with respect to the EA. As we can see in fig.3.23, the sensitivity of the form of the variation is quite high for orientations of the unidirectional term ε between 0° and 45° and becomes much smaller for higher values of the parameter. The variation of the parameter between 0° and 180° has shown that, from a qualitative point of view, a good agreement between

simulation and experimental data points was reached for values of ε between 90° and 110° as shown in fig.3.24. Here we plotted only the extremes of the range for clarity.

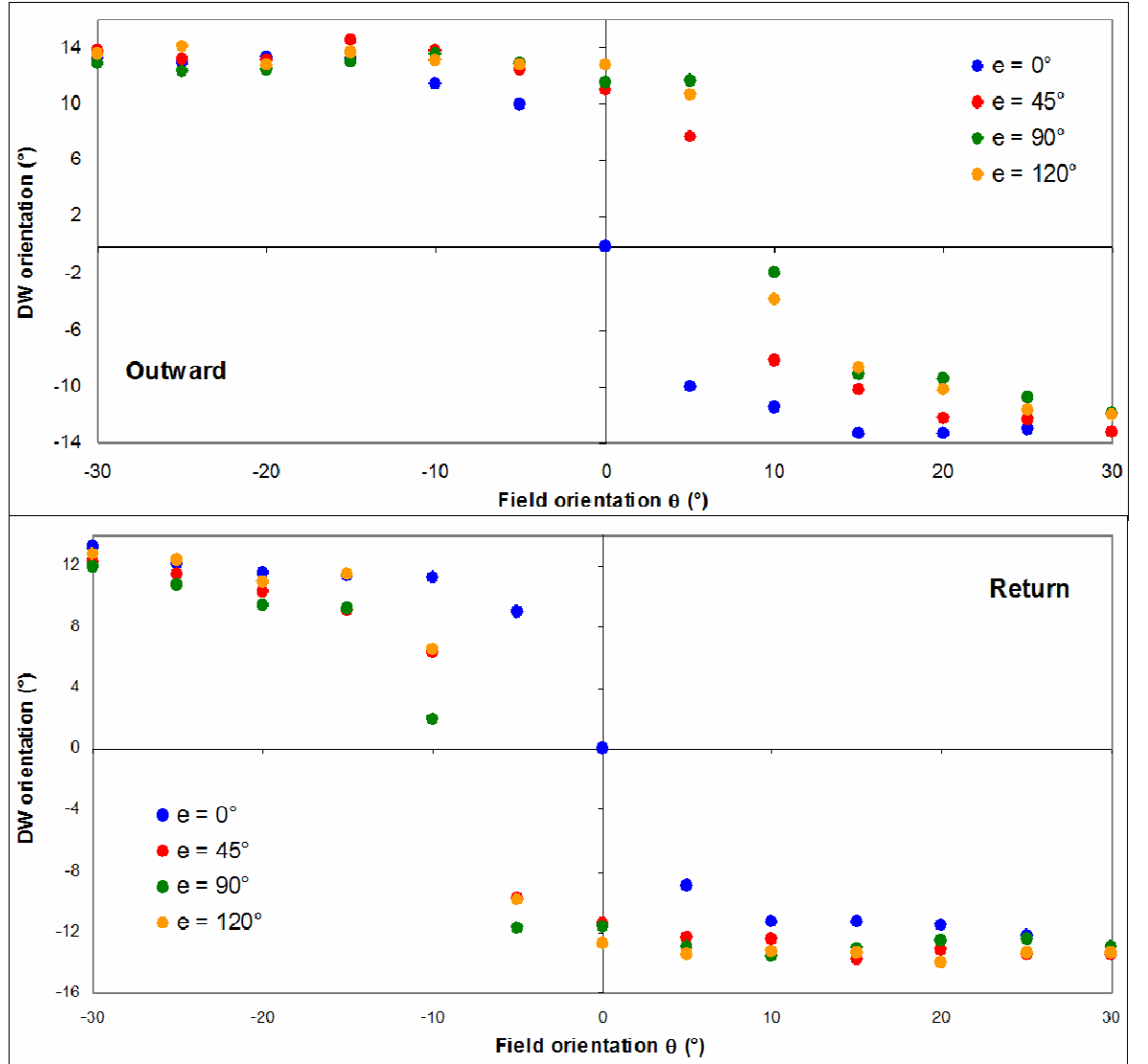


Figure 3.23: Plot of the simulated orientation of domain walls forming during the outward (top) and return (bottom) path of the hysteresis loop for field orientation in the range -30° off the EA, 30° off the EA, calculated with respect to the orientation of the EA obtained for $H_k=60$ Oe, $H_u=10$ Oe, and different values of ε .

In order to understand which value of ε gives the best agreement with the experimental results and which is the lowest value of the parameter that still give a good agreement with the experimental results, we used the χ^2 test. We defined our χ^2 as:

$$\chi^2 = \sum_{k=1}^n \frac{y_k^{\text{exp}} - y_k^{\text{sim}}}{\sigma_{k,\text{exp}}^2} \quad (3.4)$$

where y_k^{exp} is the measured DW orientation at a certain field direction, y_k^{sim} is the simulated DW orientation at the same field direction, $\sigma_{k,exp}$ is the standard deviation of y_k^{exp} , n is the number of experimental and simulated points.

For our test we considered the reduced chi squared $\tilde{\chi}^2$ which is the χ^2 normalised to the number of degrees of freedom ν . We can define $\nu = n - p$, where n is the number of points (11 in our case), and p is the number of parameters that is 1 (ε). Thus we considered $\nu = 10$. To carry out the test we calculated the probability P that the theoretical value of $\tilde{\chi}^2$ is equal or larger than the observed value $\tilde{\chi}_0^2$ which is indicated as $P(\tilde{\chi}^2 \geq \tilde{\chi}_0^2)$ for a given number of degrees of freedom ν (in our case $\nu = 10$). If the probability P is high, the experimental distribution can be described with the theoretical model; if P is lower than 5% it is unlikely that the experimental distribution can be described by this theoretical model.

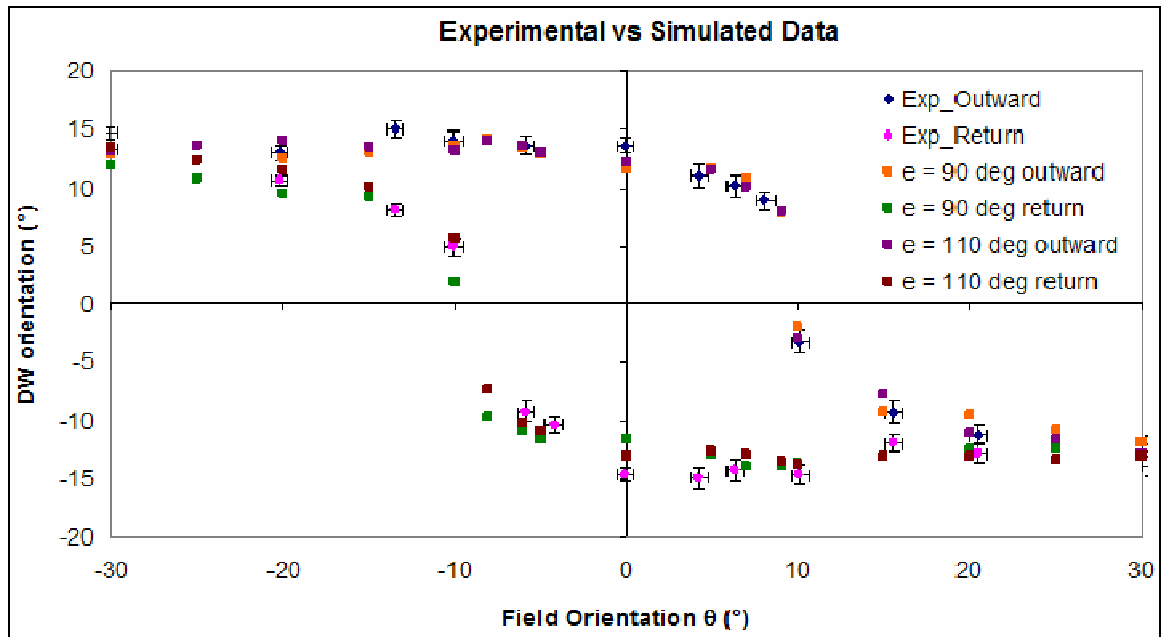


Figure 3.24: Comparison between experimental and simulated domain wall orientations for $H_k = 60$ Oe, $H_v = 10$ Oe and $\varepsilon = 90^\circ, 110^\circ$.

To obtain the value of ε that gives the best agreement with the experimental results, we need to find the value of ε that gives the highest probability for the outward and return DW orientations. Table 1 summarises the probabilities found for the outward and return DW orientations for ε between 70° and 110° .

ε / Probability	outward	return
70°	5%	9%
75°	10%	23%
80°	23%	24%
85°	50%	70%
90°	44%	75%
95°	50%	95%
100°	50%	88%
105°	98%	97%
110°	70%	10%

Table 1: $P(\tilde{\chi}^2 \geq \tilde{\chi}_0^2)$ for distributions with ε varying from 70° to 110° for outward and return DW orientations.

What the table shows is that the value of ε with the highest probability in both outward and return path is 105°. Thus we can estimate this value as the best fit value for the parameter ε . Moreover from the table we can say that the value of ε where we start to get a good agreement between experimental and simulated data is 85°.

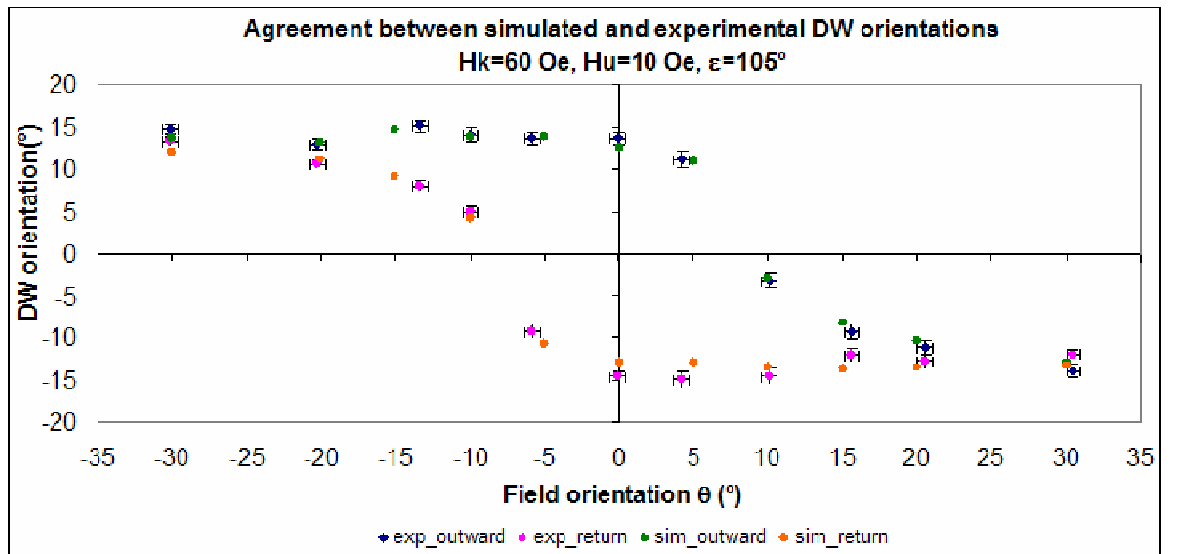


Figure 3.25: Plot displaying the agreement between experimental and simulated domain wall orientations for $H_k = 60$ Oe, $H_u = 10$ Oe and $\varepsilon = 105^\circ$.

The excellent agreement between simulated and experimental DW orientations is also shown in fig.3.25 where we compare the experimental with the best fit simulated data points ($H_k = 60 \text{ Oe}$, $H_u = 10 \text{ Oe}$, $\varepsilon = 105^\circ$).

3.6 Discussion on the physical meaning of the unidirectional term.

In section 3.4 we found that a particular characteristic of the 14 Å CoFeB layer is the variation of domain wall angle during the outward and return path of the hysteresis loop (fig.3.14), seen when varying the orientation of the applied field around the easy axis direction (fig.3.16). To assist in the interpretation of this asymmetric behaviour, we built a phenomenological model based on the Stoner-Wohlfarth model, described in section 3.5, where we introduced a unidirectional anisotropy. We found a good agreement between experimental and simulated domain wall orientation, however we need to try to understand a possible basis for presence of the unidirectional anisotropy. We propose the possibility of formation of an interfacial structure that can give rise to an exchange bias effect, an effect that has been seen from other studies. In the next two sections an explanation is given of the exchange bias effect and why it could be considered a possible explanation of the behaviour seen in our specimen, by looking at recent work found in literature.

3.6.1 Exchange bias: a brief overview.

Exchange bias, discovered by Meiklejohn and Bean in 1956 [19] is one of the phenomena associated with the exchange anisotropy created at the interface between an antiferromagnetic (AFM) and a ferromagnetic (FM) material [20]. From the macroscopic point of view there are two main phenomena that one can observe, when the AFM-FM system is cooled down from a temperature below the Curie temperature T_C to the Néel temperature T_N (T_N and T_C are respectively the ordering temperature for an antiferromagnet and a ferromagnet), in presence of a static magnetic field. First of all a shift of the hysteresis loop along the field axis, which is generally known as exchange bias H_E with different coercive fields for decreasing and increasing field, as the hysteresis loop in fig.3.26. The second macroscopic observation is seen in torque magnetometry experiments. Instead of uniaxial anisotropy, i.e. two equivalent easy configurations in

opposite directions, the magnetisation in the AFM-FM system has only one easy direction, often denoted as unidirectional anisotropy [21].

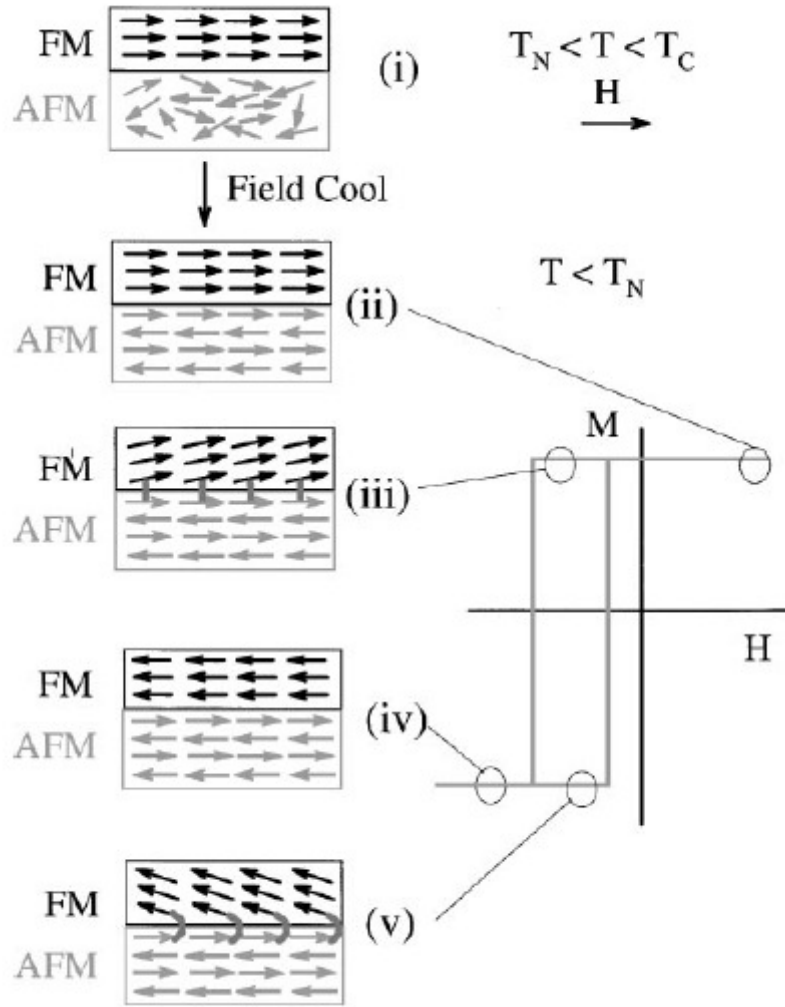


Figure 3.26: Schematic diagram of the spin configuration of an FM-AFM bilayer (a) at different stages (i)-(v) of an exchange biased hysteresis loop (b). From [20].

A simple picture can be used to explain qualitatively exchange bias and unidirectional anisotropy. Let's consider a bilayer composed by a ferromagnetic (FM) and antiferromagnetic layer (AFM). When a field H is applied in a temperature range between the Néel (T_N) and Curie (T_C) temperature (where T_N and T_C are respectively the ordering temperature for an antiferromagnet and a ferromagnet), the spins in the FM layer align with the field, whereas in the AFM layers the spins remain random as shown in fig. 3.26(a)i. When cooling down to T_N , in the presence of the field, and due to the interaction at the interface, the AFM spins next to the FM align ferromagnetically to those of the FM. The other spin planes in the AFM follow the AFM order and a net zero magnetisation is

produced (fig.3.26(a)ii). When the field is reversed, the FM spins start to rotate and if the AFM anisotropy is sufficiently high, the AFM spins remain unchanged (fig.3.26(a)iii). At the interface the AFM spins exert a microscopic torque on the FM spins to keep them in their original position (ferromagnetically aligned at the interface). Therefore the spins have one single stable configuration, i.e. the anisotropy is unidirectional. Thus the field required to reverse completely a FM layer will be larger if it is in contact with an AFM, because an extra field is required to overcome the microscopic torque exerted by the AFM spins (fig.3.26(b)). However, once the field is rotated back to its original direction, the FM spins will start to rotate at a smaller field, due to the interaction with the AFM spins (which now exert a torque in the same direction as the field, as shown in fig. 3.26(a)v and 3.26(b)). The material behaves as if there was an (internal) biasing field, therefore the FM hysteresis loop is shifted in the field axis (fig.3.27(b)), i.e. exchange biased [20].

3.6.2 Possible evidence for an interfacial exchange bias effect.

The investigations on the sample with 14 Å CoFeB layer shows elements similar to an exchange bias being present. Indeed, the switching fields found during the easy axis magnetising sequence were -5 Oe and 17 Oe (fig.3.14), different in absolute value and they show a shift in the hysteresis loop on the field axis on the positive field side. Moreover the observation of different DW orientations during outward and return paths of the hysteresis loop for EA and around EA directions led to the construction of a model that includes a unidirectional term. The excellent agreement between the fitted simulation results compared to the experimental data makes a strong case for the presence of a unidirectional anisotropy, which is typical of an exchange bias system. Of course, a single CoFeB layer cannot strictly be an exchange bias system, unless we assume the formation of interfacial structures, in this case it would be at the interface between CoFeB and the bottom MgO layer during the deposition and/or annealing process. Possible candidate antiferromagnetic species are FeO, CoO or perhaps both. In such a way we would have CoFeB (ferromagnetic layer) and FeO-CoO (antiferromagnetic layer) and this would explain the occurrence of an exchange bias type behaviour. That deposition and/or annealing can induce the formation of FeO_x/CoO_x at the interface between CoFeB and MgO, has been demonstrated recently by Read *et al.* [22] and Hindmarch *et al.* [23].

Read *et al.* [22] investigated the composition of CoFeB/MgO bilayers with XPS (x-ray photoemission spectroscopy). In their study 20 nm thick CoFeB layers were deposited by dc magnetron sputtering in Ar from an alloy target, whereas MgO with two different thickness (1 and 2 nm) was deposited by three different methods (electron beam evaporation, rf magnetron sputtering and dc sputtered Mg layer + MgO rf magnetron sputtered). The results of interest are those obtained with MgO deposited by rf magnetron sputtering. In the case of the as deposited sample, the oxygen spectrum of the sample with 1 nm MgO shows a peak at ~530 eV attributable to FeO_x. The 2 nm MgO sample shows a peak which can be fitted with two more peaks. The one with lower binding energy is likely the convolution of MgO, FeO_x and CoO_x signals. The effect of annealing (at 375°C in vacuum) was to significantly reduce the Co and Fe oxide peaks and shift the FeO_x peak to lower binding energy, indicating a reduction in the oxidation state. It was proposed that B escapes from the CoFeB electrode and oxidises with the O liberated by the Co and Fe oxides during the annealing process. Thus Read *et al.* demonstrated in their work the formation of FeO_x and CoO_x in CoFeB/MgO layer during rf magnetron sputtering of MgO, which although reduce in concentration are still present after annealing, as confirmed by XPS.

Another investigation that supports the hypothesis of formation of interfacial structures in the specimen with CoFeB 14 Å investigated in this chapter, was the one of Hindmarch *et al.* [23]. They studied the effect of annealing on the interface magnetisation in a CoFeB/MgO structure which models the lower electrode in a MTJ. They used soft x-ray absorption spectroscopy (SXAS) and soft x-ray magnetic circular dichroism (SXMCD) to study the influence that post-deposition annealing has on the magnetic properties of the CoFeB/MgO interface alone. The combination of these techniques provides a surface sensitive, element specific probe, of both magnetism and oxidation state in the vicinity of the electrode/barrier interface as shown in [24], but at the same time, quantitative analysis of SXMCD data is nontrivial as the result is strongly dependent on subtle details of the SXAS background subtraction as shown in [25]. The specimens investigated were Ta[20 Å]/Ru[200 Å]/Co₄₀Fe₄₀B₂₀[30 Å]/capping layer[20 Å], with capping layer being either Ta or MgO. Metallic layers were deposited by dc magnetron sputtering, whereas MgO layers were deposited by rf magnetron sputtering. A 150 Oe forming field is applied in the plane of the sample to induce a weak in-plane uniaxial magnetic anisotropy. Annealing was performed at 375 °C for 30 min in-situ after measurement of the as-deposited SXAS and SXMCD. As far as the as deposited sample is concerned, SXAS spectra showed peak-

shifts and splitting at both Fe and Co absorption edges due to oxide formation close to the interface. both the energy shift and peak splitting are far more pronounced in the case of Fe sites than for Co sites. This can be explained in terms of formation enthalpies which is lower for FeO_x than for CoO_x . This confirms that Fe–O bond formation should be energetically favorable over Co–O bond formation: thus oxidation proceeds more readily at interfacial Fe sites in comparison to Co. Additionally, the SXAS intensity close to the Fe absorption edges is significantly greater than that close to the Co edges and this indicates that the surface region of the CoFeB film is Fe-rich. As concerned the SXMCD spectra, the dichroism signal around the Fe edges is smaller than that around the Co edges. This can be explained because as it is predominantly Fe sites close to the interface which have bonded with oxygen, the magnetic moment associated with metallic Fe sites is diluted. In a full MTJ device structure this loss of interfacial Fe moment would result in a significant drop in tunneling spin-polarization, and hence a reduced TMR. This would, probably, explain the drop in TMR observed by Wisniowski *et al.* [13] seen at the beginning of the chapter and attributed to the deposition of a discontinuous CoFeB. The SXAS spectra achieved after annealing showed that the CoFeB/MgO sample is Fe-rich close to the interface. It seems as if some fraction of the Fe spontaneously segregates out toward the surface of amorphous CoFeB in the presence of oxygen, with which it then reacts, preferentially forming Fe–O bonds over Co–O. Thus the compositional inhomogeneity persists after annealing, resulting in an Fe-rich CoFeB/MgO interface region. The SXMCD spectra after annealing showed that the Fe dichroism signal is greatly enhanced; Fe–O bonded sites are reduced back to metallic Fe and the previously diluted interface magnetization is recovered as well as spin polarisation and TMR. However the presence of an Fe-rich region at the interface could then be detrimental to the temperature and bias-dependencies of TMR, and modify the TMR.

3.7 Summary

The present chapter described an investigation using conventional transmission electron microscopy (TEM) and Lorentz microscopy to characterise respectively the physical microstructure and the domain structure of the CoFeB free layer of a MTJ, embedded in a multilayer composed by SiN/MgO(50)/CoFeB(t)/MgO(15), with t from 30 Å down to 14 Å. As regards the physical microstructure, the TEM images and their respective diffraction

patterns show that the CoFeB layer appears polycrystalline in character and continuous. Thus physically the plan view sections show the structure of the films to be quite similar.

The magnetization reversal behaviour observed during Lorentz TEM experiments are found to vary considerably with the CoFeB thickness, with both domain wall formation and magnetisation rotation seen. Experiments were carried out by applying field in the range 90 Oe to -90 Oe. In the thicker film the behaviour was characteristic of a typical soft magnetic material with uniaxial anisotropy. However the magnetic reversal of the thinner film was more complex and no evidence of a superparamagnetic behaviour has been observed. A particular characteristic of the 14 Å CoFeB layer is the variation of domain wall angle seen when varying the orientation of the applied field. This wall asymmetry suggests the presence of a unidirectional anisotropic energy term. To assist in the interpretation of these experimental results a modified Stoner–Wohlfarth model has been constructed and calculations have been carried out by using a MATLAB code. The calculations gave a good agreement with the experimental results for the set of parameters: $H_k=60$ Oe, $H_u=10$ Oe, $\varepsilon=105^\circ$. The agreement with the experimental results pose a question on which physical phenomenon is the possible origin of the unidirectional anisotropy. There is evidence in literature that deposition and/or annealing would produce interfacial effects in CoFeB/MgO bilayers and such effects become more important for decreasing thickness of the ferromagnetic layer. This is supported by results obtained by experiments performed by Read *et al.* [22] and Hindmarch *et al.* [23] that have shown the formation of interfacial effects in CoFeB/MgO bilayers that could possibly lead to exchange bias properties.

In the next chapter the investigation of electrodeposited Ni₈₀Fe₂₀/Cu nanowires for spin transfer torque based devices will be presented.

Bibliography

- [1] Lee Y.M. *et al.*, *Appl. Phys. Lett.*, (2007), **90**, 212507.
- [2] Parkin S.S.P. *et al.*, *Nature Materials*, (2004), **3**, 862.
- [3] Djayaprawira D.D. *et al.*, *Appl. Phys. Lett.*, (2005), **86**, 092502-1.
- [4] Yuasa S. *et al.*, *Science*, (2002), **297**, 234.
- [5] Nagahama T. *et al.*, *Phys. Rev. Lett.*, (2005), **95**, 086602.
- [6] Zhang X.G. and Butler W.H., *Phys. Rev. B*, (2004), 70, 172407.
- [7] Yuasa S. *et al.*, *Nature Materials*, (2004), **3**, 868.
- [8] Tondra M. *et al.*, *J. Appl. Phys.*, (1998), **83**, 6688.
- [9] Lacour D. *et al.*, *J. Appl. Phys.*, (2002), **91**, 4655.
- [10] Malinowski G. *et al.*, *Appl. Phys. Lett.*, (2003), **83**, 4372.
- [11] Van Dijkena S. and Coey J. M. D., *Appl. Phys. Lett.*, (2005), **87**, 022504.
- [12] Jang Y. *et al.*, *Appl. Phys. Lett.*, (2006), **89**, 163119.
- [13] Wiśniowski P. *et al.*, *J. Appl. Phys.*, (2008), **103**, 07A910.
- [14] Gillies M. F. *et al.*, *J. Magn. Magn. Mater.*, (1995), **140-144**, 721.
- [15] De Hosson J.Th.M. *et al.*, *Microsc. Microanal.*, (2002), **8**, 274.
- [16] Hoffman H., *IEEE Trans. Magn.*, (1968), **4**, 32.
- [17] Gentils A., *J. Appl. Phys.*, (2005), **98**, 053905.
- [18] Labrune M. *et al.*, *J. Magn. Magn. Mat.*, (1997), **171**, 1.
- [19] Meiklejohn W.H. and Bean C.P., *Phys. Rev.*, (1956), **102**, 1413.

- [20] Nogués J. and Schuller I.K., *J.Magn. Magn. Mat.*, (1999), **192**, 203.
- [21] Takahashi M. *et al.*, *Jpn. J. Appl. Phys.*, (1980), **19**, 1093.
- [22] Read J.C. *et al.*, *Appl. Phys. Lett.*, (2007), **90**, 132503.
- [23] Hindmarch A.T. *et al.*, *Appl. Phys. Lett.*, (2010), **96**, 092501.
- [24] Miyokawa K. *et al.*, *Jpn. J. Appl. Phys. Part 2*, (2005), **44**, L9.
- [25] Hindmarch A.T. *et al.*, *Phys. Rev. Lett.*, (2008), **100**, 117201.

CHAPTER 4

Investigation of electrodeposited $\text{Ni}_{80}\text{Fe}_{20}/\text{Cu}$ nanowires for applications in spin transfer torque devices

4.1 Introduction

The theoretical predictions of spin-transfer interaction between the conducting electrons and a macroscopic magnetic moment [1-3] have led to many experimental investigations on current-induced magnetization switching (CIMS) [4,5]. In terms of applications, the interest of CIMS is considerable, since it provides a reliable way to commute the magnetic state of a spintronic device by using a spin current instead of a current induced magnetic field. The potential applications are very promising, for example as a new way to write the information in non-volatile memories. Furthermore, when a high current is injected in the presence of a high magnetic field, the spin transfer torque (STT) generates steady magnetisation precession in the GHz range that leads to microwave emission. This opens the possibility for the development of nanosized tunable microwave oscillators to be employed in high frequency telecommunications [6, 7].

Experimentally, most studies of the spin-transfer phenomena have been performed on magnetic nanopillars composed of a stack: thin magnetic layer/ nonmagnetic metal (or insulator)/ thick magnetic layer designed as a nanopillar by electron beam lithography. The actual area of the nanopillars must be less than a few hundred nm^2 in order to reach the critical current densities (around 10^7 A/cm^2) required to induce magnetic excitations or even magnetisation reversal in multilayer spin valves. This makes more challenging the fabrication process required to obtain these structures.

A simple and low-cost alternative could be to use electrodeposition on nanoporous templates since it leads naturally to nanowires having diameters comparable to nanopillars. Electrodeposition of nanowires in porous templates was extensively described in section 2.2.2. In the past, magnetic nanowires composed of magnetic multilayers have been extensively used as model systems to validate the theoretical predictions of the current perpendicular-to-plane giant magnetoresistance (CPP-GMR) effect [8,9]. Moreover, the nanowire geometry has already been used for spin-transfer studies (indeed among the first), for example, with magnetic nanowires in nanoporous track etched polycarbonate membranes [10]. However, nothing was reported on current-induced magnetization precession in nanowires, although this corresponds to the situation for which the advantages of this approach are extremely promising. Indeed, the electrodeposition method could be of high interest for the subsequent fabrication of spin-transfer nano-oscillators coupled either through the emitted spin waves [11] or by an electrical coupling [12].

Blon *et al.* [13] have performed resistance measurements on single nanowires composed of Co/Cu/Co trilayers electrodeposited in an Al₂O₃ nanoporous template. They found that for small applied magnetic fields the resistance as a function of the dc current injected through the nanowire is hysteretic. This behaviour is ascribed to spin polarised current induced magnetic reversal due to the spin-transfer torque mechanism. They also found critical current densities of the order of 10^7 A/cm² that can trigger irreversible magnetisation switching and for high magnetic fields differential resistance exhibit peaks ascribed to free layer magnetisation excitation. Thus electrodeposited nanowires constitute appropriate systems for spin-transfer studies. Piraux *et al.* [14] developed a reliable method for the electrical connection of one single nanowire in a large assembly of wires embedded in anodic alumina template and supported on a Si substrate. They made use of this method to contact single electrodeposited NiFe/Cu/NiFe trilayer nanowires grown in an alumina template. Then they performed transport measurements where they demonstrated both magnetic excitations and switching phenomena driven by a spin-polarized current. Therefore, this novel approach promises ultimately to be of strong interest for the subsequent fabrication of coupled spin transfer nano-oscillators either through the emitted spin waves or by an electrical coupling.

In view of these interesting applications, it is extremely important to be able to control the physical structure, the chemical modulation of the layered structure, the composition of each individual layer and ultimately the magnetic properties of individual nanowires. The

purpose of the project presented in this chapter was the advanced characterisation of multilayered electrodeposited NiFe/Cu nanowires grown by the group of Prof. Chiriac at The National Institute for Research and Development of Technical Physics (NIRDTP) Iasi (Romania), both in alumina and polycarbonate templates. In particular the objective was the characterisation of the structure and local chemistry of the nanowires by TEM and the classification of nanowire switching deduced by Lorentz microscopy experiments, which are challenging for this specific material system. As said in section 2.2.2, in order to perform TEM studies on single nanowires, they should be extracted from their template. The dissolution of the template is performed by chemical etching. Part of the resulting solution containing single nanowires or clusters is then dispersed on holey carbon grids. The grid we used initially was a copper grid, since it is the most commonly used for TEM experiments. However for analytical experiments using a grid material which is also a component of the nanowire causes serious problems in interpreting data from that element. Therefore we decided instead to use holey carbon films on gold grids. The chemical etching used to remove the nanowires from the template in addition to issues related to the deposition of Cu, led to nanowires with edge and compositional irregularities, detrimental for their magnetic properties. Indeed, we were not able to classify the nanowire switching and investigate domain walls forming during the reversal process, but we could only observe a change in the magnetising state. A lot of the work described in this chapter deals with the difficulties associated with imaging these challenging nanowires. Issues were discovered that may have resulted from deposition and/or etching for TEM preparation, therefore we do rely heavily on simulations and calculations to point the way forward for a future study. These are initial results from one of the first attempts at Lorentz TEM imaging of such nanowires.

4.2 Nanowires grown in anodic alumina templates

Following the studies of Blon *et al.* [13] and Piraux *et al.* [14], we investigated, initially nanowires grown in anodic alumina template. Electrodeposition in porous templates and the dissolution of the template in order to get single nanowires was already described in section 2.2.2. The nominal diameter of the nanowires measured by SEM at NIRDTP (Romania) is (35 ± 5) nm and the composition along the length is 800 sequences of Ni₈₀Fe₂₀(50 nm)/ Cu(10 nm) and Cu on the top and on the bottom, as schematised in fig. 4.1. Single nanowires in solution (composed of residual of KOH used for the chemical

removal of the template and distilled water to rinse the nanowires) were dispersed on a holey carbon grid, with the grid made of Cu, and investigations of the morphology, physical structure and composition were carried out. They will be all described in the following subsections.

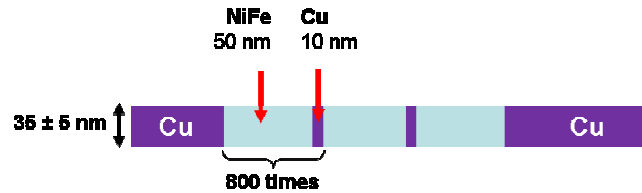


Figure 4.1: Schematic of a single nanowire grown in the anodic alumina template.

4.2.1 Morphology

The investigation of the morphology was carried out with the SEM incorporated in the FEI Nova 200 Dualbeam FIB system. The study of the morphology was performed to evaluate the length, the diameter and its variability, and the nature of the edges of a significant number of nanowires.

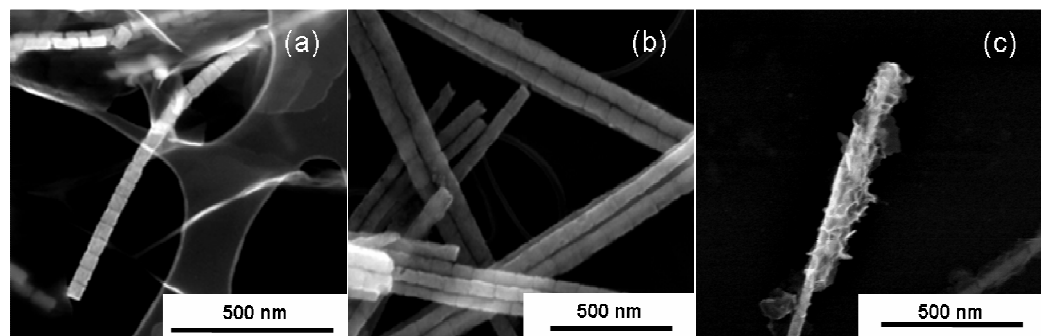


Figure 4.2: SEM images showing (a) an isolated nanowire, (b) a cluster of nanowires, (c) a nanowire with coating.

Fig.4.2 shows an isolated nanowire dispersed on (a) a holey carbon grid, (b) a cluster of nanowires and (c) a nanowire with apparent residual material from the template associated with the etching process. In fig.4.2(a) the nanowire exhibits a quite regular shape. In addition a multilayered structure is clearly visible and no such residual material is present, in contrast to the nanowire shown in (c) where the residual material completely covers the nanowire. Measurements on a significant number of nanowires led to the determination of the diameter $d = (40 \pm 10)$ nm. Moreover we found the length of nanowires ranging between 365 nm and 1.9 μ m. Fig. 4.2(b) shows an example of clusters of nanowires. The

clustering observed quite often was due possibly to magnetostatic interactions and/or electrostatic interactions due to the process used to remove the template.

4.2.2 Physical Structure

The physical structure of the samples was investigated by conventional TEM with a FEI T20. We were interested to see whether the layers are monocrystalline, polycrystalline or amorphous. In case the nanowires were polycrystalline we needed to measure the grain size and its variability. Moreover we were interested to distinguish whether the nanowires were uniform or compositionally modulated and in the latter case we intended to characterise the regularity of interfaces. Nevertheless we are dealing with a material system with a repeated structure and composed of chemical elements with very close atomic number (Z is 26 for Fe, 28 for Ni and 29 for Cu). Thus the contrast in the BF image produced by the presence of these elements will be similar, and it is likely that we will be unable to distinguish the different layers. This makes it challenging to investigate aspects of the structure and composition of the nanowires.

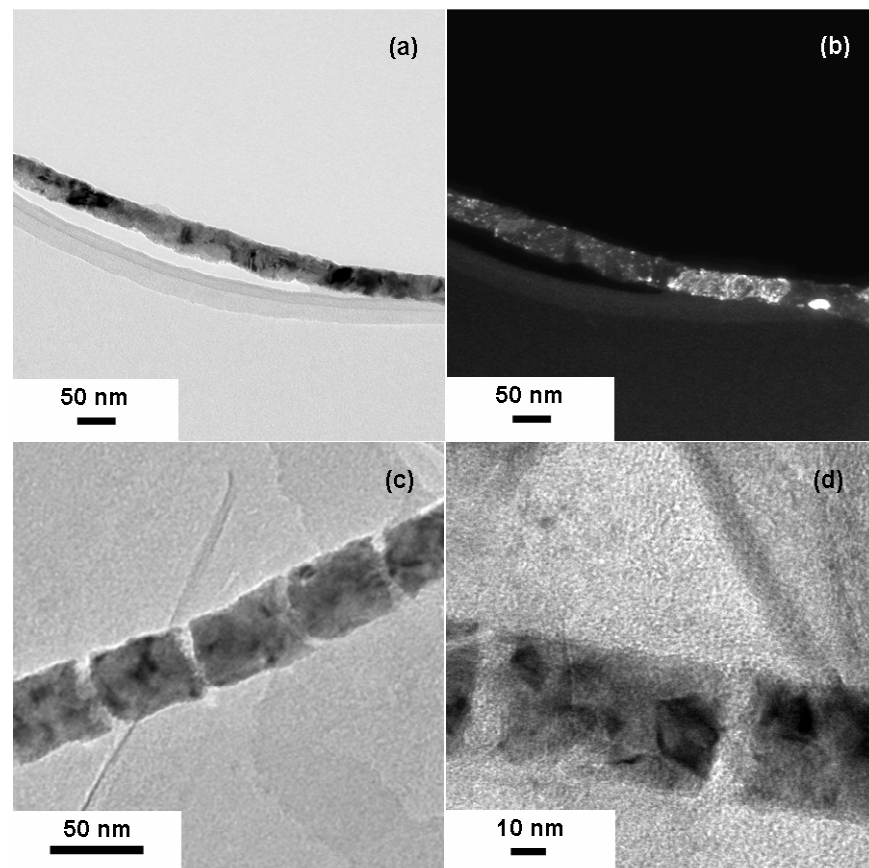


Figure 4.3: (a, c, d) TEM BF and (b) DF images of (a, b) nanowires with homogeneous contrast in the BF image and (c, d) nanowires alternating thick and thin layers.

Fig.4.3 represents an example of (a, c, d) TEM bright field images and (b) a dark field image of individual nanowires. If we look at the images we can see that nanowires are polycrystalline and there are two types of nanowires: nanowires with homogeneous contrast in the BF image, as the one in fig.4.3(a, b) shows, and nanowires with clearly alternating wide and narrow layers, as the one shown in fig.4.3(c, d). The first type of nanowire is probably what we would expect to see, because of the closeness of the atomic number of Ni, Fe and Cu. But the presence of grains larger than 50 nm, as the one in the DF image in fig.4.3(b) shows, put a question on whether the nanowire has a repeated structure or is more uniform. Grain size measurements carried out on a sample of 20 nanowires led to the measured distribution shown in fig.4.4. The distribution appears approximately log-normal and the peak value of the grain size is in the range 5-10 nm.

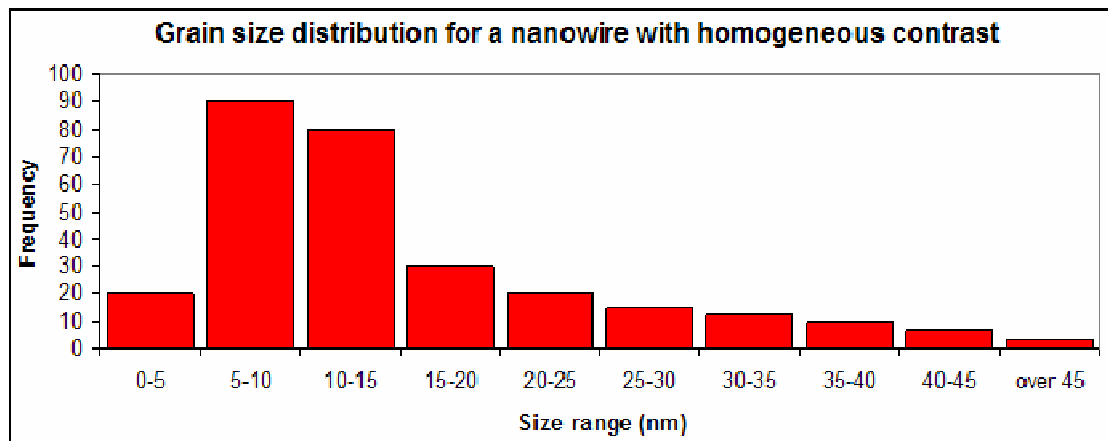


Figure 4.4: Grain size distribution for nanowires with homogeneous contrast. It is approximately a log-normal distribution peaked at the grain size range 5-10 nm.

The second type of nanowire shown in fig.4.3(c, d) consists of alternate layers with wide layers of about 50 nm and narrow layers of about 10 nm, as we would expect from the information obtained by the growers. However, the thinner layers of the periodic structure, i.e where we would expect the copper, appear transparent. This is clearly shown in fig.4.3(d) at high magnification. For these nanowires we repeated the measurement of the grain size. The distribution is shown in fig. 4.5 and it appears similar to the one shown previously. It is again approximately a log-normal distribution, with a shorter tail than in the previous case and the peak value of the grain size is again in the range 5 -10 nm.

The possible uniformity of nanowires with homogeneous contrast, and the transparency of the thinnest layers of nanowires alternating narrow and wide layers, are features that we didn't expect to see during the experiments and require further investigation, especially

from the compositional point of view. They put a question on whether there are issues related to the deposition process or to the dissolution of the template by chemical etching.

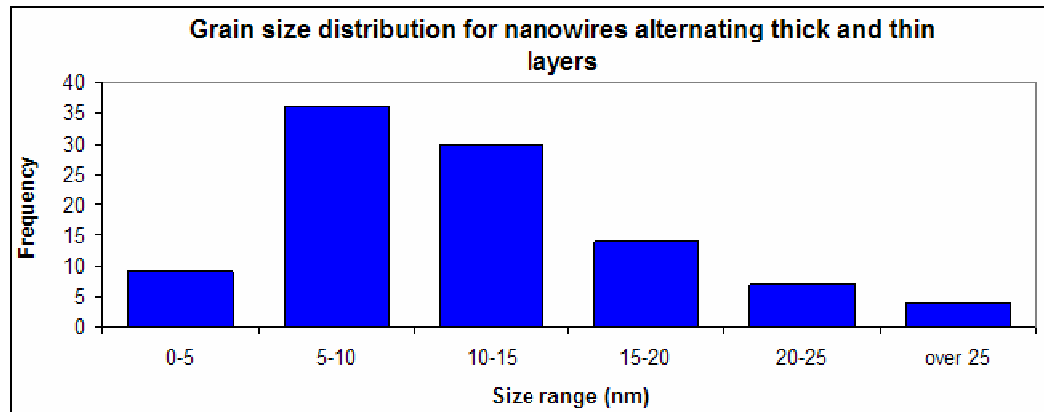


Figure 4.5: Grain size distribution for nanowires alternating narrow and wide layers. It is approximately a log-normal distribution peaked at the grain size range 5-10 nm.

4.2.3 Composition

The elemental composition of the nanowires was investigated by EELS and EFTEM with a FEI T20 and by EDX with the FEI TF20. The purpose of this type of analysis was to check the integrity of the nanostructure for nanowires with different physical structure identified from the previous section.

In the case of the wires with homogeneous contrast in the BF images, we saw in the previous section that the presence of grains larger than 50 nm, put a question on whether the nanowire has a repeated structure or is more likely a uniform Py ($\text{Ni}_{80}\text{Fe}_{20}$) nanowire. In order to see if a repeated structure could be identified, EFTEM (energy filtered TEM) was used to get compositional information. As we said in section 2.6.2, with this technique it is possible to obtain images of a two-dimensional distribution of a specific element. In this way we will be able to locate the Cu layers and the Py layers, if they are present. The first step we did, before the EFTEM experiments, was to see if Ni, Fe and Cu were all present in the nanowire by taking EELS spectra. Two examples of EELS spectra are shown in fig. 4.6. They refer to the nanowire with homogeneous contrast shown in fig.4.3(a, b) and they were acquired from the central area of the wire. Fig. 4.6(a) represents the portion of the core loss spectrum from 420 eV to 920 eV. The spectrum shows the presence of Ni and Fe (the peaks are labelled in the figure) and the measurements of the integrated area under the peaks show that the two chemical elements are in a 4:1 ratio, as expected in Py.

A large peak due to oxygen, also labelled in the spectrum, is an indication of a possible oxidation of the nanowire. The spectrum in fig. 4.6(b) represents the portion of the core loss spectrum from 720 eV to 1250 eV. The spectrum shows the clear presence of Ni (labelled in the figure) and we put a label where we expected to observe the spectral feature of Cu. What we can say about Cu is that if there is Cu, the spectral feature is located in the level of the noise. Thus from EELS measurements we can say that Ni and Fe are present in the nanowire and are in the right proportion; the nanowire is oxidised; if there is Cu in the nanowire, its concentration is very low.

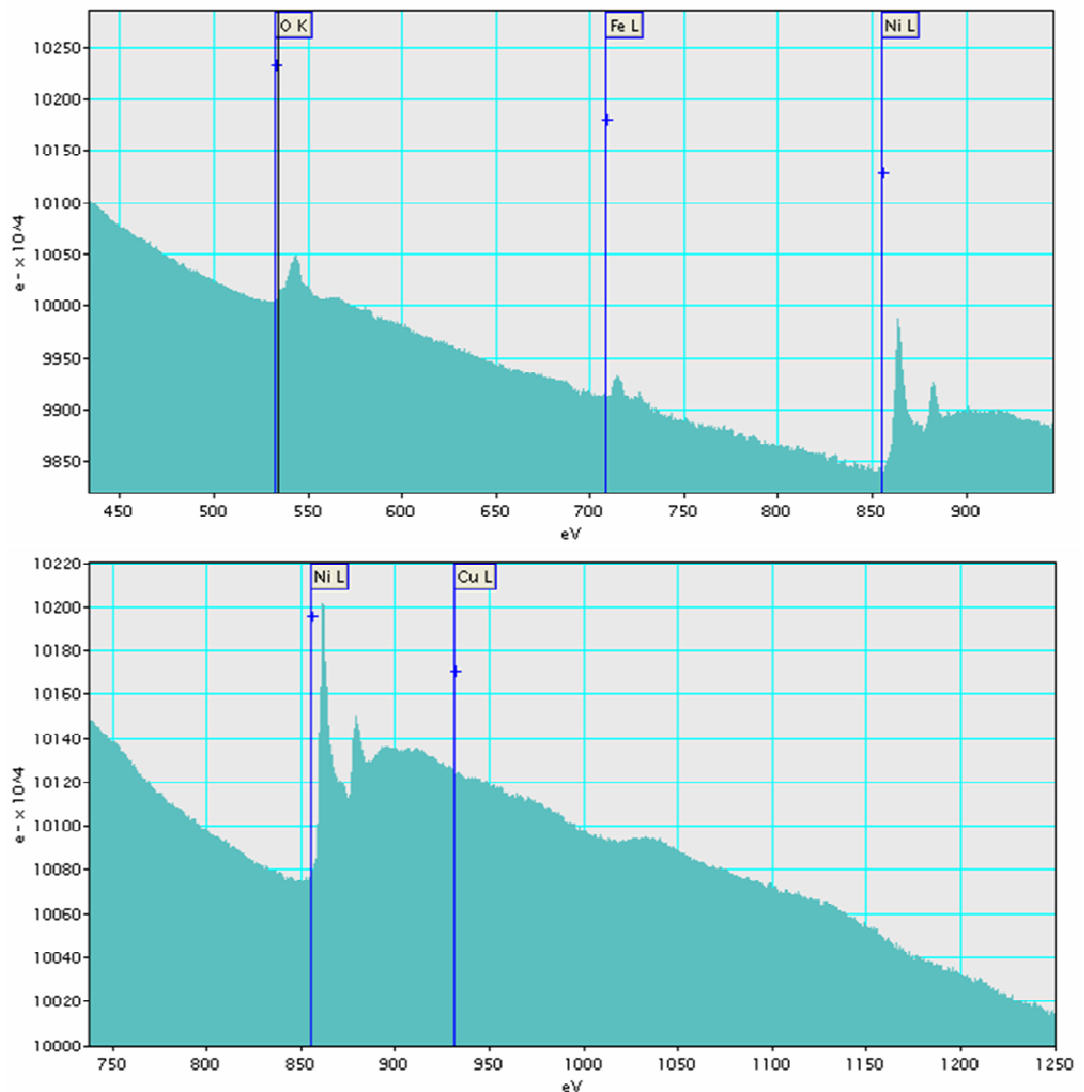


Figure 4.6: EELS spectra of the nanowire displayed in fig. 4.3(a) e (b) acquired at 450 eV (a) and 800 eV (b). The position in energy of the element of interest (Ni, Fe, Cu) are labelled in the spectra.

The EELS study was followed by EFTEM, carried out again with a FEI T20. The elemental maps in fig.4.7 refers to the same nanowire chosen to illustrate EELS results. Since EELS didn't provide a visible signature of the presence of Cu, the maps acquired

refer to Fe (fig.4.7(a)) and Ni (fig.4.7(b)) the two elements composing Permalloy (Py), C (fig.4.7(c)), which is the material supporting the nanowire. The variations of intensity in fig.4.7(a, b) cannot be related to the presence of a periodicity in the nanowires, but are possibly produced by the presence of residual diffraction contrast. These results lead to the conclusions that there is no evidence of a Py/Cu multilayer structure in these wires which showed reasonably uniform BF contrast along their length.

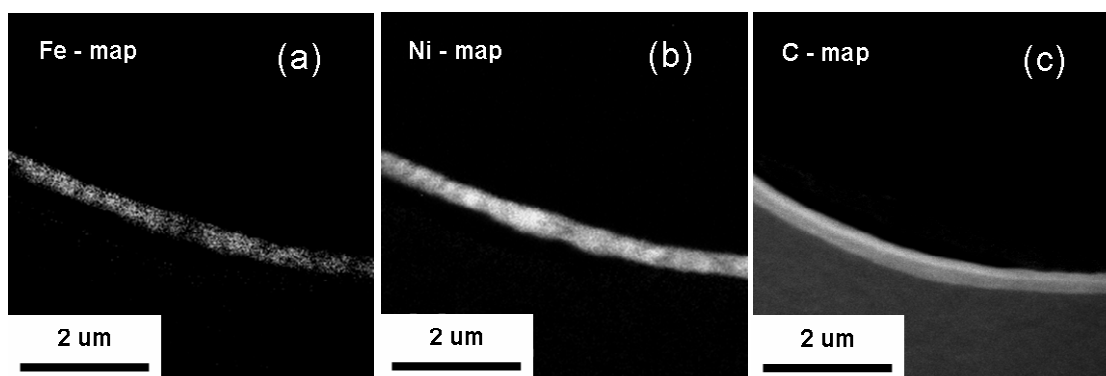


Figure 4.7: EFTEM (a) Fe, (b) Ni, and (c) C maps of the nanowire displayed in fig. 4.3(a) and (b).

In the case of the nanowires with narrow and wide layers, shown in fig.4.3(c, d), we need to investigate the composition of the transparent and non-transparent regions identified in the BF images. To this purpose we decided to carry out EDX, performed with a FEI TF20, which is a more appropriate technique to investigate materials composed of elements with higher Z. Fig.4.8(a, b) shows (a) the HAADF (high angle annular dark field) image of one of the periodical nanowires investigated and (b) the intensity profile along the red line in fig.4.8(a). The profile follows the shape of the nanowire and shows irregularities in shape, especially close to the edges.

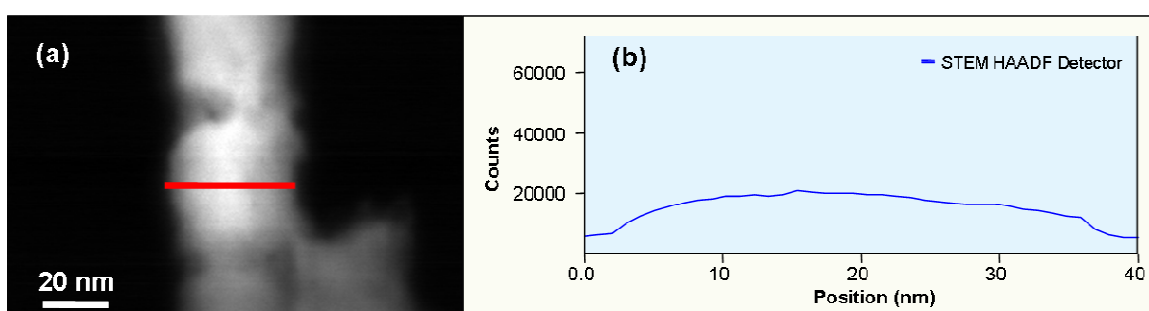


Figure 4.8: (a) HAADF image of a periodical nanowire and (b) the intensity profile along the red line. It reproduces the shape of the nanowire.

A series of EDX spectra was acquired along the red line shown in fig.4.8(a) to investigate the composition of the thick layers of nanowires alternating wide and narrow layers. An

example spectrum is shown in fig.4.9(a) and it refers to the central point of the red line. The peaks labelled are the K lines (on the right) and some of the L lines (on the left) of Ni and Fe, elements composing the nanowires.

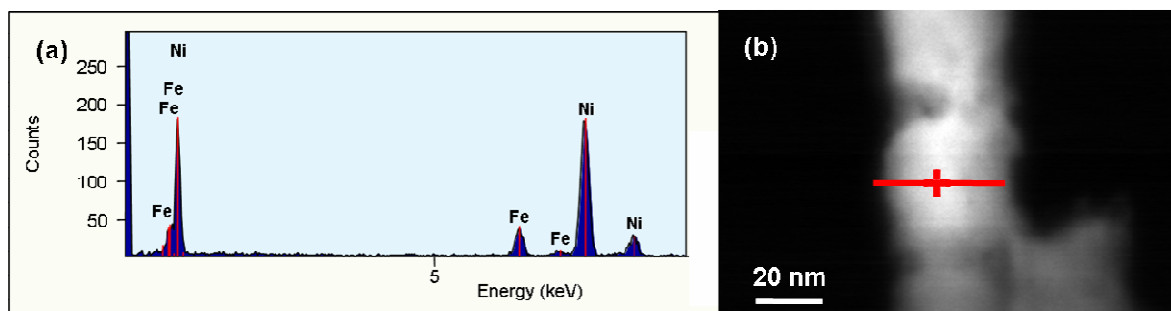


Figure 4.9: (a) EDX spectrum acquired at the central point of the line trace in the HAADF image (b). In the spectrum the peaks related to the K lines and some of the L lines of Ni and Fe, are labelled. The K lines are the peaks on the right, whereas the L lines are the on the left.

We performed the quantification of the 40 spectra acquired along the line. The quantification was carried out with TIA, the software used for the acquisition and analysis of STEM BF, HAADF images and EDX spectra and we specifically used an automated routine in four steps: background correction, peak identification, peak fitting and quantification. The background correction was performed with the modelled polynomial correction mode. This mode consists in fitting the background with a polynomial function (of 3rd order in our case) and this polynomial fit is then subtracted from the spectrum to correct for background effects. Once the background is removed from the spectrum, the EDX peaks present in the spectrum are identified. Once the peaks of interest have been identified, TIA performs a fitting of Gaussian peaks on the EDX spectrum. The resultant fit spectrum will be used in any subsequent quantification. The fitting used in our case is mixed. Mixed mode uses standards for elemental peaks in the standards list and theoretical Gaussians for peaks not in the standards list.

The quantification was carried out and the results were then normalised to the total atomic percent. What we found was that Ni and Fe are present in that region, but we could not see any spectral feature related to Cu. Thus we used the data obtained with quantification to get a plot of the concentration profile of Fe and Ni along the red line, as shown in fig.4.10. We can see that the concentration of Ni along the line is around $87 \pm 1 \%$, for Fe it is around $13 \pm 1 \%$. We calculated the Ni to Fe ratio along the red line and we found an average Ni to Fe ratio of $(5.9 \pm 0.9) : 1$, which is not the one expected for the Py deposited

(4:1 ratio). Thus we found that Ni and Fe are not in the expected proportions in this region and we could not see any spectral feature of Cu along the line.

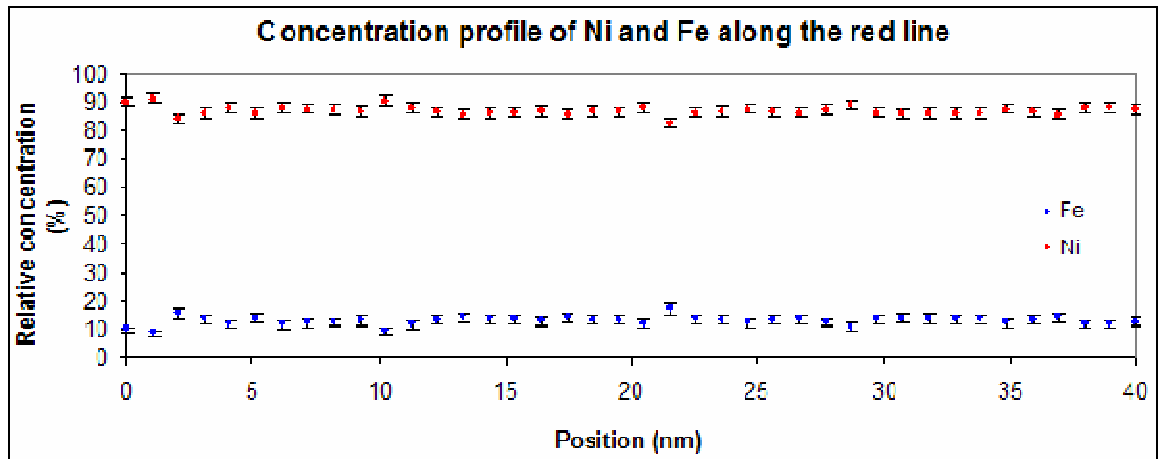


Figure 4.10: Relative concentration profile of Ni and Fe. The concentration of Ni along the line is around 87 ± 1 %, for Fe it is 13 ± 1 %.

To investigate the transparent region, to look at the interface and to see the differences with the composition of the non-transparent region, we took a series of EDX spectra along the red oblique line shown in the HAADF image in fig.4.11(a). The HAADF intensity profile in (b) shows that the intensity in the transparent region is about half the intensity in the non transparent region. This indicated a lower density of material in the first region with respect to the second region.

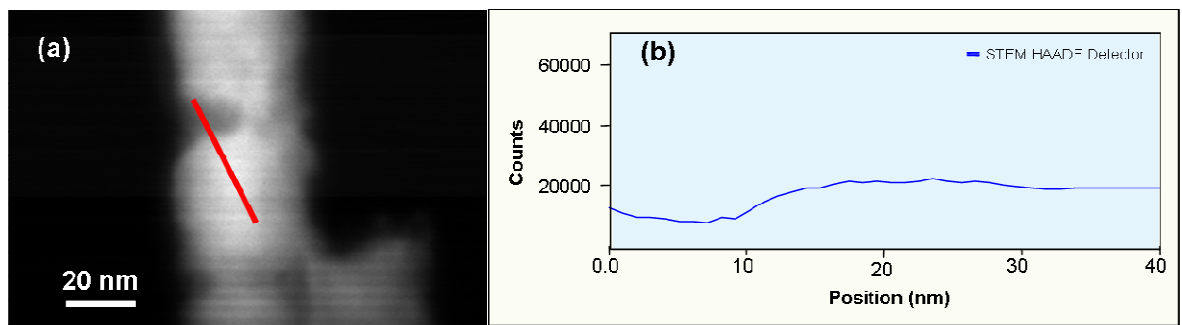


Figure 4.11: (a) HAADF image of a nanowire alternating thin and thick layers and (b) the intensity profile along the red line. The starting point is at the top-left corner of the line, the ending point is at the bottom right corner. The profile shows a low intensity area in the thinnest layer, an increasing intensity at the interface and a constant intensity region within the thicker layer.

We performed again the quantification of the 40 spectra acquired along the line, as described previously, and we found Ni, Fe and Cu within the thinnest layer, whereas only Ni and Fe in the thick layer. The concentration profile of Fe, Ni and Cu along the red line

in fig.4.11(a), is shown in fig.4.12. We can see that the concentration of Ni decreases at the beginning of the line and in the middle of this region the integrated intensity of the Ni K peaks is 1425 ± 181 ; reaches the minimum at the centre of the thin layer; then increases until the interface with the thick layer and in the middle of this region the integrated intensity is 3499 ± 283 ; and then it keeps constant around 86 ± 2 % and in the middle of this region the integrated intensity is 5485 ± 349 . The behaviour of Fe is exactly the opposite: the integrated intensity in the middle of the first region is 990 ± 153 , in the middle of the second region is 682 ± 129 and in the middle of the third region is 732 ± 136 , where it reaches a concentration of around 14 ± 2 %. By taking into account the accuracy of the measurements we found a Ni to Fe ratio of $(5.7 \pm 0.9) : 1$, comparable to the value obtained previously.

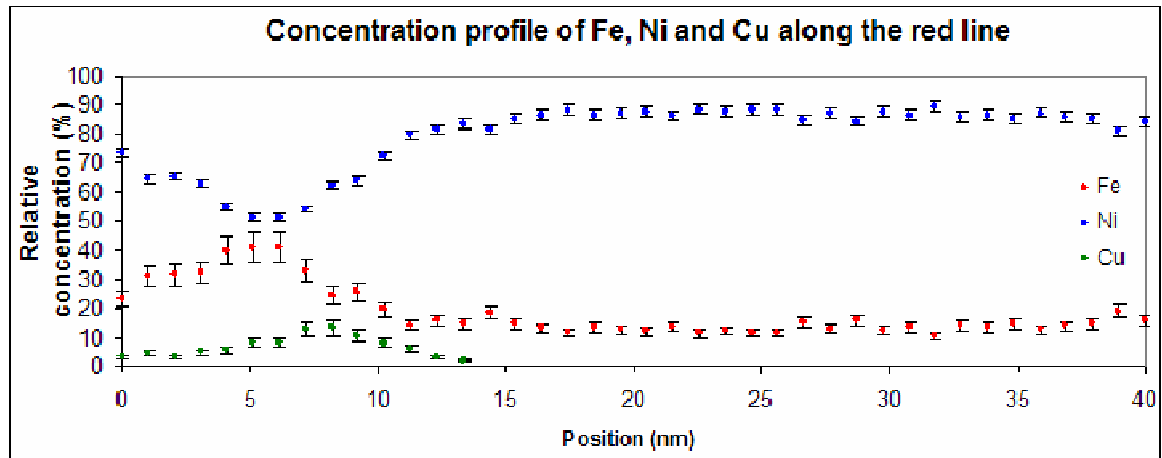


Figure 4.12: Relative concentration profile of Ni, Fe and Cu along the line in fig.4.11(a). The concentration of Ni decreases until the centre of the transparent area is reached, then increases until the interface with the non-transparent region, and then it keeps constant around 86 ± 2 %; the behaviour of Fe is the opposite and its concentration is around 14 ± 2 % in the constant region; Cu is detected in the transparent region and its maximum concentration is 13 ± 1 %.

We could detect Cu only in portion of the red line which lies in the thin layer, as expected from the arrangement of the layers in the nanowires provided by the growers. In the middle of the first region the integrated intensity is 236 ± 83 and in the middle of the second region is 269 ± 87 . The maximum concentration measured was 13 ± 3 %. Such a high error is due to the K lines being noisy and very close to the background level as shown in fig.4.13. Here we can see the K_{α} line of Cu and the K_{β} line for Ni. They are very close to each other, but they can be distinguished. At the interface between thick and thin layer we

cannot see the Cu K_{α} lines anymore, as shown in the spectrum in fig.4.13(c), but we can see only the K_{β} line for Ni.

The investigation by EDX of nanowires alternating wide and narrow layers has shown that in the thick layer there is no Cu, and Ni and Fe do not appear to be in the right proportion to that expected for the deposited Py. In the thin layer we found a lower density of material, Ni and Fe are in different proportion, and we could detect Cu, but with a large error associated with it. The results of the compositional investigation, appear to indicate there are issues with the deposition of the nanowire and possibly the etching for TEM preparation.

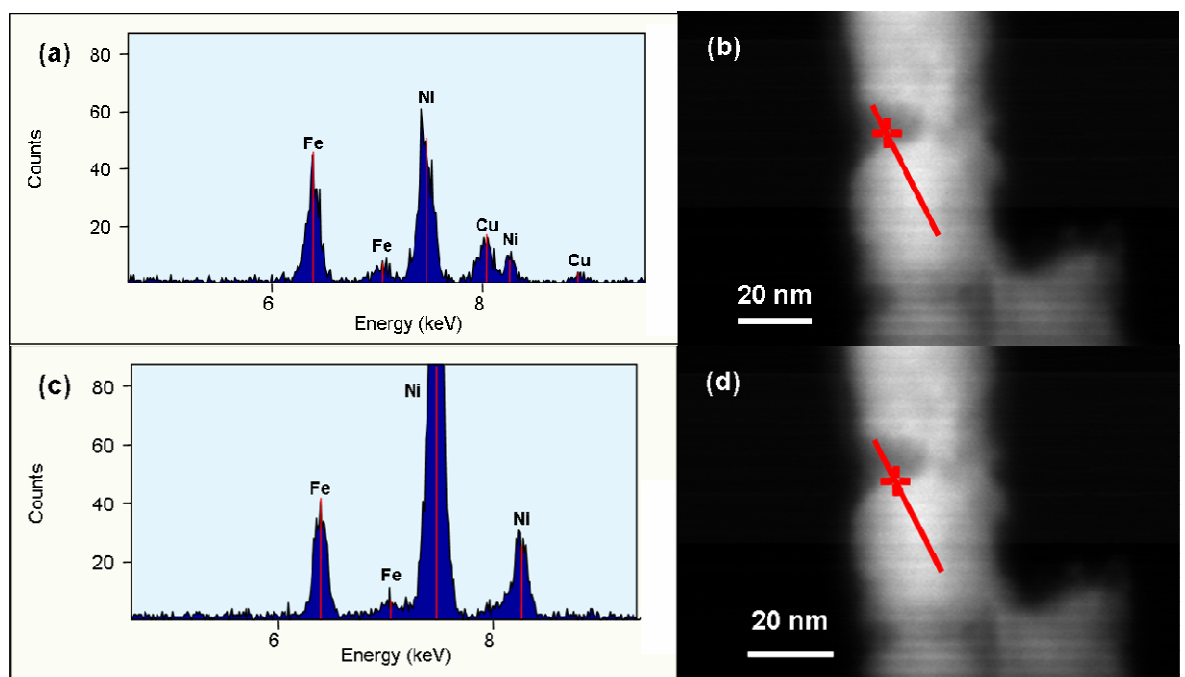


Figure 4.13: (a) EDX spectrum acquired in the centre of the thin layer, as marked in the (b) HAADF image where the concentration of Cu is the highest. We can clearly see two separated peaks for the Cu K_{α} line and the Ni K_{β} line. (c) EDX spectrum acquired at the interface between the thin and thick layer, as marked in the (d) HAADF image. We cannot see here a peak for the Cu K_{α} line, but only the peak for the Ni K_{β} line.

4.3 Nanowires grown in polycarbonate templates

In an attempt to identify the problems found in the previous section, and caused by issues with the deposition technique and removal of the template, the growers decided to carry out the deposition of two new sets of nanowires in a different template, made of polycarbonate. Nevertheless, the polycarbonate template produced nanowires with 100 nm

diameter, which represents a limiting thickness to get electron transparency, and thus would make difficult to carry out TEM investigations.

As already mentioned, the nominal diameter of the two sets of nanowires is 100 nm and the composition along the length is 800 sequences of Ni₈₀Fe₂₀(32 nm)/Cu(8 nm) and Ni₈₀Fe₂₀(53 nm)/Cu(9 nm) with Cu on the top and on the bottom, as schematised in fig. 4.14. Single nanowires in solution (composed of residual of trichloroethylene used for the chemical removal of the template and distilled water to rinse the nanowires) were dispersed on a holey carbon grid, with the grid made of Au. Analysis of the physical structure and composition were carried out. They will be described in the following subsections.

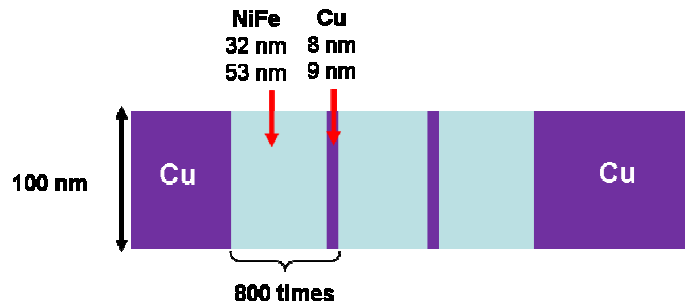


Figure 4.14: Schematic of a single nanowire grown in the polycarbonate template.

4.3.1 Physical Structure

The physical structure of the new samples was investigated by conventional TEM with a FEI T20. As for the nanowires grown in alumina templates, we were interested to see whether the layers are monocrystalline, polycrystalline or amorphous. In case the nanowires were polycrystalline we needed to measure the grain size and its variability. Moreover we were interested to distinguish whether the nanowires were uniform or compositionally modulated. We know that chemical elements included in the nanowires have very close atomic number (Z is 26 for Fe, 28 for Ni and 29 for Cu), and in the bright field images, in principle, we would not expect to see strong differences in contrast between NiFe and Cu. So again to restate it might not be possible to distinguish the layered structure using BF images alone.

In the investigation of nanowires grown in alumina template, we found nanowires with homogeneous contrast, composed of simply a Ni-Fe alloy, and nanowires alternating wide

and narrow layers composed of bits with Ni and Fe in a $(5.9 \pm 0.9) : 1$ ratio and bits with a lower density of material and composed of Ni and Fe in different proportions and traces of Cu. This was attributed to possible issues with the deposition technique and/or issues with the removal of the alumina template by chemical etching. We want to understand which of these factors is mainly affecting the structure and composition of the nanowires.

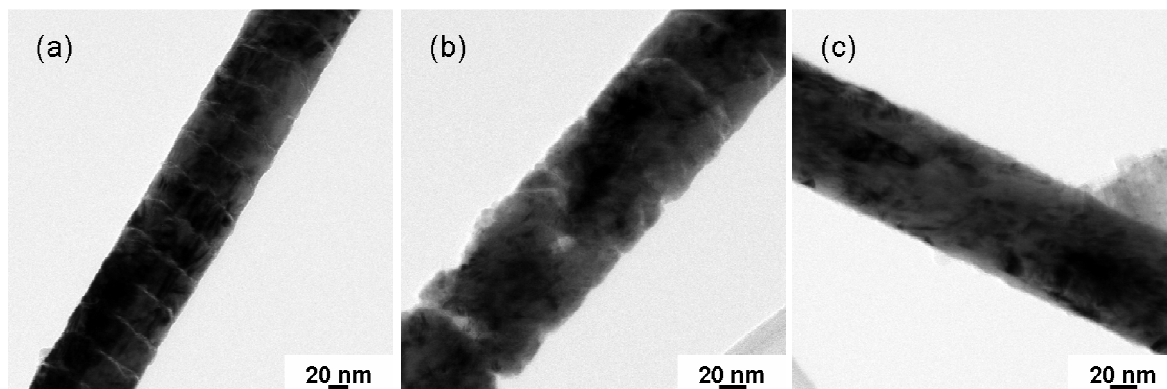


Figure 4.15: BF images of nanowires in sample NiFe (32 nm)/Cu (8 nm). (a) Nanowire alternating wide and narrow layers with regular edges; (b) nanowire with irregular edges and some regions alternating wide and narrow layers; (c) nanowire with homogeneous contrast.

Fig.4.15 shows three representative bright field (BF) images of nanowires found in sample NiFe(32 nm)/Cu(8 nm). They show a nanowire alternating wide and narrow layers with regular edges (fig.4.15(a)), a nanowire with irregular edges and some regions alternating wide and narrow layers (fig.4.15(b)), and an apparent nanowire with homogeneous contrast (fig.4.15(c)). The nanowires all appear to be polycrystalline and we measured the grain size. As shown in fig.4.16 the grain size distribution is slightly asymmetric, and peaked at a size between 10 and 15 nm. The results are indicative of a log-normal distribution.

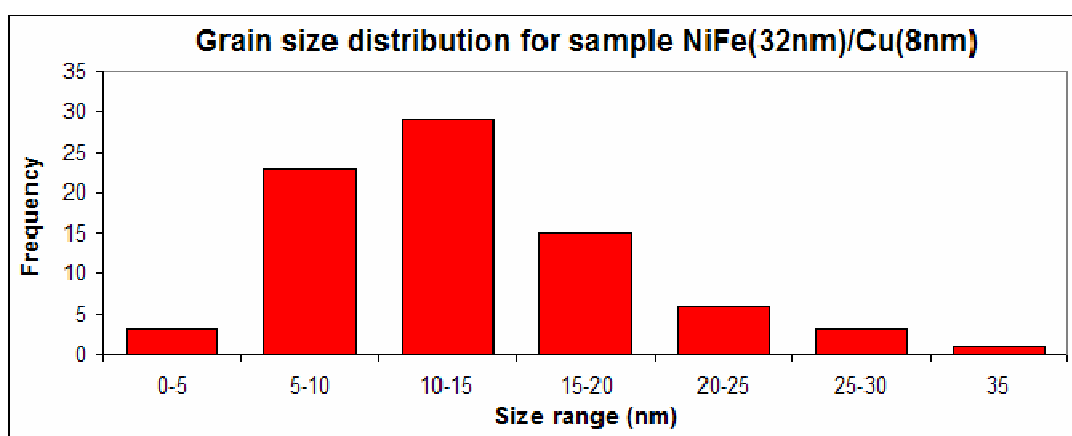


Figure 4.16: Grain size distribution for sample NiFe (32 nm)/Cu (8 nm). It is approximately a log-normal distribution peaked at the grain size range 10 -15 nm.

Fig.4.17 shows three representative bright field (BF) images of nanowires found in sample NiFe (53 nm)/Cu (9 nm). These show a nanowire alternating wide and narrow layers with regular edges (fig.4.17(a)), a nanowire alternating wide and narrow layers with irregular edges and with apparent excess of material around it along the edges (fig.4.17(b)), a nanowire alternating wide and narrow layers with what looks like over-etched edges (fig.4.17(c)) and a nanowire with homogeneous contrast (fig.4.17(d)). The nanowires appear again to be polycrystalline and the grain size was measured as shown in fig.4.18, and it is consistent with the grain size of the samples grown in alumina template.

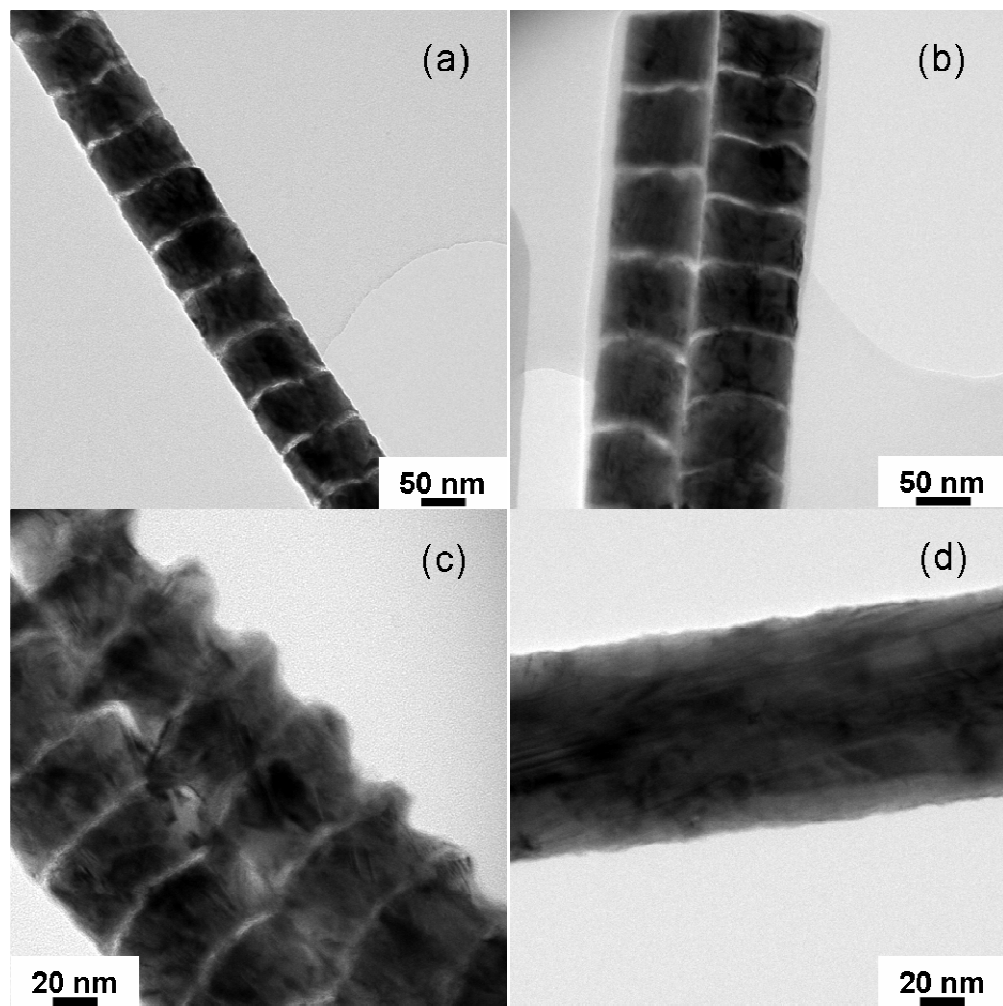


Figure 4.17: BF images of nanowires in sample NiFe(53 nm)/Cu(9 nm). (a) Nanowire alternating wide and narrow layers with regular edges; (b) nanowire alternating wide and narrow layers with irregular edges and with apparent excess of material around it along the edges; (c) nanowire alternating wide and narrow layers with over-etched edges; (d) nanowire with homogeneous contrast.

We measured, then, the diameter of the nanowires and the thickness of layers of the ones alternating wide and narrow layers, to see whether they were in agreements with the

nominal thicknesses of Py and Cu. As we can see from table 4.1 the measured values are in good agreement with the nominal values.

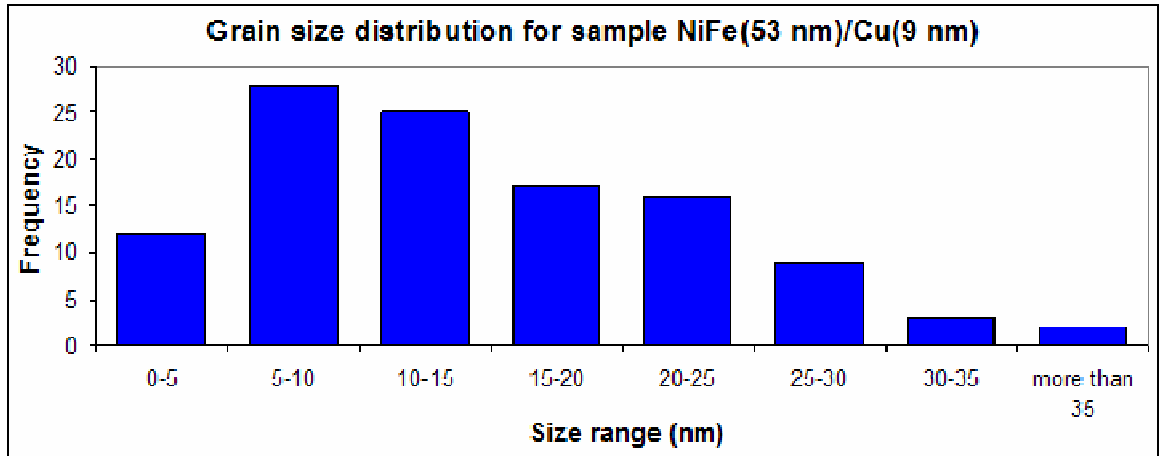


Figure 4.18: Grain size distribution for sample NiFe(53 nm)/Cu(9 nm). It is approximately a log-normal distribution peaked at the grain size range 5 -10 nm.

	Sample 1		Sample 2	
	TEM	Nominal values (provided by the growers)	TEM	Nominal values (provided by the growers)
Diameter (nm)	95 ± 5	100	99 ± 5	100
NiFe (nm)	29 ± 2	32	52 ± 4	53
Cu (nm)	7 ± 1	8	11 ± 3	9

Table 4.1: Comparison between TEM measurements of diameter, Py and Cu thickness and their nominal values provided by the growers for NiFe(32 nm)/Cu(8 nm) and NiFe(53 nm)/Cu(9 nm).

During the investigation of the structure of the nanowires grown in the polycarbonate template we didn't find strong differences with what was seen during the investigation of the structure of nanowires grown in alumina: we found again nanowires alternating wide and narrow layers and nanowire with homogeneous contrast, with differences in the regularity of the edges; the grain size is slightly larger for sample NiFe(32 nm)/Cu(8 nm), whereas for sample NiFe(53 nm)/Cu(9 nm) is the same. Further study to investigate the composition was then carried out as detailed in the next section.

4.3.2 Composition

The composition of the nanowires was investigated by EDX with the FEI TF20. The purpose was to characterise any periodicity in composition for the wires studied by BF imaging in section 4.3.1 where different physical structure appeared to be present in the nanowires shown.

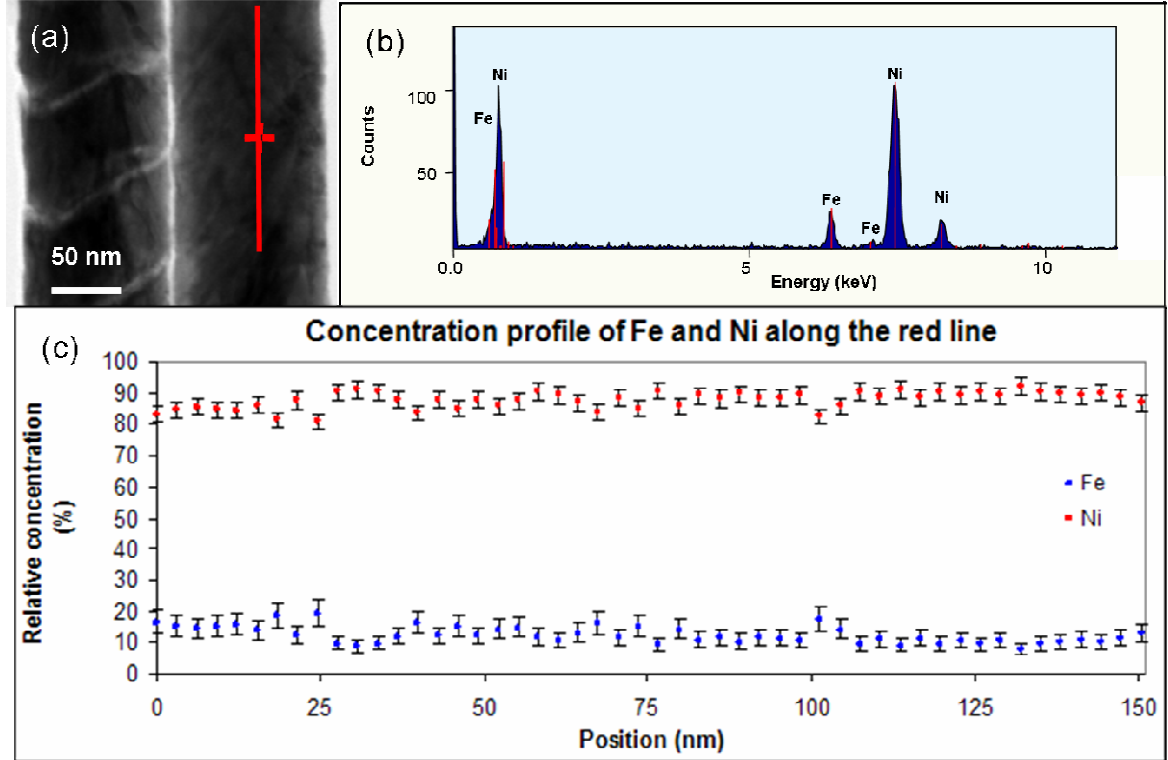


Figure 4.19: (a) STEM BF image of a nanowire alternating wide and narrow layers and a homogeneous nanowire of sample NiFe(53nm)/Cu(9nm). The red line is the line trace where a series of EDX spectra was acquired and the cross is the point where the spectrum in (b) was acquired. (c) Concentration profile of Ni and Fe along the red line in (a). The average concentration of Ni along the line is 88 ± 3 % and for Fe is 12 ± 3 %.

As concerned the investigation of a nanowire with homogeneous contrast, an example of what we observe is summarised in fig.4.19. In fig.4.19(a) is shown a BF image of a couple of nanowires: one alternating wide and narrow layers on the left and one with homogeneous contrast on the right. We acquired a series of 50 spectra along the line trace (red vertical line). An example of the EDX spectrum (acquired where the red cross is located) is shown in fig.4.19(b). The spectrum shows clearly the K and L lines from Ni and Fe, but we didn't see spectral features attributable to Cu. We performed the quantification of the spectra acquired, with the same procedure described in 4.2.3 and in fig.4.19(c) is

displayed the concentration profile. The average concentration of Ni along the line is 88 ± 3 % and the one of Fe is 12 ± 3 %. Such a large error can be attributed to the presence of a noisy K_{β} line for Fe and that the peak is very close to the background level. The Ni to Fe ratio for a nanowire with homogeneous contrast along the length, taking into account the accuracy of the measurements, is $(6 \pm 1) : 1$ which is consistent to the value found for nanowires grown in alumina template.

We also want to understand now what happens for nanowires which display alternating wide and narrow layers in the BF images. An example of what we observe is summarised in fig.4.20. In fig.4.20(a) is shown a BF image of this type of nanowire. We acquired a series of spectra along the two line traces: 50 for line trace 1, which is located in the wide layer and 25 for line trace 2, which is located in the narrow layer. Let's start from the thicker layer. An example of EDX spectrum (acquired where the red cross is located) is shown in fig.4.20(b). The spectrum, again, shows clearly the K and L lines from Ni and Fe, but no spectral features of Cu. Fig.4.20(c) displays the concentration profile of Ni and Fe along line trace 1. Ni has an average concentration of 84 ± 2 %, whereas Fe has an average concentration of 16 ± 2 %. We calculated the Ni to Fe ratio and after taking into account the accuracy of the measurements, we found a ratio of $(4.8 \pm 0.7) : 1$, which is in agreement with the 4:1 ratio typical of Py. We investigated, then, the composition of the thin layer. We performed the quantification of the EDX spectra acquired along line trace 2 and the concentration profile obtained is shown in fig.4.20(d). We detected, again, only Ni and Fe, and no spectral features of Cu were seen. The average concentration of Ni is 66 ± 6 %, whereas the average concentration of Fe is 34 ± 6 %. After taking into account the uncertainties of measurements, we found in this region a Ni to Fe ratio of $(1.5 \pm 0.3) : 1$, which is not in agreement with the typical ratio of Py.

Thus we found that in nanowires with homogeneous contrast in BF images, Ni and Fe are in $(6 \pm 1) : 1$ ratio instead of the $4 : 1$ ratio of Py and we could not detect any Cu; in nanowires alternating thick and thin layers, Ni and Fe are in $(4.8 \pm 0.7) : 1$ ratio, which is in better agreement with the ratio expected in Py, whereas in thin layers, we could not detect any Cu and Ni and Fe are in a $(1.5 \pm 0.3) : 1$ ratio along the line trace. These findings, which present some similarities to what observed in nanowires grown in alumina templates, would suggest that there is a serious issue with the deposition of the Cu, and the lack of Cu would not depend on the chemical used to perform the dissolution of the

template. However, we have identified that the magnetic elements are present, and further investigation was carried out to characterise the magnetic structure.

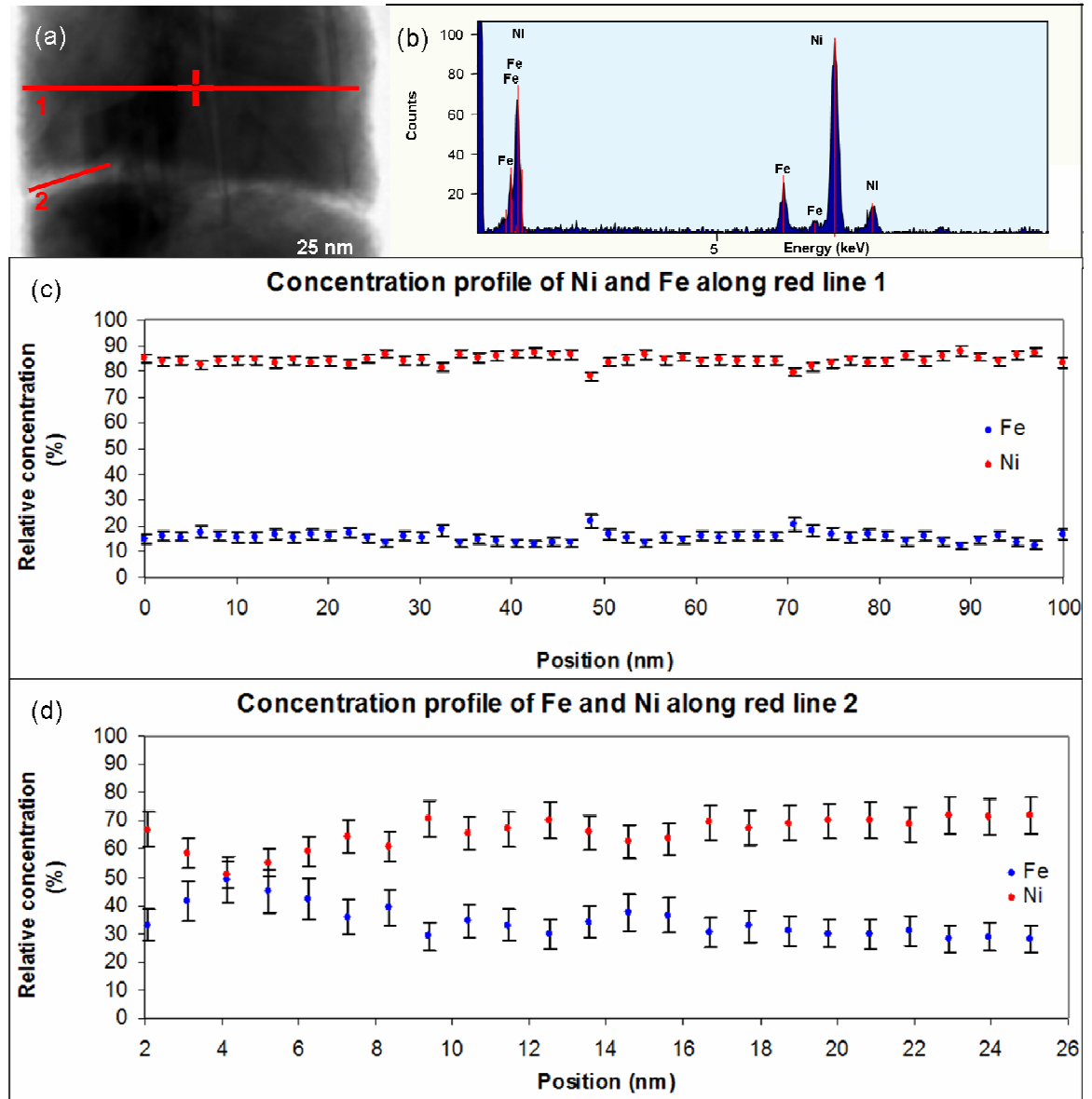


Figure 4.20: (a) STEM BF image of a nanowire alternating wide and narrow layers of sample NiFe(53nm)/Cu(9nm). The red line 1 is the line trace where the EDX spectrum in (b) was acquired at the cross and from where the concentration profile in (c) was obtained. The red line 2 is the line trace from where the concentration profile in (d) was obtained. (b) The EDX spectrum shows the K lines (on the right) and the L lines (on the left) of Ni and Fe. (c) Concentration profile of Ni and Fe along line trace1: Ni has an average concentration of 84 ± 2 %, whereas Fe has an average concentration of 16 ± 2 %. (d) Concentration profile of Ni and Fe along line trace2: the average concentration of Ni is 66 ± 6 %, whereas the average concentration of Fe is 34 ± 6 %.

4.4 Characterisation of magnetic properties of nanowires grown in polycarbonate templates

As mentioned in the introduction to this chapter, magnetic nanowires are currently the subject of much interest with potential applications as SST-based devices. To this purpose, it is extremely important to investigate the magnetic properties of nanowires in addition to morphology, structure and composition. As nanowires have strong shape anisotropy, normally the ground state will be for them to be uniformly magnetised along their length. However, during switching of the nanowires DW formation is expected to be an important part of the reversal mechanism and magnetic states which support DWs are of interest for applications.

As far as electrodeposited nanowires are concerned, previous studies [15] performed by other groups on uniform Ni nanowires with a diameter $d < 100$ nm deduced, from SQUID measurements and simulations, that magnetization reversal proceeded by a distortion of the magnetisation followed by a nucleation and propagation process of a vortex wall along the wire. Furthermore, as mentioned in section 1.5, micromagnetic simulations performed by Prof. Luis Lopez Diaz at University of Salamanca (Spain), predicted the formation of vortex states (the results will be briefly described in section 4.4.3).

In this current section we will describe the investigation of the magnetic states of electrodeposited nanowires by Lorentz microscopy. We used nanowires grown in polycarbonate template from sample NiFe(53nm)/Cu(9nm). First of all the results from Fresnel images simulations (section 4.4.1) and experimental Fresnel images (section 4.4.2) will be presented. Then a brief description of micromagnetic simulations performed at University of Salamanca, will be provided (section 4.4.3). They were used to carry out DPC image simulations, described in section 4.4.4. Results from DPC imaging experiments will be shown in section 4.4.5 and a discussion of all these findings will be found in section 4.4.6.

4.4.1 Fresnel Images Simulations

The first mode to be used in the Lorentz microscopy investigations of the magnetic materials is Fresnel imaging since it is operationally straightforward and can provide good overall information related to domain and domain wall structure in a wide range of

experimental situations (with or without an external applied field, for example, or while current pulses are injected).

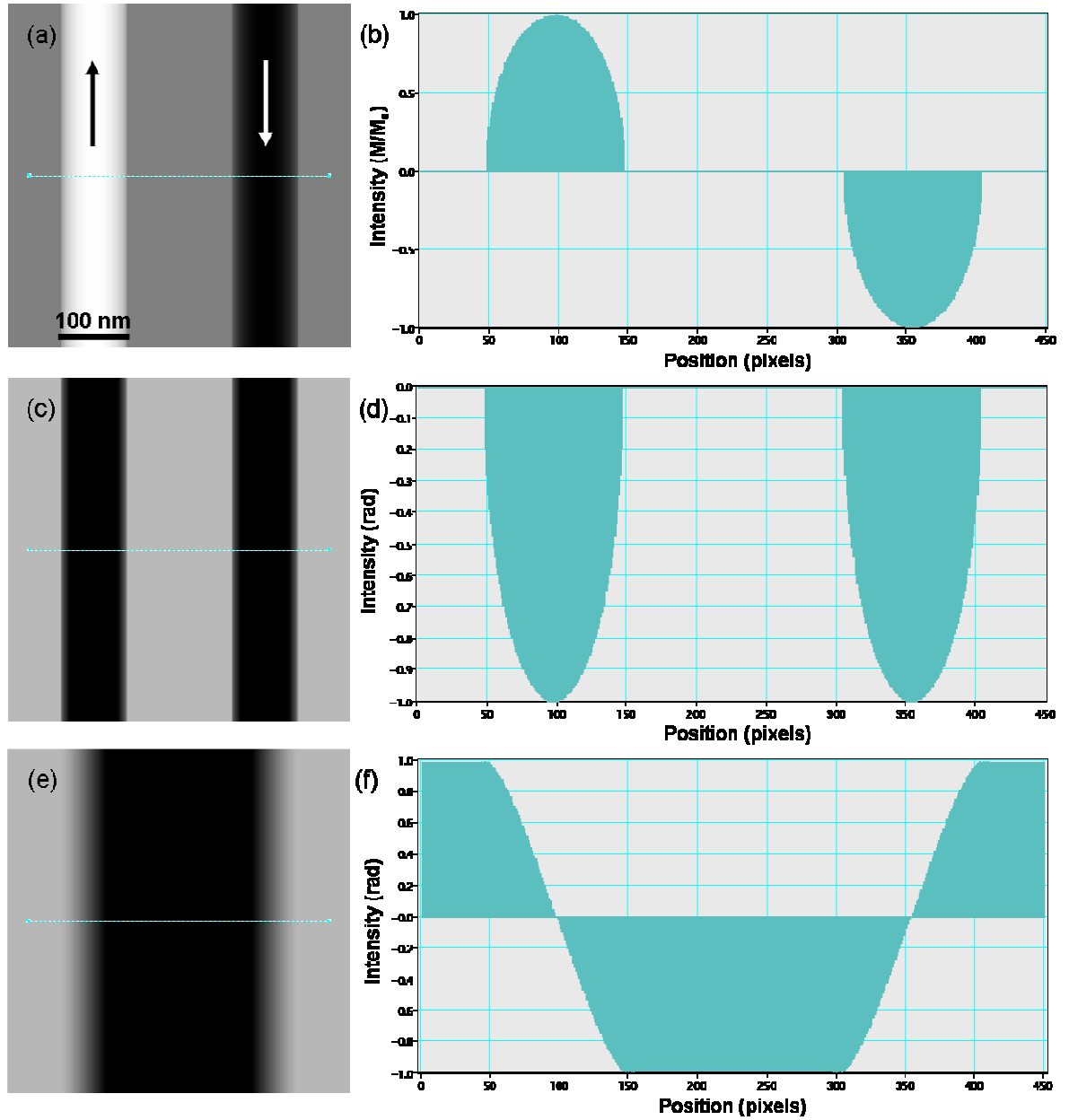


Figure 4.21: (a) Schematic of a couple of 100 nm Py nanowires oppositely magnetised. The arrows represent the magnetisation direction. (b) Intensity profile that shows the circular cross section and that they are oppositely magnetised. (c) Electrostatic phase and (d) its phase profile. (e) Magnetic phase and (f) its phase profile.

In order to establish the experimental conditions and to get an idea of contrast levels due to magnetic and electrostatic contributions, image simulations have been performed. Firstly the contrast from two perfectly cylindrical $\text{Ni}_{80}\text{Fe}_{20}$ nanowires, with a diameter of 100 nm, with their magnetisation oriented along the axis of the cylinder and pointing in opposite

directions has been considered. In fig.4.21(a) an image of the simulated nanowires and (b) their profile, (c) the electrostatic and (e) magnetic phase and their profile (respectively (d) and (f)) is provided. They were calculated by mean of the equations shown in section 2.5 and with the aid of Digital Micrograph™ scripts developed by the Solid State Physics group at the University of Glasgow.

Fresnel image calculations were carried out for a range of defocus values up to $\pm 480 \mu\text{m}$ including both magnetic and electrostatic phase contributions in order to evaluate the contrast levels due to each phase contribution and to select appropriately the defocus value to be used in experiments. The difficulty associated with the presence of the electrostatic phase contribution can be illustrated with these simulations as we can separate out these two phase contributions. We measured the electrostatic and magnetic contributions at the edge for increasing defocus. The results of the measurements are summarised in table 4.2. We can see that value the magnetic contribution increases, but also the electrostatic contribution increases. Thus we need to find out a suitable value of defocus that gives a reasonable balance between electrostatic contribution and magnetostatic contribution and that gives more chances to see variations of contrast produced by a change in magnetic induction in the real images. We decided to use $\pm 120 \mu\text{m}$ defocus that gives around 4% for the magnetic contrast and as electrostatic phase contrast ~35%. The outcomes of the simulations obtained with this value of defocus are shown in fig.4.22.

Defocus value (μm)	Electrostatic contribution at the edge (%)	Magnetic contribution at the edge (%)
-10 μm	~22%	~0.5%
-40 μm	~27%	~1%
-80 μm	~30%	~2%
-120 μm	~35%	~4%
-240 μm	~47%	~8%
-480 μm	~56%	~10%

Table 4.2: Variation of the electrostatic and magnetic contrast levels for increasing values of defocus.

Fig. 4.22(a, b) show (a) the contrast in the image and (b) intensity line trace respectively, associated with two nanowires in which the magnetisation is set to zero i.e. only the

electrostatic phase (from fig 4.21(c,d)) is included and at a defocus value of $-120\ \mu\text{m}$. It can be seen that the bi-polar edge contrast at opposite edges is highly symmetric.

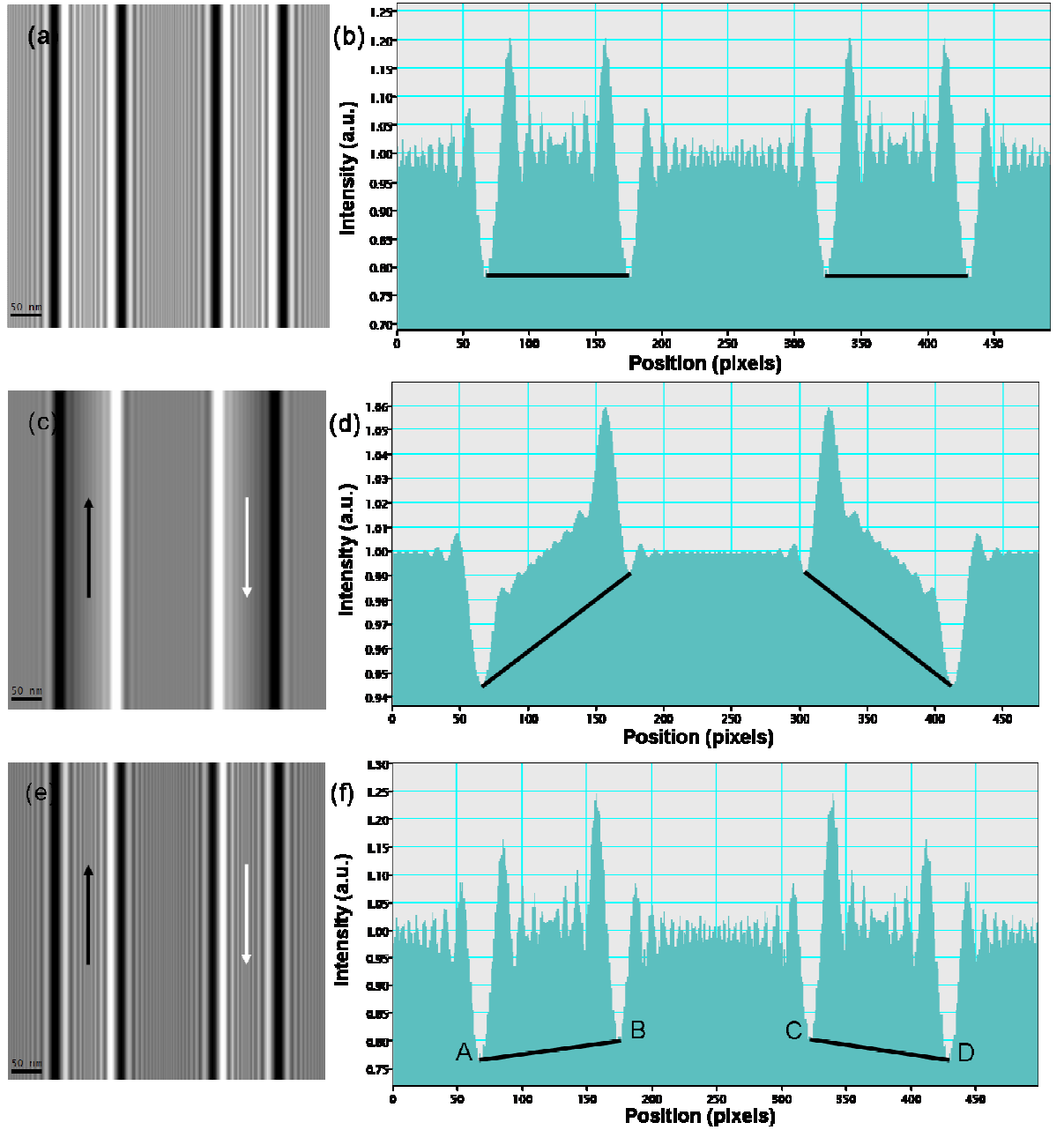


Figure 4.22: Simulated Fresnel images on the left column (a, c, e) and their intensity profiles on the right column of two nanowires (b, d, f) for a defocus value of $-120\ \mu\text{m}$, where (a) and (b) include only electrostatic contribution, (c) and (d) include only the magnetic contribution, and (e) and (f) have both magnetic and electrostatic contributions. The vertical scale in (b) is ten times higher than the vertical scale in (d) and this indicates that the in the case of the magnetic phase contribution, the signal is a factor of 10 times weaker.

Fig.4.22(c, d) represent the simulated Fresnel image (c) and the corresponding intensity profile (d) achieved including only the magnetic phase (from fig.4.21(e, f)). Of particular

note is the clear difference in level of the edge contrast, noting that in the case of uniform magnetisation the magnetic contrast is present at the edges. One should note the vertical scale in this line trace compared to that for the electrostatic phase, in the case of the magnetic phase the signal is a factor of ten times weaker. The magnetic contribution can be seen by the different levels of the two sides, showing a relative slope difference due to the different direction of magnetisation in each wire (indicated by the black lines on the figure). There is also contrast in the middle of the wire. However there we expect with amplitude contrast this would be very difficult to see in practise. Fig.4.22(e, f) represent (e) the simulated Fresnel image and (f) corresponding intensity profile achieved including electrostatic and magnetic phase. We can still see the magnetic contribution by the different levels of the two sides, AB and CD, showing a relative slope difference due to the different direction of magnetisation in each wire (indicated by the black lines on the figure). We should note, however, that this effect is small and the simulation is noise free. In a real situation we have to deal with other contrast mechanisms. As said before, the difference observed in the two edges due to the magnetic contrast is $\sim 4\%$ of the background signal whereas the electrostatic phase contrast level is around 35% at the edge. The relatively small contrast variation due to the magnetic induction is an indication of the difficulty in identifying this feature in a real image. Furthermore the simulation assumes that no diffraction contrast is present in these images, or noise from gun and/or detector.

4.4.2 Experimental Fresnel Imaging

In-focus images of the wires, shown in fig.4.15 and 4.17 in the previous section, indicate further some of the challenging issues in imaging the magnetic structure of these wires.

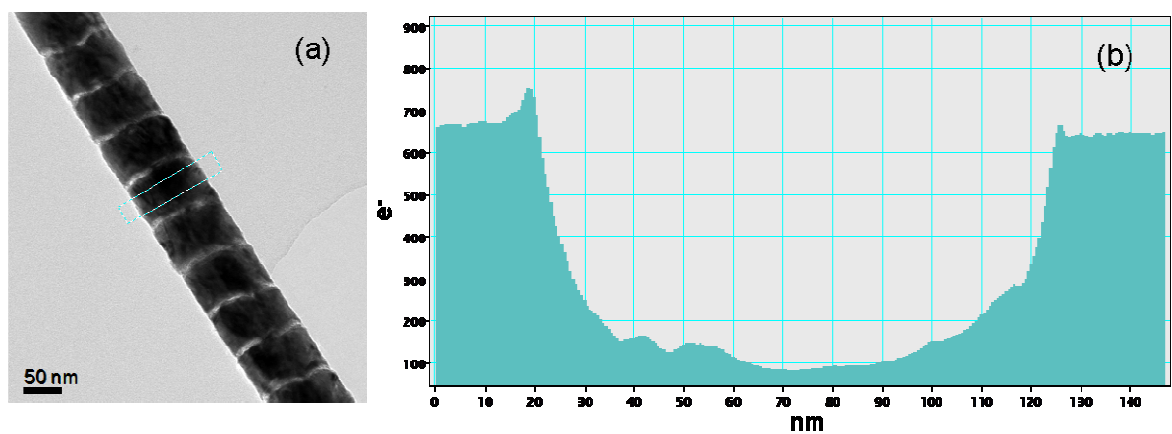


Figure 4.23: (a) In-focus image of a nanowire alternating thin and thick layers and (b) its intensity profile. The nanowire looks well defined, however the edges presents non uniformities. This is

particularly evident in the profile (b) where, at the edges, we can see peaks at different intensity, but also the internal part of the nanowires has irregularities.

In our simulations we took into account only the phase effects. However, we need to recognise that in experimental Fresnel images there is also amplitude contrast. Fig.4.23(a) shows strong diffraction contrast and a layer structure that was not present in our simulations. The nanowire looks reasonably well defined, but if we look at an intensity profile across an in-focus image of the nanowire, as the one shown in fig.4.23(b), we can see asymmetry at the edges (higher peak on the left, lower peak on the right) that is a topographic effect and the asymmetry, for the line trace considered, is 12% of background. Thus, topographic effects would be significant for phase imaging.

In fig.4.24 Fresnel images of a nanowire belonging to sample with repeat structure NiFe(53nm)/Cu(9nm) are shown. They were acquired with the TEM Philips CM20. Fig. 4.24 (a, b, c, d) represent images and the relative intensity profile of the same nanowire in two different magnetic states when a defocus of $-120\text{ }\mu\text{m}$ is used. We call magnetic state 1 the one with magnetisation pointing upwards, and magnetic state 2 the one with magnetisation pointing downward. The wire was magnetized along its length with fields of $\pm 0.7\text{ T}$ to change the magnetic state. Fig.4.24(a, b) refer to state 1 and fig.4.24(c, d) to state 2 which should be oppositely magnetised. It is clear that the electrostatic phase contribution is very strong as expected in the images and the intensity line traces. However, the asymmetry appears to be the same in each case. Furthermore from the in-focus image and line trace (fig.4.24(e, f)) of the same nanowire in the same position, it is apparent that there is a degree of asymmetry present here suggesting that the real nanowire does not possess the perfect symmetry of the modelled one, as we saw already at the beginning of this section.

Any asymmetry in the circular cross-section of the nanowire will result in asymmetric electrostatic phase contrast at the edges thus making determination any magnetic phase contribution extremely difficult. Even though the asymmetric contrast makes observation of the magnetic contrast difficult attempts were made to subtract images in from different states but with the same defocus. In principle this should leave just the magnetic contrast. An example of image subtraction process is shown in fig.4.25. We magnetised the nanowire first in state 1, then in state 2, and finally in state 3 (which, in principle, should be the same as state 1) and we acquired each time Fresnel images at $-120\text{ }\mu\text{m}$ defocus. Based on the results of the simulations, if we subtract the Fresnel image of the nanowire in

magnetic state 1 and the Fresnel image of the nanowire in magnetic state 2, we would get, in principle, an image with only magnetic contrast with magnetisation pointing upwards, a black a white line at the edges and an uniform gray background inside and outside the nanowire. If we subtract the Fresnel image of the nanowire in magnetic state 2 and the Fresnel image of the nanowire in state 3 we would get, in principle, exactly the opposite. If we subtract the Fresnel image of the nanowire in magnetic state 1 and the Fresnel image of the nanowire in state 3 we would get, in principle, no magnetic contribution.

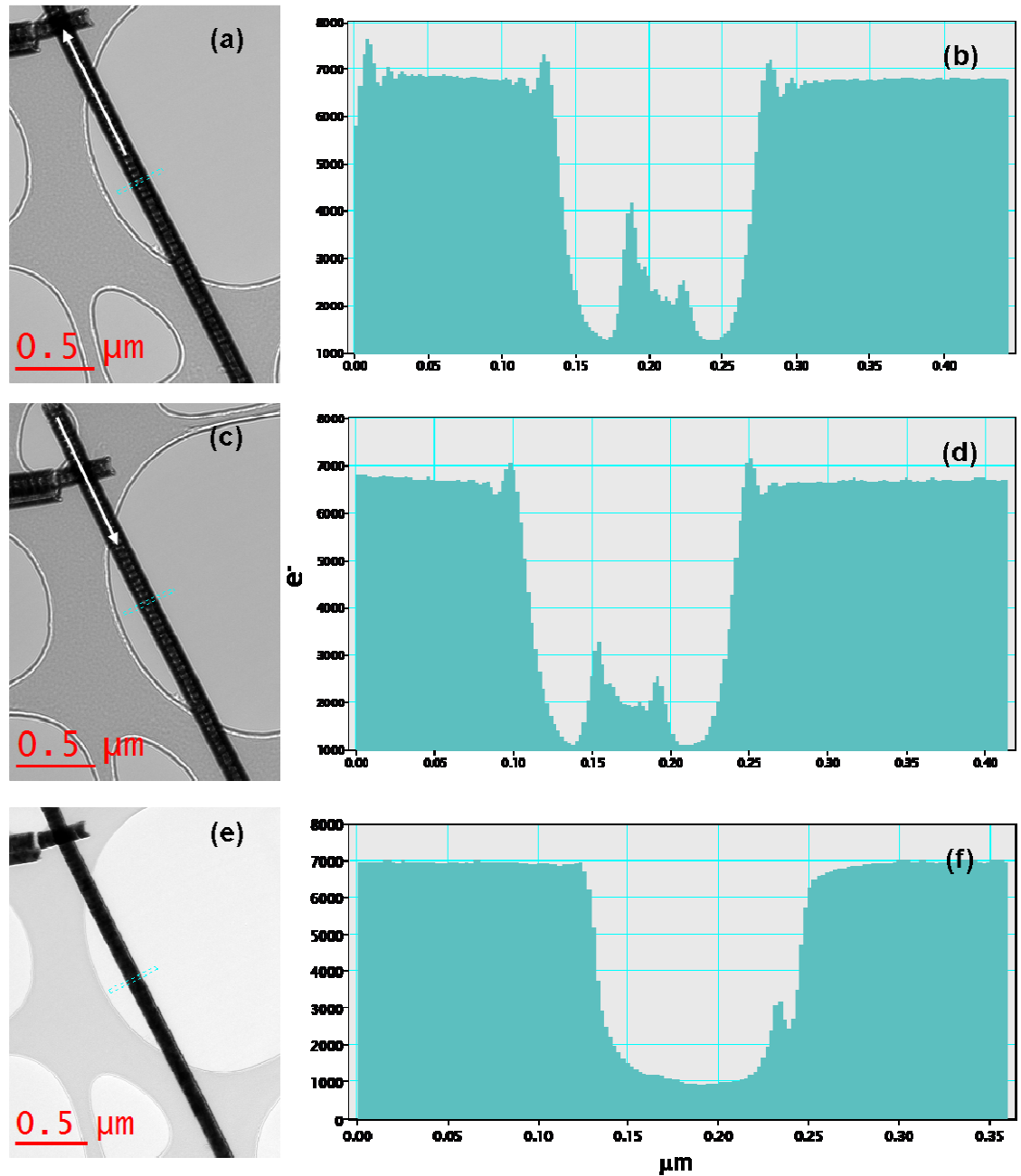


Figure 4.24: (a) Fresnel image of a nanowire with magnetisation pointing upwards (magnetic state 1) and -120 μm defocus, (c) with magnetisation pointing downwards (magnetic state 2) and -120 μm defocus, (e) in-focused nanowire, and the respective intensity profiles (b), (d) and (f).

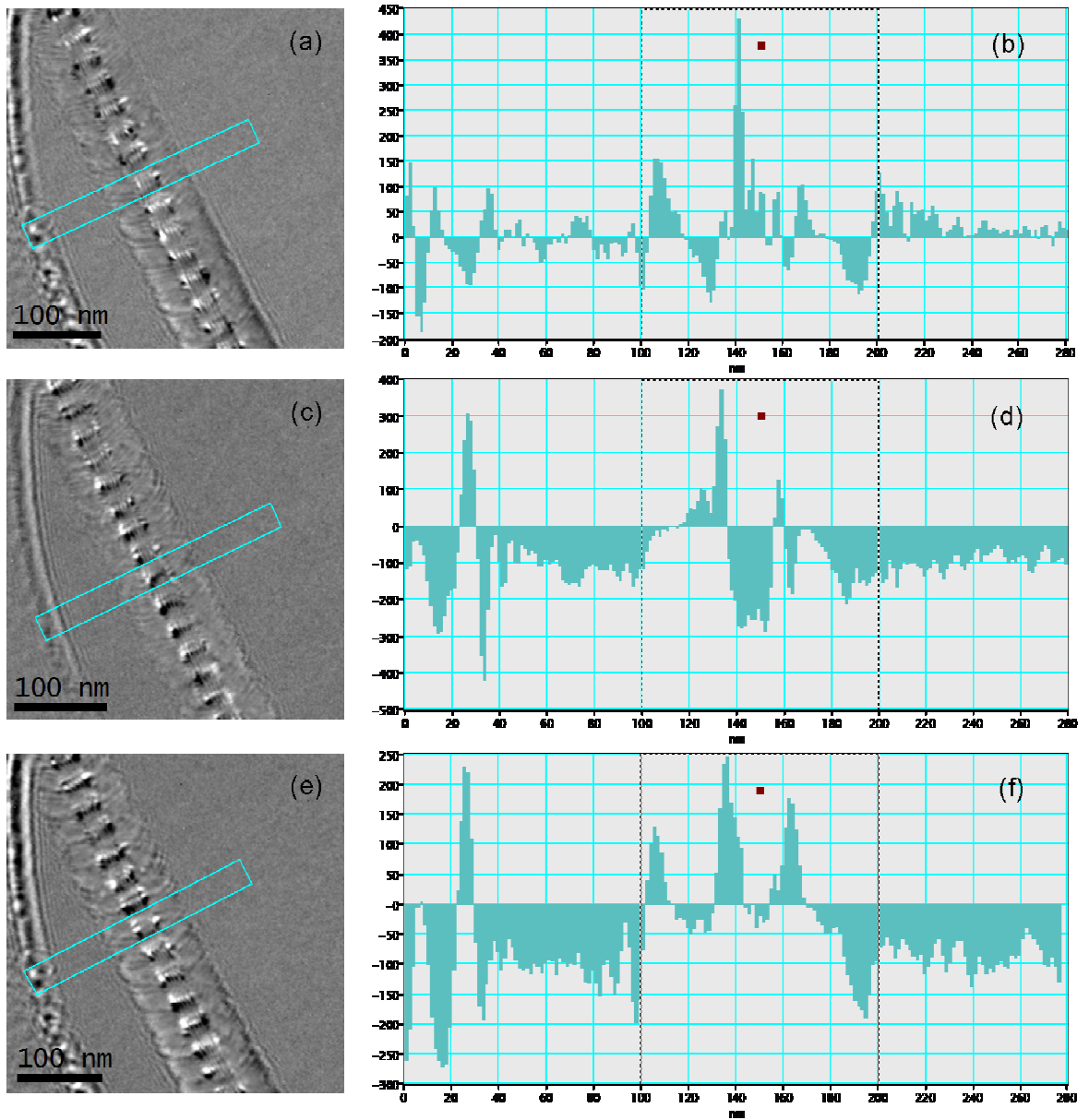


Figure 4.25: (a) Fresnel image and (b) the intensity profile obtained after subtraction of the Fresnel image of the nanowire in magnetic state 1 and the Fresnel image of the nanowire in magnetic state 2 acquired at $-120\ \mu\text{m}$ defocus. (c) Fresnel image and (d) the intensity profile obtained after subtraction of the Fresnel image of the nanowire in magnetic state 2 and the Fresnel image of the nanowire back in magnetic state 3 acquired at $-120\ \mu\text{m}$ defocus. (e) Fresnel image and (f) the intensity profile obtained after subtraction of the Fresnel image of the nanowire in magnetic state 1 and the Fresnel image of the nanowire in magnetic state 3 acquired at $-120\ \mu\text{m}$ defocus. The dashed vertical lines in (b, d, f) mark the position of the edges.

Fig.4.25(a, b) shows the image and the intensity profile obtained after subtraction of the Fresnel image of the nanowire in magnetic state 1 and the Fresnel image of the nanowire in magnetic state 2, fig.4.25(c, d) show the image and the intensity profile obtained after subtraction of the Fresnel image of the nanowire in magnetic state 2 and the Fresnel image

of the nanowire back in magnetic state 3. Fig.4.25(e, f) show the image and the intensity profile obtained after subtraction of the Fresnel image of the nanowire in magnetic state 1 and the Fresnel image of the nanowire in magnetic state 3. The images possess no distinctive characteristics of what we would expect from the magnetic states. The profiles show a signal variation that bears no resemblance to expected magnetic effects, in fact they all appear rather similar. This would suggest that the contrast in the images is not of magnetic origin but perhaps arises from topographic effects, image misalignment and small differences in intensity of the images. Given the relatively small signal expected from magnetic effects from the simulations together with the inhomogeneities observed from the TEM and analytical studies this results is perhaps not unexpected. This experiment proved inconclusive and we can say that from experimental Fresnel images of the wires it was not possible to determine any magnetic contribution conclusively. The other possibility is that the magnetic state simulated may not be representative of the states supported by the wires, we explore this in the next section before attempting quantitative DPC imaging of the wires.

4.4.3 Micromagnetic Simulations

OOMMF micromagnetic simulations of the EA cycle were performed to start identifying the magnetic states supported by this material system. They were carried out by Prof. Luis Lopez Diaz at University of Salamanca (Spain). The structure simulated is composed of five repetitions of Py (60 nm) and Cu (10 nm) with a circular cross section. A schematic of this structure is reproduced in fig.4.26. The material parameters for Py are: saturation magnetisation $M_s = 860 \times 10^3 \text{ A/m}$; exchange constant $A = 13 \times 10^{-12} \text{ J/m}$; damping constant $\alpha = 0.5$. The cell size is $2.5 \times 2.5 \times 5 \text{ nm}$ which is a value close to the exchange parameter for Py.

Micromagnetic simulations were used to obtain the magnetisation configurations required to perform DPC image simulations. They were not used for Fresnel image simulations because OOMMF would have provided the same information as for a uniform cross section. Indeed the problem for Fresnel imaging is related to the edges, and with OOMMF we simulate a structure with regular edges, analogous to what we did previously. We chose, at first instance, three configurations: the initial state at $H = 0.2 \text{ T}$, the remanent state at $H = 0 \text{ T}$ and the final state at $H = -1 \text{ T}$.

They are shown in fig. 4.27 where (a, c, e) represent the central slice of the nanowire with the arrows being the orientation of magnetisation with respect to the z, whereas (b, d, f) represent the top view of the first Py layer of the nanowire. In the first and second saturated states (fig.4.27(a, b, e, f)) the nanowire is uniformly magnetised, and the magnetisation follows the direction of the applied field (along $\pm z$ axis).

The reversal will proceed through the formation of vortex states as shown in fig.4.27(c, d), which represent the nanowire in the remanent configuration. Vortices form in each Py layer and they have the same polarity (up), but they do not have the same chirality. In the first two layers the chirality is counter clockwise, whereas in the last three layers the chirality is clockwise.

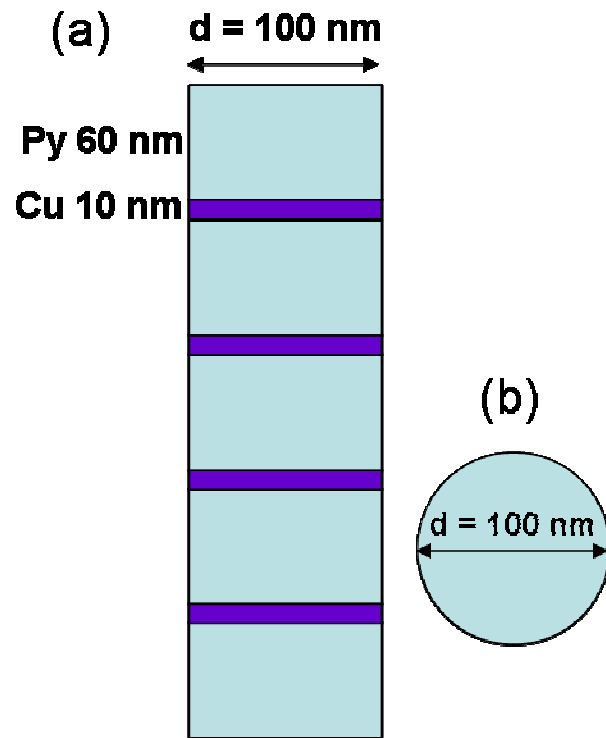


Figure 4.26: Schematic of the simulated structure: (a) vertical section, (b) cross section.

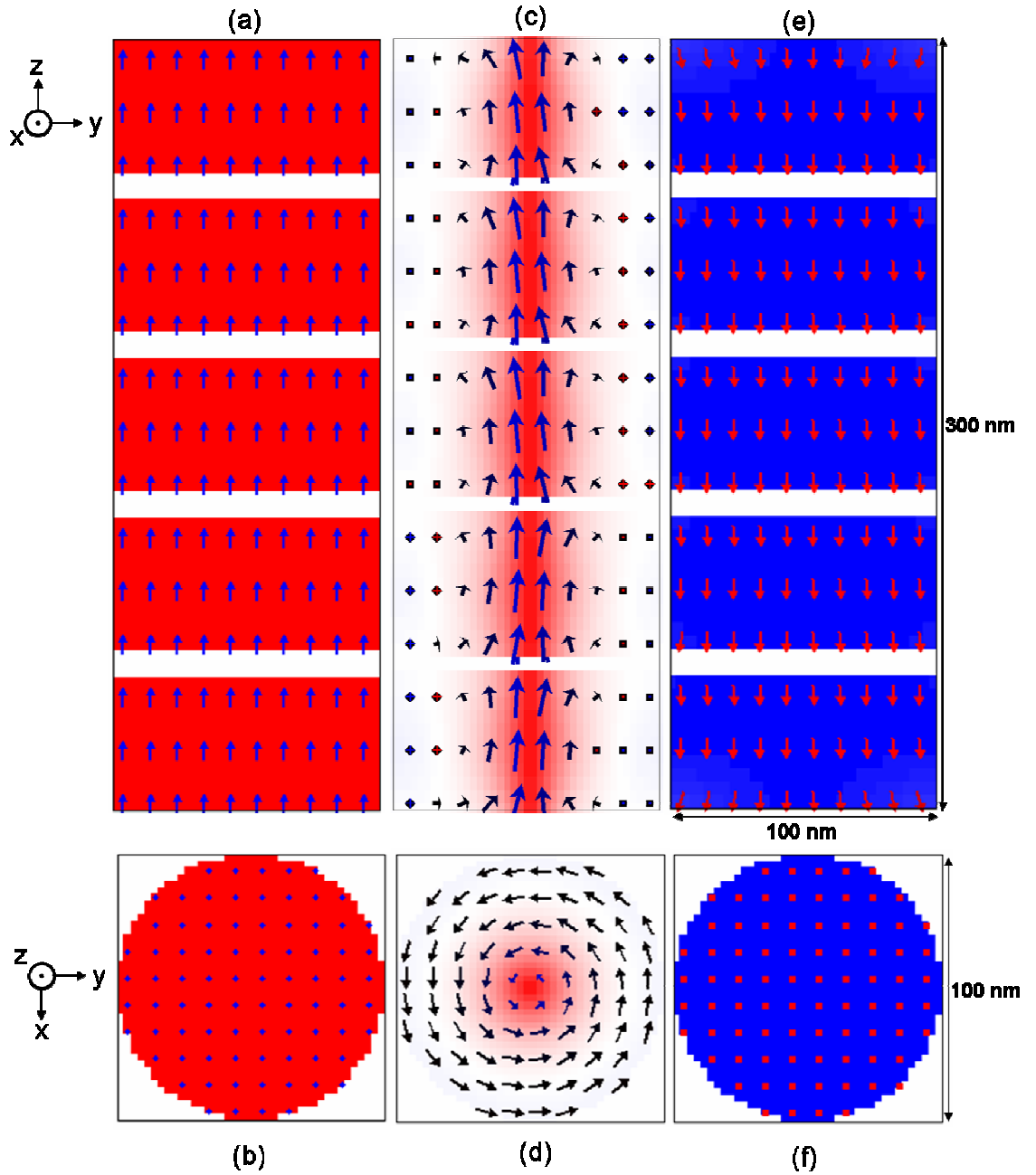


Figure 4.27: OOMMF simulations of configurations used to get an idea of DPC sensitivity. (a) Vertical and (b) cross section at the initial state (0.2 T); (c) vertical and (d) cross section at the remanent state; (e) vertical and (f) cross section at the final state (-1 T).

4.4.4 DPC Images Simulations

As the topography looks to be a limiting factor with the Fresnel imaging, DPC offers the prospect of imaging the projected stray field outside of the wire in free space to possibly determine their magnetic state. In order to establish the experimental conditions and for the possible identification of wall type and extent of contrast expected, simulations of the stray field distribution have been performed. The images were simulated with the They were

with the aid of Digital Micrograph™ scripts developed by the Solid State Physics group at the University of Glasgow. We simulated four different states: uniform continuous nanowire magnetised upwards or downwards (fig.4.28); uniform layered nanowire magnetised upwards or downwards (fig.4.29); uniform continuous nanowire with an abrupt head to head domain wall in the middle (fig.4.30) and a layered nanowire in the remanent state (fig.4.31). First of all, simulations of a uniform nanowire, uniformly magnetised along the length has been considered. The outcome of the simulation is shown in fig. 4.28 where in (a) and (d) the magnetisation is reproduced for the nanowire simulated, in (b) and (e) the map of the perpendicular component of the integrated magnetic induction and in (c) and (f) the parallel component of the integrated magnetic induction. Then, simulations of a multilayered nanowire, uniformly magnetised along the length have been carried out. Magnetisation configurations used here are the ones calculated by micromagnetic simulations (initial state at 0.2 T and final state at -1T) and displayed in fig.4.27 (a, b, e, f). The outcomes of the simulations are shown in fig. 4.29 where in (a) and (d) is reproduced the nanowire simulated, in (b) and (e) the map of the perpendicular component of the integrated magnetic induction and in (c) and (f) the parallel component of the integrated magnetic induction.

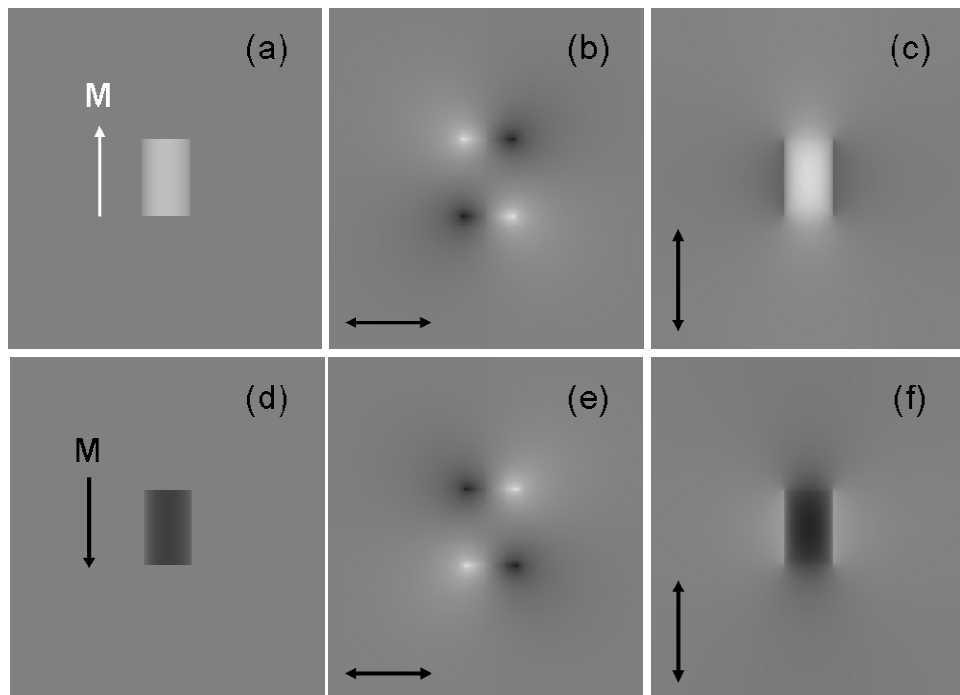


Figure 4.28: Simulated DPC images of a uniform nanowire magnetised along the length (a) upwards and (d) downwards. (b) and (e) represent the maps of the perpendicular component of the integrated magnetic induction, whereas (c) and (f) the parallel component of the integrated magnetic induction.

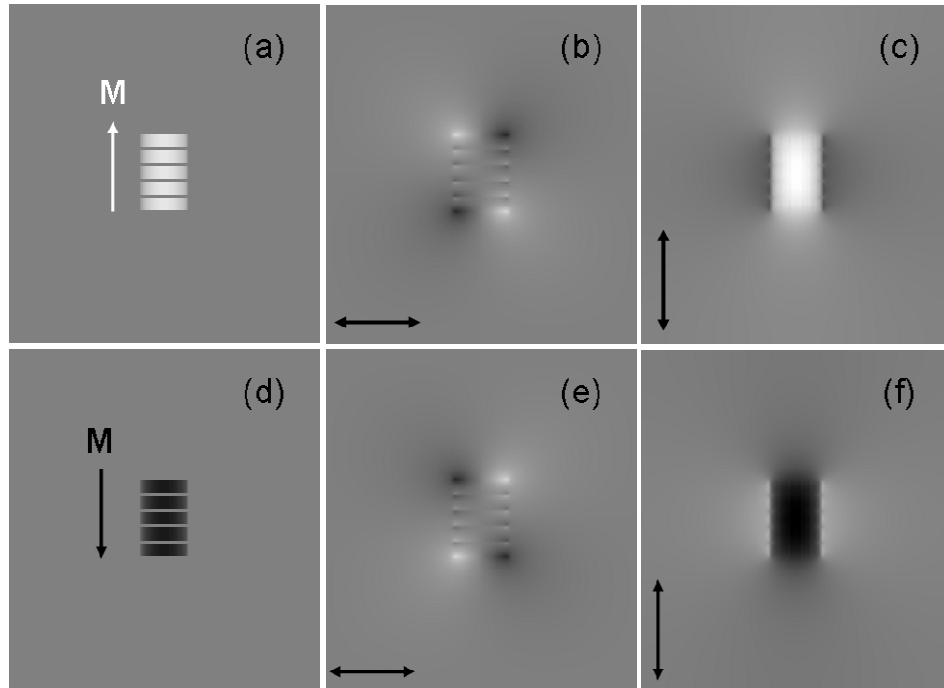


Figure 4.29: Simulated DPC images of a multilayered nanowire uniformly magnetised along the length (a) upwards and (d) downwards. (b) and (e) represent the maps of the perpendicular component of the integrated magnetic induction, whereas (c) and (f) the parallel component of the integrated magnetic induction.

In order to understand what a domain wall in a nanowire would look like, we performed the simulation of a uniform nanowire with an abrupt head to head domain wall (fig.4.30(a)). The maps of the perpendicular and parallel component of the magnetic induction are shown in fig.4.30(b, c). Finally the simulations of the multilayered nanowire in the remanent state have been carried out (fig.4.31). Here vortices with the same polarity but different chirality formed as seen in section 4.4.3. The maps of the perpendicular and parallel component of the magnetic induction are shown in fig.4.31(b, c).

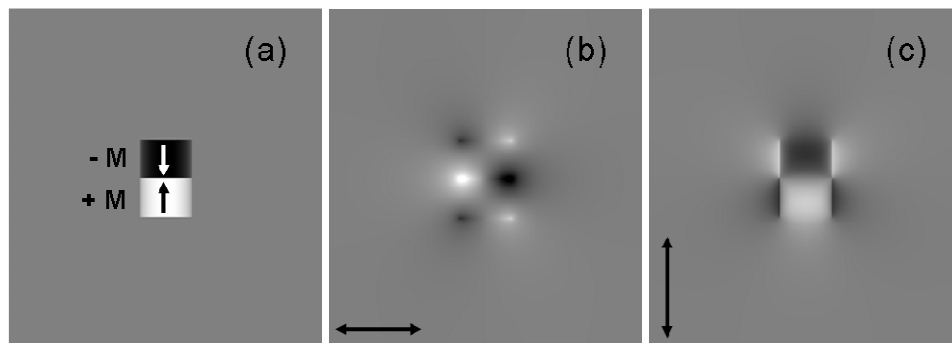


Figure 4.30: (a) Simulated DPC images of a multilayered uniform nanowire with an abrupt head to head domain wall. (b) represents the maps of the perpendicular component of the integrated magnetic induction, whereas (c) the parallel component of the integrated magnetic induction.

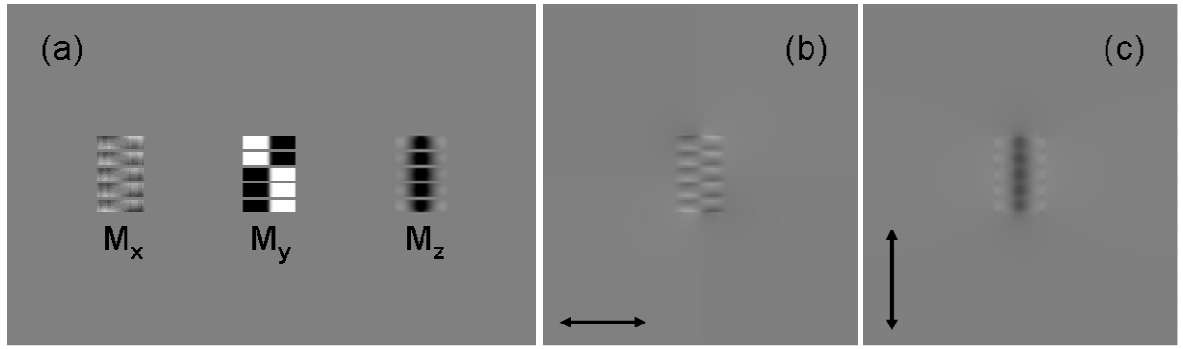


Figure 4.31: (a) Simulated images of the x, y and z component of magnetisation of a multilayered nanowire in the remanent state with vortex states in each Py layer. (b) represents the maps of the perpendicular component of the integrated magnetic induction, whereas (c) the parallel component of the integrated magnetic induction.

As we saw in section 4.4.3, real nanowires can be several microns long and simulations of such a length of wire it is not practical because it would require too long a computation time. Thus, as shown in fig.4.29 - 4.31 we simulated a segment of 300 nm of the total length, and to make a comparison between simulated and experimental images we will concentrate on the analysis of the flux emanating from the end of the nanowires. In particular we will make a comparison of the line traces perpendicular to the wire length in the maps of the longitudinal component of integrated magnetic induction. The comparison will be based on the measurements of the peak value of the integrated field relative to the maximum for the wire $B_{st,max}$ (100 T nm), and the full width at half maximum (FWHM) relative to the diameter of the nanowire (100 nm). In this section we will make a comparison between the four different simulated states.

Fig.4.32 shows simulated maps of the parallel component of magnetic induction of (a) a uniform continuous nanowire magnetised upwards or downwards, (c) a uniform layered nanowire magnetised upwards or downwards, (e) a uniform continuous nanowire with an abrupt head to head domain wall in the middle, (g) a layered nanowire in the remanent state and (b, d, f, h) the stray field profile from a line trace positioned 40 nm from the top-edge of the nanowire.

The profiles allowed the calculation of the peak value of the integrated field relative to the maximum for the wire $B_{st,max}$, and the full width at half maximum (FWHM) relative to the diameter of the nanowire. The results are summarised in table 4.3.

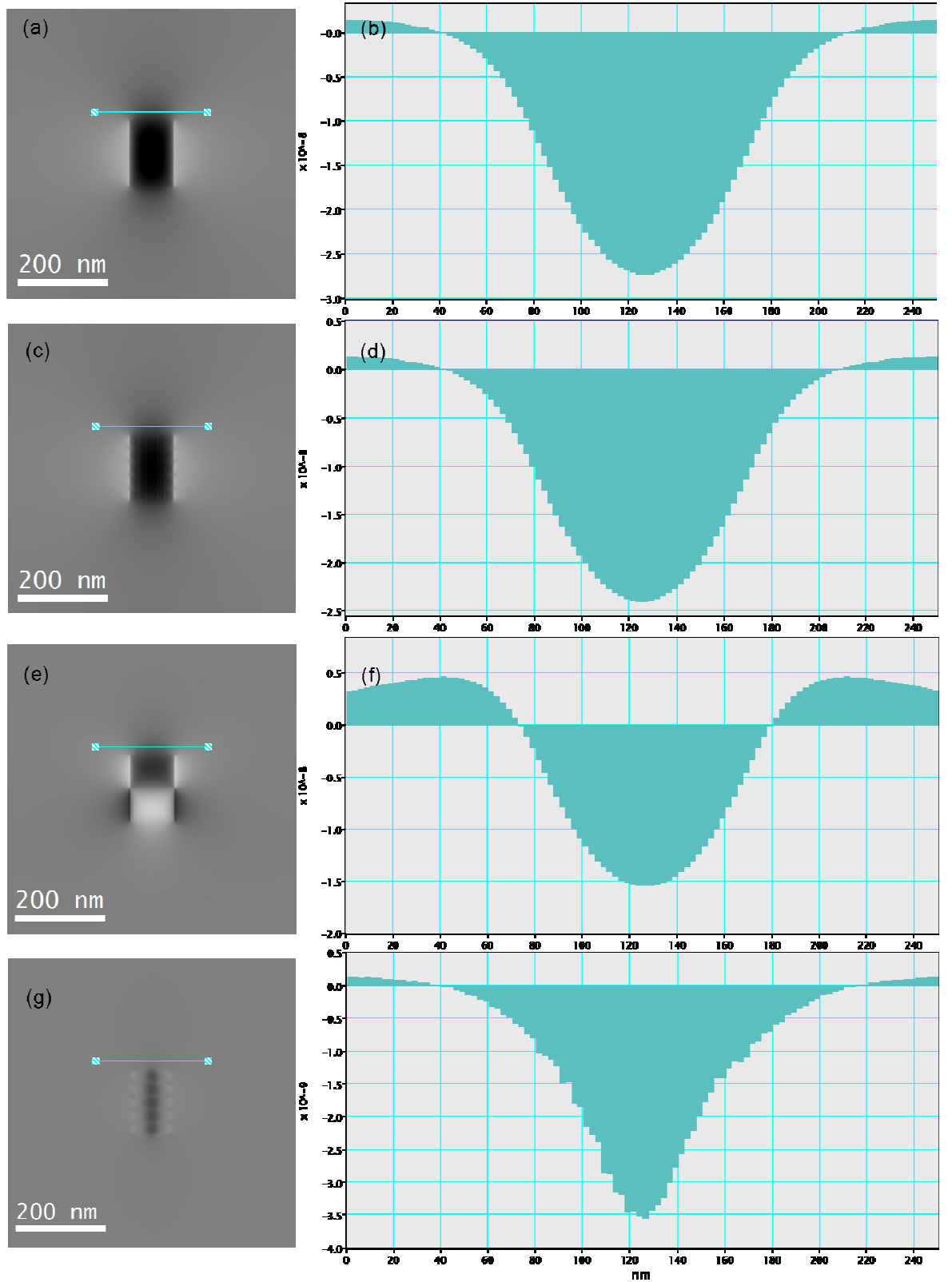


Figure 4.32: Simulated maps of the parallel component of integrated magnetic induction of (a) uniform nanowire magnetised downwards along the length, (c) multilayered nanowire uniformly magnetised downwards along the length, (e) uniform nanowire with an abrupt tail to tail domain wall, (g) nanowire in the remanent state with vortex states in each Py layer. (b, d, e, f) Relative stray field profile from a line trace 40 nm from the top-edge of the nanowire.

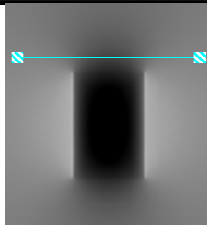
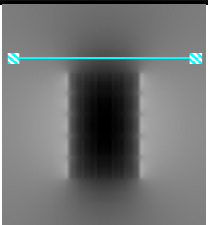
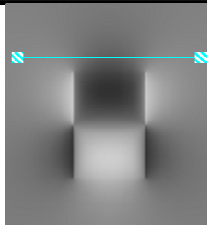
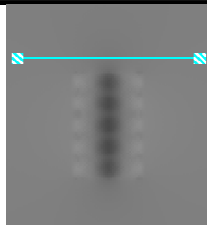
				
	Uniform continuous nanowire magnetised ↓	Uniform layered nanowire magnetised ↓	Nanowire with a head to head wall	Layered nanowire in the remanent state with vortices
$B_{st} / B_{st,max}$	0.272	0.239	0.154	0.035
FWHM / d	0.875	0.85	0.725	0.575

Table 4.3: Comparison between the measurements of the peak value of the integrated field relative to the maximum for the wire $B_{st,max}$ (100 T nm), and the full width at half maximum (FWHM) relative to the diameter of the nanowire (100 nm), for the nanowire states considered.

The table shows that the difference in the FWHM for a uniform continuous and a uniform layered nanowire is very small, thus in a real image where we need to take into account the presence of noise, distinguishing these two cases might be rather difficult. Therefore the line traces (Fig. 4.32 (b) and (d)) in these cases are really very similar other than a slightly smaller peak integrated field for the layered nanowire. Concerning the nanowire with an abrupt head to head wall, the FWHM is a little less than the one found for the uniform nanowire, but the peak value is almost half. Thus we could probably distinguish whether a domain wall is present if the wall is located close to the end of the wire. However for a long wire, with a wall far from the end, this is unlikely to be significantly different. If we look at the values for the nanowire in the remanent state with vortex states in each layer, we can notice that the peak value is around ten times smaller than the value found for the uniform continuous nanowire and the FWHM is almost half. Whilst this is very different from the other cases the small peak signal is likely to be a limiting factor when trying to image this experimentally.

4.4.5 DPC Imaging

DPC imaging was carried out with a TEM Philips CM20. The experiment relies on imaging in free space where the end of the nanowires suspended over a hole in the holey carbon film on which they were dispersed. This strategy was used to reduce any signal variation from a substrate which would be nonmagnetic, and to this purpose vacuum represents an ideal substrate. Initial experiments were carried out to image a nanowire in

oppositely magnetized states by imaging the stray field emanating from the end of the wire, this being the region where the magnetic induction signal is strongest outside the nanowire.

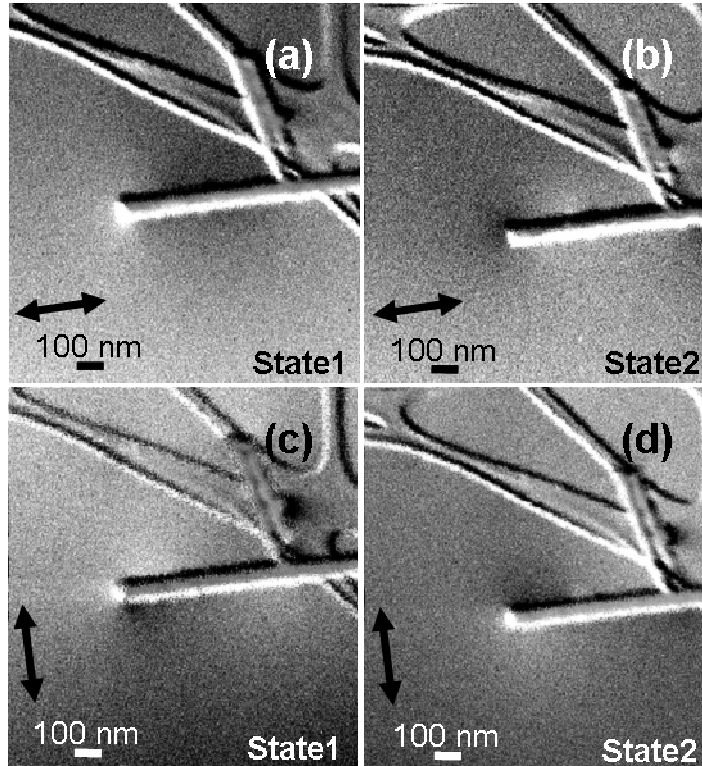


Figure 4.33: DPC images of a nanowire magnetised along the length under the application of an external field of ± 0.7 T. (a) and (b) represent the map of the component of the integrated magnetic induction parallel to the nanowire; (c) and (d) represent the component of the magnetic induction perpendicular to the nanowire.

The nanowire was magnetised along its length in different directions under application of ± 0.7 T external field. DPC images of the nanowire in two different magnetic states are shown in fig.4.33 where (a) and (b) represent the map of the component of the integrated magnetic induction parallel to the nanowire, whereas (c) and (d) represent the component of the magnetic induction perpendicular to the nanowire. These images show evidence of a change in the magnetic state of this single nanowire. Indeed we can see a reversal of the contrast when we change the magnetic state from (a, c) state 1 to (b, d) state 2. If we look at the top edge of the nanowire in the map of the parallel component of integrated magnetic induction and we take a sum of 10 line traces 30 nm from the top edge and parallel to it (fig.4.34), as was done for simulations in the previous section, we can see that the signal in intensity profile in (b) is inverted with respect to the signal in (d).

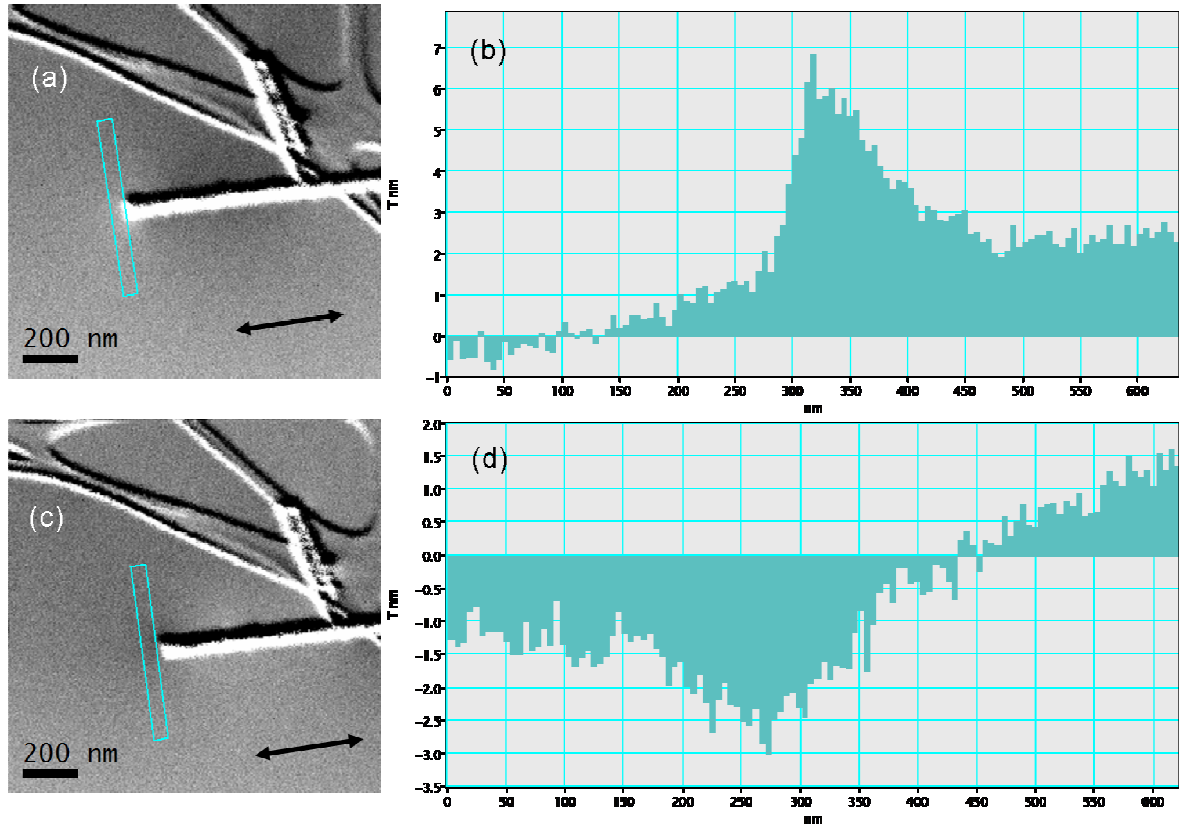


Figure 4.34: (a, c) Maps of the component of the integrated magnetic induction parallel to the nanowire; (b) and (d) are the intensity profiles of the sum of 10 line traces located 30 nm from the nanowire top edge.

The intensity profiles in (b) and (d) appear very noisy and this makes difficult an accurate quantification of the intensity of the peaks and the FWHM to compare with the values obtained from simulations. However, we can still try to give an estimate of the peak value of the integrated field relative to the maximum for the wire $B_{st,max}$ (100 T nm), and the full width at half maximum (FWHM) relative to the diameter of the nanowire (100 nm).

Fig.4.35 shows how the values were estimated, taking into account the background level. We found a value of 0.041 ± 0.014 for $B_{st}/B_{st,max}$ and 0.79 ± 0.34 for $FWHM/d$. Such a large error on the measurements is due to the high level of noise being present and background signal variation. We can make a comparison of the values of intensity and FWHM of the peaks measured from simulated and experimental images. These values are included in table 4.4.

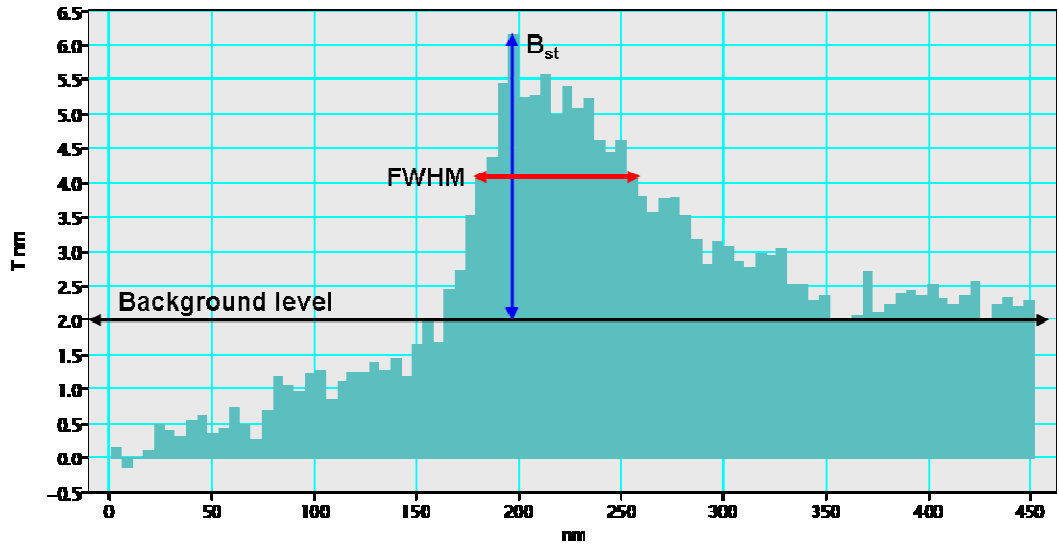


Figure 4.35: Intensity profiles of the sum of 10 line traces located 30 nm from the nanowire top edge for the nanowire shown in fig.4.33(a). The black arrow indicates the background level, the blue arrow the value of B_{st} from the background level and the red arrow indicates the FWHM relative to the peak measured from the background level.

	$B_{st} / B_{st,max}$	FWHM / d
Experimental nanowire	0.041 ± 0.014	0.79 ± 0.34
Uniform continuous nanowire magnetised ↓	0.272	0.875
Uniform layered nanowire magnetised ↓	0.239	0.85
Nanowire with a head to head wall	0.154	0.725
Layered nanowire in the remanent state with vortices	0.036	0.575

Table 4.4: Comparison between experimental and simulated $B_{st} / B_{st,max}$ and FWHM / d of the peaks measured from the experimental and simulated intensity profiles shown in fig.4.35.

Experimental $B_{st}/B_{st,max}$ is one order of magnitude weaker than the value found for the simulated uniform layered nanowire and appears comparable to the value found for a layered nanowire in the remanent state with vortices. However, due to the large error associated with this measurement, it would appear that the state is likely to be non uniform state though with a significant component of magnetisation along the length. Additionally we found that the experimental FWHM, although the error here is quite large, is more consistent with the values for the uniformly magnetised states. In the comparison between experimental and simulated data we need to remember that real nanowires have an irregular topography, as shown in fig.4.23, whereas simulated nanowires have a perfect geometry. The structural and compositional investigation found significant differences

between the experimental nanowires and the nominal structure and composition used in the simulations. Thus these factors, in addition to the presence of a noise in the experimental images, suggest that the two systems may be quite different and the assumptions about the structure may well be misguided. It is clear further work is necessary though the techniques of TEM can prove extremely useful in analysing this system.

4.5 Summary

The present chapter described the characterisation by electron microscopy of morphology, physical structure, composition and magnetic configuration of $\text{Ni}_{80}\text{Fe}_{20}(\text{Py})/\text{Cu}$ nanowires grown by electrodeposition in anodic alumina and polycarbonate templates. These studies are of great importance in view of applications of nanowires as spin transfer torque based devices. First of all the characterisation of nanowires grown in anodic alumina templates was described (section 4.2). The nanowires have a polycrystalline structure with a large grain size distribution and irregular topography. Nanowires alternating thick and thin layers with transparent thin layers and nanowires with homogeneous contrast in BF images were found in the same population. As concerned the composition, nanowires with homogeneous contrast appear to be uniform NiFe nanowires because we could not detect any Cu. The investigation of nanowires alternating thick and thin layers by EDX has shown that in the non-transparent region there is no Cu, and Ni and Fe are not in the correct proportions compared to the intended deposited Py (we found a $(5.9 \pm 0.9) : 1$ ratio, instead of a $4 : 1$ ratio). The transparent region is an area with a lower density of material where we can find Ni and Fe in different proportion. We could detect Cu, whose K lines are very noisy, very close to the background level and to the Ni K_{β} peak. The results of the compositional investigation, shed light on possible issues related to the deposition of the different chemical elements and the removal of the template by chemical etching.

In order to minimise the problems found in the previous section, a new set of nanowires was grown in a polycarbonate template. The structural and compositional characterisation was described in section 4.3. Nanowires grew polycrystalline, with a large grain size distribution, and their topography was more regular than the nanowires previously described. From the compositional point of view we found that in nanowires with homogeneous contrast Ni and Fe are in $(6 \pm 1) : 1$ ratio instead of the $4 : 1$ ratio of Py and we could not detect any Cu; in nanowires showing apparent alternating thick and thin layers, Ni and Fe are in a $(4.8 \pm 0.7) : 1$ ratio, close to what expected in Py in the thick

layers, whereas in thin layers we could not detect any Cu and Ni and Fe are in different concentrations along the line trace. These findings, similar to that observed in nanowires grown in alumina templates, would suggest that there may be a serious issue with the deposition of the Cu., Alternatively the lack of Cu may be due to the chemical used to perform the dissolution of the template, although this appears rather unlikely. In any case the structural integrity of the nanowires did not resemble the intended deposited structure.

Section 4.4 was dedicated to the description of the characterisation of the magnetic properties of nanowires grown in polycarbonate template by Lorentz microscopy. The first mode to be used in the Lorentz microscopy investigations of magnetic materials is Fresnel imaging. In order to establish the experimental conditions and to get an idea of contrast levels due to magnetic and electrostatic contributions, Fresnel image simulations have been performed (section 4.4.1) to get an idea of the nature of the contrast expected for uniformly magnetised nanowires. From the experimental point of view (section 4.4.2), it was not possible to determine any magnetic contribution conclusively, almost certainly due to small changes in intensity, alignment and issues with normalisation of the signal which occurs between images and the low level of the magnetic contrast. Micromagnetic simulations (section 4.4.3) predict the reversal of magnetisation during EA cycle through formation of vortex states. Magnetisation configuration of the initial state, remanent state and final state were used to carry out simulations of DPC images. Calculations of stray field distributions were performed (section 4.4.4) for different configurations: uniform continuous nanowire magnetised upwards or downwards, uniform layered nanowire magnetised upwards or downwards, uniform continuous nanowire with an abrupt head to head domain wall and a layered nanowire in the remanent state. In reality the nanowires can be many microns long and the simulations of such lengths it is not practical because it would require too long computation time. To make a comparison between simulated and experimental images we concentrated on the analysis of the flux emanating from the end of the nanowires. We made a comparison of the line traces perpendicular to the wire length in the maps of the longitudinal component of integrated magnetic induction. The comparison was based on the measurements of the peak value of the integrated field relative to the maximum for the wire $B_{st,max}$, and the full width at half maximum (FWHM) relative to the diameter of the nanowire. Based on these measurements, the small difference found for a uniform continuous and a uniform layered nanowire we can say that we might not be able to distinguish whether the nanowire is continuous or layered. Concerning the nanowire with an abrupt head to head wall, it may be possible distinguish whether a domain wall is

present compared to a nanowire with no wall, however this would be unlikely for a very long wire. If we look at the values for the nanowire in the remanent state with vortex states in each layer, we can notice that the peak value is ten times smaller than the value found for the uniform continuous nanowire and the FWHM is almost half, thus it would then provide a challenge to image the nanowire in this state.

During DPC imaging experiments (section 4.4.5) it was possible to observe a change in magnetic state of the nanowire, confirmed by a change in sign from negative to positive in the intensity of the stray field peak. We found only a qualitative agreement with different simulated states performed in the previous section. However no one simulation gave an agreement with the albeit noisy experimental images. This may have been due to a number of factors, for example irregularities in the topography of real nanowires compared to the perfect geometry of simulated nanowires; also differences in composition and structure between the observed nanowires and those simulated.

These are initial results from one of the first attempts at Lorentz TEM imaging of such nanowires. The awareness of the limitations of these experiments and the results of the simulations and calculations will point the way forward for a future study with nanowires with the desired properties.

In the next chapter the behaviour in temperature of magnetic multilayers with perpendicular anisotropy to be employed as SST-TA MRAMs will be described.

Bibliography

- [1] Slonczewski J.C., *J. Magn. Magn. Mater.*, (1996), **159**, L1.
- [2] Berger L., *Phys. Rev. B*, (1996), **54**, 9353.
- [3] Stiles M.D. and Miltat J., *Spin Dynamics in Confined Magnetic Structures, III*, edited by B. Hillebrands and A. Thiaville, Springer, Berlin, (2006).
- [4] Katine J.A. *et al.*, *Phys. Rev. Lett.*, (2000), **84**, 3149.
- [5] Grollier J. *et al.*, *Appl. Phys. Lett.*, (2001), **78**, 3663.
- [6] Kaka S. *et al.*, *Nature*, (2005), **437**, 389.
- [7] Mancoff F.B. *et al.*, *Nature*, (2005), **437**, 393.
- [8] Fert A. and Piraux L., *J. Magn. Magn. Mater.*, (1999), **200**, 338.
- [9] Valet T. and Fert A., *Phys. Rev. B*, (1993), **48**, 7099.
- [10] Wegrowe J.E. *et al.*, *Appl. Phys. Lett.*, (2002), **80**, 3775.
- [11] Pufall M.R. *et al.*, *Phys. Rev. Lett.*, (2006), **97**, 087206.
- [12] Grollier J. *et al.*, *Phys. Rev. B*, (2006). **73**, 060409(R).
- [13] Blon T. *et al.*, *J. Appl. Phys.*, (2007), **102**, 103906.
- [14] Piraux L. *et al.*, *Nano Lett.*, (2007), **7(9)**, 2563.
- [15] Wernsdorfer W. *et al.*, *Physical Review Letters*, (1996), **77**, 9.

CHAPTER 5

Investigation of temperature-induced anisotropy crossover in magnetic multilayers for storage applications.

5.1 Introduction

A thermally assisted MRAM (TA-MRAM) incorporating a perpendicular MTJ (pMTJ) with multilayered electrodes constitutes a potential candidate for the next generation of MRAMs (described in section 1.8.4). It is well known that with increasing temperature competing anisotropies, especially arising from interface/surface layers, cause a rotation of the easy axis from a perpendicular to an in-plane magnetic orientation. This will produce first the reduction and then the vanishing of the perpendicular magnetic anisotropy of the free layer with the subsequent loss of thermal stability and increase of the intrinsic switching current density J_{c0} which is not advantageous for the operation of the device. This makes essential the investigation of the reorientation process and the evaluation of the reorientation temperature which should be above the blocking temperature T_b of the AFM layer used in the TA-MRAM scheme (typically 150°C - 200°C) to ensure a good operation of the device.

The research presented in this chapter describes the investigation of the reorientation process of two different multilayer systems and the evolution of their domain structure for increasing temperature. The two multilayers represent the free layer of a pMTJ and this study represents a state of development of materials for pMTJs. Experiments were performed by MOKE magnetometry in polar configuration and Lorentz Microscopy in Fresnel mode. Materials were prepared in Spintec-CEA, Grenoble (France) where the MOKE experiments were also carried out, and Lorentz Microscopy experiments were performed in Glasgow. The outcomes of this research will be shown throughout the chapter.

5.2 Experimental details

The specimens investigated were two: a Ta(3)/Pt(20)/(Co(0.45)/Pt(0.6)/Ni(0.5)/Pt(0.6))₃/CoFeB(1.8)/MgO(1.4) multilayer (the thicknesses of the layers in brackets are expressed in nm) shown schematically in fig.5.1(a) and a Pt(3)/CoFeB(1)/MgO(1.4) multilayer shown schematically in fig.5.1(b). Both samples were deposited by Sebastien Bandiera (Spintec-CEA, Grenoble) on a Si₃N₄ membrane, described in section 2.2, by magnetron sputtering (section 2.2.1).

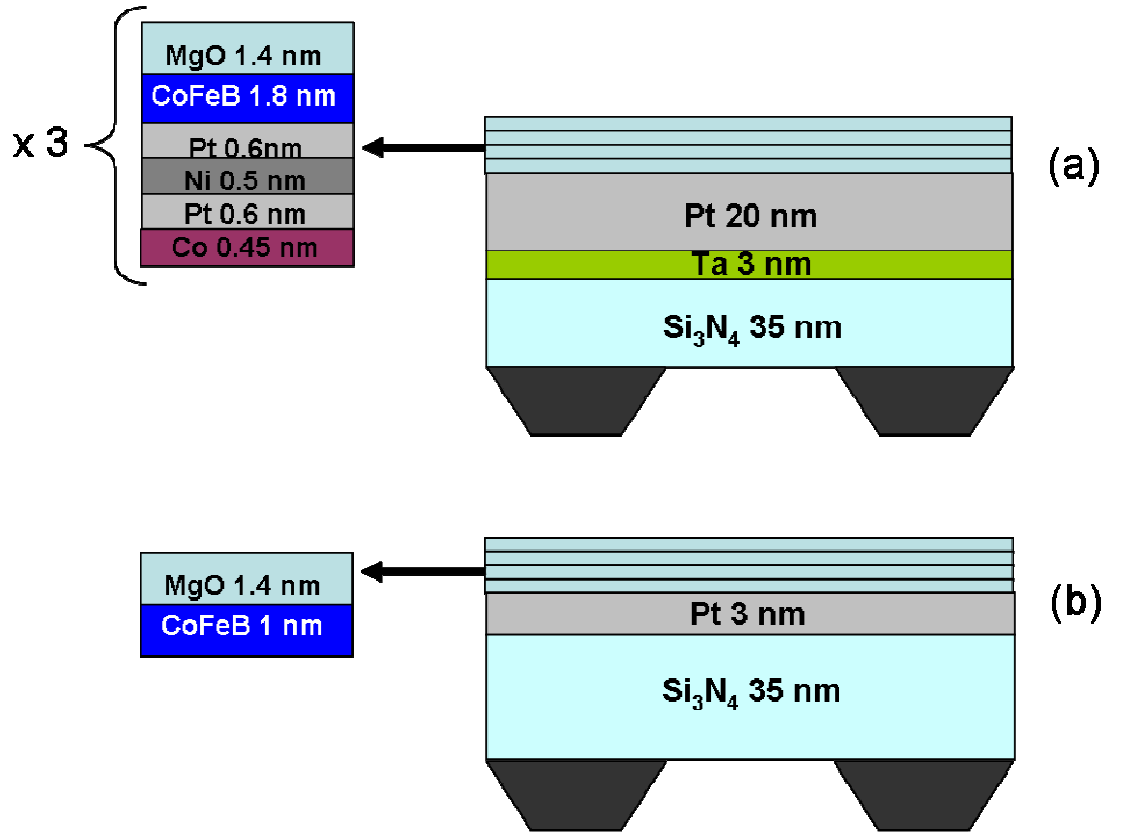


Figure 5.1: (a) Schematic diagram of Ta(3)/ Pt(20)/ (Co(0.45)/ Pt(0.6)/ Ni(0.5)/ Pt(0.6))₃/ CoFeB(1.8)/MgO(1.4) multilayer and (b) Pt(3)/CoFeB(1)/MgO(1.4).

The purpose of the research presented in this chapter is the investigation of the reorientation process of the two different multilayer systems and the evolution of their domain structure for increasing temperature. This step is essential for the development of the future devices, because, as said in the introductory section, the reorientation temperature should be above the blocking temperature T_b of the AFM layer used in the TA-MRAM scheme to ensure a good operation of the device. Moreover the development of materials with the required properties is also essential for the good operation of the

device. To this purpose the role of this research was to study the reorientation process of the easy axis for both specimens and try to understand the role of the insertion of a Co/Pt/Ni/Pt multilayer from a microscopic point of view.

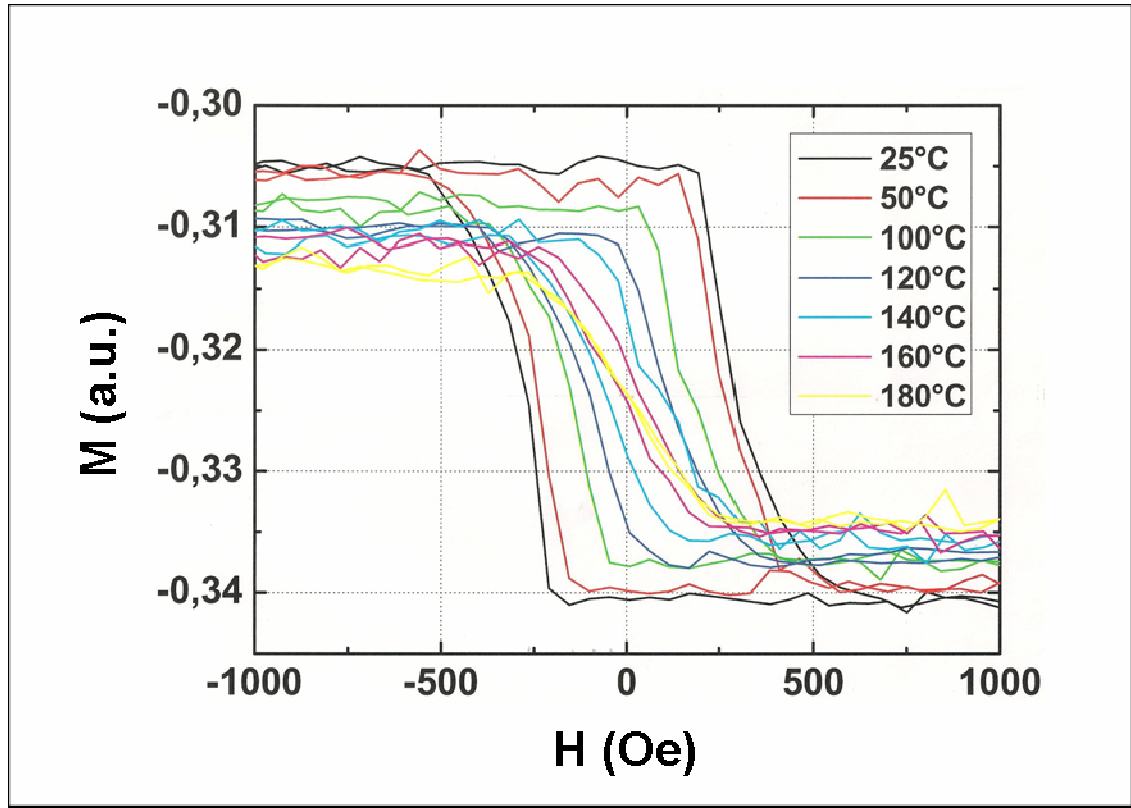


Figure 5.2: Hysteresis loops acquired with MOKE in polar configuration of Ta(3)/ Pt(20)/ (Co(0.45)/ Pt(0.6)/ Ni(0.5) /Pt(0.6))₃/CoFeB(1.8)/ MgO(1.4) multilayer for temperature between T_a (25°C) and 180°C, measuring the out of plane component of magnetisation. The curves shows a decrease of coercivity for increasing temperature and the reorientation occur at a temperature between 160°C and 180°C when the coercivity vanishes.

In order to initially evaluate the reorientation temperatures of both multilayer systems, MOKE experiments in polar configuration (section 2.7) were carried out. They were performed during a secondment at Spintec - CEA, Grenoble (France). From the hysteresis loops the process of the reorientation of the magnetisation can be recognised because, above the reorientation temperature, the loop becomes anahysteretic. In fig.5.2 a set of MOKE hysteresis loops for increasing temperature is shown. The loops were acquired for temperatures between room temperature (25°C) and 180°C. A decrease in coercivity for increasing temperature can be observed and it can be assessed that the reorientation temperature is between 160°C and 180°C, because in that range of temperatures the coercivity vanishes and the loop becomes anahysteretic.

In Fig.5.3 a set of MOKE hysteresis loops for increasing temperature for Pt(3)/CoFeB(1)/MgO (1.4) is shown. The loops were acquired in the temperature range 25°C - 230°C. The field range of the hysteresis loops here is dramatically different from the one of fig.5.2. The coercive fields are much smaller and the decrease in coercivity with temperature is faster than for the Ta(3)/ Pt(20)/ (Co(0.45)/ Pt(0.6)/ Ni(0.5)/ Pt(0.6))₃/ CoFeB(1.8)/MgO(1.4) multilayer. The reorientation occur at a temperature between 200°C and 220°C when the coercivity vanishes.

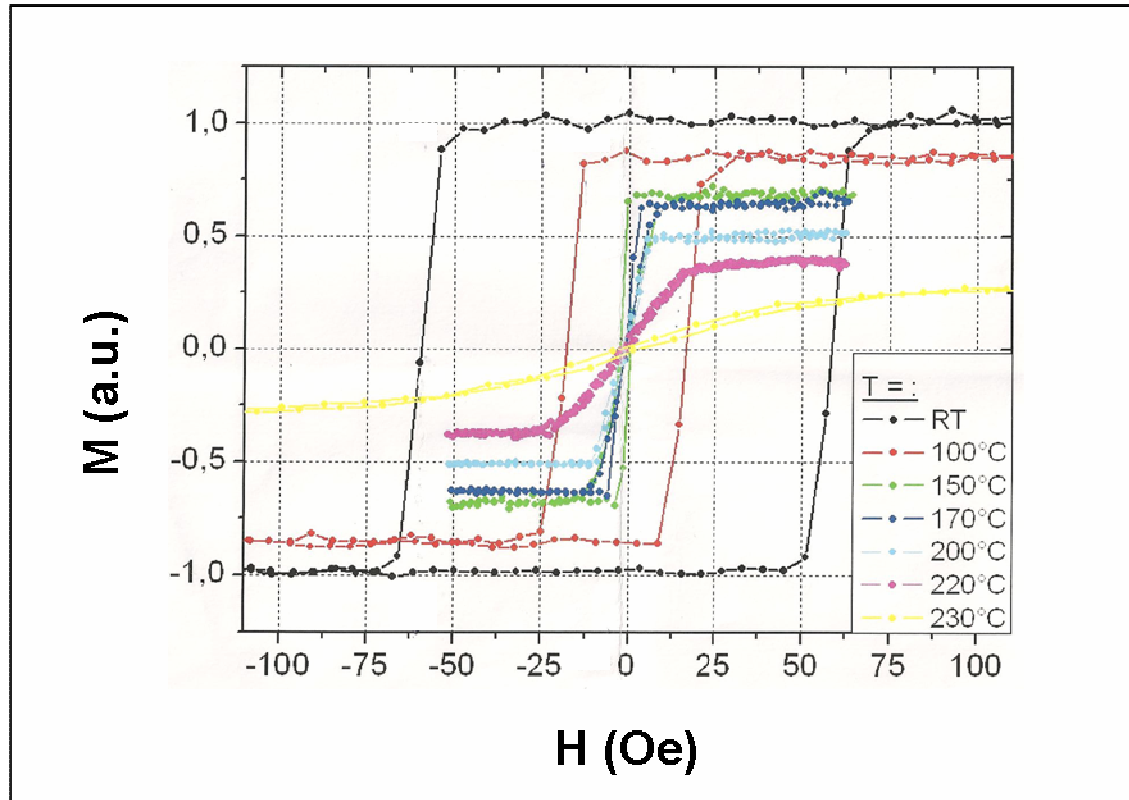


Figure 5.3: Hysteresis loops acquired with MOKE in polar configuration of Pt(3)/ CoFeB(1)/ MgO(1.4) multilayer for temperature between T_a (25°C) and 230°C, measuring the out of plane component of magnetisation. The curves shows a decrease of coercivity for increasing temperature and the reorientation occur at a temperature between 200°C and 220°C when the coercivity vanishes.

As far as Fresnel imaging is concerned, when a sample is perpendicularly magnetised, as for the specimens under investigation, there is no in-plane magnetic induction, and an electron beam will pass through undeflected at normal incidence, as shown in figure 5.4(a). This results in an image with no magnetic information. However, on tilting the sample there is now a component of the magnetic induction perpendicular to the beam as shown in figure 5.4(b). This causes a deflection in the incident electron beam resulting in an image with domain wall contrast, as in standard Fresnel imaging described in section 2.5.1. In

order to observe the magnetic behaviour throughout a full hysteresis loop in a sample perpendicularly magnetised, it is necessary to tilt the sample by an angle α , defocus the image and then gradually increase the objective lens current keeping the tilt angle α fixed. This procedure will modify the electro-optical setup each time and will make the execution of the experiment more difficult than in the case of a sample magnetised in plane. To reverse the perpendicular magnetisation direction, a magnetic field must be applied in the opposite direction by reversing the direction of current flow in the objective lens. The choice of the tilt angle depends on the coercivity and is a value typically selected that allows a better contrast. For these experiments we used a tilt angle α of 30° .

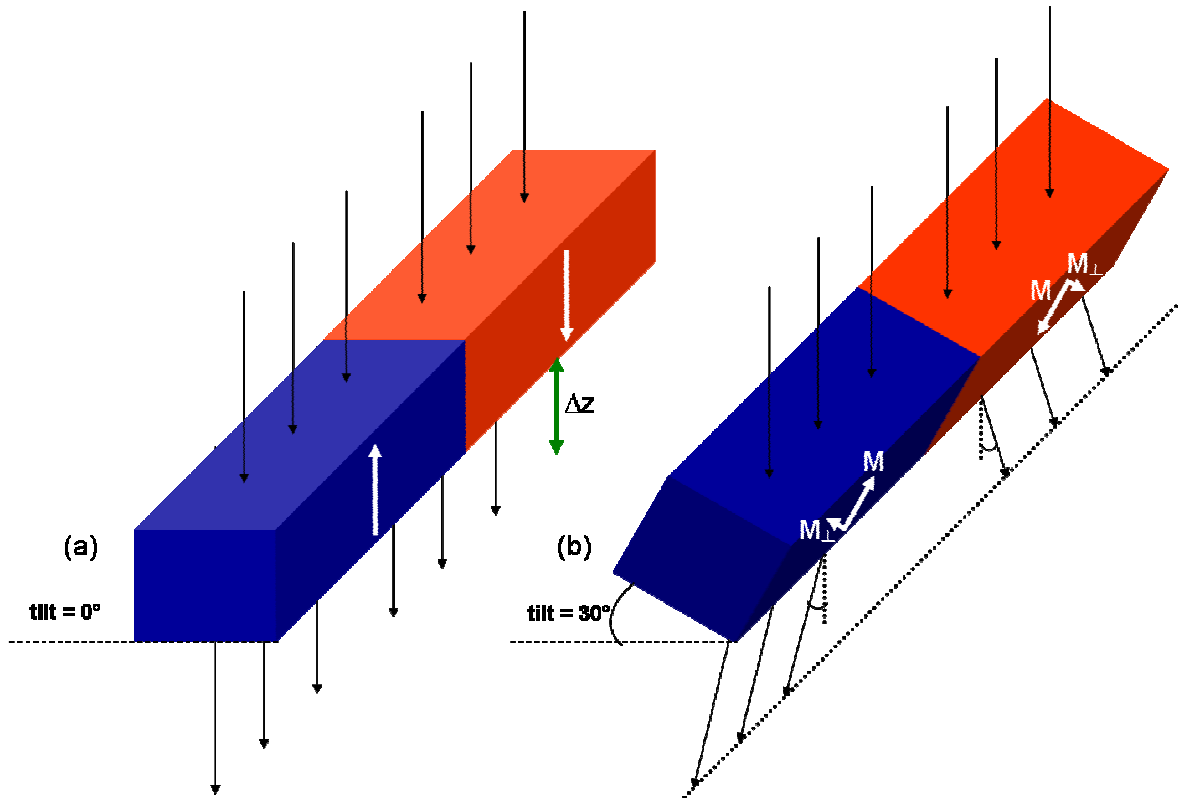


Figure 5.4: Imaging a sample with perpendicular magnetic anisotropy: (a) untitled sample with undeflected electron beam, (b) tilted sample by an angle $\alpha = 30^\circ$ with component of magnetic induction perpendicular to the beam resulting in deflection of the beam and magnetic contrast.

Fig.5.5 shows a schematic diagram of the reorientation process for both samples investigated. At ambient temperature T_a the magnetisation is out of plane (fig.5.5(a)). This results in a MOKE hysteresis loop with the highest coercivity as shown in fig.5.2 and 5.3. For $T_l > T_a$ the reorientation process starts (fig.5.5(b)), and we can see that the magnetisation has a large component out of plane and a weak component of in-plane. This results in a MOKE hysteresis loop with decreased coercivity. For increasing temperature

(fig.5.5(c-d-e-f)) the out of plane component of magnetisation decreases and the in-plane component becomes larger and larger. This results in a reduction of coercivity in MOKE hysteresis loops for increasing temperature. At the reorientation temperature T_r , the magnetisation is completely in-plane (fig.5.5(g)) and the hysteresis loops become anhysteretic. From the Fresnel imaging point of view this means that if we untilt the sample when the reorientation process starts, due to the presence of a weak component of magnetic induction, we can see contrast. And this contrast increases for increasing temperature until the reorientation temperature is reached, since there is an increase of the in-plane component of magnetic induction. In this way, the reorientation process of magnetisation for increasing temperature can be easily monitored.

For the experiments presented in this chapter we used a TEM temperature rod that can be used, in principle, to heat specimens up to 1000°C. It doesn't allow the rotation of the sample with respect to the in plane field direction, but this does not represent a limitation for the experiments because the samples are perpendicularly magnetised and their behaviour is expected to be isotropic in the plane of the film.

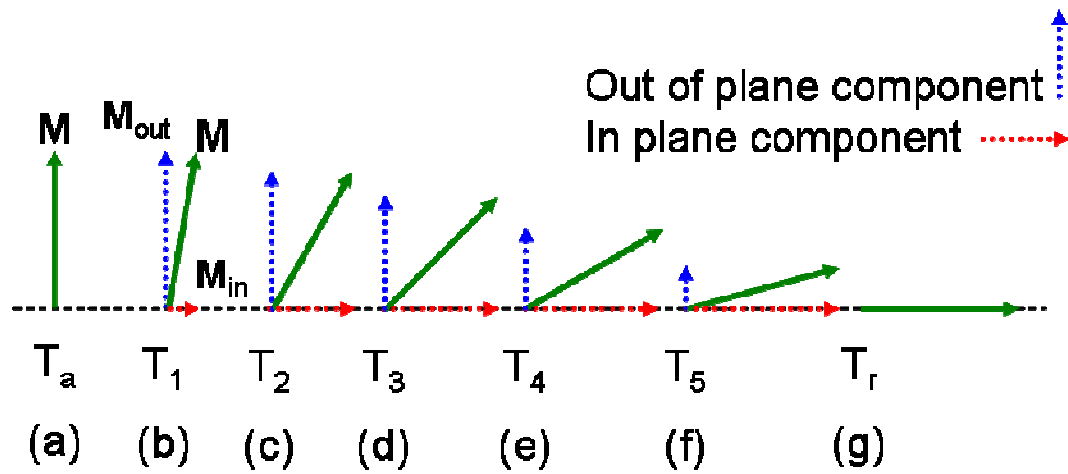


Figure 5.5: Schematic diagram of the reorientation process of magnetisation. (a) At ambient temperature T_a the magnetisation is out of plane. (b) For $T_1 > T_a$ the reorientation process starts, and there is a large component of the magnetisation out of plane and a weak component of the magnetisation in-plane. (c - d - e - f) For increasing temperature we can see a reduction of the out of plane component of magnetisation and an increase of the in-plane component of magnetisation. (g) At the reorientation temperature T_r , the magnetisation is completely in-plane.

5.3 Investigation of the magnetic behaviour in temperature of Ta(3)/Pt(20)/(Co(0.45)/Pt(0.6)/Ni(0.5)/Pt(0.6))₃/CoFeB(1.8)/MgO(1.4) multilayer

As mentioned in the previous section, in order to initially evaluate the reorientation temperatures of the multilayers, MOKE experiments in polar configuration (section 2.7) were carried out. The results were shown in the previous section, where we found that the reorientation temperature is between 160°C and 180°C (fig.5.2). Fresnel imaging experiments allowed a detailed investigation of the reorientation process. The experiments carried out allowed identification of three temperature regimes: regime 1 for 25°C < T < 130°C, regime 2 for 130°C < T < 220°C and regime 3 for 220°C < T < 300°C. They will be described in detail in the next subsections.

5.3.1 Investigation of regime 1 (25°C < T < 130°C)

Regime 1 occurs when the specimen is heated in a range that goes from room temperature (25°C) to 130°C. It is characterised by magnetisation being out of plane everywhere in the multilayer and by a small scale random domain structure visible. As described in section 5.2, to observe the magnetic behaviour throughout a full hysteresis loop in a sample perpendicularly magnetised, we tilted the sample by 30°, defocused the image and then gradually increased the objective lens current keeping the tilt angle fixed.

To be sure that the magnetisation is effectively out of plane everywhere in the sample we performed a simple experiment during the acquisition of the magnetising sequences. We took first an image at the coercive field with the sample tilted at 30° and then we took an image with the sample untilted. If the sample is magnetised out of plane we would not expect to see any domain structure. Indeed, for this range of temperature we could not see a domain structure with the sample untilted, thus the magnetisation is aligned out of plane. Fig.5.6 shows the images acquired during this experiment at T = 25°C, 60°C, 100°C, 120°C. The images in the first column (fig.5.6(a-c-e-g)) are the ones tilted, the images in the second column (fig.5.6(b-d-f-h)) are the ones untilted.

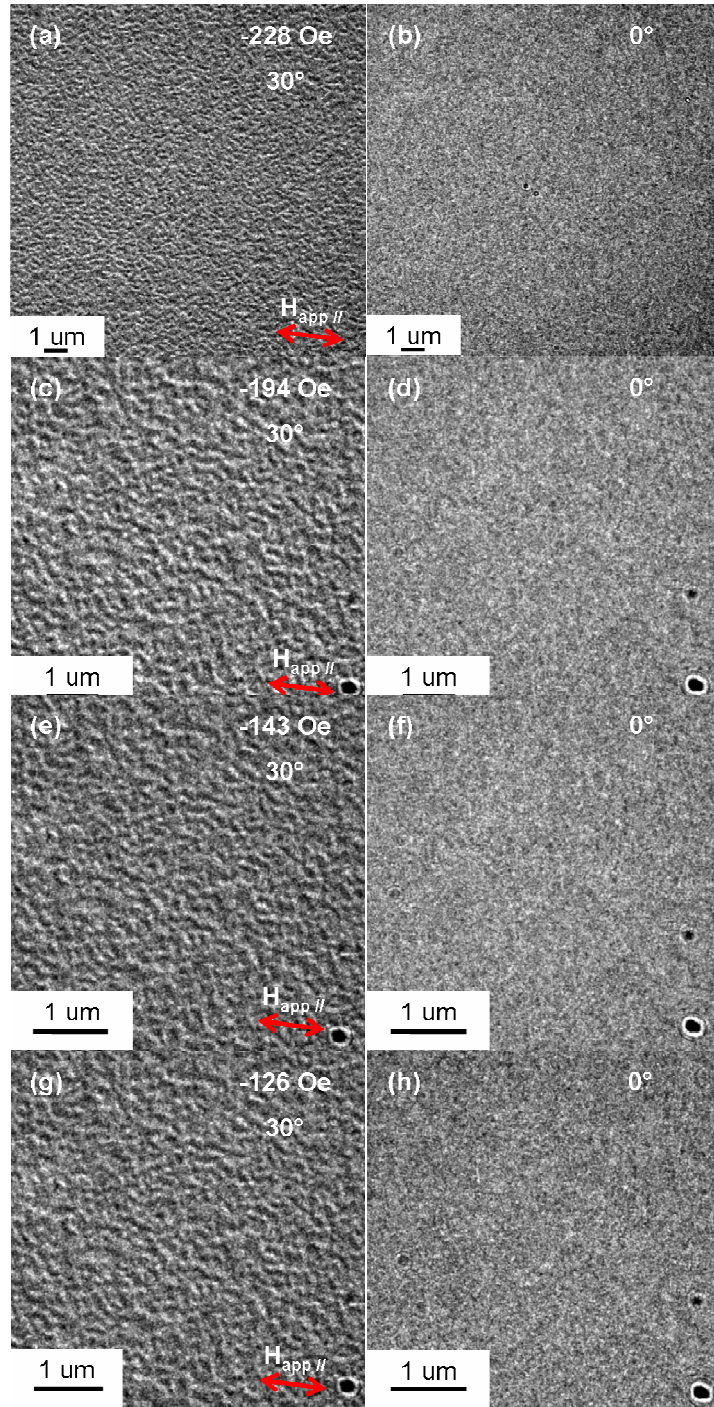


Figure 5.6: Images acquired at the coercive field and at room temperature (a-b), 60°C (c-d), 100°C (e-f), 120°C (g-h). The pairs of images prove that the magnetisation, for this range of temperature, is completely out of plane. (a-c-e-g) are taken at 30° tilt and they show the presence of an out of plane component of magnetic induction because the small scale random domain structure is present; (b-d-f-h) are taken at 0° tilt and they show a lack of an in-plane component of magnetic induction, because any domain structure seems to be present.

A typical sequence of a hysteresis loop of Ta(3)/ Pt(20)/ (Co(0.45)/ Pt(0.6)/ Ni(0.5)/ Pt(0.6))₃/ CoFeB(1.8)/ MgO(1.4) multilayer acquired at room temperature, at a tilt angle of 30° and by changing the objective lens current is depicted in fig.5.7. In fig.5.7(a) we see

that at -135 Oe small scale random domains start to nucleate. For decreasing fields (fig.5.7(b-c)) the density of domains increases. The maximum density of domains is reached at -215 Oe (fig.5.7(d)) and this state represents the coercivity for this temperature. When the field is further decreased (fig.5.7(e)), many areas have switched and the sample is in the saturated state at -365 Oe (fig.5.7(f)).

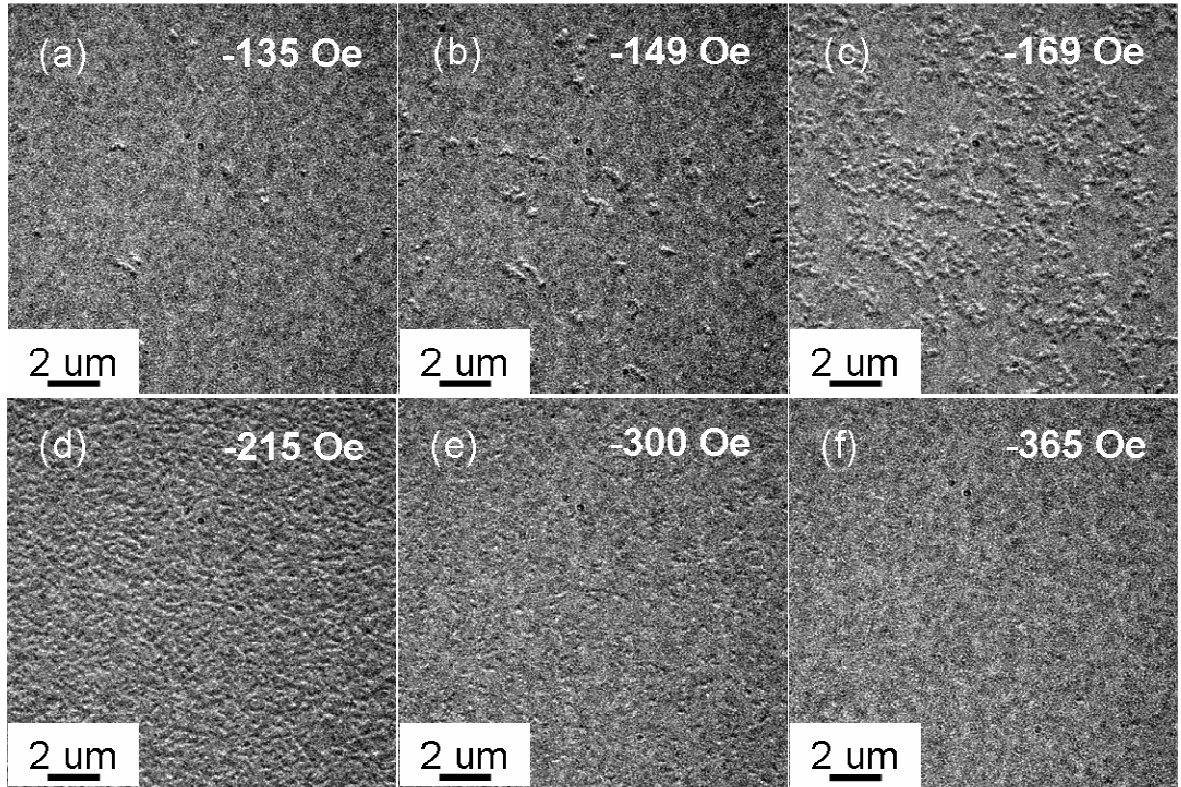


Figure 5.7: Typical sequence of the outward path of the hysteresis loop of Ta(3)/Pt(20)/(Co(0.45)/Pt(0.6)/Ni(0.5)/Pt(0.6))₃/CoFeB(1.8)/MgO(1.4) multilayer acquired at room temperature, at a tilt angle of 30° and by changing the objective lens current. (a) Small scale random domains start to nucleate. (b-c) The density of domains increases. (d) The maximum density of domain is reached and this state represents the coercivity for this temperature. (e) Many areas switched. (f) The sample is in the saturated state.

If the sequence is taken at lower magnification, it can be noticed that in different regions of the sample the highest density of domains is reached at different fields, as shown in fig.5.8. This could be due to a possible presence of a temperature gradient in the sample or some inhomogeneity within the multilayer. Indeed, due to the small thicknesses of the magnetic layers in the (Co(0.45)/Pt(0.6)/Ni(0.5)/Pt(0.6))₃ multilayer, it is possible that some island like area may be present during deposition.

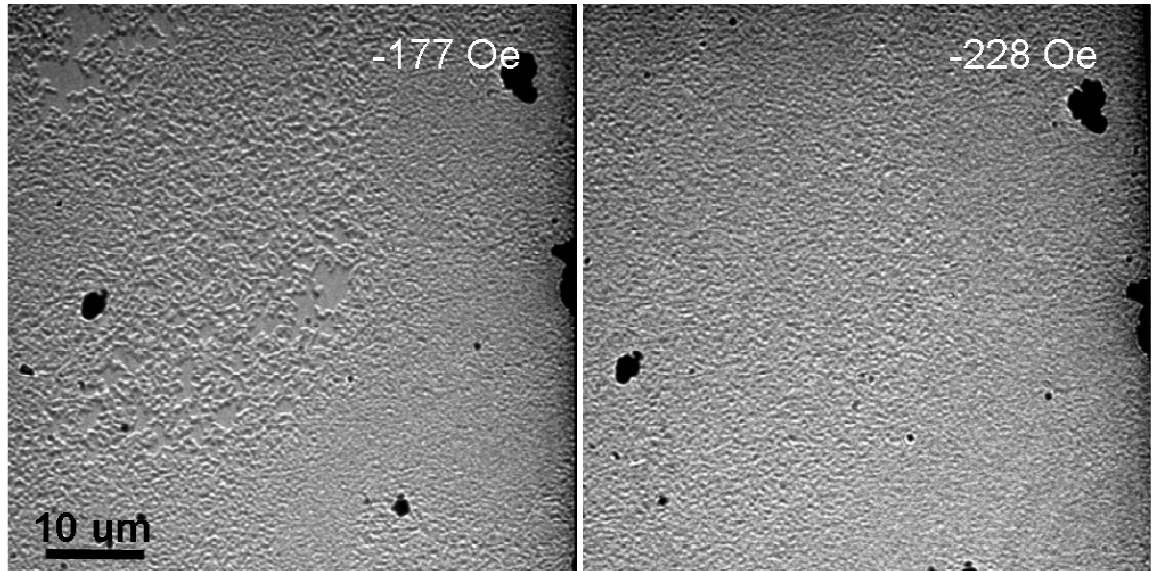


Figure 5.8: Images taken from the sequence of a hysteresis loop of Ta(3) /Pt(20) /(Co(0.45) /Pt(0.6) /Ni(0.5) /Pt(0.6))₃ /CoFeB(1.8)/ MgO(1.4) multilayer at room temperature acquired at lower magnification. They show that the highest density of domains is reached at different fields in different regions of the sample due to a possible inhomogeneous distribution of the materials in the multilayer or a presence of a temperature gradient.

For increasing temperature within the regime 1, the film behaviour is similar to the one found at room temperature except for the coercive field that decreases for increasing temperature, consistently with the MOKE hysteresis loops shown in fig.5.2. A summary with the coercivities for increasing temperature is shown in table 5.1. The images at the coercive field allowed the measurement of the domain size. This can be done directly from the image or by mean of the Fast Fourier Transform (FFT). We will show later (fig.5.13), that the domain size decreases for increasing temperature.

Temperature (°C)	Coercivity Fresnel (Oe)	Coercivity MOKE (Oe)
25	228 ± 6	270 ± 14
60	194 ± 6	-
100	143 ± 6	150 ± 8
120	126 ± 6	90 ± 5

Table 5.1: Values of the coercivity estimated from the Fresnel image sequences acquired at T = 25°C, 60°C, 100°C, 120°C.

5.3.2 Investigation of regime 2 ($130^{\circ}\text{C} < T < 220^{\circ}\text{C}$)

Regime 2 is characterised by contrast due to both out of plane and in plane magnetisation located in separate regions. This occurs for $130^{\circ}\text{C} < T < 220^{\circ}\text{C}$. The domain structure is still a small scale random domain structure in the region magnetised out of plane. Contrast arising from out of plane magnetisation can be observed when the sample is tilted at 30° (the optimum angle to observe contrast due to out-of-plane magnetisation), whereas at 0° , contrast due to out of plane magnetisation is not present, for the reasons explained in section 5.2, but small scale domains can be seen, and this can be attributed to the beginning of the reorientation process. This is visible in fig.5.9 where an image acquired at 130°C when the sample is (a) tilted and (b) untilted is shown.

The reorientation of magnetisation starts when the specimen is heated to 130°C . At the remanent state, as shown in fig.5.9, when the specimen is tilted at 30° (fig.5.9(a)), we can see, as for the lower temperatures, a small scale random domain structure. When the tilt angle is positioned at 0° (fig.5.9(b)), differently from the lower temperatures, we can see contrast of a small scale domain structure, similar to the contrast due to out of plane magnetised domains, which is a first indication that the reorientation process has begun.

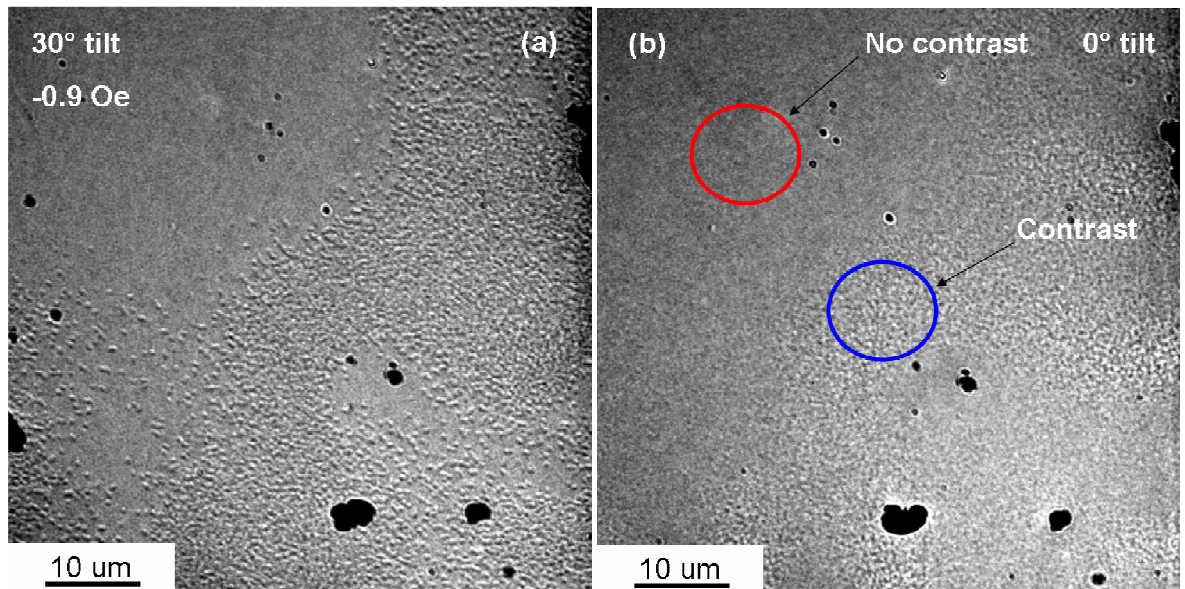


Figure 5.9: Fresnel images at the remanent state of the specimen heated at 130°C when (a) tilted at 30° and (b) untilted. In (b) the red circle represents an example of area without contrast, as expected for a sample magnetised out of plane, whereas the blue circle represents an example of an area with small scale domain contrast which can be attributed to the presence of a component on in-plane magnetisation.

As the specimen is heated up, the in-plane component of magnetisation becomes larger and the out of plane component becomes smaller, as shown in fig.5.10. When the specimen is tilted, as displayed in fig.5.10(a), we can see two different types of contrast: contrast arising from the presence of an out of plane component of magnetisation as in the area marked with a red circle, and contrast arising from the presence of an in-plane component of magnetisation as in the area marked with a blue circle. When we untillt the sample (fig.5.10(b)), no contrast attributable to out of plane magnetisation can be seen, as in the area marked with a red circle. The contrast from the in plane component, as shown in the area marked with the blue circle, becomes stronger than the contrast that we saw in fig.5.9(b) for the specimen heated at 130°C.

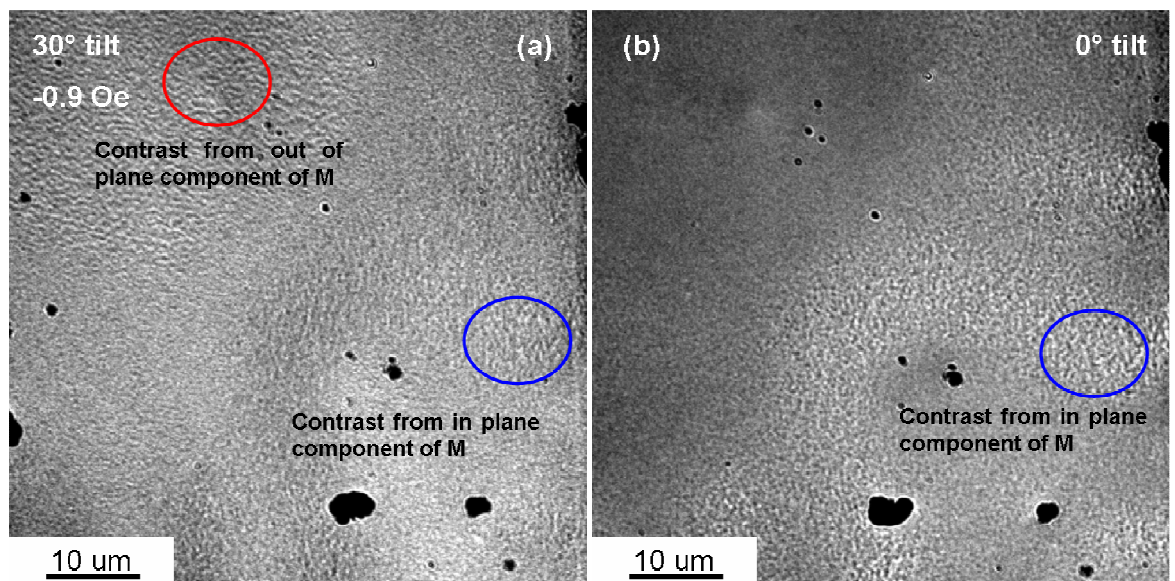


Figure 5.10: Fresnel images at the remanent state of the specimen heated at 180°C when (a) tilted at 30° and (b) untilted. In (a) an example of area that shows contrast from out of plane component of magnetisation is marked with a red circle, whereas an example of area with contrast from in plane component of magnetisation is marked with a blue circle. In (b) an example of area with contrast from in plane component of magnetisation is marked with a blue circle. In a) the contrast is strictly from the tilted out of plane component.

A typical magnetising sequence of the specimen in regime 2 is shown in fig.5.11, for the specimen heated at 180°C. Again, the sequences for the other temperatures investigated are similar, except for the coercivity that decreases, consistent with the results of MOKE experiments. The sequences were acquired in the same way as in regime 1, with the sample tilted at 30° and gradually increasing the objective lens current.

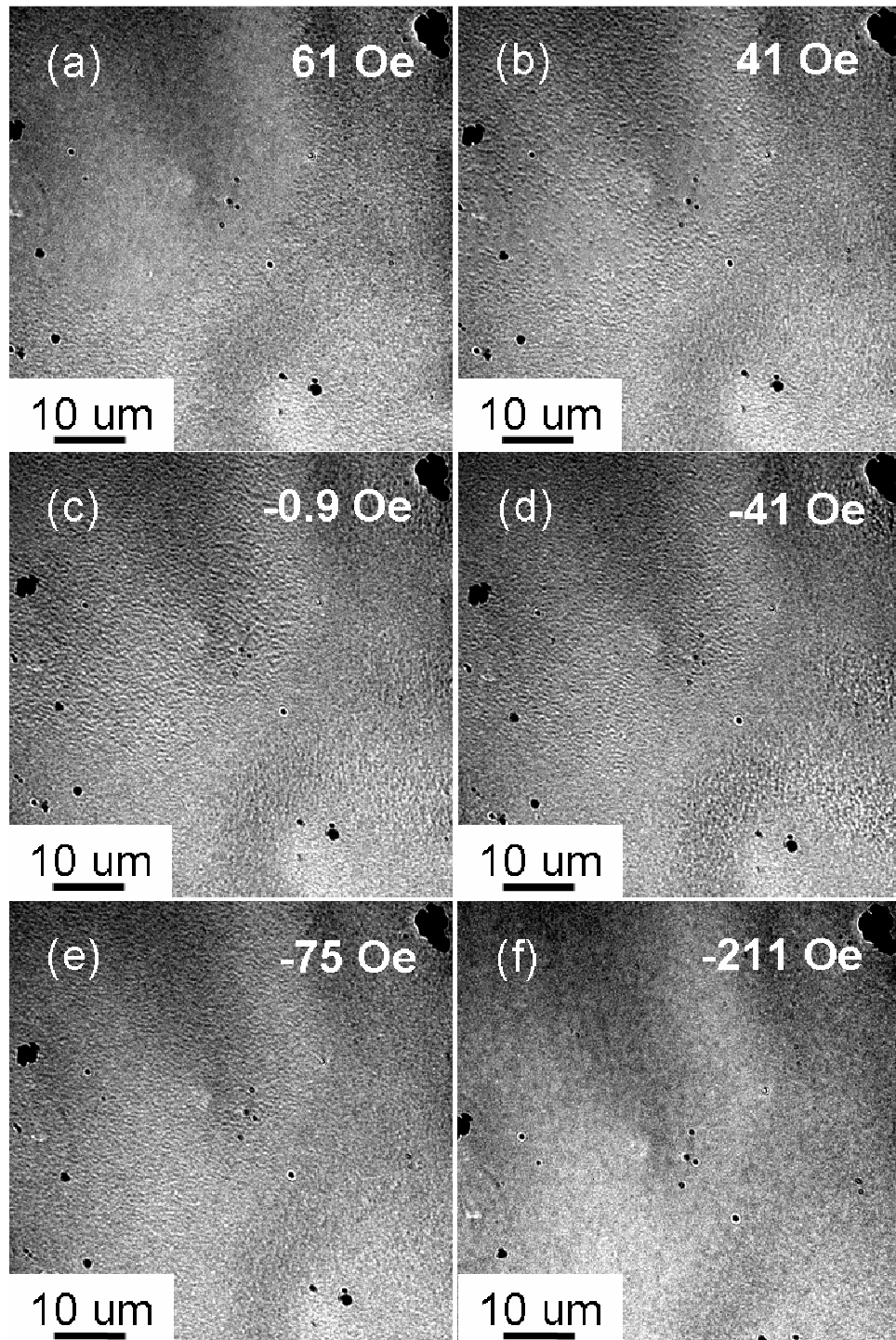


Figure 5.11: Fresnel magnetising sequence of the outward path of the hysteresis loop of Ta(3)/Pt(20)/(Co(0.45)/Pt(0.6)/Ni(0.5)/Pt(0.6))₃/CoFeB(1.8)/MgO(1.4) multilayer acquired at 180°C at a tilt angle of 30°. (a-b-c) Small scale random domains nucleate and increase in density in top-left area and contrast from in plane magnetisation becomes more intense. (d) The maximum density of small scale random domain and the strongest intensity of contrast from in plane magnetisation are reached, and this state represents the coercivity for this temperature. (e) The density of domains and the intensity of the ripple decrease. (f) The sample is in the saturated state.

The images in fig.5.11 show the presence of both a contribution from the out of plane component (top-left area) and the in-plane component (bottom-right area) of magnetisation. The behaviour in the top-left area is similar to the one found in regime 1, with (a-b-c) nucleation and increase of density of small scale random domains, the highest density of domains reached in (d), decrease of domain density (e) and the sample back in the saturated state (f). What changes is the bottom-right area where a contrast from the in-plane component of magnetisation is present. For decreasing field (fig.5.11(a-d)) the ripple becomes more pronounced; at the coercive field (fig.5.11(d)) the ripple has its highest visibility, and then they become less and less intense for decreasing field (fig.5.11(e)) and they disappear in the saturated state (fig.5.11(f)).

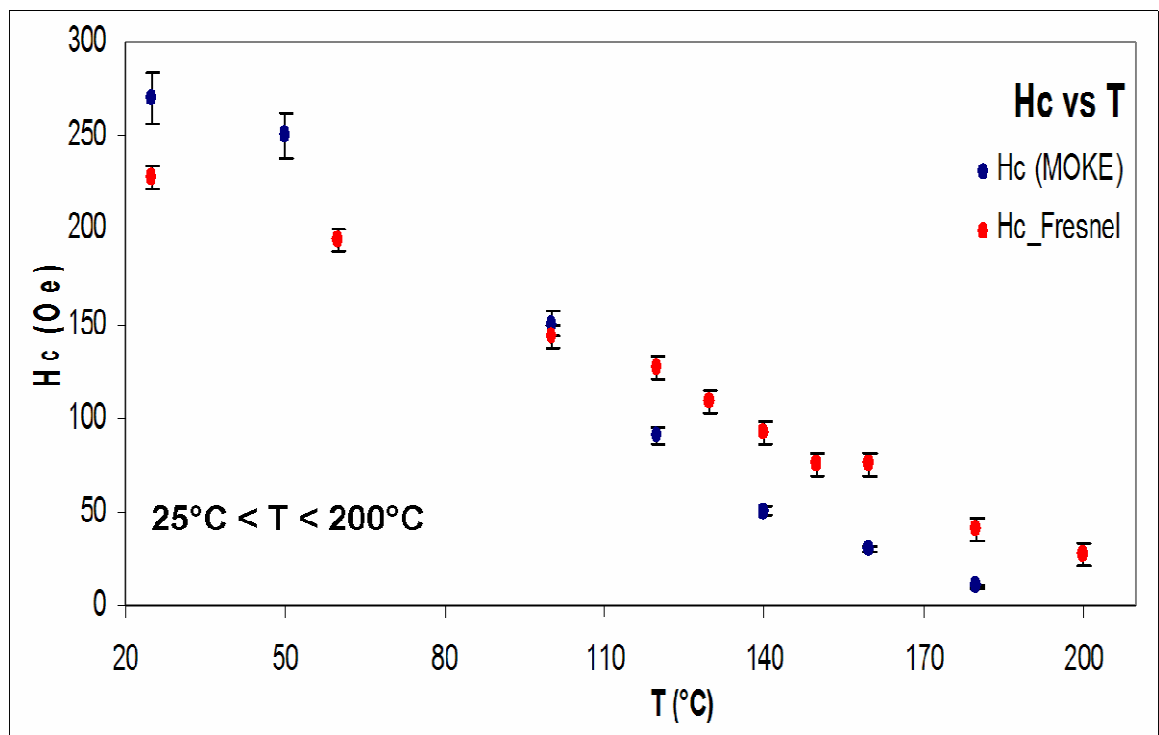


Figure 5.12: Variation of coercivity for increasing temperature measured by MOKE hysteresis loops (blue dots) and Fresnel imaging (red dots).

As in regime 1, a result of the increase in temperature is a decrease in coercivity, consistent with what was observed in the MOKE hysteresis loops. In fig.5.12 the variation of coercivity, for temperatures between 25°C and 200°C, measured from MOKE hysteresis loops and Fresnel imaging in regime 1 and 2 is shown. Both variations are in agreement because they both show a decrease in coercivity for increasing temperature. Nevertheless the variations have different slopes, possibly due to different ways of applying the magnetic field with the two techniques. With MOKE the applied field is perpendicular to

the sample, whereas in Fresnel imaging there is an in plane component of the applied field. The variation of the size of perpendicularly magnetised domain size for increasing temperature in regime 1 and 2 is shown in fig.5.13. The diagram shows a clear decrease in domain size.

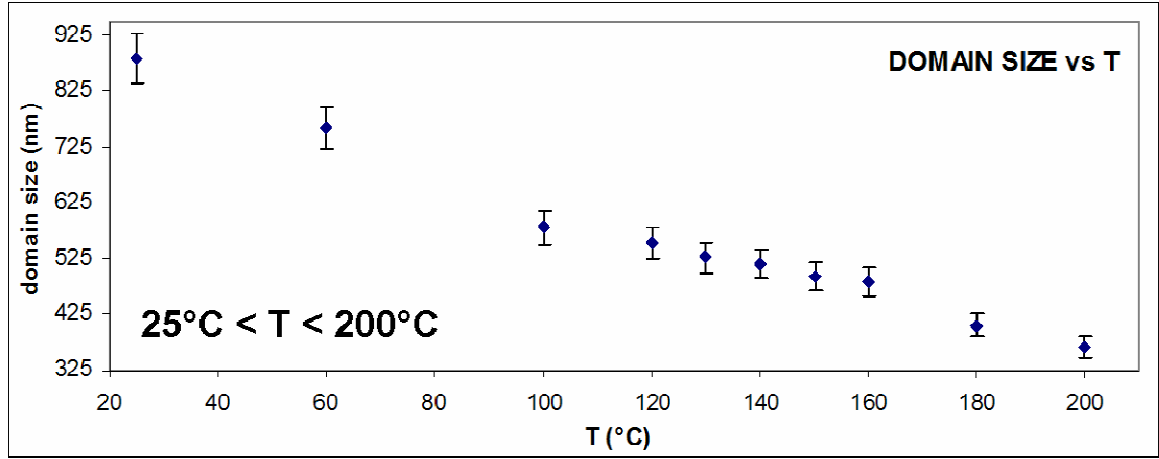


Figure 5.13: Variation of domain size for increasing temperature measured by Fresnel imaging at the coercive field.

At 220°C the reorientation process was completed with the sample being magnetised in-plane as described in the next section.

5.3.3 Investigation of regime 3 ($220^{\circ}\text{C} < T < 300^{\circ}\text{C}$)

Regime 3 is characterised by magnetisation having an in-plane component everywhere in the multilayer (we cannot see the small scale random domain structure at any tilt angle and temperature) and strong magnetisation ripple. This occurs for $220^{\circ}\text{C} < T < 300^{\circ}\text{C}$. In this temperature regime, the coercivity is very small (below 1 Oe). For the sequences acquired in this regime, differently from the previous cases, we kept the objective lens current fixed and we varied the tilt angle, analogously to what we do for standard Fresnel imaging of in plane magnetised specimens. The average orientation of magnetisation was evaluated by means of the fast Fourier transform (FFT) image of a smaller areas where the contrast is stronger, as seen in section 3.4.

Fig.5.14 represents the outward path of the hysteresis loop of the specimen heated at 220°C . The Fresnel images show the presence of ripple and magnetisation dispersion. The processes observed when the field is decreased from positive fields to negative fields are: rotation of magnetisation clockwise (fig.5.14(a - b)), increase in magnetisation dispersion

(fig.5.14(c - d)), decrease in magnetisation dispersion (fig.5.14(e - f)), abrupt change in magnetisation orientation (fig.5.14(g)) and magnetisation rotation anticlockwise (fig.5.14(h)). The dark contrast present in the images, suggests that areas of the film may not be completely flat and we can see that this effect varies with field.

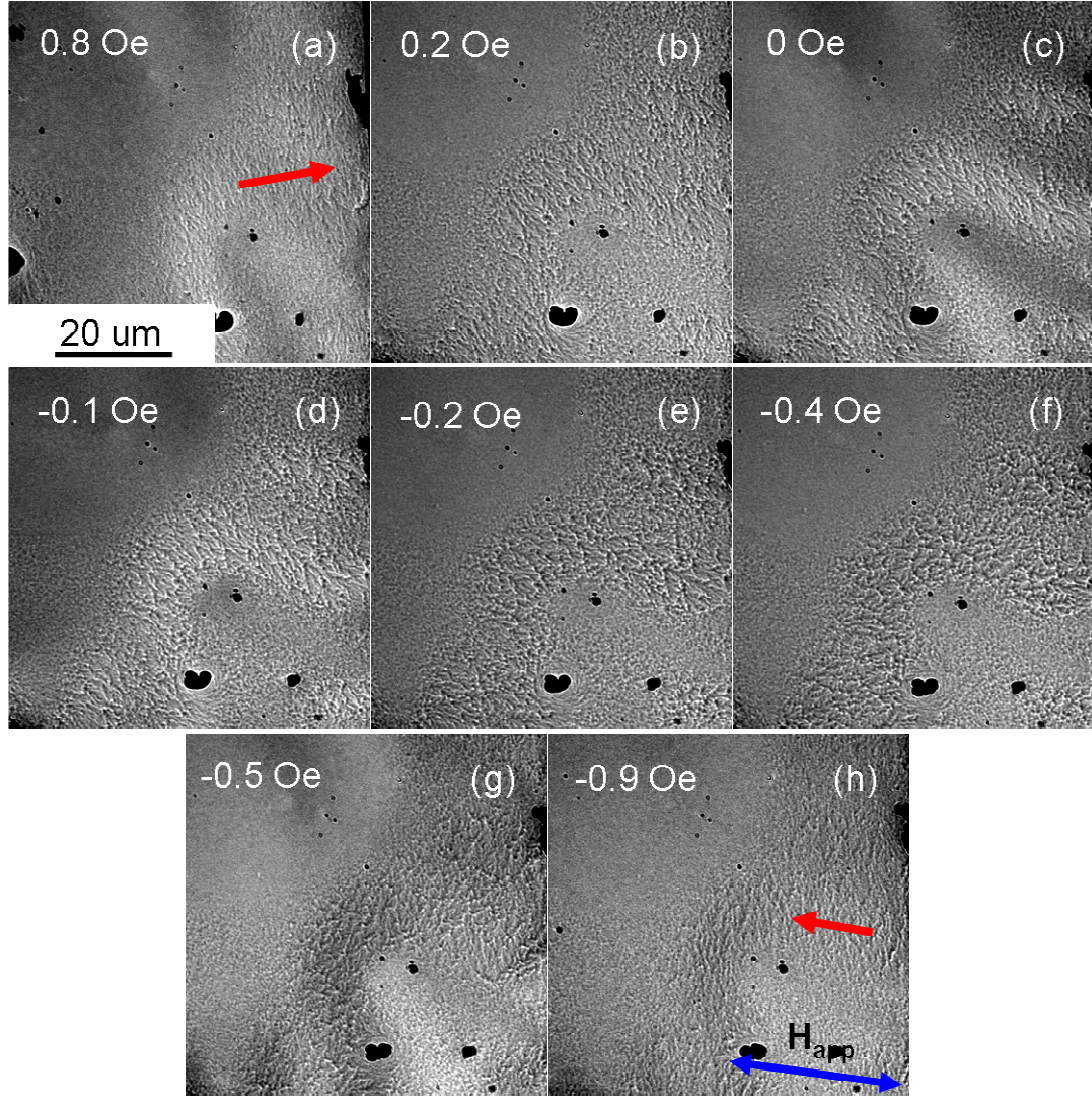


Figure 5.14: Fresnel images displaying the outward path of the hysteresis loop for $T = 220^\circ\text{C}$. The orientation of magnetisation in each frame was evaluated by mean of FFT images of small areas where the contrast is stronger.

Fig.5.15 represents the outward path of the hysteresis loop of the specimen heated at 300°C . The Fresnel images show the presence of ripple, magnetisation dispersion, and formation of large domains. The first processes observed are magnetisation rotation and increase in dispersion (fig.5.15(a-c)). Then, dispersion continues to increase, we can see regions with different magnetisation, and large domains form and propagate (fig.5.15(d-e)) reversing the magnetisation of the film (fig.5.15(f)) that gets close to saturation (fig.5.15(g-

h)). We can see again the dark contrast in the images, which is stronger in this case, and that suggests that areas of the film are less flat than for $T = 220^\circ\text{C}$.

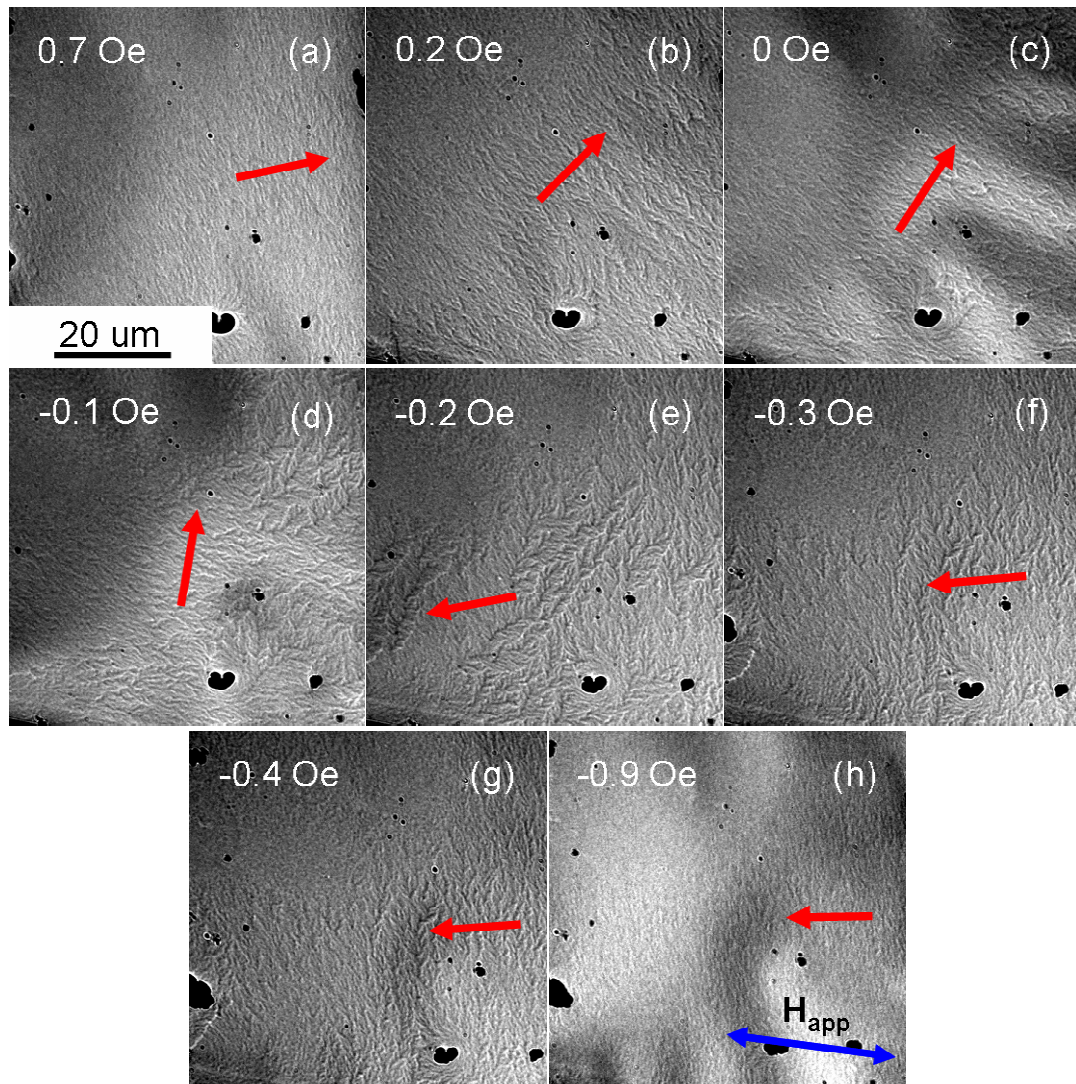


Figure 5.15: Fresnel images displaying the outward path of the hysteresis loop for $T = 300^\circ\text{C}$. The orientation of magnetisation in each frame was evaluated by mean of FFT images of small areas where the contrast is stronger.

The two loops at the extremes of this temperature range show an in-plane component everywhere in the multilayer though this is not seen completely homogeneously. The very small coercivity is typical of a soft magnetic material and their behaviour appears similar to the behaviour found in the CoFeB film 30\AA thick described in chapter 3 where magnetisation rotation and formation and propagation of large domains was seen.

To conclude we can say that for lower temperatures ($25^\circ\text{C} - 220^\circ\text{C}$) the specimen appears to have a strong perpendicular anisotropy. We observed a small scale random domain structure that we can ascribe to perpendicularly magnetised domains. For higher

temperatures (220°C - 300°C) we found a behaviour typical of a soft magnetic material magnetised in plane with low anisotropy and high susceptibility.

5.4 Investigation of the behaviour in temperature of Pt(3)/CoFeB(1)/MgO(1.4) multilayer

The purpose of the investigation of the Pt(3)/CoFeB(1)/MgO(1.4) multilayer, is to understand how the reorientation process and the domain structure changes without the presence of the Co/Pt/Ni/Pt piece in the multilayer. The MOKE hysteresis loops in fig.5.3, as shown in section 5.2, show that the field range of the loops is dramatically different from the one of fig.5.2. The coercive fields are much smaller and the decrease in coercivity with temperature is faster than for the Ta(3)/ Pt(20)/ (Co (0.45)/ Pt(0.6)/ Ni(0.5)/ Pt(0.6))₃/ CoFeB(1.8)/ MgO(1.4) multilayer. This is an indication that the sample is made of a very permeable material. The reorientation occurs at a temperature between 200°C and 220°C when the coercivity vanishes. In order to perform a complete investigation with Fresnel imaging, we need to be able to apply small fields to the specimen. It is very hard to get fields lower than 15 -20 Oe for experiments that require to keep fixed the tilt angle and change the objective lens current to vary the external applied field. This limitation is due to the presence of a remanent field of 10-20 Oe coming from the polepieces of the objective lens. For this reason we were not able to investigate the magnetic behaviour of Pt(3)/CoFeB(1)/MgO(1.4) multilayer for temperatures above 110°C.

To be sure that the magnetisation is effectively out of plane everywhere in the sample we performed a simple experiment during the acquisition of the magnetising sequences. We took first an image at the coercive field with the sample tilted at 30° and then we took an image with the sample untilted. If the sample is magnetised out of plane we would not expect to see any domain structure. Indeed, for this range of temperature we could not see a domain structure with the sample untilted, thus the magnetisation is aligned out of plane. Fig.5.16 shows the images acquired during this experiment at T = 35°C, 50°C, 100°C, 110°C. The images in the first column (fig.5.16(a-c-e-g)) are the ones tilted, the images in the second column (fig.5.16(a-c-e-g)) are the ones untilted. The images in the first column show a deep change in the domain structure before applying a temperature of 100°C and after heating the sample with a temperature of 100°C.

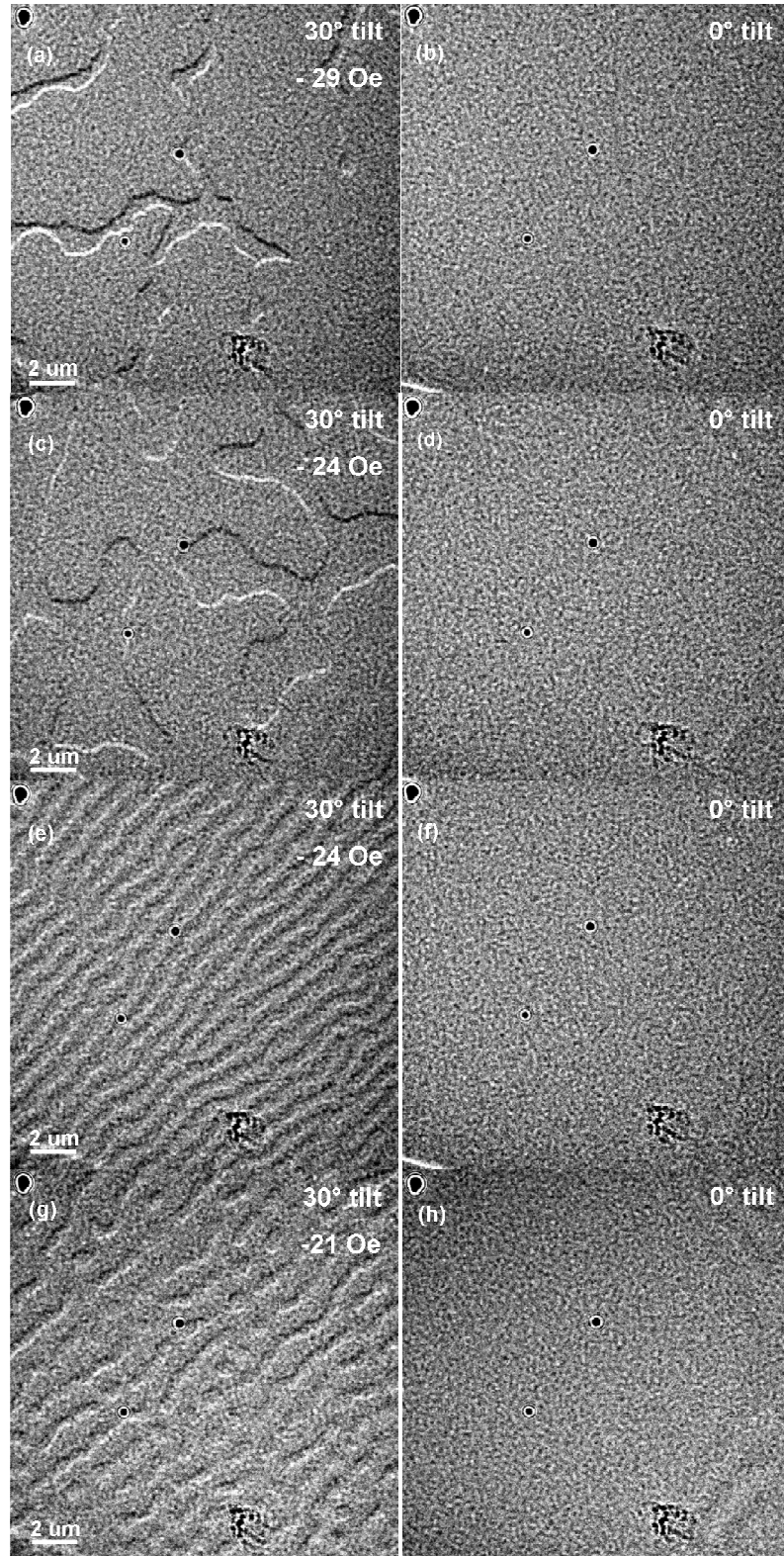


Figure 5.16: (a-b) Images acquired at the coercive field and at room temperature, (c-d) 50°C, (e-f) 100°C, (g-h) 110°C. Each pair of images prove that the magnetisation, for these temperatures, is completely out of plane. (a-c-e-g) are taken at 30° tilt and they show the presence of an out of plane component of magnetic induction because a domain structure is present; (b-d-f-h) are taken at 0° tilt and they show a lack of an in-plane component of magnetic induction, because no domain structure seems to be present.

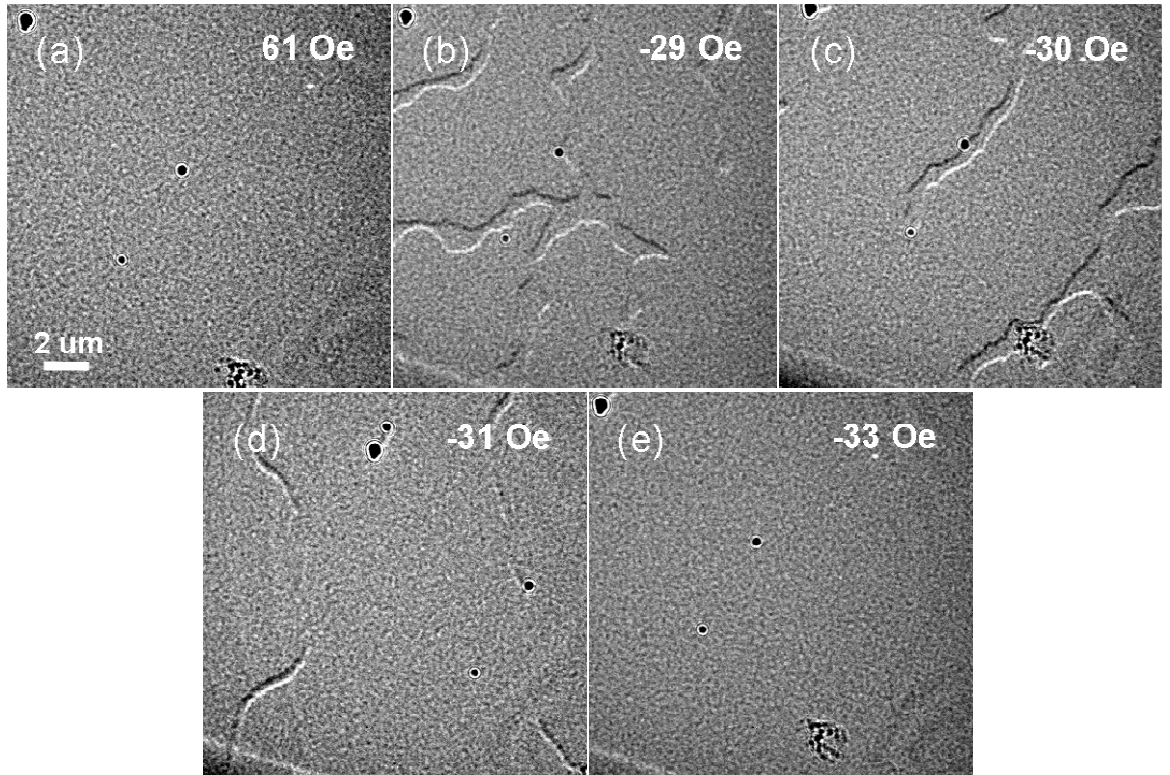


Figure 5.17: Typical sequence of the outward path of the hysteresis loop of Pt(3)/CoFeB(1)/MgO(1.4) multilayer acquired at room temperature. (a-b) The sample is in the saturated state. (c) Suddenly a large serpentine type domain structure forms. (d) The domain structure expands. (e) The magnetisation of the film is reversed and (f) the film is again in the saturated state.

A typical sequence of the outward path of the hysteresis loop of Pt(3)/CoFeB(1)/MgO(1.4) multilayer acquired at room temperature is depicted in fig.5.17. The experiment was carried out with the tilt angle kept fixed at 30° and by changing the objective lens current because the sample is magnetised out of plane. The sample is in the saturated state (fig.5.17(a)). The field is decreased from positive to negative fields. Suddenly at -29 Oe a large serpentine type domain structure forms (fig.5.17(b)). This domain structure changes (fig.5.17(c, d)), and then leads to a rapid reversal of the magnetisation seen in the reverse saturated state (fig.5.17(e)). This is consistent with the sharp hysteresis loops shown in fig.5.3.

The behaviour found when the temperature is increased at 50°C (fig.5.18) is similar to the one found at room temperature and again a serpentine type domain structure forms (fig.5.18(c)). In this case the coercivity is slightly smaller (26 Oe instead of 29 Oe) as well as the periodicity of the domain structure, as we will show later in fig.5.22.

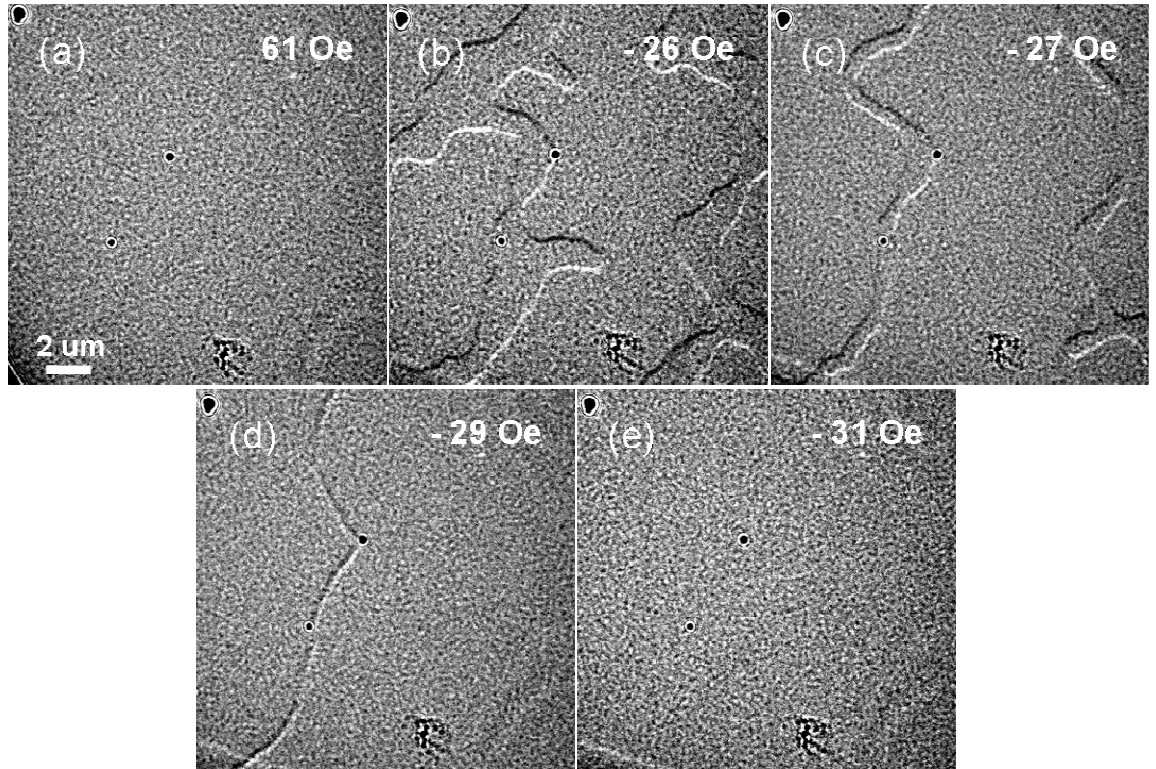


Figure 5.18: Typical sequence of the outward path of the hysteresis loop of Pt(3)/CoFeB(1)/MgO(1.4) multilayer acquired at 50°C. (a-b) The sample is in the saturated state. (c) Suddenly a smaller serpentine type domain structure forms. (d) The domain structure expands. (e) The magnetisation of the film is reversed and the film is again in the saturated state.

The sequence of the outward path of the hysteresis loop acquired at 100°C is shown in fig.5.19. The sample is, first, in the saturated state (fig.5.19(a)). Some circular shaped domains start to form on the sample surface at -20 Oe (fig.5.19(b)). These circular domains elongate (fig.5.19(c)) and they turn into regular stripes with directionality (fig.5.19(d)). The stripes shrink (fig.5.19(e)) and the film is again in the saturated state (fig.5.19(f)). The coercivity is 24 Oe and we found a regular stripe domain structure that develops with a certain directionality from the bottom-left corner to the top-right corner.

The last temperature we could investigate with our setup was 110°C. The behaviour found is similar to the one found at 100°C (fig.5.20). A stripe domain structure forms (fig.5.20(d)), with a less regular structure than at 100°C and a smaller periodicity. The stripes have the same directionality as seen in fig.5.19(d). From the density of domain walls we can see that the coercivity is 20 Oe.

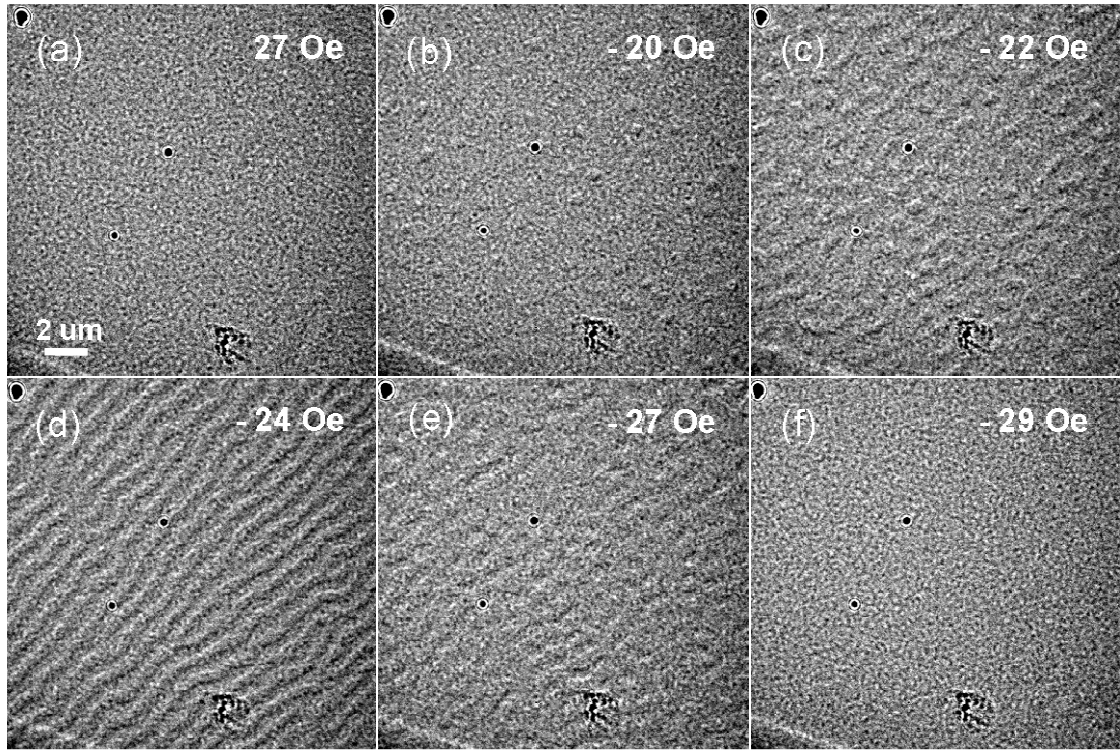


Figure 5.19: Typical sequence of the outward path of the hysteresis loop of Pt(3)/CoFeB(1)/MgO(1.4) multilayer acquired at 100°C. (a) The sample is in the saturated state. (b) Some circular domains starts to form on the sample surface. (c) The bubbles elongate. (d) A stripe domain structure forms. (e) The stripes shrink. (f) The film is again in the saturated state.

When we heated the sample at 120°C we could not see any contrast from a domain structure, as at all field values the images appeared as fig.5.20(a, f). This is due to the fact that we cannot apply magnetic fields smaller than the remanence of the objective lens field with this type of experiment.

Fig.5.21 shows a comparison between the coercivity measured at different temperature with MOKE and the one measured from Fresnel images. Both variations are in agreement because they both show a decrease in coercivity for increasing temperature. Nevertheless the variations have different slopes, possibly due to different ways of applying the magnetic field with the two techniques. The variation of the periodicity of the domain structure for increasing temperature is shown in fig.5.22. The diagram shows a clear decrease in the periodicity, as seen already qualitatively in the Fresnel images.

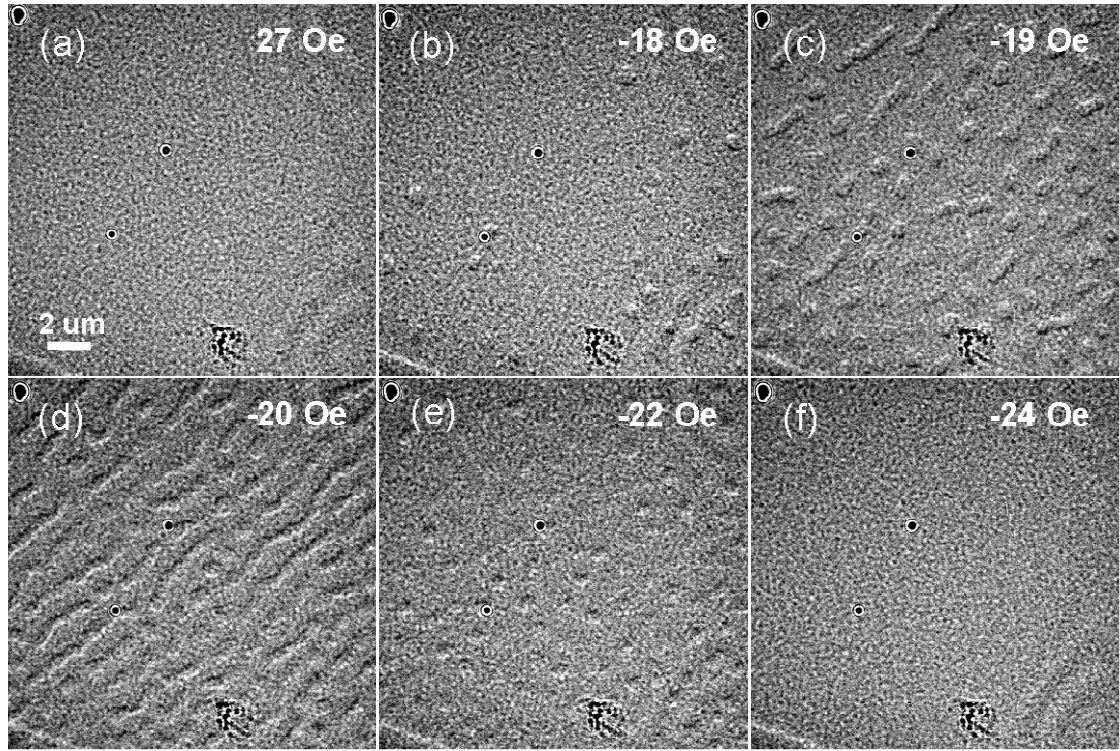


Figure 5.24: Typical sequence of the outward path of the hysteresis loop of Pt(3)/CoFeB(1)/MgO(1.4) multilayer acquired at 110°C. (a) The sample is in the saturated state. (b) Some circular domains starts to form on the sample surface. (c) The bubbles elongate. (d) An irregular stripe domain structure forms. (e) The stripes shrink and becomes again bubbles. (f) The film is again in the saturated state.

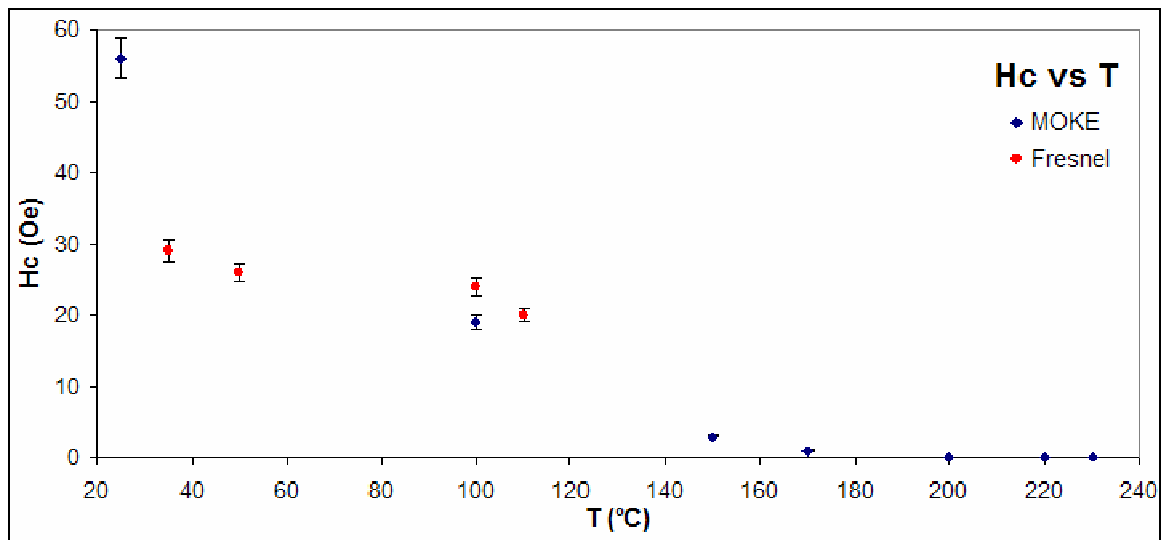


Figure 5.21: Variation of coercivity for increasing temperature measured by MOKE hysteresis loops (blue dots) and Fresnel imaging (red dots).

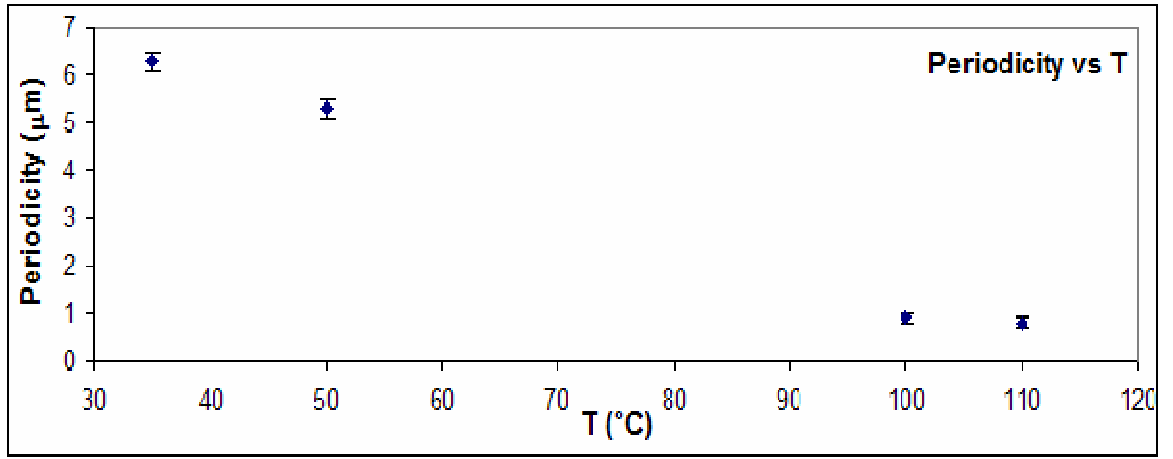


Figure 5.22: Variation of domain size for increasing temperature measured by Fresnel imaging (yellow dots) at the coercive field.

5.5 Summary

The research presented in this chapter described the investigation of reorientation process of magnetisation from out of plane to in plane, for increasing temperature of two different multilayer systems: a Ta(3) /Pt(20) /(Co(0.45) /Pt(0.6) /Ni(0.5) /Pt(0.6))₃ /CoFeB(1.8) /MgO(1.4) and a Pt(3)/CoFeB(1)/MgO(1.4) multilayer, and the evolution of their domain structure. This was performed by MOKE magnetometry in polar configuration and Lorentz Microscopy in Fresnel mode. The purpose of the investigation was to study the reorientation process in presence or absence of the Co/Pt/Ni/Pt multilayer and to separate the effects on the domain structure of Co/Pt/Ni/Pt and CoFeB.

As far as Ta(3) /Pt(20) /(Co(0.45) /Pt(0.6) /Ni(0.5) /Pt(0.6))₃ /CoFeB(1.8) /MgO(1.4) multilayer is concerned, MOKE hysteresis loops for increasing temperature showed first of all that the loops develop over a large field range. Then, we can also see a decrease in coercivity for increasing temperature. The reorientation temperature can be deduced to fit between 160°C and 180°C when the coercivity vanishes.

Fresnel imaging experiments allowed a detailed investigation of the reorientation process. The experiments carried out allowed identification of three temperature regimes:

- for 25°C < T < 130°C (regime 1), the magnetisation in the multilayer is out of plane everywhere because when the sample is tilted a small scale random domain structure is observed, whereas when we untilt the sample at the same field the domain structure disappear and we cannot see magnetic contrast. The domain structure and the magnetic

behaviour is the same for all temperatures in the range, but the magnetising sequences at different temperatures shows a decrease in both coercivity and domain size. Moreover the coercivity is reached at different fields in different areas of the sample, possibly due to an inhomogeneous distribution of the magnetic material or to the presence of a temperature gradient in the sample.

- for $130^{\circ}\text{C} < T < 220^{\circ}\text{C}$ (regime 2), contrast due to both out of plane and in plane magnetisation located in different regions is observed, due to the presence of a small in-plane component of magnetic induction. The domain structure is still a small scale random domain structure in the region magnetised out of plane. Contrast arising from out of plane magnetisation can be observed when the sample is tilted at 30° , whereas at 0° , the contrast present is an indication of the beginning of the reorientation process. As the specimen is heated up, the in-plane component of magnetisation becomes larger and the out of plane component becomes smaller. Contrast arising from the presence of an in-plane component is visible also when the specimen is tilted at 30° and becomes stronger for increasing temperature when the sample is at 0° tilt.
- for $220^{\circ}\text{C} < T < 300^{\circ}\text{C}$ (regime 3), the magnetisation has an in plane component everywhere and strong magnetic ripple. The coercivity is very small in this temperature range and this is typical of a soft magnetic material magnetised in plane. Indeed the behaviour appears similar to the one found in the CoFeB film 30\AA thick investigated in chapter 3.

To conclude for this specimen, we can say that for lower temperatures ($25^{\circ}\text{C} - 220^{\circ}\text{C}$) the specimen appears to have a strong perpendicular anisotropy. We observed a small scale random domain structure that we can ascribe to perpendicularly magnetised domains. For higher temperatures ($220^{\circ}\text{C} - 300^{\circ}\text{C}$) we found a behaviour typical of a soft magnetic material magnetised in plane with low anisotropy and high susceptibility.

The purpose of the investigation of the Pt(3)/CoFeB(1)/MgO(1.4) multilayer, is to understand how the reorientation process and the domain structure changes without the presence of the Co/Pt/Ni/Pt piece in the multilayer. The MOKE hysteresis loops for increasing temperature show that the loops develop in a field range dramatically smaller than in the first sample. The coercive fields are much smaller and the decrease in coercivity with temperature is faster than for the Ta(3)/Pt(20)/(Co(0.45)/Pt(0.6)/Ni(0.5)/Pt(0.6))₃/CoFeB(1.8)/ MgO(1.4) multilayer. The reorientation occurs at a temperature between 200°C and 220°C when the coercivity vanishes.

Fresnel imaging experiments, that allowed a detailed investigation of the reorientation process for Ta(3) /Pt(20) /(Co(0.45) /Pt(0.6) /Ni(0.5) /Pt(0.6))₃ /CoFeB(1.8) /MgO(1.4) multilayer, were not so effective for Pt(3)/CoFeB(1)/MgO(1.4) multilayer. Indeed, for instrumental reasons, we were not able to investigate the magnetic behaviour of the specimen for temperatures above 110°C. The magnetisation was observed to be out of plane for all the temperatures investigated. The sample develops a different domain structure when the sample is heated above or below 100°C. In the latter case isotropic serpentine domain structure is visible, with a large periodicity, whereas in the former case, an anisotropic stripe domain structure is visible with a small periodicity.

Our results for both samples are consistent with the experimental works of Allenspach and Bishop [1] and Berger and Hopster [2]. In [1] the magnetisation direction reorientation from out of plane to in plane in Fe/Cu epitaxial films was studied by SEMPA (spin-polarised scanning electron microscopy). They found that the multi-domain state with alternating out of plane domain magnetisation is the lowest energy state for films with an out of plane magnetisation. An analogous result was found in [2], where the magnetisation reversal properties near the reorientation phase transition of ultrathin Fe/Ag films were studied by MOKE experiments. They also found that the multi-domain state with alternating out of plane domain magnetisation is the favourable energy state for films with an out of plane magnetisation, and also that the occurrence of the in-plane magnetisation marks the real reorientation transition. An analogous result was obtained in the theoretical work of Kashuba and Pokrovsky [3] where they presented a theory of stripe domain structure in a thin ferromagnetic film. They predicted a multi-domain structure with domain magnetisation perpendicular to the surface at temperatures below the reorientational phase transition from out-of-plane to in-plane magnetization. Another study consistent with our findings is the one of Xiao *et al.* [4]. They found a linear decrease of coercivity with increasing temperature during the study of magnetic reorientation in Pd/(Pt/Co/Pt) multilayers.

We were able to successfully image the re-orientation process for the thicker sample whereas the thinner sample presented practical problem when the coercivity dropped below 20 Oe. The conclusion of this work is of great importance in the light of the recent findings of Ikeda *et al.* [5], who reported a TMR over 120% in perpendicular MTJs consisting of Ta/CoFeB/MgO/CoFeB/Ta. The investigation of the reorientation process of the magnetisation in the thinnest sample could be pursued with the new microscope at

Glasgow to be installed next year in which any programmable will be possible and this will be ideal for studying ultra-soft magnetic materials.

In the next chapter conclusions and future work will be discussed.

Bibliography

- [1] Allenspach R. and Bischof A., *Phys. Rev. Lett.*, (1992), **69**, 3385.
- [2] Berger A. and Hopster H., *J. Appl. Phys.*, (1996), **79**, 5619.
- [3] Kashuba A.B. and Pokrovsky V.L., *Phys. Rev. B*, (1993), **48**, 10335.
- [4] Xiao Y. *et al.*, *J. Appl. Phys.*, (1996), **79**, 6267.
- [5] Ikeda S. *et al.*, *Nat. Mater.*, (2010), **9**, 721.

CHAPTER 6

General summary and future work.

6.1 Summary

The work presented in this PhD thesis described the characterisation of the physical structure, composition and domain structure of advanced magnetic materials by electron microscopy within the FP6 European Research Training Network "Spinswitch". We investigated MgO/CoFeB/MgO multilayers to be employed in magnetic sensors; Ni₈₀Fe₂₀/Cu electrodeposited nanowires to be employed as spin transfer torque devices; multilayers with perpendicular anisotropy which represent potential candidates to be employed in the next generation of MRAMs.

In Chapter 3 we described an investigation using conventional transmission electron microscopy (TEM) and Lorentz microscopy to characterise respectively the physical microstructure and the domain structure of the CoFeB free layer of a MTJ, embedded in a multilayer composed by SiN/MgO(50)/CoFeB(t)/MgO(15) (units in Å), with thickness, t , from 30 Å down to 14 Å. As regards the physical microstructure, the TEM images and their respective diffraction patterns show that the CoFeB layer appears polycrystalline in character and continuous. Thus physically the plan view sections show the structure of the films to be quite similar.

The magnetization reversal behaviour observed during Lorentz TEM experiments are found to vary considerably with the CoFeB thickness, with both domain wall formation and magnetisation rotation seen. Experiments were carried out by applying field in range 90 Oe to -90 Oe. In the thicker film the behaviour was characteristic of a typical soft magnetic material with uniaxial anisotropy. However the magnetic reversal of the thinner film was more complex. A particular characteristic of the 14 Å CoFeB layer is the variation of domain wall angle seen when varying the orientation of the applied field. This wall asymmetry suggests the presence of a unidirectional anisotropic energy term. To assist in the interpretation of these experimental results a modified Stoner–Wohlfarth model has been constructed and calculations have been carried out by using a MATLAB

code. The calculations gave a good agreement with the experimental results for the set of parameters which showed that a unidirectional anisotropy term was present almost orthogonal to the uniaxial anisotropy with a characteristic field a small fraction of the anisotropy field. The agreement with the experimental results poses a question as to the physical phenomenon that is the possible origin of the unidirectional anisotropy. There is evidence in literature that deposition and/or annealing would produce interfacial effects in CoFeB/MgO bilayers and such effects become more important for decreasing thickness of the ferromagnetic layer. This is supported by results obtained by experiments performed by Read *et al.* [22] and Hindmarch *et al.* [23] that have shown the formation of interfacial effects in CoFeB/MgO bilayers that could possibly lead to exchange bias properties.

In Chapter 4 we described the characterisation by electron microscopy of morphology, physical structure, composition and magnetic configuration of Ni₈₀Fe₂₀(Py)/Cu nanowires grown by electrodeposition in anodic alumina and polycarbonate templates. These studies are of great importance in view of applications of nanowires as spin transfer torque based device. First of all the characterisation of nanowires grown in anodic alumina template was described (section 4.2). The nanowires have a polycrystalline structure with a large grain size distribution and irregular topography. Nanowires alternating thick and thin layers with transparent thin layers and nanowires with homogeneous contrast in BF images were found in the same sample. As concerned the composition, nanowires with homogeneous contrast appeared to be uniform NiFe nanowires because we could not detect any Cu in the nanowire. The investigation of nanowires with alternating thick and thin layers by EDX has shown that in the non-transparent region there is no Cu, and Ni and Fe are not in the proportion of the nominally deposited Py. The transparent region is an area with a lower density of material where we can find Ni and Fe in different proportion, but we found also Cu. The results of the compositional investigation highlight possible issues related to the deposition of the different chemical elements and the removal of the template by chemical etching.

In order to minimise these problems, a new set of nanowires was grown in polycarbonate template. Nanowires grew polycrystalline, with a large grain size distribution, and their topography was more regular than the nanowires previously described. From the compositional point of view we found that in nanowires with homogeneous contrast Ni and Fe were again in different proportions to the intended deposited values and no Cu was detected. In the nanowires with apparent alternating thick and thin layers, Ni and Fe were

found to be in the ratio $(4.8 \pm 0.7):1$ ratio, close to what expected in Py in the thick layers, whereas in thin layers we could not detect any Cu and the Ni to Fe ratio was different from the thicker layers. These findings, similar to what observed in nanowires grown in alumina templates, would suggest that there is a serious issue with the deposition of the Cu, and the lack of Cu probably did not depend on the chemical used to perform the dissolution of the template.

We then characterised the magnetic properties of nanowires grown in polycarbonate template by Lorentz microscopy. The first mode to be used in the Lorentz microscopy investigations of magnetic materials is Fresnel imaging. In order to establish the experimental conditions and to get an idea of contrast levels due to magnetic and electrostatic contributions, Fresnel image simulations were performed. From the experimental point of view, it was not possible to determine any magnetic contribution conclusively, almost certainly due to small changes in intensity, alignment and issues with normalisation of the signal which occurs between images and the low level of the magnetic contrast. Micromagnetic simulations predicted the reversal of magnetisation during EA cycle through formation of vortex states. Magnetisation configuration of the initial state, remanent state and final state were used to carry out simulations of DPC images. Calculations of stray field distributions were performed for different configurations: uniform continuous nanowire magnetised upwards or downwards, uniform layered nanowire magnetised upwards or downwards, uniform continuous nanowire with an abrupt head to head domain wall and a layered nanowire in the remanent state. In reality the nanowires can be many microns long and the simulations of such lengths it is not practical because it would require too long computation time. To make a comparison between simulated and experimental images we concentrated on the analysis of the flux emanating from the end of the nanowires as this would be in free space where the noise level in the images would be much lower. We made a comparison of the line traces perpendicular to the wire length in the maps of the longitudinal component of integrated magnetic induction. The comparison was based on the measurements of the peak value of the integrated field relative to the maximum for the wire $B_{st,max}$, and the full width at half maximum (FWHM) relative to the diameter of the nanowire. Based on these measurements, the small difference found for a uniform continuous and a uniform layered nanowire we can say that we may find it difficult to distinguish whether the nanowire is continuous or layered. Concerning the nanowire with an abrupt head to head wall, it may be possible distinguish whether a domain wall is present compared to a nanowire with no

wall, however this would be unlikely for a very long wire. If we look at the values for the nanowire in the remanent state with vortex states in each layer, we can notice that the peak value is ten times smaller than the value found for the uniform continuous nanowire and the FWHM is almost half, thus it would then provide a challenge to image the nanowire in this state.

During DPC imaging experiments it was possible to observe a change in magnetic state of the nanowire, confirmed by a change in sign from negative to positive in the intensity of the stray field peak. We found only a qualitative agreement with different simulated states performed in the previous section. However no one simulation gave an agreement with the albeit noisy experimental images. This may have been due to a number of factors, for example irregularities in the topography of real nanowires compared to the perfect geometry of simulated nanowires; also differences in composition and structure between the observed nanowires and those simulated.

Finally the research presented in Chapter 5 described the investigation of reorientation process of magnetisation from out of plane to in plane, for increasing temperature of two different multilayer systems: a Ta(3) /Pt(20) / (Co(0.45) /Pt(0.6) /Ni(0.5) /Pt(0.6))₃ /CoFeB(1.8) /MgO(1.4) and a Pt(3)/CoFeB(1)/MgO(1.4) multilayer, and the evolution of their domain structure. This was performed by MOKE magnetometry in polar configuration and Lorentz Microscopy in Fresnel mode. The purpose of the investigation was to study the reorientation process in presence or absence of the Co/Pt/Ni/Pt multilayer and to separate the effects on the domain structure of Co/Pt/Ni/Pt and CoFeB.

As far as Ta(3) /Pt(20) /(Co (0.45) / Pt(0.6) /Ni(0.5) /Pt(0.6))₃ /CoFeB(1.8) /MgO(1.4) multilayer is concerned, MOKE hysteresis loops for increasing temperature showed first of all that the loops develop over a large field range. Then, we can also see a decrease in coercivity for increasing temperature. The reorientation temperature can be deduced to fit between 160°C and 180°C when the coercivity vanishes.

Fresnel imaging experiments allowed a detailed investigation of the reorientation process. The experiments carried out allowed identification of three temperature regimes:

- for 25°C < T < 130°C (regime 1), the magnetisation in the multilayer is out of plane everywhere because when the sample is tilted a small scale random domain structure is observed, whereas when we untilt the sample at the same field the domain structure disappear and we cannot see magnetic contrast. The domain structure and the magnetic

behaviour is the same for all temperatures in the range, but the magnetising sequences at different temperatures shows a decrease in both coercivity and domain size. Moreover the coercivity is reached at different fields in different areas of the sample, possibly due to an inhomogeneous distribution of the magnetic material or to the presence of a temperature gradient in the sample.

- for $130^{\circ}\text{C} < T < 220^{\circ}\text{C}$ (regime 2), contrast due to both out of plane and in plane magnetisation located in different regions is observed, due to the presence of a small in-plane component of magnetic induction. The domain structure is still a small scale random domain structure in the region magnetised out of plane. Contrast arising from out of plane magnetisation can be observed when the sample is tilted at 30° , whereas at 0° , the contrast present is an indication of the beginning of the reorientation process. As the specimen is heated up, the in-plane component of magnetisation becomes larger and the out of plane component becomes smaller. Contrast arising from the presence of an in-plane component is visible also when the specimen is tilted at 30° and becomes stronger for increasing temperature when the sample is at 0° tilt.
- for $220^{\circ}\text{C} < T < 300^{\circ}\text{C}$ (regime 3), the magnetisation has an in plane component everywhere and strong magnetic ripple. The coercivity is very small in this temperature range and this is typical of a soft magnetic material magnetised in plane. Indeed the behaviour appears similar to the one found in the CoFeB film 30\AA thick investigated in chapter 3.

To conclude for this specimen, we can say that for lower temperatures ($25^{\circ}\text{C} - 220^{\circ}\text{C}$) the specimen appears to have a strong perpendicular anisotropy. We observed a small scale random domain structure that we can ascribe to perpendicularly magnetised domains. For higher temperatures ($220^{\circ}\text{C} - 300^{\circ}\text{C}$) we found a behaviour typical of a soft magnetic material magnetised in plane with low anisotropy and high susceptibility.

The purpose of the investigation of the Pt(3)/CoFeB(1)/MgO(1.4) multilayer, is to understand how the reorientation process and the domain structure changes without the presence of the Co/Pt/Ni/Pt piece in the multilayer. The MOKE hysteresis loops for increasing temperature show that the loops develop in a field range dramatically smaller than in the first sample. The coercive fields are much smaller and the decrease in coercivity with temperature is faster than for the Ta(3)/ Pt(20)/ (Co(0.45)/ Pt(0.6)/ Ni(0.5) /Pt(0.6))₃/ CoFeB(1.8)/ MgO(1.4) multilayer. The reorientation occur at a temperature between 200°C and 220°C when the coercivity vanishes.

Fresnel imaging experiments, that allowed a detailed investigation of the reorientation process for Ta(3) /Pt(20) /(Co(0.45) /Pt(0.6) /Ni(0.5) /Pt(0.6))₃ /CoFeB(1.8) /MgO(1.4) multilayer, were not so effective for Pt(3)/CoFeB(1)/MgO(1.4) multilayer. Indeed, for instrumental reasons, we were not able to investigation of the magnetic behaviour of the specimen for temperatures above 110°C. The magnetisation is out of plane for all the temperatures investigated. The sample develops a different domain structure when the sample is heated below 100°C or above 100°C. In the first case isotropic serpentine domain structure is visible, with a large periodicity, whereas in the second case, an anisotropic stripe domain structure is visible with a small periodicity.

We were able to successfully image the re-orientation process for the thicker sample whereas the thinner sample presented practical problem when the coercivity dropped below 20 Oe. The investigation of the reorientation process of the magnetisation in the thinnest sample could be pursued with the new microscope at Glasgow to be installed next year in which any programmable will be possible and this will be ideal for studying ultra-soft magnetic materials.

6.2 Future work

Several issues were left open in this PhD work, due to time constraints, which can be the subject of future work.

In the case of MgO/CoFeB/MgO multilayers, we need direct evidence of formation of interfacial structures that could give rise to an exchange bias effect. HRTEM and analytical TEM experiments would be a good starting point for a detailed investigation of the possible presence of interfacial structures. Additionally, it would be interesting to investigate the physical structure and magnetic behaviour of multilayers with thinner CoFeB layer to see if we can observe changes with respect to the thicknesses investigated so far.

In Chapter 4 we showed initial results from one of the first attempts at Lorentz TEM imaging of electrodeposited nanowires. The awareness of the limitations of these experiments and the results of the simulations and calculations will point the way forward for a future study, however it is apparent that good quality nanowires are essential for such

a study on the integrity of the nanowires structure would need to be proven to survive the etching process to remove the templates.

In chapter 5 we said that the new microscope at Glasgow to be installed next year, would give the opportunity to pursue the investigation of Pt(3)/CoFeB(1)/MgO(1.4) multilayer for higher temperatures. The conclusion of this work is of great importance in the light of the recent findings of Ikeda *et al.*¹, who reported a TMR over 120% in perpendicular MTJs consisting of Ta/CoFeB/MgO/CoFeB/Ta. Another effect that can be investigated is the effect of the number of repetitions of Co(0.45)/Pt(0.6)/Ni(0.5)/Pt(0.6) on the domain structure of the specimen. This can be a good opportunity to see whether we can increase the range of temperatures where the magnetisation is out of plane everywhere by simply change the number of repetition of Co(0.45)/Pt(0.6)/Ni(0.5)/Pt(0.6) in the specimen.

¹ Ikeda S. *et al.*, *Nat. Mater.*, (2010), **9**, 721.

APPENDIX 1 - MATLAB CODE USED FOR CALCULATIONS IN SECTION 3.5

```
clear

% set up parameters;

Theta    = -20:10:20;

HK       = 120;

hStep    = 1;

phi      = 5:365;

h        = -150:hStep:150;

[H,Phi] = meshgrid(h,phi);

Hcycle   = [h,flipplr(h)];


keepETot          = zeros(length(Theta),length(phi),length(h));

keepMinPos        = zeros(length(Theta),length(Hcycle));

keepPeakPos       = zeros(length(Theta),6); % 6 is probably the max
numpeaks!

keepPhiSwitch_pre = zeros(length(Theta),6);

keepPhiSwitch_post = zeros(length(Theta),6);


options
optimset('Display','notify','GradObj','off','LargeScale','off');

for Inc = 1:length(Theta)

    theta          = Theta(Inc);

    keepETot(Inc, :, :) = HK*sind(Phi).^2-2*H.*cosd(theta-Phi);

    [dummy,StartPoint] = min(keepETot(Inc, :, 1));

    StartPoint       = phi(StartPoint)+rand*5;
```

```

    for i = 1:length(Hcycle) % Now determine the minimum point for each H
value
        Efunction      = @(x) HK*sind(x).^2-2*Hcycle(i).*cosd(theta-x);

        [MinPos(i),dummy,exitflag] =
fminunc(Efunction,StartPoint,options);

        if exitflag<=0, disp(['exitflag = ' num2str(exitflag) ' at h(i) =
' num2str(Hcycle(i))]); end

        StartPoint      = MinPos(i) + rand(1)*5; % give a random kick so
don't start at minimum.

    end;

    % Wrap values onto -pi to =2pi

    MinPos = mod(MinPos-min(phi),360) + min(phi);

    keepMinPos(Inc,1:length(MinPos)) = MinPos(:);


    % Get rid of the line joining the points that have been unwrapped

    CutOff = 5;

    [howbig,where]=sort(abs(diff(MinPos)),'descend');

    while (abs(abs(howbig(1))-360)<1), howbig(1)=[]; where(1)=[]; end;

    NumPeaks      = sum(howbig >= CutOff);

    PeakPos      =
Hcycle(where(1:NumPeaks))+(Hcycle(where(1:NumPeaks)+1)-
Hcycle(where(1:NumPeaks)))/2;

    keepPeakPos(Inc,1:length(PeakPos)) = PeakPos(:);

    PhiSwitch_pre  = MinPos(where(1:NumPeaks));

    keepPhiSwitch_pre(Inc,1:length(PhiSwitch_pre)) = PhiSwitch_pre(:);

    PhiSwitch_post = MinPos(where(1:NumPeaks)+1);

    keepPhiSwitch_post(Inc,1:length(PhiSwitch_post)) = PhiSwitch_post(:);


    disp(['At theta = ' num2str(theta) ', found ' num2str(NumPeaks) '
peaks: ' num2str(PeakPos)]);

```



```

        disp(['At theta = ' num2str(theta) ', found ' num2str(NumPeaks) ' pre
switching angles at: ' num2str(PhiSwitch_pre)]);

        disp(['At theta = ' num2str(theta) ', found ' num2str(NumPeaks) '
post switching angles at: ' num2str(PhiSwitch_post)]);

end

% code to plot out a chosen contour plot

pickplot = 1;

figure; contour(H, Phi, squeeze(keepETot(pickplot, :, :)), 20);

axis square; xlabel('H (Oe)'); ylabel('Phi (Degrees)'); colormap jet;

hold on

plot(Hcycle(1:length(h)), keepMinPos(pickplot, 1:length(h)), 'k', ...

Hcycle((length(h)+1):end), keepMinPos(pickplot, (length(h)+1):end), 'k:');

```